Structural Dynamic Analysis of Spent Nuclear Fuel

Spent Fuel and Waste Disposition

Prepared for
U.S. Department of Energy
Spent Fuel and Waste Science and Technology

Nicholas A Klymyshyn, Pavlo Ivanusa, Kevin Kadooka, Casey Spitz, Elias D Irick, Philip J Jensen, Steven B Ross, Brady D Hanson

Pacific Northwest National Laboratory

September 30, 2019
SFWD-SFWST-M2SF-19PN010202014
PNNL-29150

SUMMARY

This unlimited distribution milestone report is the deliverable for M2SF-19PN010202014.

This report completes the modeling and analysis related to the Equipos Nucleares Sociedad Anónima/U.S. Department of Energy (ENSA/DOE) spent nuclear fuel (SNF) multimodal transportation test (MMTT) campaign performed in 2017. A previous report studied the shock and vibration data generated during the MMTT and determined effective modeling and analysis methodologies and strategies. This report completes the modeling and analysis activity by applying the structural dynamic analysis models and methods to the Atlas railcar system. This analysis demonstrates that the MMTT configuration provided a conservative, bounding shock and vibration environment for SNF in comparison to finite element model results that are configured to represent the Atlas railcar system and all of its SNF package combinations.

Additionally, this report establishes a technical basis for recommending that no further analysis is necessary to demonstrate that SNF cladding will remain intact during shock and vibration loading conditions that occur during normal conditions of transportation (NCT). 10 CFR 71.71 defines package tests to demonstrate acceptable package performance under NCT conditions. The focus of this work is to demonstrate that SNF cladding will remain intact within the package while it is subjected to what 10 CFR 71.71 calls: Vibration normally incident to transport. The MMTT recorded negligible shock and vibrations on the SNF cladding during the test campaign, and this analysis supports the conclusion that intact fuel rods carried in any current SNF transportation package will experience similar, negligible, shock and vibration conditions.

This analysis follows a methodology that uses commercially available finite element software to generate dynamic and structural dynamic finite element models. The NUCARS (New and Untried Car Analytic Regime Simulation) software is used to create railcar dynamics models, using railroad industry standard modeling techniques with a few best-practice modeling features that were developed in the previous report. The LS-DYNA explicit finite element analysis code is used to implement a structural dynamic model of a single fuel rod. With the low magnitude of shock and vibration loads observed during the MMTT and related structural dynamic analyses of NCT shock and vibration conditions, it is sufficient to analyze the response of a single fuel rod because the fuel rod deflections are not large enough to cause contact between adjacent fuel rods in an assembly.

This analysis evaluates a large number of railcar dynamic responses to different track conditions at speeds of up to 80 mph. The dynamic loads generated during these railcar events create a library (or database) of loading conditions that are then applied to the single fuel rod structural dynamic model to calculate the strains, strain energy, and deformation of the fuel rod. An important trend observed in the calculation results is that lighter packages tend to cause a larger response from the fuel rods. However, even the lightest package predicts strains, strain energies, and fuel rod deflections that are lower than the test data that was collected during the MMTT.

Several variables and potential sensitivities were evaluated. The most significant feature evaluated is the potential diametrical gap in packages that carry a fuel canister. A non-zero diametrical gap is expected in all such systems to allow the canister to be loaded and unloaded. It is estimated that SNF in canister systems could experience loads that are four to six times higher than a bare fuel cask, but the potentially higher strains are still not significant when compared to the fuel cladding failure limit or the fuel cladding fatigue limits. Changes in grid spacer configuration, boiling water reactor fuel rod geometry, fuel rod stiffness, and the localized cladding strain effects caused by fuel pellets are all too insignificant to be of concern during NCT shock and vibration loading.

A fatigue evaluation was completed based on the library of structural dynamic results. Compared to the fuel cladding strain data recorded during the MMTT, the models of the Atlas railcar system predict even

lower fatigue damage to the cladding. In both configurations, it is reasonable to conclude that the fatigue damage is approximately zero.

The key argument to support the conclusion that no further NCT strain or fatigue analysis is needed is that both testing and analysis arrive at the conclusion that NCT shock and vibration is negligible. Consideration of the full fleet of licensed transportation packages and the railcar design that is anticipated to carry the majority of SNF in the United States leads to the conclusion that any practical SNF transportation campaign will experience negligible shock and vibration loads. There are no known variables or uncertainties that could alter the system parameters enough to magnify the shock and vibration to a magnitude that challenges the strength of the cladding material.

ACKNOWLEDGEMENTS

The authors would like to express our sincere thanks to the project's DOE sponsors, Ned Larson and John Orchard for supporting and funding this work.

The authors would also like to thank our collaborators on the multimodal transportation test (MMTT) campaign, including staff from Sandia National Laboratories, Equipos Nucleares S.A, S.M.E (ENSA), Korean Atomic Energy Research Institute (KAERI), and the Association of American Railroads Transportation Technology Center, Incorporated (TTCI).

We would also like to acknowledge and express our appreciation for additional organizations that helped make the MMTT possible with their contributions, including: ENUSA Industrias Avanzadas, S.A., S.M.E. (ENUSA), Empresa Nacional de Residuos Radioactivos SA (ENRESA), Korean Radioactive Waste Agency (KORAD), KEPCO Nuclear Fuel Company (KNF), Argonne National Laboratory (ANL), Objective Engineers Inc., and Coordinadora.

This page is intentionally left blank.

CONTENTS

This page is intentionally left blank.

LIST OF FIGURES

LIST OF TABLES

ACRONYMS

AAR	Association of American Railroads
ASTM	ASTM International
BWR	boiling water reactor
CG	center of gravity
CIRFT	cyclic integrated reversible-bending fatigue tester
DOE	U.S. Department of Energy
EI	fuel rod stiffness (modulus of elasticity multiplied by area moment of inertia)
ENSA	Equipos Nucleares Sociedad Anónima
FEA	finite element analysis
FFT	fast Fourier transform
FY	fiscal year
ID	internal diameter
Mb	bending moment
MMTT	multimodal transportation test
NCT	normal conditions of transportation
NUCARS	New and Untried Car Analytic Regime Simulation
OD	outer diameter
ORNL	Oak Ridge National Laboratory
PNNL	Pacific Northwest National Laboratory
PSD	power spectral density
PWR	pressurized water reactor
RMS	root mean square
SDOF	single degree of freedom
S-N	strain cycle amplitude vs number of cycles to failure
SNF	spent nuclear fuel
SNL	Sandia National Laboratories
TTCI	Transportation Technology Center Inc.
UNF	used nuclear fuel

This page is intentionally left blank.

SPENT FUEL AND WASTE SCIENCE AND TECHNOLOGY/STORAGE AND TRANPORTATION

STRUCTURAL DYNAMIC ANALYSIS OF SPENT NUCLEAR FUEL

1. Introduction

The 2017 Equipos Nucleares Sociedad Anónima/U.S. Department of Energy (ENSA/DOE) multimodal transportation test (MMTT) campaign provided a significant amount of practical test data that were useful for validating the structural dynamic finite element models and analysis methods used in the structural analysis of spent nuclear fuel (SNF) under normal conditions of transportation (NCT). In support of the MMTT and prior dynamic testing, Pacific Northwest National Laboratory (PNNL) provided modeling support, including pretest modeling to inform the test plans and post-test modeling to evaluate the results and validate models for future use. In 2018, a report (Klymyshyn et al. 2018) detailed the modeling and analysis activities performed to study the test data and determine effective structural dynamic analysis modeling methods. This report applies the modeling and analysis lessons learned from studying and modeling the test conditions to the topic of general structural dynamic analysis of SNF transportation in the United States. The goal of this report is to demonstrate reasonable modeling and analysis methods that are validated by the MMTT test data and can be used to demonstrate that NCT shock and vibration do not present a challenge to fuel cladding integrity.

The MMTT was a multinational collaborative research and development activity that involved organizations from the United States, Spain, and Korea. In 2017, DOE sponsored a test campaign that measured the shock and vibration in SNF under NCT. DOE partnered with ENSA, a Spanish manufacturer of used nuclear fuel (UNF) dry storage and transportation casks, to conduct the test campaign with a newly fabricated ENUN 32P dual-purpose bare fuel storage and transportation cask. Three surrogate instrumented fuel assemblies (containing surrogate mass instead of real radioactive fuel pellets) were placed inside the cask to record accelerations and strains on the fuel cladding during cask handling, truck transportation, ship transportation, rail transportation, and captive track testing at the Transportation Technology Center Inc. (TTCI) Facility for Accelerated Service Testing in Pueblo, Colorado. The MMTT test plan was documented by McConnell et al. (2018); the data and analysis of the data were documented by Kalinina et al. (2018).

One of the key results of the MMTT was that the shock and vibration environment SNF is subjected to during NCT is very benign. The peak strains recorded on the fuel rods containing surrogate fuel pellet mass was less than approximately 0.0001 mm/mm. This report typically reports strain in the non-standard units of microstrain, using the symbol uE. For example, 1 uE is equal to 0.000001 mm/mm. It is useful to discuss strains in this manner because the range of cladding strains recorded in the MMTT and discussed by Klymyshyn et al. (2018) was 1 uE to 100 uE. The strain values discussed in this report are also generally in the range of 1 uE to 100 uE. Note that the significance of these low strains was discussed in Klymyshyn et al. 2018. The strain range of 1 uE to 100 uE is far below irradiated zirconium alloy cladding yield strength (about 10,000 uE). Klymyshyn et al. 2018 used 10 uE as a threshold to count fatigue cycles, but 100 uE is a more practical threshold for determining if a strain cycle would contribute to cumulative fatigue damage.

The relatively low strains in the fuel rod cladding also relates to relatively low strain energy in the fuel rod cladding. The finite element models used to calculate transient fuel rod deflection during dynamic loading scenarios calculate strain energy in the fuel rod cladding as well as stress and strain. It is important to point out that the range of strain energies calculated for fuel rods in the MMTT load cases is

below 5 mJ, which is within the kinetic energy range of a flying insect or a raindrop (Klymyshyn et al. 2018). This illustrates how low the shock and vibration range of SNF fuel rods is during NCT. This low energy level is what makes it possible to conduct a generic structural analysis that covers a broad range of SNF transportation scenarios. The energy is so low that the anticipated differences in design and transportation configurations that may exist in the practice of real SNF transportation are not significant enough to create a sufficiently higher energy environment to challenge fuel cladding integrity.

The analysis methodology used in this report is described in Section 2. A number of commercial finite element codes and analysis software are required to complete the structural dynamic analysis of SNF transportation. No user subroutines or novel pieces of software were needed to complete this analysis. The analysis made use of software scripting languages to build models and automate the calculation of many analysis cases, but everything described in this report could be reproduced using other commercial software packages.

The MMTT used the ENSA ENUN 32-P dual-purpose (dry storage and transportation) cask, which is a bare fuel cask that has a mass and storage capacity similar to other cask systems licensed for use in the United States. The cradle (or skid) is the structure that holds the cask in place and connects it to the conveyance system. In the case of the MMTT, the cradle design permitted transportation on any flatbed conveyance, including trailers and railcars. During the ship transportation legs of the MMTT, the cask and cradle were situated on trailers that were secured in place. Not all cask and cradle designs have the same level of flexibility. In terms of structural dynamics, the mass of the cask and the stiffness and damping characteristics of the cradle are important specific design features that affect the transmission of loads to SNF. Section 3 discusses how variation in cask and cradle design was accounted for.

In terms of vehicle dynamics, the MMTT used a general-purpose railcar designed and approved for hauling heavy freight on US rail lines. Test data collected during the captive rail tests at TTCI indicate that the as-tested railcar-cradle-cask system would not pass the Association of American Railroads (AAR) standard S-2043 (AAR 2017), which defines dynamic performance requirements for railcars transporting SNF. S-2043 requirements tend to drive the railcar design toward a softer ride, but the purpose of S-2043 is to minimize the potential for derailments of the railcar system. S-2043 is not concerned with the ride quality, or the characteristics of shock and vibration loads transmitted to the SNF. In general, it can be assumed that a S-2043 railcar would provide a gentler shock and vibration environment than the MMTT test, but for a defensible structural dynamic analysis of SNF transported on the US rail system, the dynamic behavior and load transmission from a S-2043 compliant railcar needs to be accounted for. The analysis described in this report uses the Atlas railcar (and 17 cask and cradle configurations) as the basis for the NCT shock and vibration environment. This topic is discussed in detail in Section 4 of this report.

In terms of SNF structural mechanics, the MMTT used a close approximation of real, irradiated SNF by using surrogate mass within zirconium alloy fuel cladding tubes. Finite element models that represent the SNF tubes as homogeneous beams calculate results that agree well with the test data. One necessary conversion from the test conditions to real SNF transportation is accounting for the contribution of fuel pellets to beam stiffness. Test data from Oak Ridge National Laboratory (ORNL) (Wang et al. 2016) indicate that some amount of stiffness contribution is appropriate. The surrogate mass used in the MMTT was not bonded to the inside of the cladding tubes, so its beam stiffness contribution was negligible. The analysis described in this report considers fuel rod equivalent beam stiffness (EI) to be an important uncertainty. Fuel rod structural mechanics is discussed in more detail in Section 5 of this report.

The cladding fatigue analysis performed on the strain gage data from the westbound rail trip of the MMTT concluded that it would take 10 billion transportation trips of 2,000 miles each to challenge fuel rod fatigue strength (Klymyshyn et al. 2018). This analysis assumed the MMTT surrogate fuel rods provided a close analog to real SNF. However, fuel rod stiffness, cask and cradle design, and railcar design all need to be accounted for when performing a defensible structural analysis of fuel cladding. This report discusses the fatigue analysis in detail in Section 6.

The results of this analysis form a rational basis for supporting the conclusion that shock and vibration loads applied to SNF during NCT are negligible for the current range of SNF transportation systems and technologies. Significant changes in fuel design or transportation modes or characteristics would be necessary to change that conclusion. Section 7 discusses this conclusion and identifies the kinds of changes that would need to happen to threaten the integrity of SNF cladding during NCT.

Appendices A and B, respectively, contain the results of the analysis of single-rod model structural dynamics and single-rod model fatigue.

This page is intentionally left blank.

2. Analysis Methodology

The structural analysis of SNF under transportation conditions is complex because the loads are dynamic and vary over time. Typical structural analysis applications assume static or quasi-static loading conditions. A structure's response to static forces is quantified in terms of stress, strain, deflection, and other metrics, and then the calculated values are compared against acceptable limits that assure function or safety. A structural dynamic analysis follows similar principles, but the goal is to calculate the deflection of a structure over time. The mechanics of rigid body motion and flexural body deflection are implemented in finite element analysis codes. Both linear elastic finite element analysis (FEA) models and nonlinear models with contact and plastic material behavior are used in this methodology.

The steps in the structural dynamic methodology are illustrated in Figure 1. These steps are summarized in this section and described in more detail in the following sections of this report.

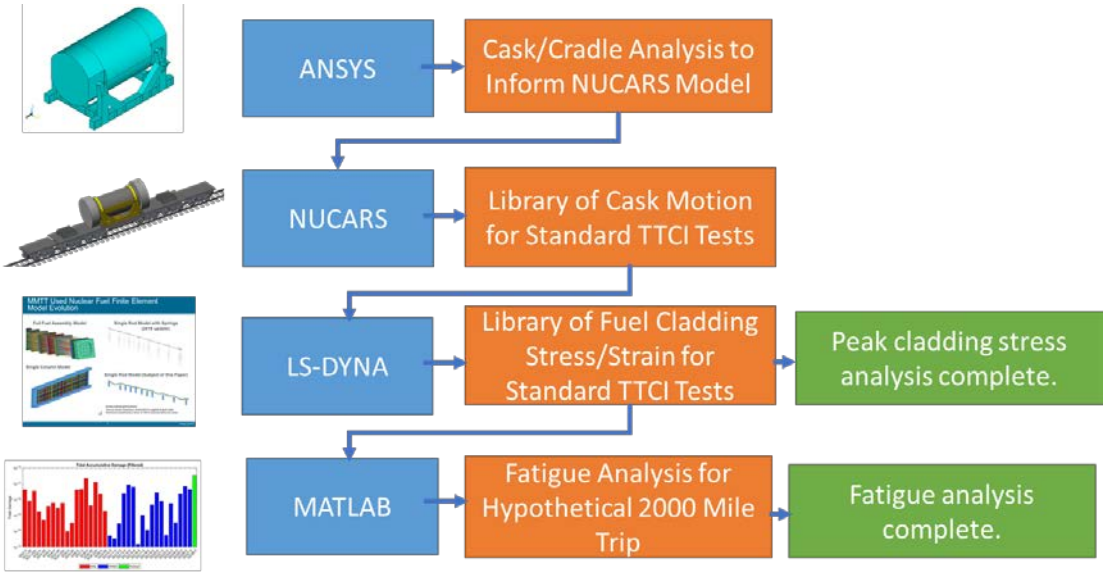

Figure 1. Analysis methodology roadmap.

The first step is a linear elastic modal analysis of the cask and cradle structure that is used to approximate the cask and cradle as a single degree of freedom (SDOF) spring-mass-damper system, as shown in Figure 2. The constants *m*, *k*, and *c* represent the mass of the package, the stiffness of the cradle, and the system damping, respectively. The SDOF model parameters are needed in the railcar dynamics modeling step, where the SDOF model parameters are implemented in the NUCARS model. Representing the cask and cradle in this manner was a modeling practice developed by Klymyshyn et al. (2018) and is justified because strong agreement with the MMTT test data was achieved. In that case, the SDOF system was defined based on MMTT test data.

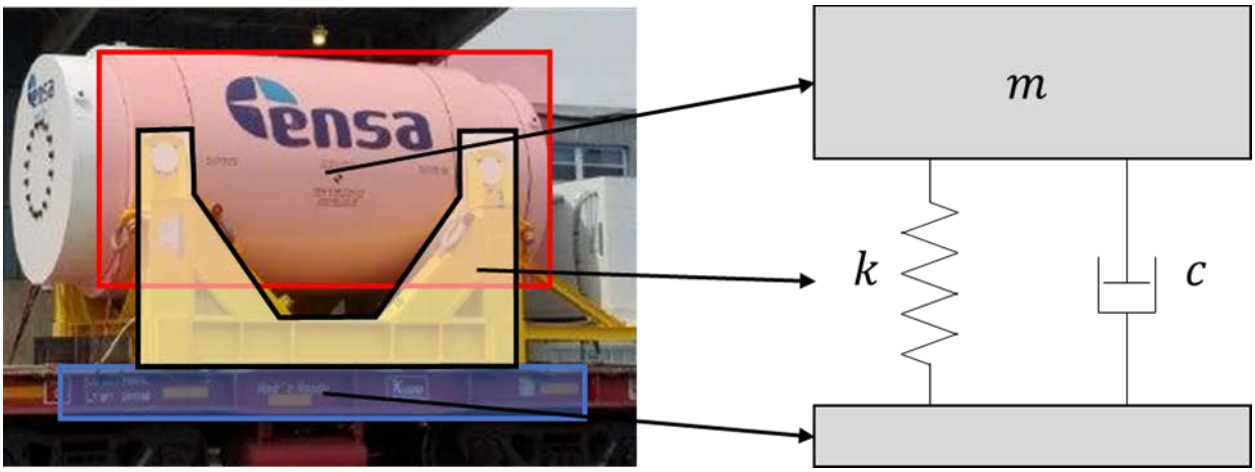

Figure 2: SDOF conceptual model sketch

Note that the SDOF model is a conceptual model of the cask and cradle behavior that is implemented in the NUCARS finite element code. The mass of the package is always known, but *k* and *c* depend on the cradle design and potentially other system features. The MMTT data was used to find a best fit approximation of *k* and *c* using optimization methods (Klymyshyn et al. 2018).

When test data are not available, analytical methods are needed to define the SDOF system. The development of the necessary SDOF constants for the Atlas railcar system is described in Section 3. Linear elastic modal analysis is used to determine the SDOF system natural frequency, which in turn is used to calculate *k* and *c* using fundamental dynamics equations, as described in Section 3.2.

An assumption of system damping must be made to complete the SDOF parameter calculations, and the MMTT data and related shaker table testing (Kalinina et al. 2019) provide insight into the range of damping. The role of damping in the SDOF model is to dissipate kinetic energy. Damping is a real phenomenon that is important to dynamics and structural dynamics, but it is not easy to predict without test data. In engineering practice, damping in safety basis calculations can be dictated by consensus codes and standards that define generic (conservatively low) damping values. Alternatively, specific mechanical testing can be done to justify higher damping values that are closer to reality. The analyses use a 20% damping in the cask-cradle SDOF model for the Atlas railcar, which is easily justified from the MMTT data. The justification is included in Section 3.

The output of the first step (ANSYS) in the analysis is SDOF model parameters (*k* and *c*, *m* is known) for every cask and cradle combination used for possible transportation of SNF in the US. In this study, 17 different cask and cradle designs are being considered; that is, the current complete set of licensed casks in the United States. The intent of this study is to cover the full range of existing casks being carried by the Atlas railcar system. If a new cask system is created and licensed in the United States, it is recommended that the new system be compared to the results of this study to determine if this structural dynamic analysis methodology should be implemented for the new cask system, or if the set of analyses described in this report is sufficient.

The second step of the methodology (NUCARS) is to perform railcar dynamics analyses to calculate the motion of the cask, which will be used as imposed boundary conditions for the fuel rod analysis in the next step of the analysis methodology (LS-DYNA). Railcar dynamics models are a standard feature of the modern railroad industry. Railcar dynamics models are used to certify railcar compliance with AAR S-2043, and other applicable standards. The typical purpose of railcar dynamics modeling and analysis is to confirm the railcar's ability to remain on the tracks under potentially challenging conditions. Ride quality is typically a secondary concern for freight car performance. SNF is sensitive to a vibration frequency range that is typically above the range of concern for derailment, but the NUCARS (New and Untried Car

Analytic Regime Simulation) (TTCI 2018) models and modeling methods discussed by Klymyshyn et al. (2018) matched the test data reasonably well. The NUCARS model is discussed in more detail in Section 4.

In this analysis, the source of the NUCARS rail car models was the Atlas railcar development project (AREVA 2018). PNNL was provided the same set of input files that were used to gain approval from AAR to proceed with the prototype testing phase of the S-2043 certification process. These models were generated by railroad modeling experts for design and certification, so they have been vetted and reviewed. PNNL used the Atlas models as the basis for the NUCARS analysis, with a few modifications that are described in detail Section 4. One of the key modifications was implementing the SDOF spring-mass-damper system to represent the cask and cradle, which was necessary to calculate the cask motion.

Cask motion is the key output of the railcar dynamics model, because it is the primary dynamic load applied to the structural dynamic model of the fuel rods. Transportation casks can be approximated as rigid structures in the typical NCT shock and vibration loading range. The output of NUCARS is rigid body motion, written as acceleration history files in ASCII file format. The ASCII output file is easily translated into a LS-DYNA (LSTC 2013) input file for completion of the third step in this methodology.

The railcar transportation load cases were selected from the normal set of test conditions that are regularly performed to demonstrate prototype railcar compliance with AAR S-2043. The tests are performed on captive track over a range of tightly-controlled speeds. Captive track is a railroad term for track that is off the open rail system, and the MMTT included captive track testing at TTCI and open rail transportation data collection (westbound and eastbound). The big difference between the two types of rail data is that the captive track testing was performed under controlled conditions (speed, track features) while the open rail transportation conditions were controlled by the railroad (speed, route, couplings, and daily progress.) The open rail MMTT data is unique because it recorded an actual cross-country transportation of an SNF railcar package, but there is no reason to expect the open rail data to include the most extreme, limiting conditions that are possible under NCT. However, the controlled, captive track tests at TTCI were designed by the railroad industry to evaluate and certify railcars. The AAR S-2043 tests were specified to provide an assurance against derailment based on railroad industry experience. Those certification tests are expected to be representative of open rail conditions and cover a broad range of potential loading conditions. This analysis selected three captive track certification tests as the basis for calculating cask motion during NCT:

- Pitch and Bounce: The rails are configured with a repeating vertical cusp shape that causes railcars to experience a combination of rotational load (pitch) and a vertical load (bounce).
- Single Bump: The rails are configured to have a single vertical perturbation. This case causes a similar response to a road crossing, and in the westbound rail transportation leg, it was a road crossing that caused the highest cask acceleration.
- Twist and Roll: The rails are configured to cause lateral and rotational loading.

These three standard railcar test cases were the same ones selected by Klymyshyn et al. (2018) to demonstrate the railcar dynamics model validation against MMTT test data. These three captive track cases were selected because they most closely represent the railcar behavior observed in the open rail MMTT data, and the three cases cover both vertical and lateral loading. The tests are always performed over a range of speeds in order to find railcar resonance responses, and the railcar dynamics models of the MMTT configuration were validated over the range of speeds within a validation acceptance range that was based on examples found in open railroad industry literature (see Klymyshyn et al. 2018 for details).

To generate the library of cask motion needed to analyze the SNF response, the 17 railcar configurations were analyzed in three track cases, at about 10 different train speeds (typically 30 mph to 80 mph in 5 mph increments), and two fuel rod stiffness assumptions, which is more than 1,600 analysis cases. These cases form the library of cask motion that was available for analysis of the fuel cladding response.

The next step of the analysis is to select cases from the cask motion library and apply them to a single fuel rod model in LS-DYNA. This step is described in detail in Section 5. A single fuel rod model is appropriate for typical SNF NCT because the magnitude of loads is relatively small.

Care must be taken to confirm that the single-rod model remains appropriate for the configuration being investigated after the analysis is completed. If SNF rod deflections are large enough to cause contact with a neighboring rod, the single-rod model stops being valid. In addition to the single-rod model, PNNL has developed and validated models of a full fuel assembly and a single column of fuel rods that can be used when fuel rod deflections are too large to justify the use of a single-rod model. For this study, it was not necessary to use the more computationally expensive single column, or single assembly models.

For this study all 1,600+ cases from the cask motion library were evaluated. The low fuel rod stiffness cases represent the configuration of the MMTT and the configuration of SNF where the fuel pellets are not bonded to cladding. The fuel rod stiffness EI was 14.3 N-m^2. The cyclic integrated reversible-bending fatigue tester (CIRFT) tests performed by ORNL (Wang et al. 2016) suggest the fuel rod stiffness can be much higher in SNF. This study also considered more than 800 cases that increased the fuel rod stiffness to 50 N-m^2, which is near the maximum theoretical stiffness value. The results of the minimum stiffness cases (EI of 14.3 N-m^2) and the maximum stiffness cases (EI of 50 N-m^2) were compared, and the minimum stiffness cases were found to be consistently more limiting than the high-stiffness cases.

In all cases considered, the fuel rod cladding peak strain was calculated to be 20 uE. This demonstrates that fuel cladding is expected to survive the peak loading conditions of NCT with a wide margin.

The last step of the analysis (MATLAB) is to complete a cladding fatigue analysis, to demonstrate that a fatigue failure is not expected in the cladding from repeated shock and vibration. The fatigue analysis is described in detail in Section 6. All dynamic results calculated in Step 3 were also evaluated for fatigue, using the same methods defined by Klymyshyn et al. (2018). The number and magnitude of strain cycles was counted. The root mean square (RMS) of the strain histories was also calculated to measure strain signal strength. This information was used to evaluate the fuel cladding fatigue using three different methods that are described in Section 6. All three methods arrive at the same conclusion, that fatigue damage from shock and vibration during NCT is negligible.

3. Cask and Cradle Dynamics Analysis

The railcar, cask, and cradle form a complex dynamic system. Loads originating at the wheel/rail interface are translated up through the system to the SNF inside the cask. The full railcar dynamics model, described in Section 4, includes the cask and cradle. The railcar dynamics model parameters for the cask and cradle come from the analysis described in this section.

The MMTT placed accelerometers at key locations on the railcar deck, cradle, and cask for the purposes of studying the dynamics of the system and validating numerical models. As described by Klymyshyn et al. (2018), the accelerometer data were evaluated and used to define a SDOF system that best approximated the cask and cradle dynamic behavior. For this study of the Atlas railcar the necessary test data are not available, so finite element modeling is used to define the constants of the SDOF system for each of the 17 cask and cradle combinations.

One of the key physical phenomena the SDOF system needs to account for is damping. The MMTT data showed that damping was significant. Damping between the railcar deck and the top of the cask was determined to be about 50% of critical damping, and this includes the effect of rubber mats that were placed between the cradle and the railcar deck. Between the bottom of the cradle and the top of the cask, the damping was about 30% of critical. Shaker table tests were performed in 2018 to study the damping effects of rubber mats and other materials (Kalinina et al. 2019). Based on all the available information, a choice of 20% was made to represent a general cask-cradle damping value. The rationale and supporting data are discussed in detail in Section 3.1.

Mass and stiffness are the other two parameters that define a SDOF spring-mass-damper system. Mass is well known and measurable. Stiffness can be calculated using linear elastic structural mechanics. For this study, FEA was used to determine the SDOF model parameters, based on models and information made available by the Atlas design project (AREVA 2018). This is described in detail in Section 3.2.

The justification for this methodology is provided in Section 3.3.

3.1 Damping Technical Basis

During the MMTT, it was learned that various materials may be placed beneath a transportation cask and cradle system during transport, which may contribute to system damping. To better understand the impact of including specific materials beneath the transportation system on system damping, shaker table tests were performed (Kalinina 2019). These shaker table tests used rubber mats, plywood sheets, and metal plates to represent the expected configurations used in SNF transportation. Rubber mats were included because they were used during the MMTT, plywood sheets were included since this is a material that is commonly available at shipping ports, and metal plates were included to represent the currently proposed Atlas railcar design. Based on the results of these shaker table tests and the MMTT data, 20% system damping was selected for a general cask-cradle system as discussed in Section 3.1.6.

3.1.1 Shaker Testing

For the shaker table testing, each of the three materials was placed beneath a steel block, and the sizing of the materials was scaled appropriately to represent the transportation configuration observed during the railcar portion of the MMTT (Kalinina 2019). Frequency sweeps were performed for varying ranges between 1 and 100 Hz. The natural frequency of the ENSA cradle design used during the transportation campaign is expected to fall within this range. Three accelerometers were placed on the steel block and three were placed on the shaker table surface for data collection. The setup for this testing is shown in Figure 3. Several tests were run for each buffer material using varying frequencies and amplitudes as input, always with a recording frequency of 10,240 Hz, which matches the highest data sampling frequency of the MMTT. Using the collected data, damping coefficients were found for each of the materials.

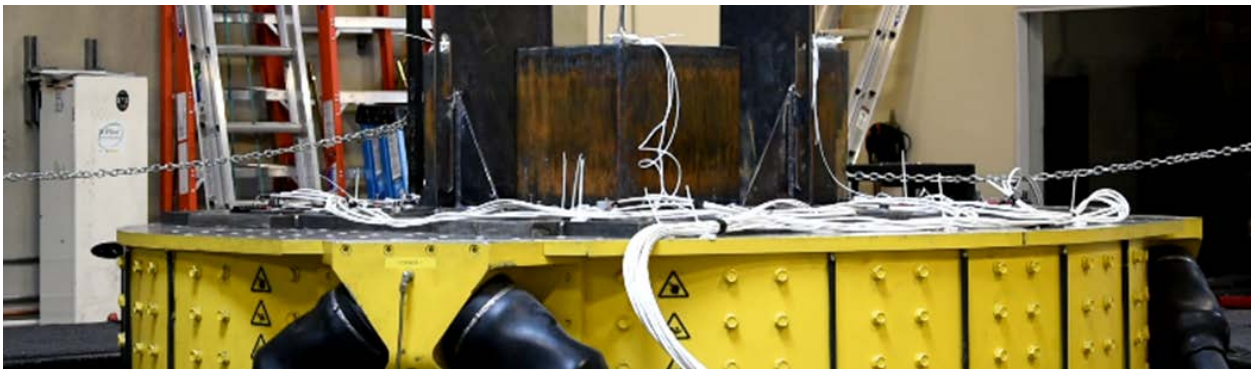

Figure 3. Shaker testing setup.

3.1.2 Half-Power Bandwidth

In structural analysis, a common method for calculating the damping ratio of a system involves the half-power bandwidth. The half-power bandwidth was formulated using the deformation response factor; however, a typical assumption that the damping is small allows for the use of acceleration transmissibility instead. Transmissibility is the ratio of the amplitude of the response to the amplitude of the excitation as a function of frequency. Equation (1) defines how the half-power bandwidth uses frequencies identified with the acceleration transmissibility curve to find damping (Chopra 2012).

$$\zeta = (f_b - f_a)/(2f_n) \text{ ¶} \quad (1)$$

where, f_n represents the natural frequency of the system and is expected to have the highest amplitude, f_a is the frequency lower than f_n at which the amplitude is $1/\sqrt{2}$ the peak amplitude, and f_b is the frequency higher than f_n at which the amplitude is $1/\sqrt{2}$ the peak amplitude. An example transmissibility curve with these frequencies and amplitudes is shown in Figure 4.

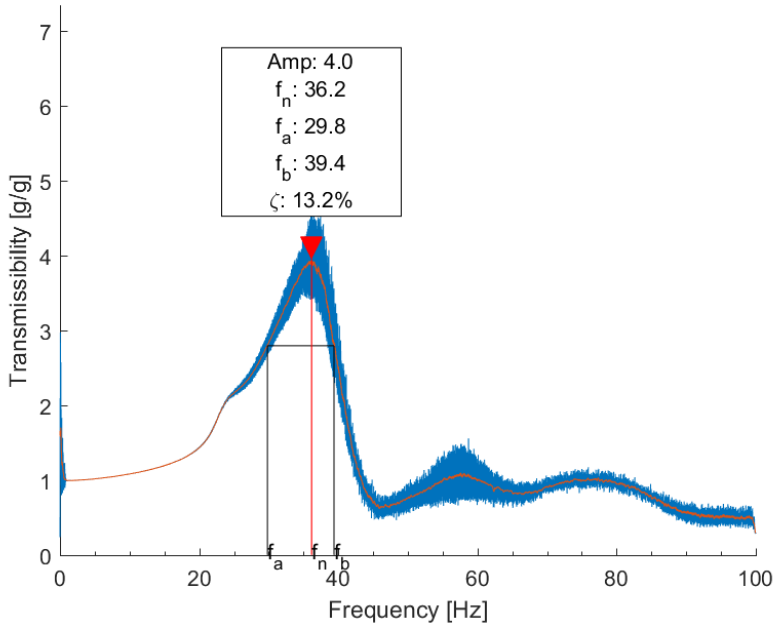

Figure 4. Example transmissibility curve with frequencies and amplitudes.

3.1.3 Method

From the acceleration data collected during shaker table testing, transmissibility spectra were found using the power spectral density (PSD) for each accelerometer. To find transmissibility from two PSDs, a signal PSD was chosen, and a response PSD was chosen. The transmissibility curve was then calculated as the square root of the PSD of the response divided by the square root of the PSD of the signal. For the shaker table testing, because three accelerometers were used on the top of the mass and three were used on the surface of the table, the PSD spectra were considered individually as well as averaged. To produce the averaged PSD, the individual PSDs were aggregated by taking the mean value at each frequency for the three accelerometers on the table and for the three accelerometers on the steel block. The averaged PSD for the accelerometers on the table was used as the signal and the averaged PSD for the accelerometers on the block was used as the response. For the individual PSDs, pairs were formed consisting of a signal accelerometer on the table and a response accelerometer on the block. Three pairs were considered based on the configuration of the test having three corners with instrumentation at the top and bottom of the corners.

To find the peak amplitude and corresponding frequencies for the half-power bandwidth method, Matlab was used (MathWorks 2019). For each transmissibility spectrum, a 20-point moving average was applied to the spectrum before using MATLAB's built-in peak-finding capability to identify the peak amplitude and the frequency at which it was found. The corresponding frequencies were then found for the half-power bandwidth using the same smoothed spectrum.

3.1.4 Results

Damping coefficients were found for each of the three buffer materials based on the tests run for each material. To avoid false positives when looking for resonant frequencies in the data, the peaks found with MATLAB were graphically down-selected to include only definite peaks. Peaks were considered indefinite based on an inability to determine the frequencies of interest for the half-power bandwidth method. The down-selected peaks for each buffer material are summarized in Table 1.

Table 1. Natural and frequency and system damping average from all tests.

	Pair 1		Pair 2		Pair 3		Averaged	
Material	f_n **(Hz)**	ζ **(%)**	f_n **(Hz)**	ζ **(%)**	f_n **(Hz)**	ζ **(%)**	f_n **(Hz)**	ζ **(%)**
Rubber	34.9	14.3	34.8	14.8	34.6	17.1	34.8	15.4
Plywood	73.3	4.2	76.7	4.0	74.4	3.1	74.2	4.2
Metal	-	-	-	-	75.0	3.3	78.8	5.2

3.1.5 Calculation Sensitivity Evaluation

Because the transmissibility curves were smoothed before using the half-power bandwidth method to find damping, it is important to understand the potential error introduced by the smoothing. A method was developed to bound the damping value calculated using a given transmissibility curve by approximating the top and bottom edges of the curve and using those edges to calculate damping. At any given amplitude, the width of the bottom edge is narrower than the width of the top edge and the peak amplitude of the top edge is higher than the peak amplitude of the bottom edge. Therefore, a low damping value is found by finding the upper and lower frequencies on the bottom edge at $1/\sqrt{2}$ the peak amplitude of the top edge, and a high damping value is found by finding the upper and lower frequencies on the top edge at $1/\sqrt{2}$ the peak amplitude of the bottom edge. Table 2 summarizes the results of using this method for all materials. Note that the maximum value for rubber damping in this sensitivity study is 21.6% (Table 2), compared to the maximum value of 17.1% damping using the normal calculation method (Table 1). The uncertainty from using a different calculation method is not large compared to the 50% damping observed in the MMTT data.

Table 2. Minimum, average, and maximum system damping from all tests.

Material	Minimum ζ (%)	Average ζ (%)	Maximum ζ (%)
Rubber	8.1	15.3	21.6
Plywood	3.0	5.1	8.4
Metal	1.8	5.1	7.4

3.1.6 Conclusions

The SDOF mode requires a damping target value in order to choose the damping parameter, C. The MMTT data indicates the damping ratio between the cask and railcar deck was 50% (Klymyshyn et al. 2018), and that includes the damping contribution of rubber pads that will not be present in the operation of the Atlas railcar system. Average rubber damping was calculated to be 15%, regardless of the method used (Section 3.1.4 or Section 3.1.5). Maximum rubber damping was calculated to be 22% (Section 3.1.5). Subtracting 22% from 50% leaves 28%, so a conservative damping ratio target is established as 20%. The SDOF parameter C is chosen to provide the system a 20% damping ratio.

Analysis of the same shaker table test data by Sandia National Laboratories (SNL) produced even lower damping ratio values for rubber that was calculated in this report. SNL used slightly different methods and assumptions (Kalanina 2019), but it supports the conclusion that 20% damping ratio for the Atlas system is likely conservative.

3.2 Cask and Cradle SDOF Parameter Identification

In lieu of physical test data, ANSYS (ANSYS Inc. 2017) finite element simulations were developed to identify the stiffness and damping parameters for the 17 casks and cradles to be employed on the Atlas railcar. The solid geometry files generated by the Atlas design project (AREVA 2018) were the basis for the finite element simulations. These models were originally intended for calculation of mass and inertial properties, not for structural dynamics simulations. As such, the model files were reworked to ensure proper contact of cradle components and avoid initial penetrations. Superfluous fine details that did not contribute to structural integrity were also removed; items such as washers were removed, and fasteners were replaced with equivalent contact pairs. Cask internals were not modeled; instead the casks were modeled as monolithic bodies that had uniform density and stiffness. The casks are expected to undergo very little deformation during NCT compared to the cradles, thus their compliance has very little effect on the natural frequency of the system.

The reworked solid geometry files were imported into ANSYS to identify the natural frequency of the cask and cradle. A series of harmonic analyses were conducted over a range of frequencies, which calculate the steady-state response of the system to sinusoidal input. For this analysis, the system was excited by vertical displacement at the base of the cradle. On the Atlas railcar, the cradles sit on steel plates on the railcar deck. An example of an ANSYS model, and the locations of input excitation, are shown in Figure 5. Although the range of motion of the cradle is limited by shear keys and lateral and longitudinal end stops, these constraints were not modeled since this analysis aims to identify the natural frequencies of the cask and cradle under NCT.

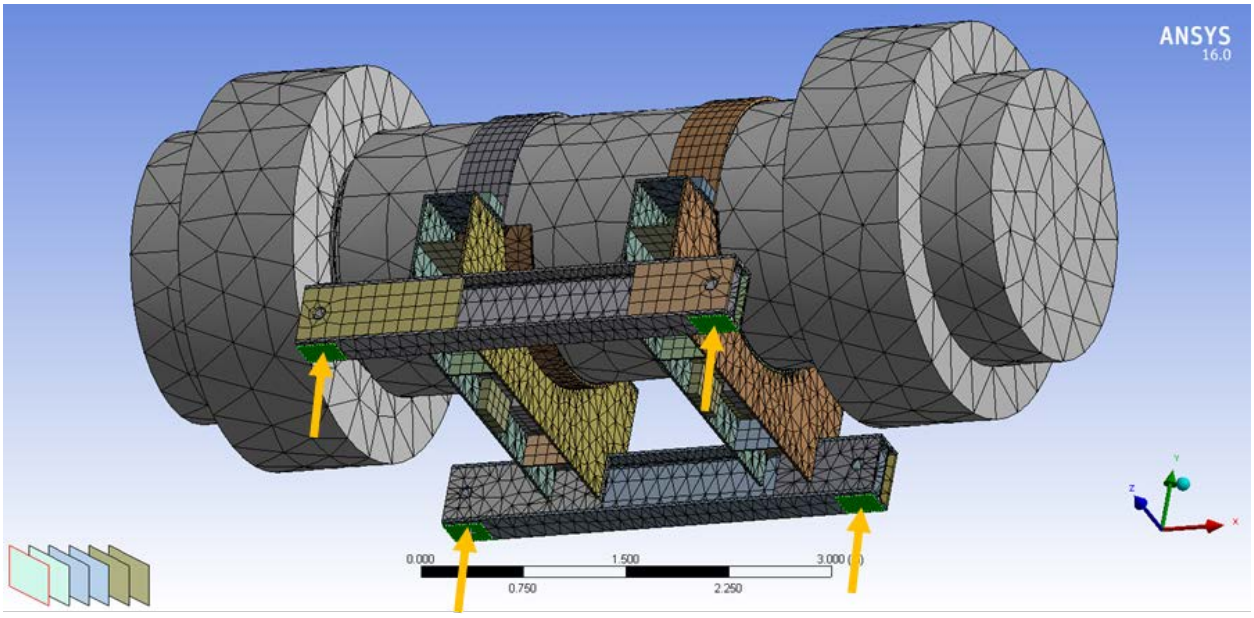

Figure 5. Example of ANSYS simulation of cask and cradle (HI-STAR 60 shown). Location of vertical displacement excitation is shown by the arrows.

The natural frequency of each of the cask and cradle combinations is the key output of these ANSYS simulations, because it is used to define the stiffness (*k*) and damping (*c*) of the SDOF system from fundamental vibrations equations. The natural frequency of the system is identified in this analysis as the frequency at which the response of the system is maximized. Figure 6 shows an example of the ANSYS output, as well as the SDOF response for two damping values, 1% and 20%. The 1% curve corresponds to the amount of damping present in the ANSYS simulations (included to prevent unbounded response at resonance) and demonstrates that there is good agreement between the response of the SDOF model and the ANSYS simulation. The 20% curve corresponds to the damping ratio assumed for the SDOF parameter calculation, as discussed in Section 3.1.

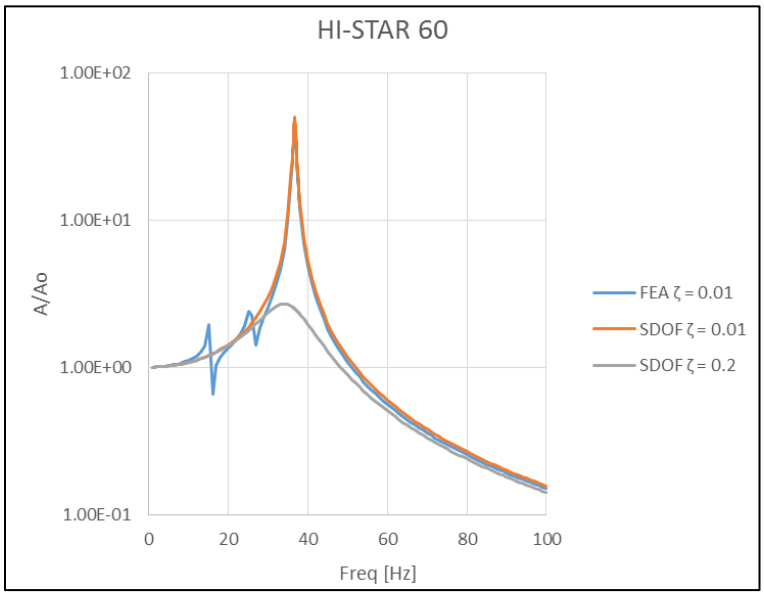

Figure 6. Example of harmonic sweep output and SDOF response (HI-STAR 60 shown). The Y-axis shows the ratio of the cask to input displacement at the base.

The procedure for calculating the three parameters for each cask and cradle SDOF system ─ mass, stiffness, and damping ─ are summarized below:

- Mass (m): The loaded mass of each cask was taken from the Atlas Railcar Phase 2 Final Report (AREVA 2018). When a range of masses was given, the midpoint between the minimum and maximum mass was chosen. The mass of the cradle was calculated by ANSYS using typical densities of structural steel and rubber (when present). The total mass of the cask and cradle is used in the SDOF system.
- Stiffness (k): Stiffness was calculated using the undamped natural frequency ω_n and total mass of the system m using the well-known equation for the natural frequency of a SDOF system, $\omega_n = \sqrt{k/m}$. The undamped natural frequency was calculated from the damped value ω_d identified in the ANSYS simulations, using the equation $\omega_d = \omega_n\sqrt{1 - \xi^2}$.
- Damping (c): Damping was calculated using the assumed damping ratio of $\xi = 20\%$ and the equation $\xi = c/c_{crit}$, where $c_{crit} = 2\sqrt{km}$.

Table 3 summarizes the SDOF parameter identification results. The natural frequencies of the 17 casks and cradles range from 24 to 63 Hz, and the associated stiffness and damping parameters have a similarly large range. This reflects the widely varying masses of the casks and designs of the cradles, which influence their dynamic response. The mass, stiffness, and damping parameters in the last three columns of Table 3 are used as input to the NUCARS railcar dynamics model to represent the cask and cradle dynamic behavior, as discussed in Section 4.

Table 3. Summary of Atlas cask and cradle SDOF results.

	ω_n (Hz)	ω_d (Hz)	ξ	m (kg)	k (N/m)	c (N·s/m)
HI-STAR 60	36.7	36.0	20%	80306	4.271E+09	7.408E+06
HI-STAR 100	47.9	46.9		134170	1.215E+10	1.615E+07
HI-STAR 100HB	31.0	30.4		90681	3.441E+09	7.065E+06
HI-STAR 180	35.4	34.7		144780	7.163E+09	1.288E+07
HI-STAR 190SL	41.0	40.2		176210	1.170E+10	1.816E+07
HI-STAR 190XL	32.6	31.9		196570	8.248E+09	1.611E+07
TN-32B	43.9	43.0		124660	9.485E+09	1.375E+07
TN-40	35.5	34.8		128490	6.393E+09	1.146E+07
TN-40HT	37.6	36.8		115270	6.434E+09	1.089E+07
NAC STC	44.6	43.7		129300	1.015E+10	1.449E+07
NAC UMS	40.8	40.0		131960	8.673E+09	1.353E+07
NAC MAGNATRAN	38.8	38.0		159010	9.451E+09	1.551E+07
MP-187	24.8	24.3		137650	3.343E+09	8.580E+06
MP-197	41.9	41.1		131270	9.099E+09	1.382E+07
MP-197 HB	63.0	61.7		148400	2.326E+10	2.350E+07
TN-68	61.9	60.7		134850	2.040E+10	2.098E+07
TS125	41.3	40.5		141640	9.539E+09	1.470E+07

3.3 Justifications of the SDOF Methodology

A major difference between SDOF parameter identification for the MMTT and the Atlas railcar was the use of accelerometer data from full-scale testing versus structural dynamic models, respectively. Both methodologies employ the same physics, in that they both fit parameters to a curve describing load transmissibility through a structure, so both methods should arrive at similar results. To demonstrate the applicability of the finite element methodology described in Section 3.2, an exercise was conducted to model the cask and cradle system used in the MMTT, and compare the calculated SDOF parameters to those computed from the MMTT data from Klymyshyn et al. (2018). The MMTT's ENSA ENUN-32P cask, cradle, and attached battery box were modeled in ANSYS, and the SDOF parameters were identified using the analysis method described in the preceding section.

The results of the analysis are shown in Table 4. Close agreement was found between the natural frequencies identified in each analysis, and likewise, similar stiffness values were computed. While the damping calculated from the MMTT test data was significantly higher than the value assumed for the Atlas railcar, the latter would tend to produce a more conservative result, because less energy is expected to be dissipated in the structure. Note that the damping ratio of 0.408 derived from test data does not include the rubber pads that were used between the cradle and railcar deck. Also remember that the damping ratio of 0.2 in the FEA row was assumed (20% damping) and was not an FEA output.

Table 4. Comparison of SDOF parameters for MMTT cask and cradle identified using test data and FEA.

	k [N/m]	**c [N·s/m]**	**ω_n [Hz]**	**ξ**
Test Data (Klymyshyn et al. 2018)	8.949E+09	2.983E+07	38.985	0.408
FEA	7.27E+09	1.32E+07	35.1	0.2

Figure 7 shows the result of modeling the MMTT railcar, cask and cradle combination using the two sets of SDOF values presented in Table 4. The results shown are of the vertical acceleration of the cask center of gravity (CG) during the pitch and bounce test at the railcar's resonance speed, 60 mph. The waveforms are virtually indistinguishable, and the model using the SDOF parameters from FEA has a negligibly greater peak-to-peak acceleration of about 1%. This is despite the sizable difference in damping value assumed in each method, which points to the cask accelerations being driven by the resonance modes of the railcar, rather than the resonance modes of the cask and cradle.

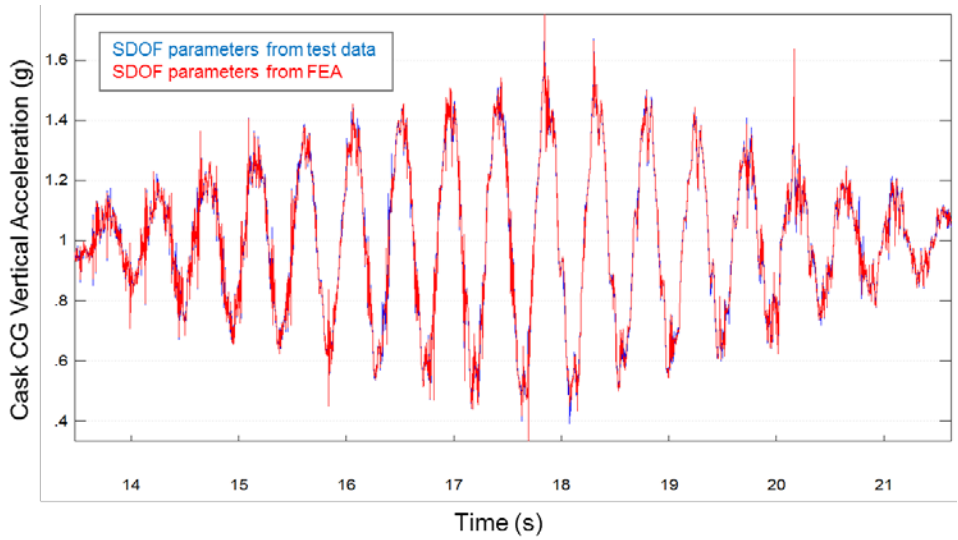

Figure 7. Response of the NUCARS model using SDOF parameters identified by test data and FEA.

This exercise demonstrates that finite element simulations are a viable alternative to using full-scale test data for SDOF parameter identification. If the geometry of the cask and cradle is known and reasonable assumptions are made regarding damping of the structure, SDOF parameters that are functionally equivalent to those calculated from the previously documented method based on full-scale test data can be calculated. The finite element methodology for parameter identification is orders of magnitude less expensive in terms of time and cost, particularly when analysis of multiple systems is required, as is the case for the Atlas railcar. Moreover, finite element simulation may be the only option for analysis of hypothetical conveyance systems, or for predicting the effect of proposed modifications of existing systems.

Representation of the cask and cradle as a SDOF system is, of course, a discrete one-dimensional approximation of a continuous, three-dimensional structure. Thus, some differences between the SDOF model and behavior of the real structure are to be expected. The SDOF system simply accounts for the most dominant vertical response mode, whereas other translational and rotational modes are neglected. Nonlinear behavior like liftoff and material plasticity are similarly neglected. However, for the purpose of fuel integrity analysis during NCT, these assumptions are reasonable. Comparison of cask acceleration simulations and test data from the MMTT were in good agreement despite the use of a SDOF approximation of the cask and cradle. Likewise, data derived from simulation of fuel rod strains and fatigue life based on the SDOF model agreed with strain gage data from the MMTT; both arrived at the conclusion that the accumulated fatigue damage was negligible. If the loads induced by NCT are within the linear analysis regime, the use of a SDOF approximation is justifiable. Sections 4 and 5 demonstrate that for the Atlas railcar, the loads and strains induced during NCT are indeed modest.

4. Railcar Dynamics Analysis

Railcar dynamics modeling is commonly used in the railroad industry to simulate the handling characteristics of rolling stock. It is often used to simulate hypothetical derailment events, while ride quality is typically of secondary or tertiary interest. In the MMTT modeling campaign, a railcar dynamics model was developed for the generic freight car and ENSA cask and cradle used during the rail segment of the journey (Klymyshyn et al. 2018). The cask motions calculated by this model were used as the base excitation for downstream analyses of fuel rod integrity. The model response was benchmarked against a selection of captive rail tests conducted at TTCI in Pueblo, Colorado. It achieved good agreement in terms of cask accelerations and fuel rod strains, despite the unconventional use of a railcar dynamics model to evaluate ride quality.

Unlike the MMTT, where a new railcar dynamics model was developed specifically for the modeling campaign, a model of the Atlas railcar had already been developed for the AAR S-2043 certification process (AREVA 2018). The S-2043 standard is concerned with dynamic performance of railcars to the extent that they shall not derail, whereas the focus of the MMTT analysis and this present work is the load transmitted to SNF during NCT. Since it was developed and vetted by railroad industry experts, the Atlas railcar model intended for the S-2043 certification forms a reliable foundation for further model development. However, because it was not intended for analyses of the shock and vibration environment, some modifications to the model were required, informed by modeling experience gained from the MMTT modeling efforts. These model modifications are discussed in Section 4.1.

The modified Atlas railcar model was used to compute cask CG motions for each of the 17 cask and cradle combinations. Three of the S-2043 test sections were analyzed: pitch and bounce, twist and roll, and single bump. Although the full set of S-2043 testing is more extensive than just these three tests, these three tests were found to closely represent the open-rail data from the MMTT, and exercise various response modes of the railcar. Cask motions were calculated in each test section over a range of train speeds, for a total of 612 NUCARS simulations. The results of the simulations are summarized in Section 4.2. The library of cask motions calculated from the railcar dynamics model was used as input for the fuel rod structural analysis LS-DYNA model of Section 5.

In the railcar dynamics model, the cask is treated as a rigid body. However, 11 of the 17 casks employed on the Atlas railcar are canister fuel systems. The fuel canisters in these casks have additional degrees of freedom that are not accounted for in the railcar dynamics model. Section 4.3 considers the effect of canister fuel on the loads transmitted to SNF.

4.1 Model Development

The Atlas railcar dynamics model used in this work is a modification of the model used by the Atlas railcar design project to gain approval for the prototyping process for AAR S-2043 certification (AREVA 2018). Simulations were performed using NUCARS, which is a standard software package used by the railroad industry, and it was also used in modeling the MMTT.

The general layout of the Atlas railcar (Figure 8) is very similar to the Kasgro railcar used in the MMTT. Both are 12-axle railcar designs, with six trucks linked to two span bolsters, and a deck on which the payload and end stops are mounted. While the Atlas railcar is designed to conform to S-2043, testing of the MMTT railcar indicated dynamic performance that did not conform to that standard. Evidently, despite being similar in structure, different dynamic behavior is expected between the Atlas and MMTT railcars.

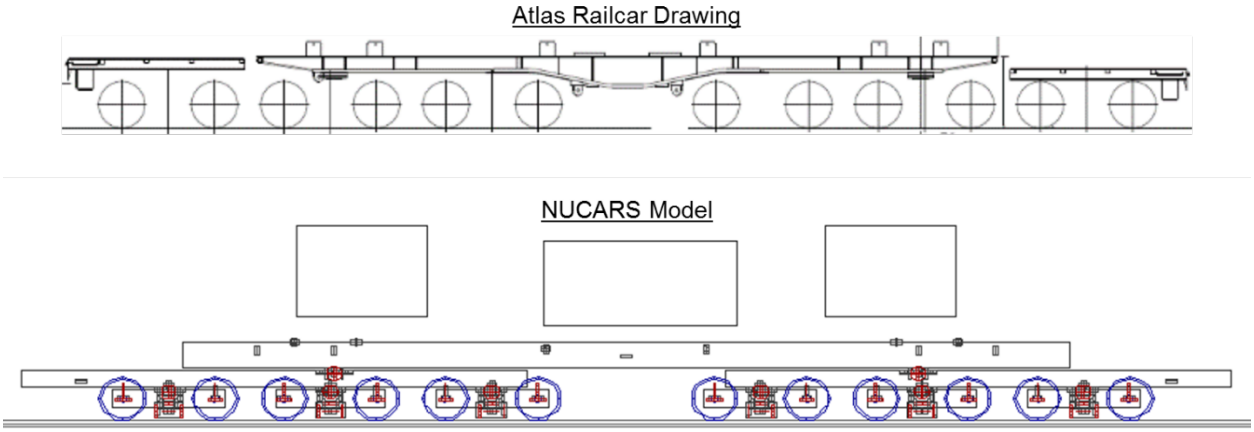

Figure 8. Schematic drawing of the Atlas railcar (top) and NUCARS representation (bottom). The NUCARS model includes independent bodies for the cask and cradle and two end stops, which are not shown in the drawing. The schematic drawing is a simplified depiction and does not fully show the trucks or span bolsters.

A review of the as-received Atlas NUCARS model identified several areas that diverged from PNNL's modeling practices implemented in the MMTT model. The following discussion details each of these areas, and the studies conducted to illustrate their effect on cask motion. All modeling results shown correspond to pitch and bounce simulations of the Atlas railcar loaded with the HI-STAR 190XL cask, which was identified as the most limiting for the S-2043 tests and was thus the best documented configuration (AREVA 2018).

1. **Cask and Cradle Model:** The as-received Atlas model simply models the cask and cradle as a rigid body, interfacing with the railcar deck via a steel-on-steel connection. PNNL's MMTT model represented the cask and cradle as a SDOF system, as described in Section 3.2. Implementing the SDOF model for the Atlas configuration caused a modest increase in cask acceleration and had a more visible impact in the frequency domain; additional high-frequency content is transmitted to the cask (Figure 9). Figure 9 (left) shows the original Atlas model and revised SDOF model calculate very similar peak cask accelerations, but Figure 9 (right) illustrates the difference in the frequency domain. SNF rods can be sensitive to the higher frequency content.
2. **Flexible Modes:** The as-received Atlas model included information to implement flexible modes of the transoms, deck, and span bolsters, yet only flexible modes for the transoms were activated. PNNL's MMTT model included flexible modes of the transoms and deck, which were found to be necessary to accurately match test data. While flexure of the deck may not be important for modeling of dynamic handling performance, deflection of the deck accounts for a portion of the cask's motion. Including the deck flexible modes causes prominent resonance at intermediate speeds (Figure 10), which was a feature of the MMTT test data. Figure 10 (left) shows the cask acceleration when the different flexible modes are implemented in the NUCARS model and Figure 10 (right) shows the effect of the different flexible modes in the frequency domain at 60 mph.
3. **Deck Camber:** The as-received Atlas model included information to induce the static curvature of the railcar deck, yet this effect was inactive due to the lack of flexible modes of that body. Including the deck's camber influences the vertical CG of the railcar, yielding a modest effect on cask accelerations. Figure 11 shows the response is very similar, with a slight speed-by-speed difference.
4. **Flexible Mode Damping:** The as-received Atlas model used much higher damping ratios for flexible modes than the PNNL MMTT model. Because the flexible bodies in the model (deck and transoms) are welded steel structures vibrating in air, relatively low damping is expected for these modes.

Reducing the damping ratios resulted in a modest increase in cask accelerations (Figure 12). Note in Figure 12 that the deck flexure is viewed as a necessary modification for this study, so the inclusion of the blue baseline curve is only for comparison to the as-received Atlas railcar model.

5. **Connection Types & Tow Rope:** The as-received Atlas model featured slightly different NUCARS connection types for some joints than the PNNL MMTT model, including the vertical-roll connection between the side frame and axles and for the main springs. In NUCARS, railcar models are constrained by a tow rope such that they remain stationary, while the track moves relative to the railcar. The tow ropes were configured differently for the two models. Changing the connection types and tow rope configurations to the same as those used in the MMTT model caused virtually no difference in cask accelerations (Figure 13).

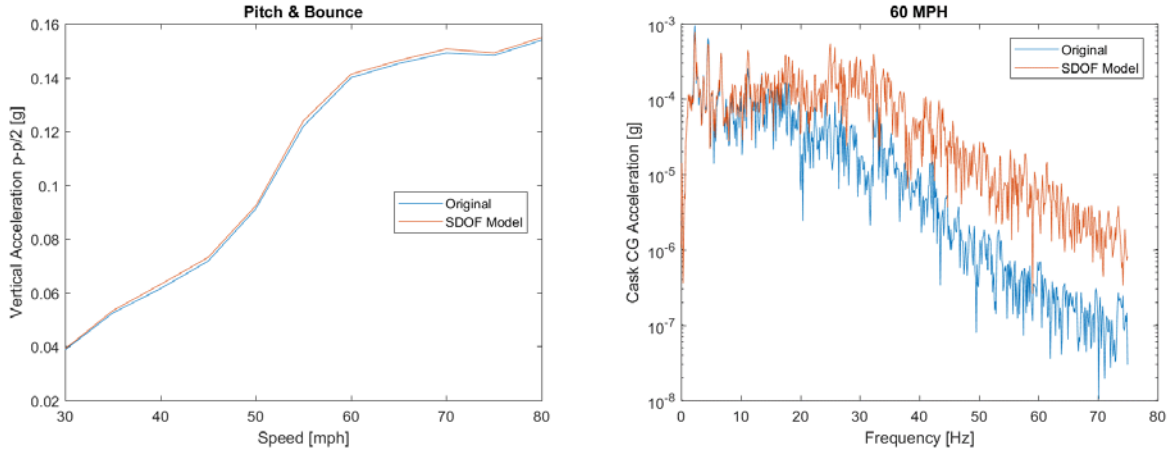

Figure 9. Effect of modeling cask and cradle as an SDOF system.

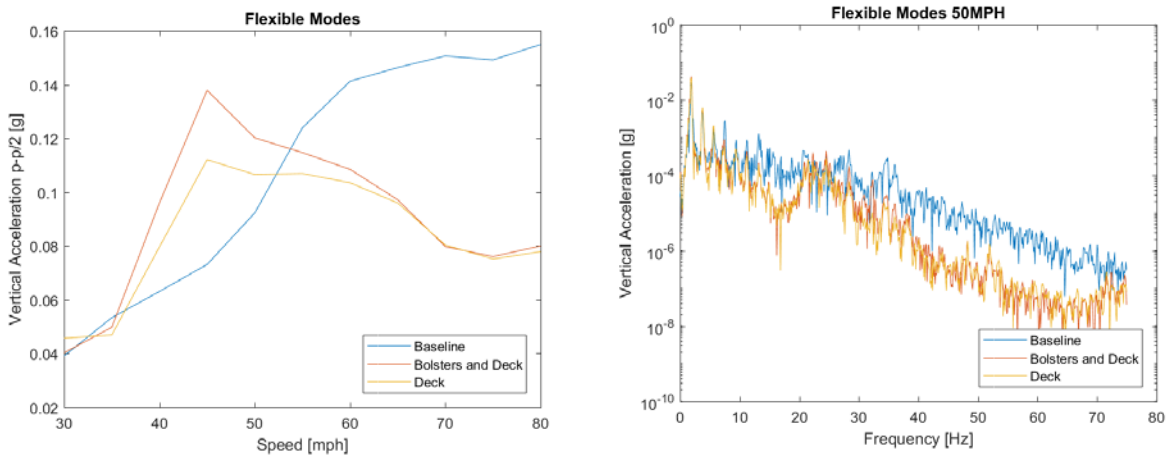

Figure 10. Effect of adding deck and span bolster flexible modes.

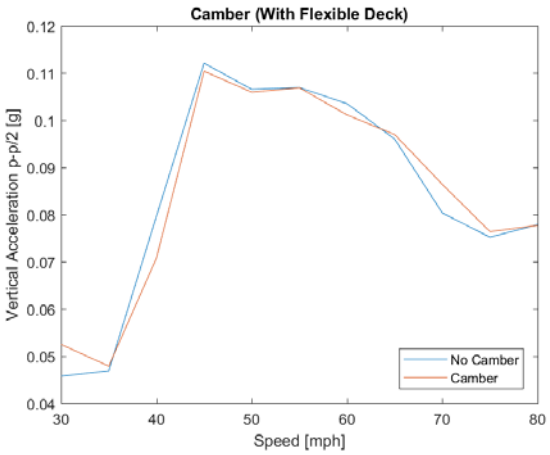

Figure 11. Effect of adding camber to the railcar deck.

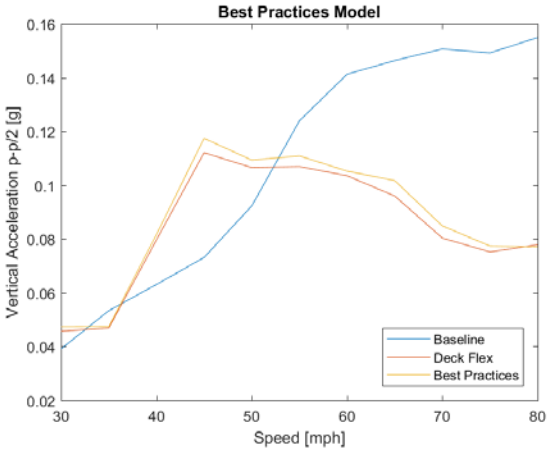

Figure 12. Effect of decreasing flexible mode damping.

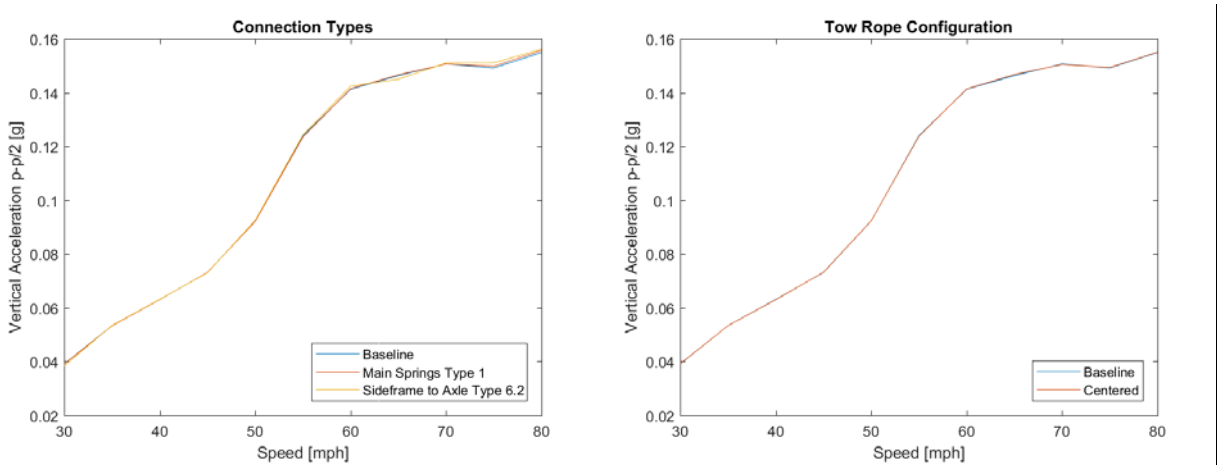

Figure 13. Effect of adjusting connection types and tow rope configurations.

Cask motions of the modified Atlas railcar model were calculated for three test sections: pitch and bounce, twist and roll, and single bump. These sections are a subset of the S-2043 tests, and they also overlap with the full-scale tests and railcar dynamics simulations conducted for the MMTT railcar. These

test sections were chosen because they exercise several different response modes of the railcar, and they resemble real-world events that were encountered during the open-rail journey in the MMTT. The following discussion outlines each of the test sections, which are illustrated in Figure 14:

- **Pitch and Bounce:** The railcar passes over evenly spaced cusp-shaped perturbations, causing vertical translation (bounce) and rotation around the railcar's lateral axis (pitch).
- **Twist and Roll:** Similar to the pitch and bounce configuration, except that the cusp-shaped perturbations are offset by a half period. This causes the railcar to rotate around its longitudinal axis (roll) and flex around the same axis (twist).
- **Single Bump:** The railcar passes over a single vertical perturbation. This imparts a vertical impulse to the railcar, exciting various vertical modes. This test section is similar to a level crossing, where a railroad crosses over a road. Similar events were encountered in the open-rail journey in the MMTT and were found to correspond to peaks in the strain gage data.

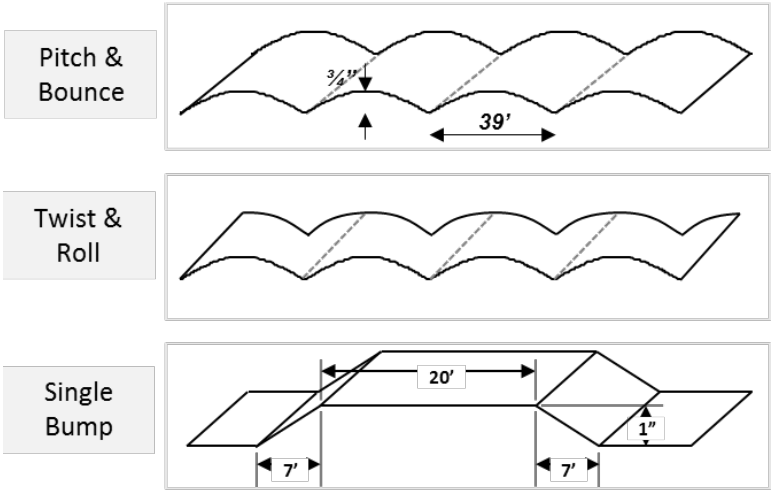

Figure 14. Test sections simulated in the railcar dynamics model.

4.2 Railcar Dynamics Model Results

Cask accelerations for each of the three test sections are plotted in Figure 15−Figure 17. Here, acceleration amplitudes are reported, and defined as half of the peak-to-peak value. To condense the data, the plots show the range of acceleration values for each test speed. Peak accelerations for each cask and test section are reported in Table 5. Vertical and lateral accelerations are reported for the twist and roll section but not for pitch and bounce nor single bump, because it is the only test of the three that has significant lateral track features.

Overall, the HI-STAR 60 tended to produce the highest accelerations, whereas the HI-STAR 190XL produced the lowest accelerations. These casks, respectively, are the lightest and heaviest casks employed on the Atlas railcar. This points to a major difference in analysis methods for dynamic handling (i.e., S-2043) and for fuel integrity analysis. While heavier casks may be more limiting for derailment events, lighter casks subject fuel to greater loads. This trend is consistent with Newton's second law, which states that for a given force on an object, acceleration is inversely proportional to the object's mass.

Simulation results for the HI-STAR 180 may be compared to the MMTT data reported by Klymyshyn et al. 2018, because it has a mass and SDOF natural frequency similar to the ENSA ENUN-32P cask used in the MMTT. Comparing cask accelerations of the two, the Atlas railcar model predicted values similar to or smaller than the MMTT data. For pitch and bounce, the cask acceleration was about three times smaller than that measured in the MMTT (0.17 g versus 0.61 g). For twist and roll and single bump, the

Atlas model predictions were about the same as the MMTT data (0.11 g versus 0.10 g, and 0.18 g versus 0.20 g, respectively). Even expanding the scope of comparison beyond the HI-STAR 180, the Atlas railcar modeling results predicted peak accelerations that were similar to (0.16 g versus 0.10 g, and 0.26 versus 0.20 g, respectively, in the case of twist and roll and single bump) or smaller than (0.30 g versus 0.61 g in the case of pitch and bounce) those of the MMTT data.

In summary, the predicted loads transmitted to SNF by the Atlas railcar are similar to, if not smaller than, those observed in the MMTT. The library of 612 cask acceleration time histories generated by the railcar dynamics model act as the base excitation for the structural analysis of fuel rods performed in LS-DYNA described in Section 5.

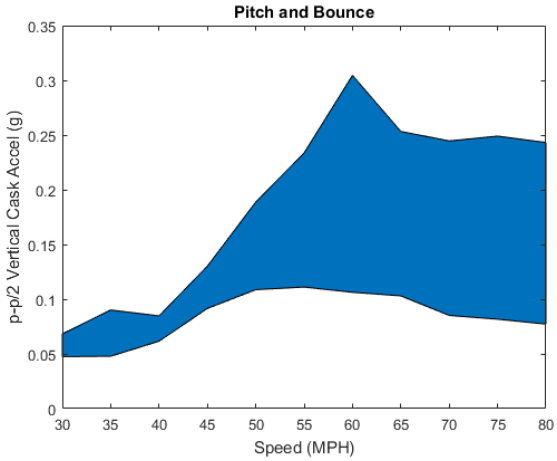

Figure 15. Range of cask vertical accelerations for all 17 casks and cradles in pitch and bounce.

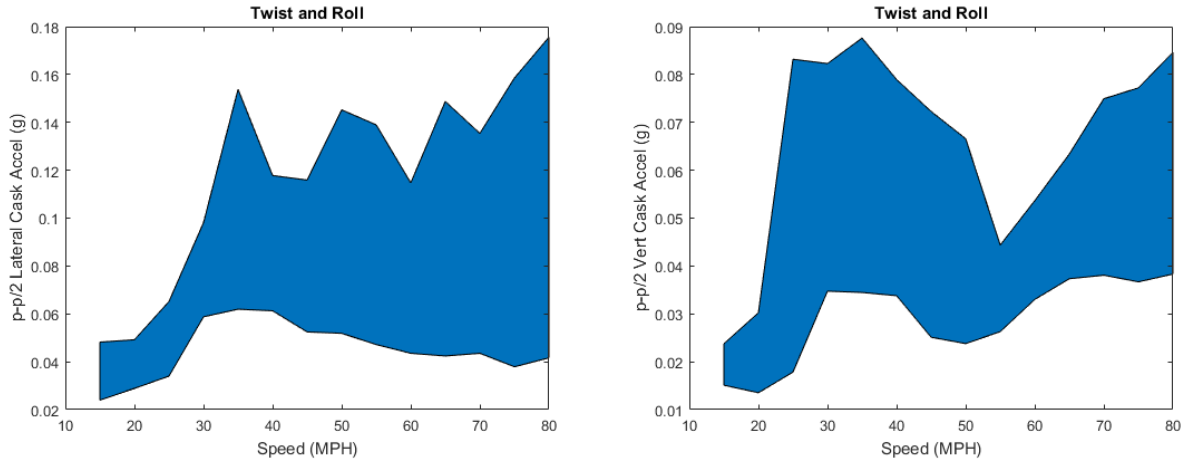

Figure 16. Range of cask lateral (left) and vertical (right) accelerations for all 17 casks and cradles in twist and roll.

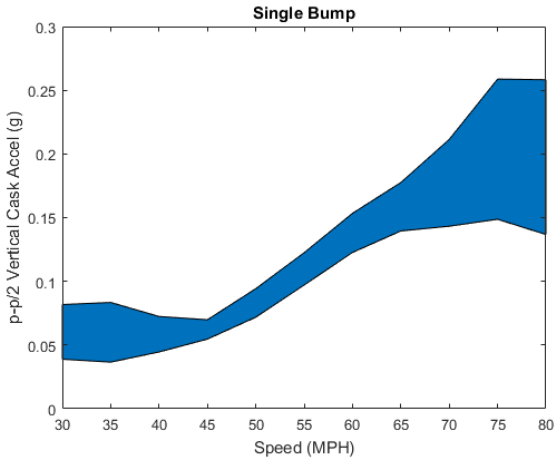

Figure 17. Range of cask vertical accelerations for all 17 cask and cradles in single bump.

Table 5. Summary of peak accelerations.

	p-p/2 Cask Acceleration (g)			
	Pitch & Bounce	Twist & Roll		Single Bump
Cask	Vertical	Lateral	Vertical	Vertical
HI-STAR100	0.17	0.10	0.08	0.19
HI-STAR100HB	0.27	0.16	0.08	0.23
HI-STAR180	0.17	0.11	0.07	0.18
HI-STAR190SL	0.13	0.07	0.05	0.16
HI-STAR190XL	0.12	0.06	0.05	0.15
HI-STAR60	0.30	0.16	0.09	0.26
MP-187	0.20	0.08	0.06	0.19
MP-197	0.23	0.08	0.07	0.20
MP-197HB	0.18	0.07	0.08	0.18
Magnatran	0.18	0.06	0.07	0.17
NACSTC	0.22	0.08	0.07	0.19
NACUMS	0.22	0.08	0.08	0.20
TN-32	0.18	0.17	0.07	0.19
TN-40	0.17	0.16	0.07	0.19
TN-40HT	0.21	0.18	0.08	0.19
TN-68	0.22	0.07	0.06	0.20
TS125	0.19	0.07	0.06	0.19

4.3 Fuel in Canister System Effects

The MMTT used a dual-purpose (storage and transportation) bare fuel cask design. The other common configuration is to have the fuel stored in multipurpose canisters that can be used in storage and transportation. The difference is that the canister is placed in a storage overpack for storage and moved to a transportation cask (or package) for transportation. In terms of dynamics, the canister system adds some

degrees of freedom of motion to the system because the outer diameter (OD) of the canister has some clearance with the internal diameter (ID) of the cask. The analysis methodology assumes that the cask motion and fuel basket motion are equal, but the diametrical clearance allows the canister to roll (slightly) within the cask. Some nominal clearance is needed to allow the canister to be placed inside the cask, so all canister designs are expected to have some clearance. The effect of this clearance is evaluated in a sensitivity study described in this section.

This sensitivity study performs a kinematics analysis of the response of a rigid canister to motion applied to a rigid cask. The cask motion comes from the NUCARS results calculated in Section 4.2. A hypothetical cask is defined according to the key parameters shown in Table 6. Two hypothetical canister designs are also defined to cover a small range of diametrical clearance (5 mm to 15 mm).

Table 6. Hypothetical cask and canister parameters.

	Cask	Canister 1	Canister 2
ID	1.8 m	-	-
OD	1.9 m	1.795 m	1.785 m
Cavity Depth/ Canister Height	4.8 m	4.78 m	4.78 m
Mass	-	38,555 kg	38,555 kg

Two railcar dynamics load cases were selected for this sensitivity study. One is a pitch and bounce case at 65 mph train speed, which provides significant vertical loading. The other is a twist and roll case at 75 mph, which provides significant lateral loading. Both cases are taken from the NUCARS model of the Atlas railcar with the HI-STAR 100HB cask, which is the lightest of all canister fuel systems and thus experiences the greatest accelerations during NCT. These two rail dynamics cases explore the boundaries of NCT railcar behavior. The two canister configurations bound the expected range of diametrical gap.

The kinematics finite element model is shown in Figure 18. It is a LS-DYNA finite element model that calculates the dynamic response of the canister caused by prescribed motion of the cask. It is called a kinematics model because the cask and canister are defined as rigid material. Typical LS-DYNA explicit finite element models use elastic, plastic, or other material models to predict the stress, strain, and deflection of flexible structures subjected to transient loads. The use of rigid bodies eliminates the flexibility of the bodies and calculates the motion of bodies based on the applied forces. The model generates contact forces based on the stiffness of steel and friction forces based on steel-to-steel contact. The contact forces and gravity act on the canister to cause rigid body motion over time. The rigid body approximation is expected to be a reasonable approximation of the cask and canister behavior because the shock and vibration loading regime is of such relatively low magnitude that deflections of the bodies are expected to be negligible.

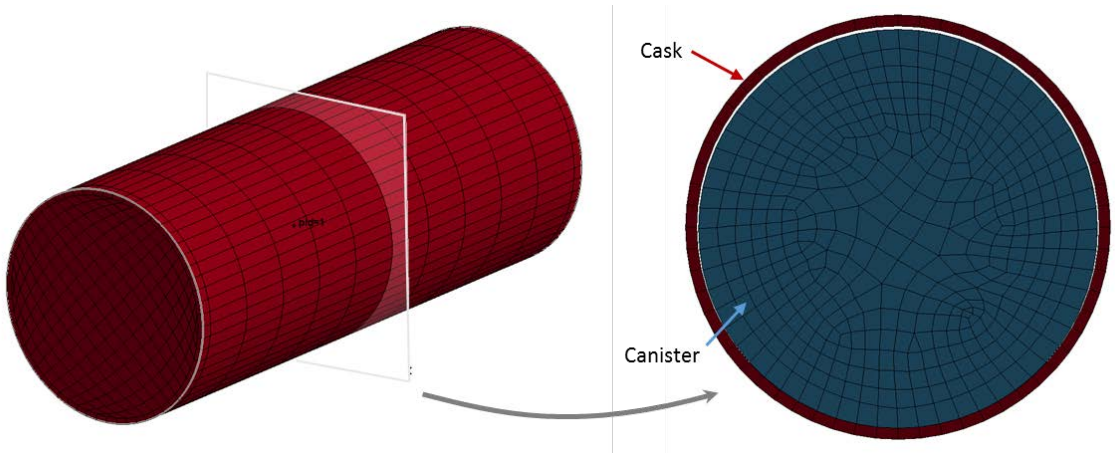

Figure 18. LS-DYNA canister kinematics model.

Comparison of the cask motion and dynamic response of the two hypothetical canisters is summarized in Figure 19 and Figure 20. Figure 19 shows the vertical acceleration response in pitch and bounce, while Figure 20 shows the lateral acceleration response in twist and roll. Both figures show the acceleration of the cask and canister CG. Figure 19 shows both hypothetical systems have nearly identical vertical accelerations, and this is discussed more in the next paragraph.

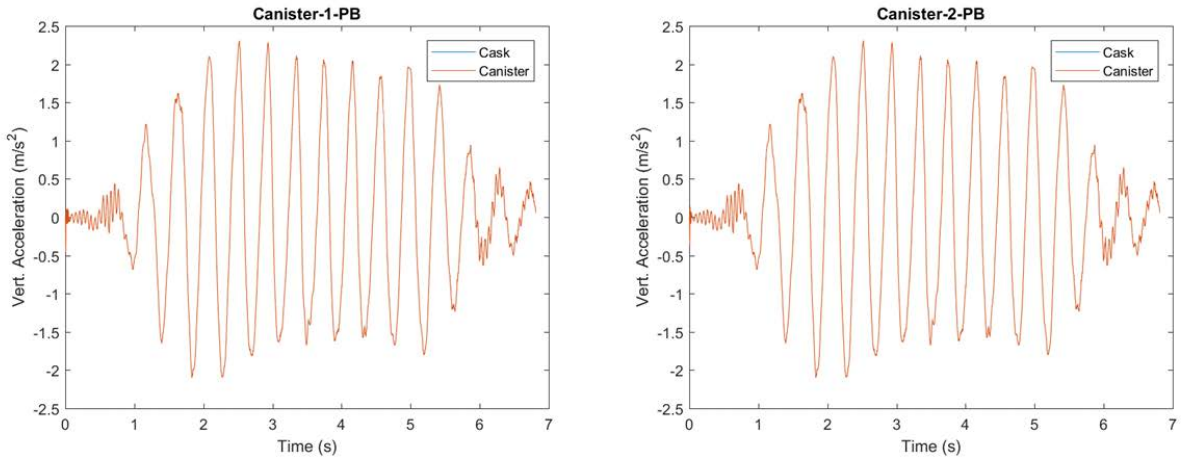

Figure 19. Vertical acceleration of hypothetical cask and canisters in the 65 mph pitch and bounce test.

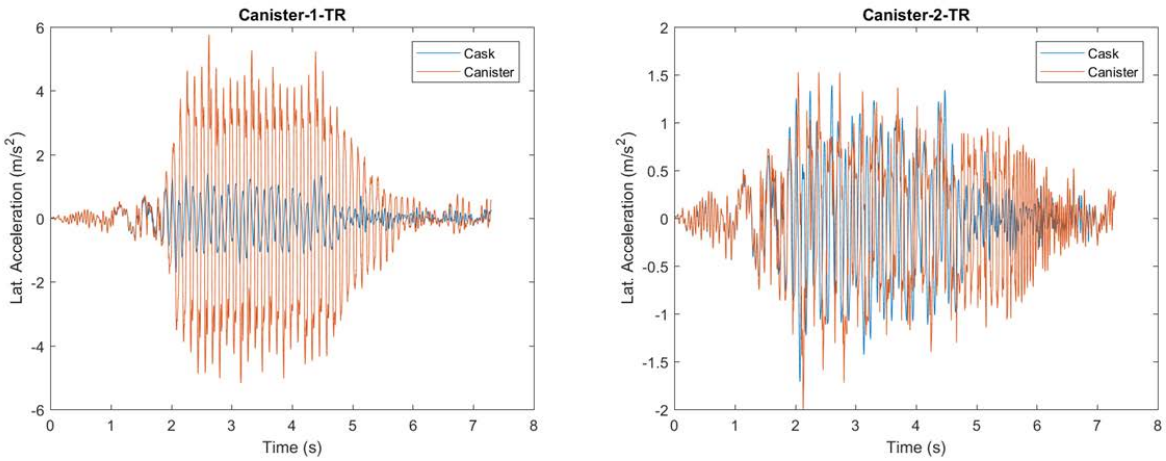

Figure 20. Lateral acceleration of hypothetical cask and canisters in the 75 mph twist and roll test.

As shown in Figure 19, the vertical accelerations of the cask and canister in pitch and bounce are virtually indistinguishable. Restraint of the canister by gravity ensures that the cask and canister essentially share the same motion, if cask acceleration is relatively small, as is the case during NCT. Figure 21 shows that the difference in vertical displacement of the cask and canister is on the order of several microns, which further illustrates this point.

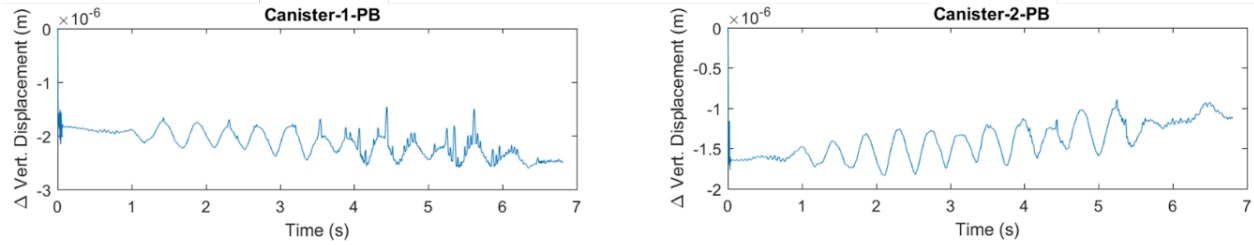

Figure 21. Difference in cask and canister vertical deflection for the 65 mph pitch and bounce test.

Figure 20 illustrates that the lateral response of the canister in twist and roll differs from the cask motion. This motion corresponds to oscillatory rolling within the cask when subjected to lateral motion. This study indicates that the canister experiences increased lateral acceleration compared to the cask. More high-frequency content is present in the canister acceleration signal, corresponding to arrest of the lateral canister motion by the inner wall of the cask (Figure 22). This study indicates that circumferential clearance between the canister and cask affects the dynamics of the system. Canister 1, with smaller clearance, demonstrated a greater amplification effect than Canister 2, which had three times greater clearance. It is hypothesized that the smaller clearance yields a more pronounced “ricochet” effect of the canister within the cask. Figure 23 illustrates the more pronounced difference in lateral displacement of the cask and canister, compared to vertical loading cases such as the pitch and bounce test.

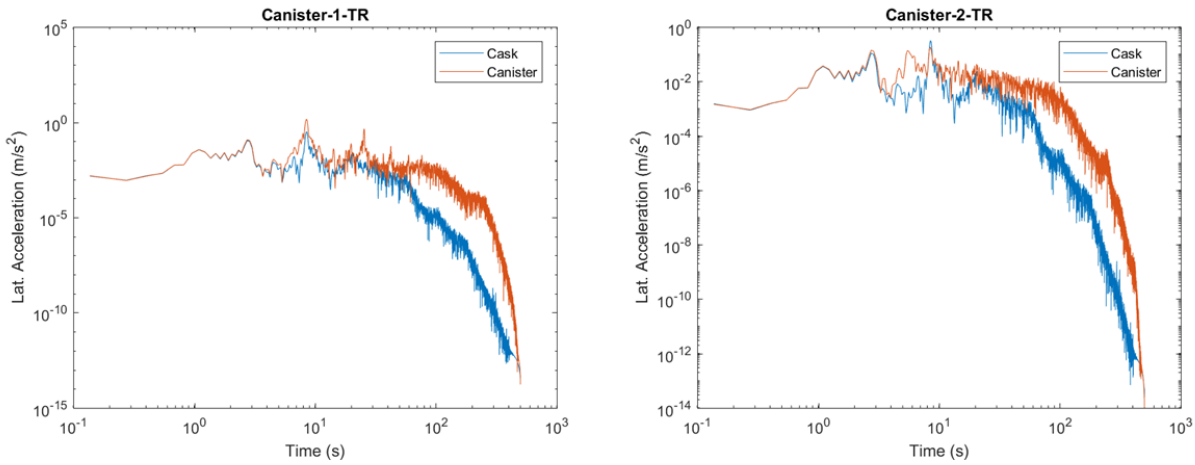

Figure 22. Fast Fourier transform (FFT) of cask and canister lateral acceleration for the 75 mph twist and roll test.

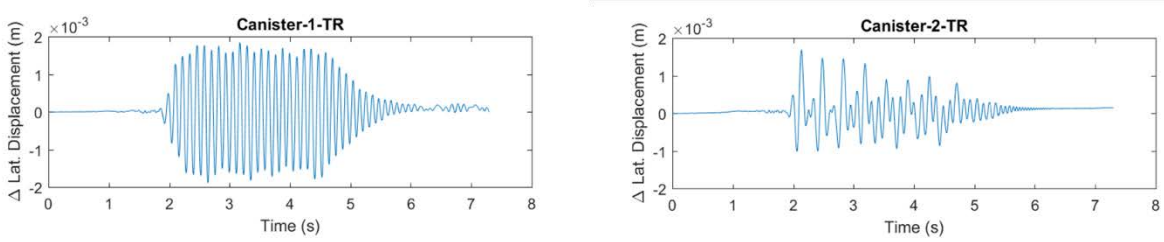

Figure 23. Difference in cask and canister lateral deflection for the 75 mph twist and roll test.

The results of this study demonstrate that the free-moving canister has a split effect on the motion of the fuel basket from the nominal cask motion, depending on the direction of loading. For the modest vertical loads expected from NCT, the canister motion is virtually identical to the cask motion, and the effect on fuel rod is expected to be infinitesimal. On the other hand, under lateral loading, the canister motion differs significantly from the cask motion, both in terms of amplitude and frequency content. Section 5.3 considers how much these small changes in motion affect the cladding strain calculation. As explained in Section 5.3, although the strains increase 4 to 6-fold, the nominal strain is small enough that the increase does not justify concern.

4.4 Conclusions, Generalizations, and Justifications

The configuration of the Atlas railcar is similar to that used in the MMTT but has several notable differences. The Atlas railcar is designed to comply with AAR S-2043, whereas the MMTT railcar is not. While the MMTT cask is designed to hold bare fuel, the Atlas railcar is designed to carry 17 different cask and cradle designs, some which would be loaded with canister fuel.

For bare fuel, this analysis predicts loads similar to or smaller than those observed during the MMTT. This is in line with pre-existing assumptions that S-2043-compliant railcars should subject SNF to smaller loads. That said, it should be noted that S-2043 is concerned primarily with preventing derailments, not with the shock and vibration environment of the payload. For instance, the limiting configuration for S-2043 dynamic handling tests is the heaviest cask (HI-STAR 190XL), whereas for cask acceleration, the lightest cask (HI-STAR 60) is the most limiting. The railcar dynamics model developed in this work is based on one created and vetted by industry experts to gain approval to start the S-2043 certification process. The modifications made to this model were based on engineering experience gained from modeling the MMTT, which itself demonstrated good agreement with data from the full-scale test.

The cask accelerations observed in these simulations were very small; the largest was only 0.30 g. This is approximately half of the peak acceleration value encountered in the equivalent set of tests for the MMTT. Section 5 details the effects of the reduced cask motion of the Atlas railcar on fuel integrity. Additionally, this validates the assumption of Section 3 that the SDOF approximation of the cask and cradle is operating in a linear regime (i.e., no nonlinear phenomena occur such as material nonlinearity, liftoff, or impact).

The sensitivity study of canister fuel in this section illustrates that the additional degrees of freedom of the canister in the cask have the potential to increase the accelerations felt by the SNF, particularly when lateral loads are present. As detailed in Section 5.3, fuel rod strains may be increased by 4 to 6 times. However, because the nominal strain is so small, the canister motion does not increase strain beyond a critical level. The study presented in this work is a bounding one for the Atlas railcar, because it focused on the cask that has the highest lateral acceleration of all canister fuel casks. Furthermore, the kinematics model used to calculate canister motion includes some degree of conservatism. A minimal amount of damping was applied for numerical stability, and no dunnage was included to limit motion of the canister within the cask.

In summary, the railcar dynamics analysis reinforces earlier conclusions that the loads on SNF during rail transportation are mild. Varying configurations of the railcar with different casks and cradles, transporting bare or canister fuel, result in varied shock and vibration environments imparted to the fuel; however, these loads are orders of magnitude lower than those needed to challenge cladding integrity.

5. Fuel Rod Structural Analysis

A structural analysis of fuel rods and fuel assembly hardware is necessary to demonstrate that the fuel cladding remains intact and the fuel assembly hardware remains undamaged. Based on the MMTT data, shock and vibration loading conditions on the SNF are expected to be mild during standard NCT operations. The NCT loading regime considered in this study includes shock and vibration loading from normal transportation and handling activities. The NCT loading requirements defined in 10 CFR 71.71 also includes a 30 cm drop of the package, but those package drop mechanical loads are not included in the current study. This analysis focuses on the shock and vibration environment expected in train transportation in the United States.

The finite element model used for this analysis is described in Section 5.1. The model represents a single fuel rod, one of many that compose a single fuel assembly. The loading conditions were calculated according to the methods described in Section 4, and the library of results are summarized in Section 4.2.

The calculated motion of the cask is applied as an imposed motion in the single-rod model. Section 5.2 summarizes the results. In this analysis all of the load cases described in Section 4.2 (612 cask motion sets) were applied to the single-rod model to generate a large library of results (1600+ fuel rod responses). These results were compiled and searched for the maximum cladding strains. The pitch and bounce and single bump cases were all calculated based on vertical cask motion. The twist and roll cases were calculated using both vertical and lateral motion because the lateral motion was relatively strong. All cases considered a minimum and maximum fuel rod stiffness to explore the effect of increased stiffness in the irradiated condition. Section 5.2 discusses fuel rod stiffness in more detail.

Section 5.3 describes sensitivity studies that were completed to supplement the main analysis. The main analysis calculates the response of a 17 x 17 pressurized water reactor (PWR) fuel assembly design. It assumes a minimum fuel rod stiffness and a maximum fuel rod stiffness. The sensitivity studies consider other fuel assembly designs and stiffness conditions. It includes PWR and boiling water reactor (BWR) cases. The results of this study demonstrate that the response does not change significantly from one configuration to the next.

Section 5.4 considers stress concentrations in the cladding caused by the fuel pellets. The single-rod model described in Section 5.1 uses a homogenized representation of the fuel cladding and fuel pellets that assumes a representative stiffness with a constant cross section in the beam elements that represent the fuel rod. The beam elements respond to applied loads according to linear elastic beam theory. The cladding stress state in real fuel rods is expected to be affected by the discrete pellets of the fuel, and the chemical or mechanical bonds that may form between irradiated fuel and cladding. The sibling rod test program is currently studying irradiated fuel and cladding behavior (Saltzstein et al. 2017) and ORNL CIRFT tests (Wang et al. 2016) have shown that the pellets contribute to net fuel rod stiffness. This sensitivity study considers whether a stress concentration factor should be applied to the results of this study.

Section 5.5 summarizes the conclusions of the fuel cladding structural analysis. It also draws on the MMTT data to justify the results and generalizes the conclusion.

5.1 Fuel Rod Model Description

PNNL has performed structural dynamic analysis of fuel assemblies and fuel assembly components for several years, evaluating the response of fuel rods and assembly components over a range of mechanical loading regimes. One example of a full fuel assembly structural dynamic finite element model is discussed by Klymyshyn et al. (2013). When the test data from the MMTT were being evaluated in 2017−2018, the question of how much detail is necessary to reasonably calculate fuel rod strains caused by NCT loads arose. Klymyshyn et al. (2018) demonstrated that a single fuel rod model was adequate for calculating cladding strains because the loads and resulting strains were very low. Reasonable agreement

was achieved using a finite element model of a single fuel rod that was loaded by applying motion directly to the rod at spacer grid locations. While that model provided reasonable results for minimal computation time, it was discovered that a better match for testing data could be achieved by adding springs to the model to represent the interaction between the spacer grids and the fuel rod.

The single fuel rod model used in this study has the configuration shown in Figure 24. The fuel rod is represented by a long line of beam elements (about 100). At the spacer grid locations are translational and rotational springs. The translational springs model the interaction between the spacer grids and fuel rods, which generically represents leaf springs, contact dimples, or other specific spacer grid design features. The rotational springs act against fuel rod rotation relative to the grids. The spring constants for both types of springs can be estimated through analysis or measured by fuel assembly mechanical testing, but both methods require access to propriety information. In this case, the spring constants were estimated analytically and then refined to match test data.

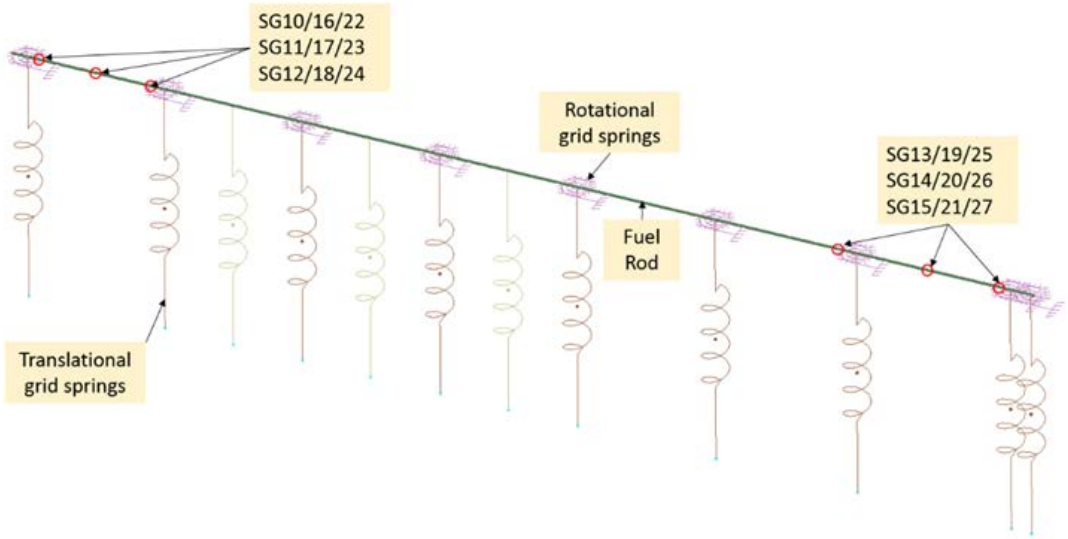

Figure 24. Single fuel rod model.

The single-rod model is designed to calculate deflection of the fuel rod in one plane. The normal loading condition is prescribed motion in the vertical direction, and the fuel rod responds by bending between the grid spacers in the vertical-axial plane. The prescribed motion is applied at the bottom end of the translational springs (see Figure 24), and forces generated through the springs are applied to the fuel rod at the grid locations. The same model is used to model the lateral response of the fuel rod in the twist and roll loading conditions, with the modification that gravity is rotated to be perpendicular to the lateral motion.

Figure 24 also identifies strain gage locations to match the MMTT. Strain gages measure strain at these locations. The finite element model discretizes the fuel rod into about 100 elements, and certain elements correspond to the strain gage locations. The post-processing scheme specifically extracts results from the elements that correspond to strain gage locations for cross comparison to the MMTT data. The strains calculated at the strain gage locations are the most accurate, because they are locally adjusted to the effect of gravity. All calculated strain results in this study are adjusted to remove the strains caused by gravity. The persistent strain caused by gravity is calculated to be on the order of 40−50 uE, which is typically larger than the transient strain caused by a shock or vibration during NCT. The model calculates absolute strains, but strain gages report strains that are relative to the gravity-loaded state. Reasonably accounting for gravity is part of the challenge of dealing with such low magnitude loading conditions. In normal

engineering applications, 50 uE is a negligible amount of strain. In this application, 50 uE is significant relative to the anticipated dynamic response to NCT.

In addition to the strain gage location strain results, the single-rod model is evaluated to report the maximum strain at any location on the fuel rod over time. This value is useful in determining if other locations on the fuel rod experience higher strains than the strain gage locations, but adjusting for gravity is less precise because the strain caused by gravity at that specific location is not readily available. Instead, the mean of the maximum rod strain over time is used to adjust for gravity. The accuracy of this method is expected to be +/-20 uE based on modeling experience (Klymyshyn et al. 2018), which is precise enough for the purposes of this study.

Another result extracted from the single-rod model is strain energy. This represents the strain energy throughout the fuel rod. In the LS-DYNA model results, strain energy is reported as internal energy, but with the elastic material model, internal energy is equal to elastic strain energy. This value is useful for quantifying the total deflection state of the fuel rod.

The final result to discuss from the single-rod model is the fuel rod deflection. This is a measure of the maximum vertical (or lateral) deflection of the fuel rod, measured as the distance between the maximum nodal location on the rod and the minimum nodal location on the rod in the vertical (or lateral) direction. This value is typically considered in the context of the existing gap space between fuel rods in the fuel assembly. If the value exceeds the available gap space between fuel rods, rod-to-rod contact could occur, and the single-rod model is not suitable for the analysis. The single-rod model can be expanded as necessary into a column of fuel rods or a full fuel assembly to explore rod-to-rod contact. In interpreting the fuel rod deflection results, note that because the nodes are located at the center of the fuel rod cross section, the OD of the rod should be added to the reported value to get the absolute dimensions of the maximum deflection state.

5.2 Single Fuel Rod Structural Dynamic Model Results

The single fuel rod model was evaluated for all 612 cask motion cases discussed in Section 4.2. The single-rod model was also evaluated for two fuel rod stiffness conditions: a low-stiffness case that represents fuel pellets being able to slide within the cladding tube, and a high-stiffness case that represents fuel pellets bonded to the cladding. The results are grouped together by track conditions (pitch and bounce, single bump, twist and roll) in the following sections. The results are summarized in Table 7.

In all cases, the peak strains calculated in the cladding are below 100 uE (the peak strain recorded in the MMTT), and are generally comparable to or lower than the strains recorded during the same tests performed at TTCI for the MMTT. This demonstrates that the MMTT was generally a good indication of fuel rod strains and the shock and vibration environment fuel rods are exposed to during cross-country rail travel. The change to the Atlas railcar from the railcar used in the MMTT did not significantly change the shock and vibration loading conditions.

The most important variable appears to be the mass of the SNF packages; the lightest packages have the highest fuel rod loads. The standard format for reporting results in the body of this report is an envelope plot, which shows the high and low values at each railcar speed. The HI-STAR 60 is the lightest package and it tends to have the highest fuel rod strains, fuel rod strain energy, and fuel rod deflection across all track conditions. The HI-STAR 190XL is the heaviest package and it tends to have the lowest fuel rod strains, fuel rod strain energy, and fuel rod deflection across all track conditions. However, package weight is not the only factor. Speed plays an important role in the response, as each cask system experiences a resonance response at a different speed. This is a normal phenomenon in railcar dynamics, and is the reason that railcars are always tested over a range of speeds. Lighter casks tend to experience resonance at higher speeds, so the ranking of responses is not always by weight at all speeds. Appendix A provides the results with more detail so the 17 packages can be compared. The body of this report

presents the results from Appendix A in envelope plots that show the maximum and minimum response of all casks at each speed, but eliminate the details of individual cask responses.

Another important trend is that the higher stiffness fuel rods tend to have much lower strain, strain energy, and deflection than the lower stiffness case. While a higher stiffness fuel rod can be expected to deflect less than a lower stiffness fuel rod for the same applied load, there was some concern that the change in the fuel rod natural frequency could alter the loads. But the analysis results demonstrate that the increase in stiffness is more consequential than altering the natural frequency. This suggests that the unbonded fuel state of the MMTT was the most limiting option, and SNF with bonded fuel would have even lower strains than those witnessed in the MMTT.

Table 7. Summary of fuel rod structural dynamic model results.

	Pitch and Bounce		Single Bump		Twist and Roll			
Direction	**Vertical**		**Vertical**		**Vertical**		**Lateral**	
Stiffness	**Low**	**High**	**Low**	**High**	**Low**	**High**	**Low**	**High**
Peak Strain (μE)	17	6	20	6	7	3	2	1
Peak Strain Energy (mJ)	0.86	0.31	0.93	0.28	0.67	0.24	0.52	0.15
Peak Deflection (mm)	0.23	0.079	0.24	0.080	0.2	0.06	0.04	0.01

5.2.1 Fuel Rod Response to Pitch and Bounce

Figure 25, Figure 26, and Figure 27 show the range of peak strain, peak strain energy, and peak deflection calculated, respectively, for each train speed analyzed for the pitch and bounce test section. These envelope plots show the maximum and minimum values calculated at each train speed, among all 17 casks. The annotations in each plot list the maximum and minimum peak values and the corresponding cask name which is not always the lightest and heaviest casks. Note that the minimum peak value refers to the peak (maximum) value of the minimum line of the envelope. The color of the annotations corresponds to the fill color on the envelope plots. Detailed plots illustrating the response of each cask are shown in Sections A-1.1 and A-2.1.

The fuel rod response closely resembles the trend of the cask motion calculated in Section 4.2. This implies that fuel rod resonance modes are not strongly excited by the cask excitation. The high-stiffness fuel rods produced peak strains, strain energies, and deflections that were universally smaller than their low-stiffness counterpart, by roughly three times. Roughly the same trends were observed for both the low and high-stiffness rods, indicating that the stiffness change did not incur strong resonance in response to the cask motion. The miniscule strains, strain energies, and deflections observed preclude any risk of immediate loss of cladding integrity or rod-to-rod contact.

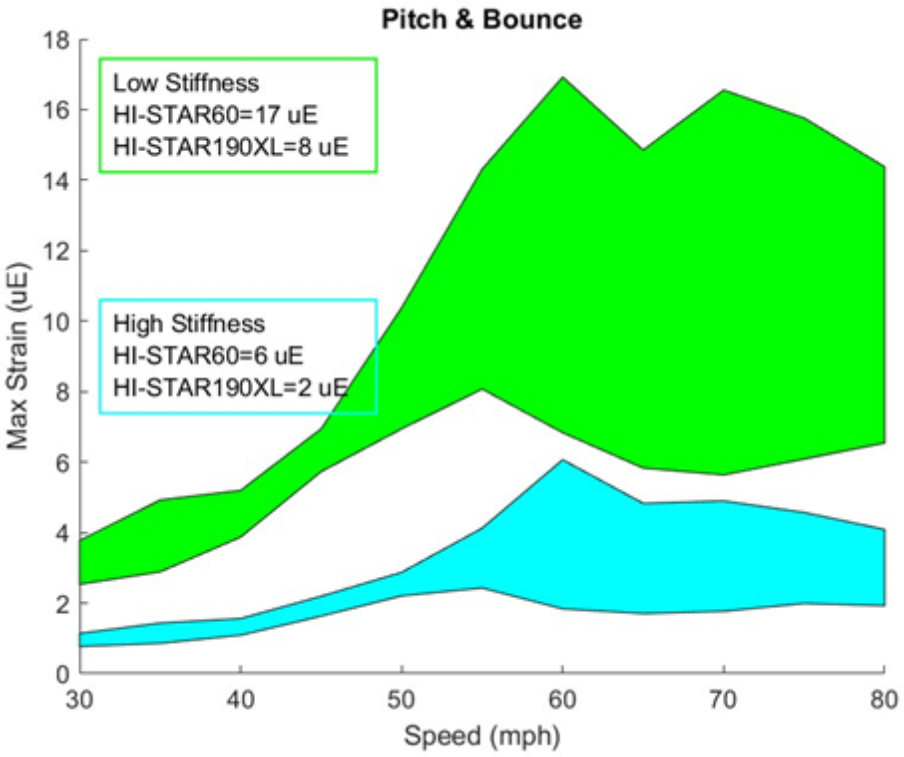

Figure 25. Maximum strain on pitch and bounce test section.

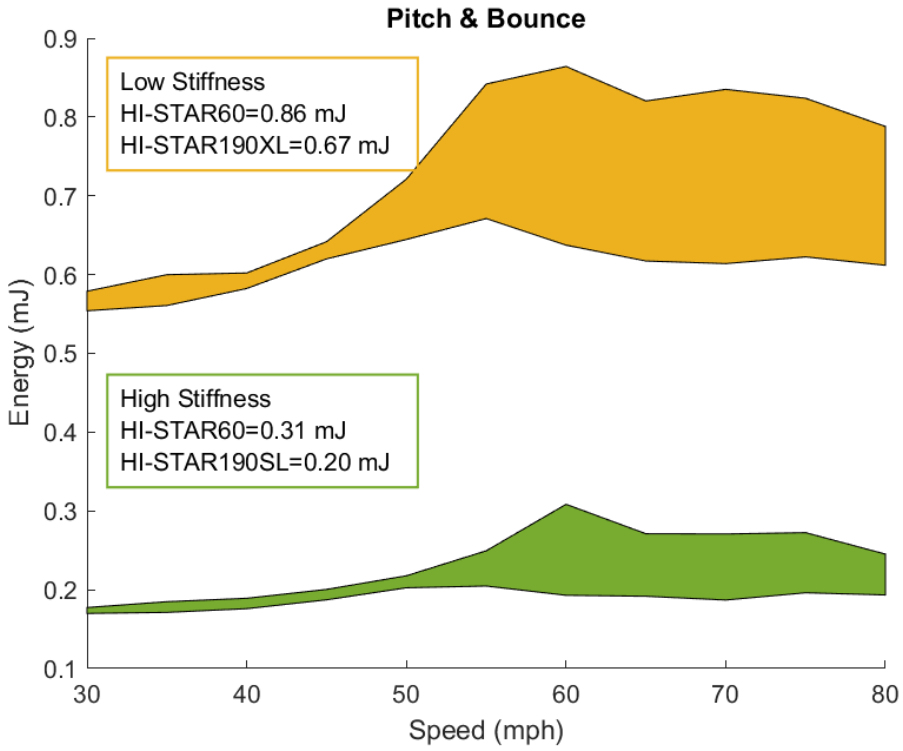

Figure 26. Maximum strain energy on pitch and bounce test section.

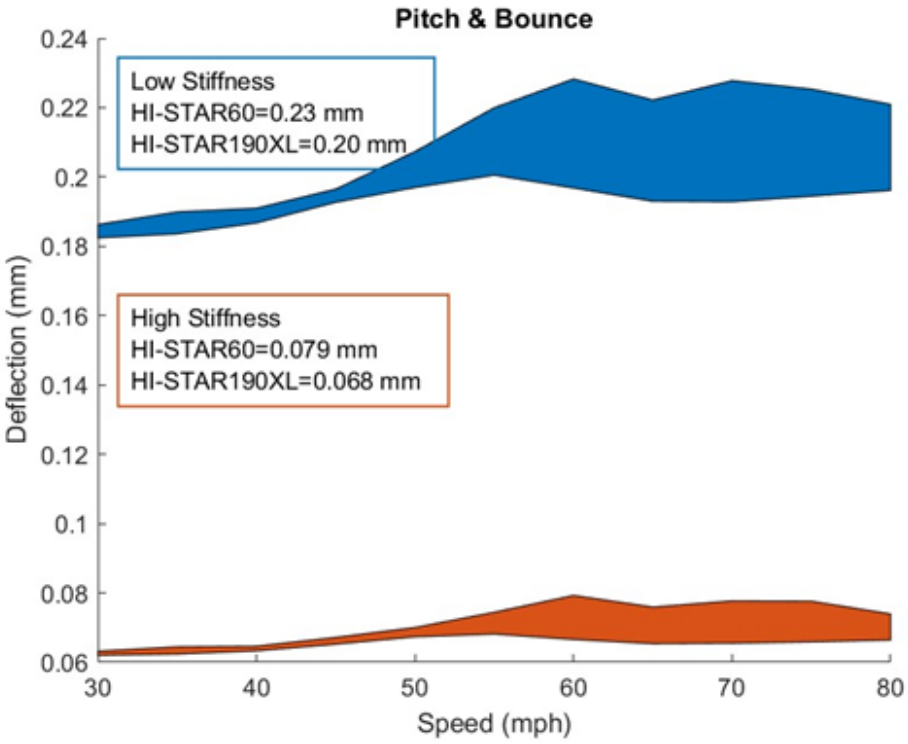

Figure 27. Maximum deflection on pitch and bounce test section.

5.2.2 Fuel Rod Response to Single Bump

Figure 28, Figure 29, and Figure 30 show the range of peak strain, peak strain energy, and peak deflection calculated, respectively, for each train speed analyzed for the single bump test section. Detailed plots illustrating the response of each cask are shown in Sections A-1.2 and A-2.2.

Similar to the pitch and bounce case, the fuel rod response to the single bump test section closely resembles the cask motion, implying that fuel rod resonances were not excited. Again, the higher stiffness fuel rods produced peak strains, strain energies, and deflections that were approximately three times smaller than their low-stiffness counterparts. The peak values were very similar to the pitch and bounce response, which similarly indicates that there is no risk to cladding integrity or rod-to-rod contact.

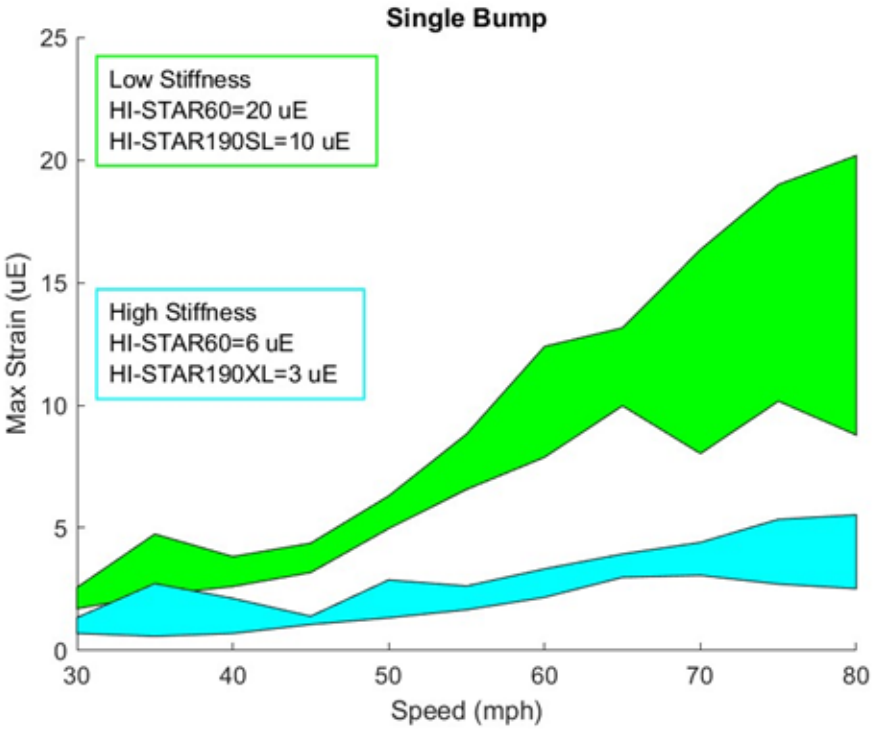

Figure 28. Maximum strain on single bump test section.

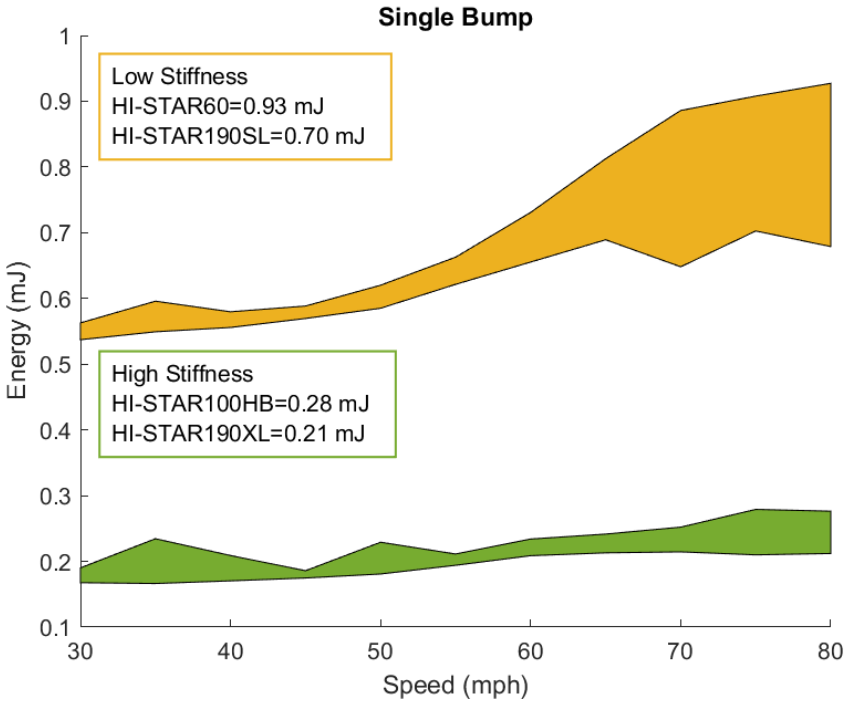

Figure 29. Maximum strain energy on single bump test section.

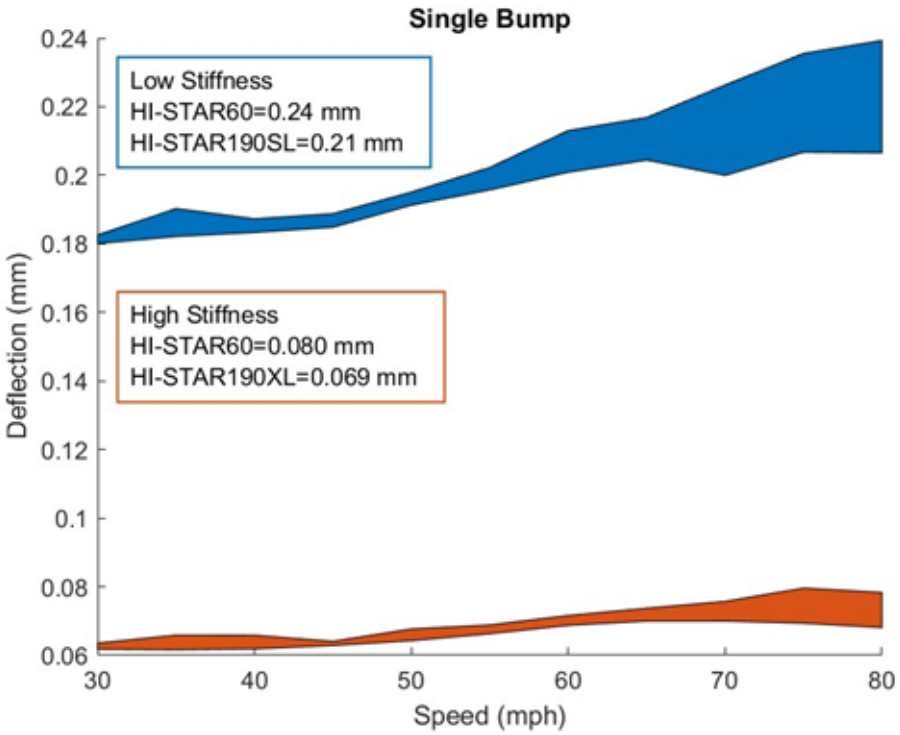

Figure 30. Maximum deflection on single bump test section.

5.2.3 Fuel Rod Response to Twist & Roll

Figure 31, Figure 32, and Figure 33 show the range of peak strain, peak strain energy, and peak deflection calculated for each train speed analyzed for the twist and roll test section. These plots correspond to the vertical cask motion calculated in Section 4.2. Detailed plots illustrating the response of each cask are shown in Sections A-1.3 and A-2.3.

As with the previous cases, the fuel rod response closely resembles the cask motion, implying that fuel rod resonances were not excited. Again, the higher stiffness fuel rods produced peak strains, strain energies, and deflections that were approximately three times smaller than their low-stiffness counterparts. The peak values were even smaller than the pitch and bounce and single bump test sections, which suggests no risk to cladding integrity or rod-to-rod contact.

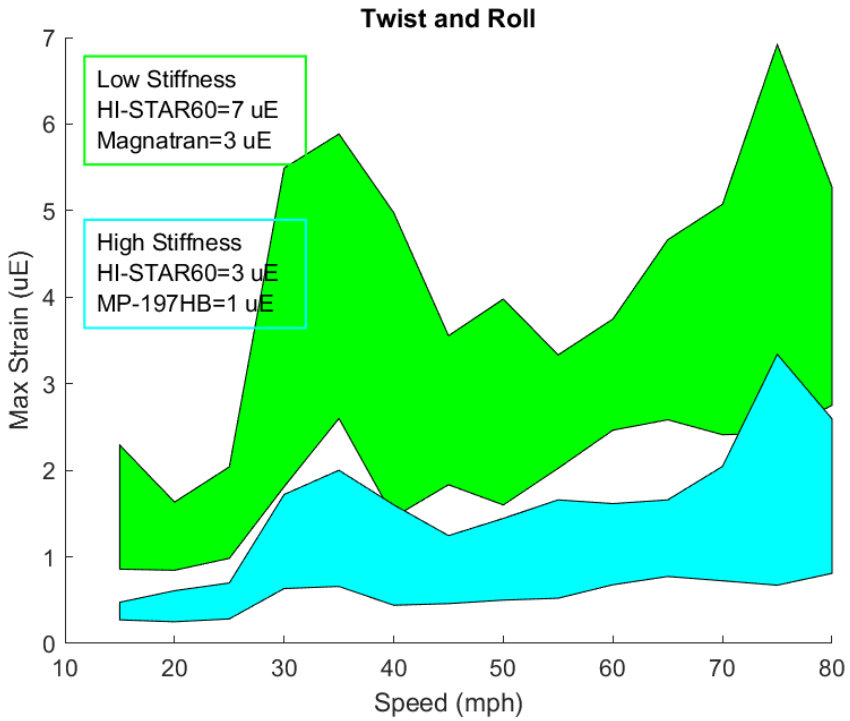

Figure 31. Maximum strain on twist and roll test section, vertical loading.

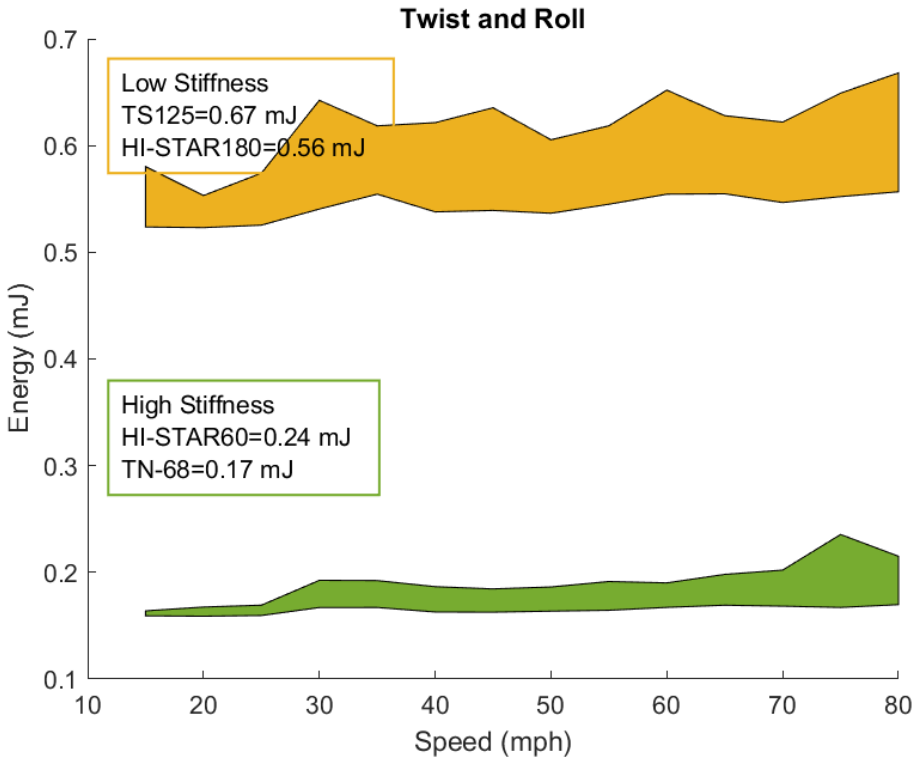

Figure 32. Maximum strain energy on twist and roll test section, vertical loading.

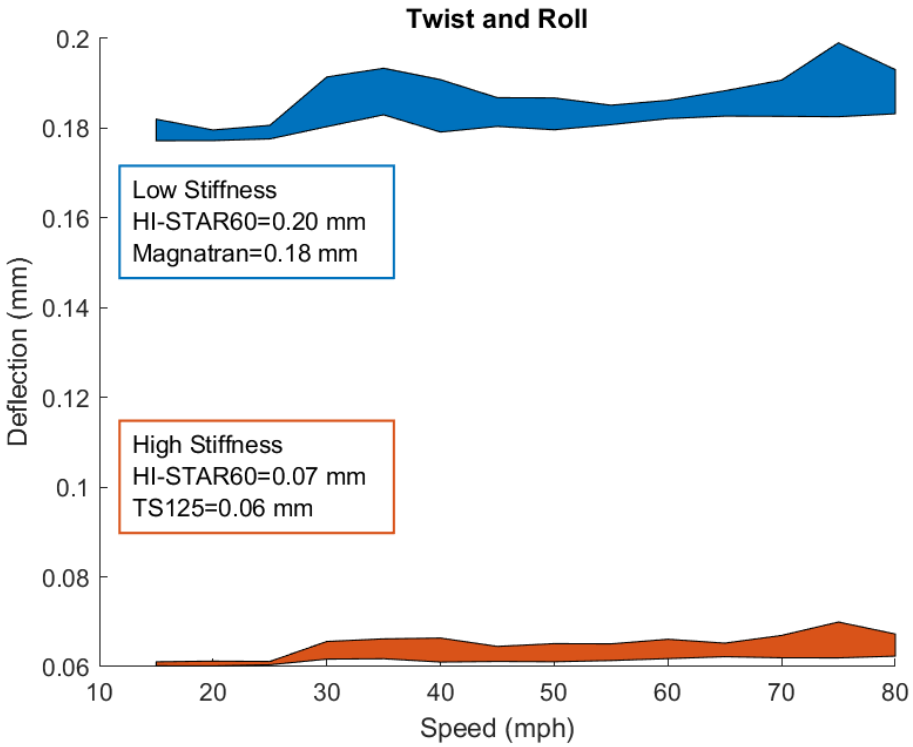

Figure 33. Maximum deflection on twist and roll test section, vertical loading.

Figure 34, Figure 35, and Figure 36 show the range of peak strain, peak strain energy, and peak deflection calculated for each train speed analyzed for the twist and roll test section. These plots correspond to the lateral cask motion calculated in Section 4.2. Detailed plots illustrating the response of each cask are shown in Sections A-1.3 and A-2.3.

Compared to the vertical response above, the strains, strain energy, and deflections, are even smaller for the lateral case. This is despite the cask accelerations being larger in the lateral direction; it is hypothesized that the fuel rods were less sensitive to the frequency content of the lateral cask motion. Nevertheless, the strains and deflections calculated are small enough to be considered negligible.

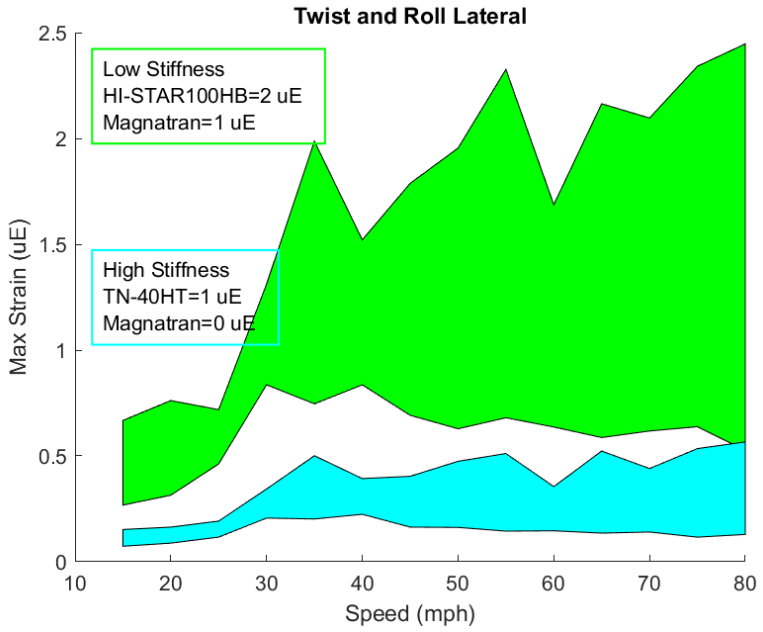

Figure 34. Maximum strain on twist and roll test section, lateral loading. The minimum value in the high-stiffness case was truncated due to rounding; the value is 0.22 µE.

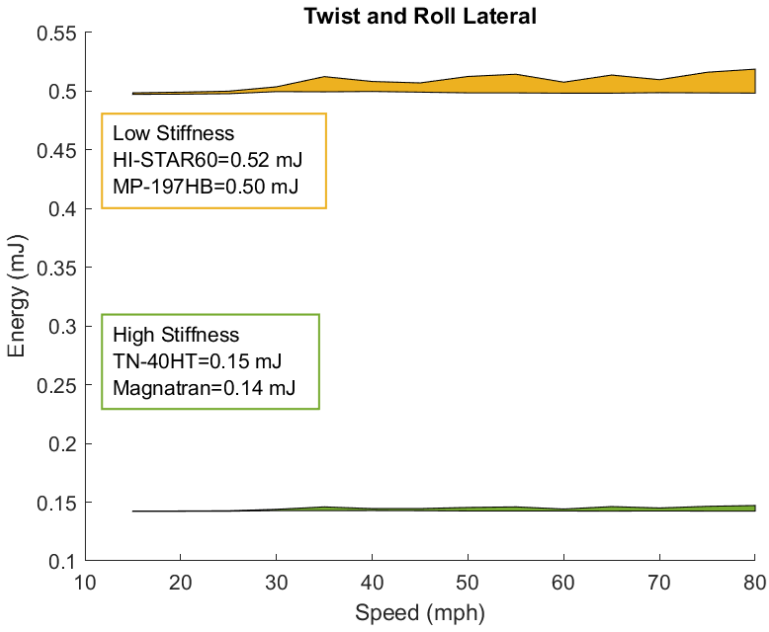

Figure 35. Maximum strain energy on twist and roll test section, lateral loading.

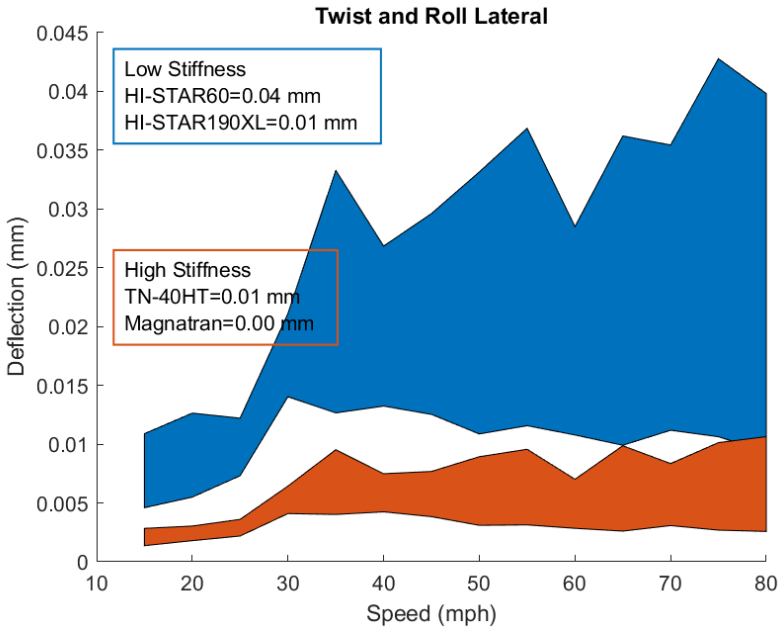

Figure 36. Maximum deflection on twist and roll test section, lateral loading. The minimum value in the high-stiffness case was truncated due to rounding, the value is 0.004 mm.

5.3 Sensitivity Studies

The library of fuel rod responses (1600+) covers a large range of shock and vibration responses for a 17 x 17 PWR fuel assembly. Both low fuel rod stiffness and high fuel rod stiffness are covered. Every anticipated cask or package configuration is covered in this study. The parameter not varied in the library of results was the fuel assembly geometry. All the cases used a fuel assembly geometry that matched the SNL assembly used in the MMTT. The distance between spacer grids, the fuel rod diameter, and wall thickness were the same in all 1600+ fuel rod analyses. This section explores the sensitivity of the calculated fuel rod response to factors such as differences in fuel assembly geometry, transportation within a canister system, and the complex strain state that can be potentially caused by fuel pellets inside cladding.

Each sensitivity study is conducted to support the conclusions of this analysis. The purpose is to check different configurations to see if a more extensive analytical study is warranted. As each case will show, the analysis of the 17 x 17 PWR fuel assembly contributed by SNL to the MMTT campaign is either more limiting than the other options or can be viewed as being representative of the other cases. SNL's 17 x 17 fuel assembly is also referred to as the "standard" PWR assembly, because it is the specific fuel assembly design that is the basis for the library of fuel rod results described in Section 5.2.

5.3.1 PWR Sensitivity Study

The PWR sensitivity study case considers a hypothetical 17 x 17 PWR assembly that is based on a design modification to the standard 17 x 17 PWR design used in this study, which eliminates some of the spacer grids and creates a longer largest span. Figure 37 shows a sketch of the hypothetical fuel assembly design, with eight total spacer grids and a longest distance between grid spaces of approximately 40 inches. The long length was chosen to study the effect of lengthening the longest unsupported fuel span. The 40-inch span is longer than any known fuel design, but that unsupported length could be achieved in a number of fuel designs if one spacer grid failed. The 80 mph single bump load case was used to generate the structural dynamic response of the hypothetical fuel rod design. The low-stiffness condition, representing

fuel and cladding in an unbonded state, was assumed because it was expected to allow the maximum deflection in the fuel rod and result in the highest strains.

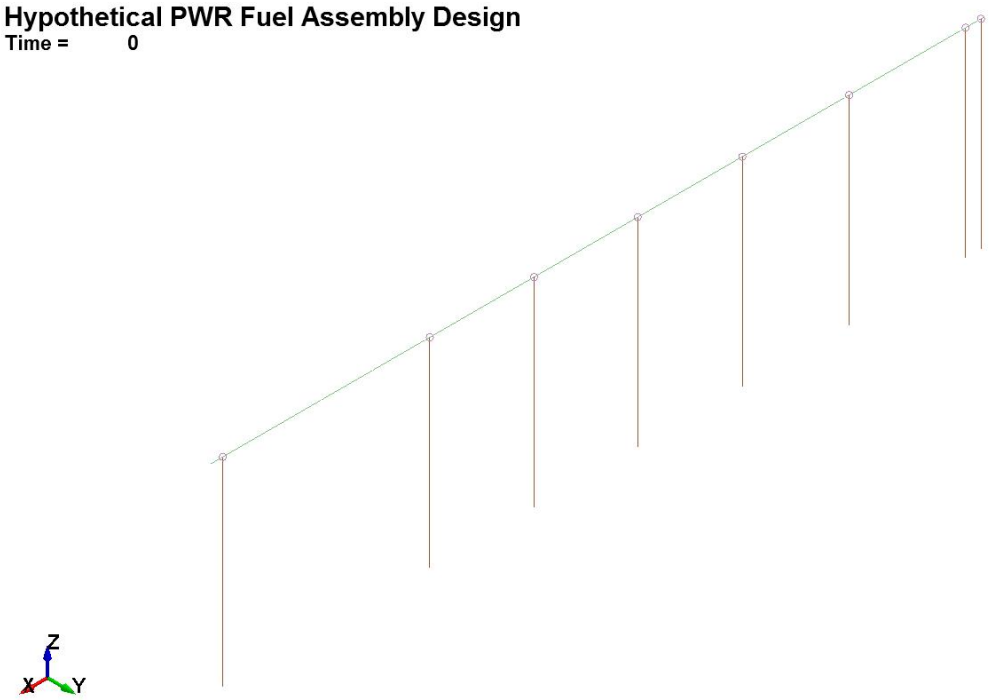

Figure 37. PWR sensitivity study fuel model sketch.

The analysis predicts relatively higher strains than in the standard 17 x 17 PWR case, but it also predicts the fuel rod deflection is too large to reasonably use the single-rod model. Figure 38 shows the maximum strain state calculated in the model. The deflections are exaggerated by a factor of 100 to show the shape of deflection. The largest span dominates the response. The highest strain occurs at the end of the unsupported span, at the spacer grid location. The strains at the center of the span are also relatively high, but not higher than the end of the span. The absolute strain is 237 uE, but the strain at that location caused by gravity (prior to the dynamic loading transient) is 191 uE (which is significantly higher than the ~50 uE maximum strain caused by gravity in the standard PWR case.) The net transient strain is 46 uE, which is more than double the 20 uE transient strain predicted for the standard PWR design. However, 46 uE is still negligible in terms of fuel rod cladding failure or fatigue failure. The maximum fuel rod strain energy in this case was 6.7 mJ, which is higher than that witnessed in the MMTT, but is still the same order of magnitude. The maximum deflection in this case is 3.4 mm, which indicates that significant rod-to-rod contact should be expected, so the single-rod model is not appropriate for precisely calculating the response of the fuel rod in this case.

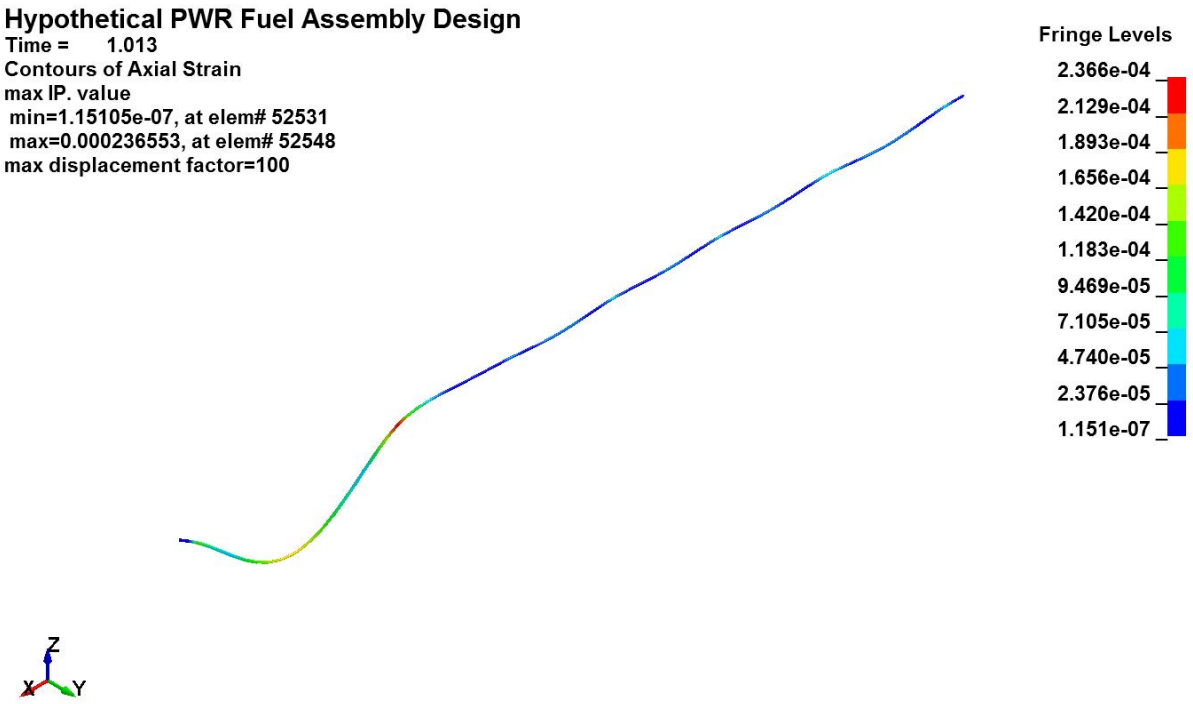

Figure 38. PWR sensitivity study hypothetical fuel rod response to 80 mph single bump (deflections amplified 100x).

The main observation from this case is that the largest span can dominate the dynamic response of a fuel rod. Away from the largest span, the removal of some of the grid spacers (lengthening some of the spans) did not have any noteworthy effect. Even though the transient strain was calculated to be higher in this case than the standard PWR case, it was not significant enough to challenge the yield strength or fatigue strength. This was a relatively large change in the geometry, and the results were still very mild.

The conclusion from this sensitivity study is that changes in span length can affect the response of a fuel assembly, but not by enough to significantly change the response.

5.3.2 BWR Sensitivity Study

The BWR sensitivity study keeps the same fuel assembly grid locations as the standard 17 x 17 PWR but increases the inner and outer diameters of the fuel rod. The BWR fuel rod stiffness (EI) is about 23 N-m^2, based on the geometry and a low burnup, unbonded material condition. The mass of the fuel rod is comparable to (but lighter than) the standard PWR fuel rod. The PWR EI values used above were 14.3 N-m^2 for the low stiffness, unbonded fuel case, and 50 N-m^2 for the high stiffness fully bonded fuel case.

The response is very similar to the standard PWR 17 x 17. The strains at the moment of maximum strain are plotted in Figure 39. The peak absolute strain is 40 uE, but the strain component caused by gravity at that location is 33 uE. The net transient strain from shock and vibration is just 7 uE, and the maximum strain energy is 0.4 mJ. Both of these values are below the standard 17 x 17 PWR fuel rod response to the 80 mph single bump loading conditions. The deflection is also lower, only 0.1 mm.

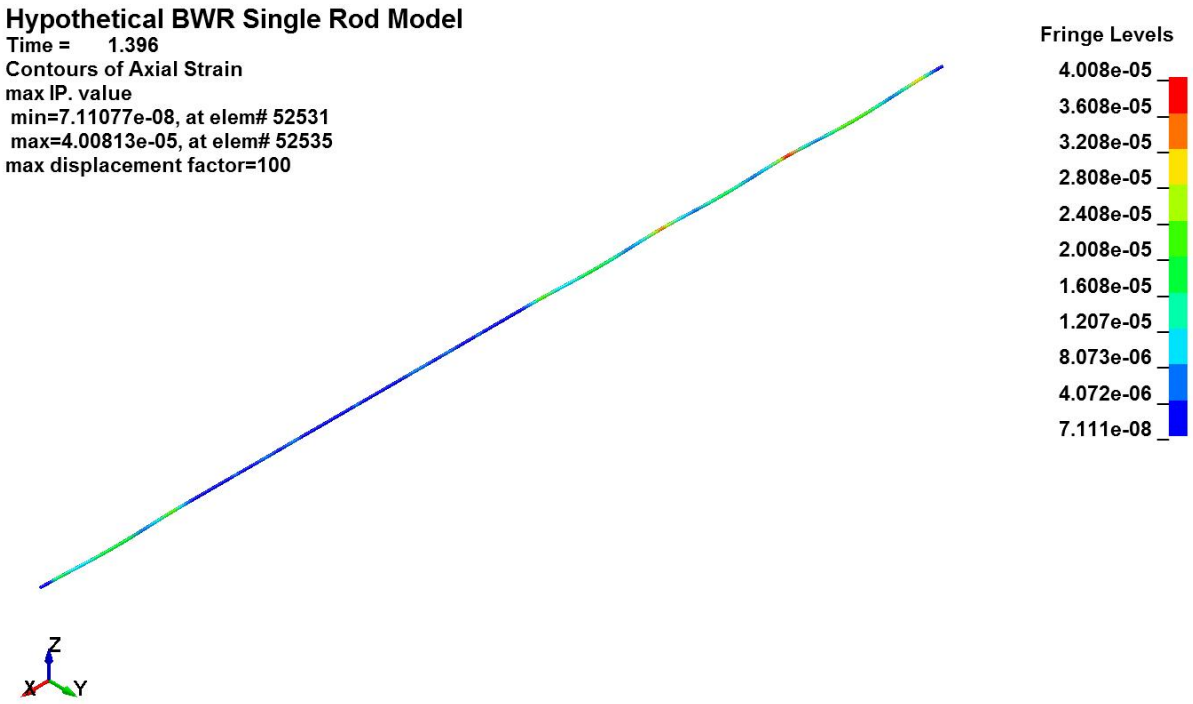

Figure 39. Hypothetical BWR response to 80 mph single bump (deflections amplified 100x).

While this model does not attempt to represent an existing BWR design, the sensitivity study case demonstrates that the larger BWR fuel rod diameter and the higher stiffness would produce lower cladding strains for the same grid spacer configuration. From this, it is concluded that there is no reason to be concerned about BWR fuel rod dynamics under shock and vibration conditions since the results are similar to those recorded in the MMTT or to the shock and vibration environment that is calculated for the Atlas railcar.

5.3.3 Canister Sensitivity Study

Section 4.3 describes a sensitivity study of the effect of a free-moving canister on the motion of the fuel basket. While the effect was minimal for vertical excitations, significant differences between canister and cask motion were observed for lateral excitations such as twist and roll. To identify the effect on fuel rod strains, acceleration time histories corresponding to nominal cask motion and the two hypothetical canisters were applied in the single-rod model. Lateral motion from the twist and roll studies were applied; the difference in cask and canister motions from pitch and bounce were so small that they were considered to have a negligible effect.

Table 8 shows the peak strains identified for the nominal cask and both hypothetical canister motions. The peak strains calculated using the canister motion were approximately 4−6 times greater than using the nominal cask motion. However, because the nominal strain is already so small, the effect of canister motion does not increase strain to a level that challenges the yield strength or fatigue strength.

Table 8. Peak strains for the canister fuel sensitivity study. Strains are adjusted for gravity.

Input Time History	Peak Strain (μE)
Cask	9.76
Canister 1	64.5
Canister 2	42.0

Figure 40 and Figure 41 show the time history and fast Fourier transform (FFT) at the location of maximum strain for the three simulated conditions. These figures illustrate a key difference between the response of canister and non-canister fuel ─ the canister fuel is subject to more high-frequency content. The nominal cask motion described in Section 4.3 is dominated by content below 10 Hz, whereas the canister motion contains additional content above this range, which appears to correspond to the arrest of the lateral canister motion by the inner wall of the cask. This additional high-frequency content overlaps with the resonant frequencies of the fuel rod (between approximately 30−50 Hz), yielding a larger strain response for the canister fuel.

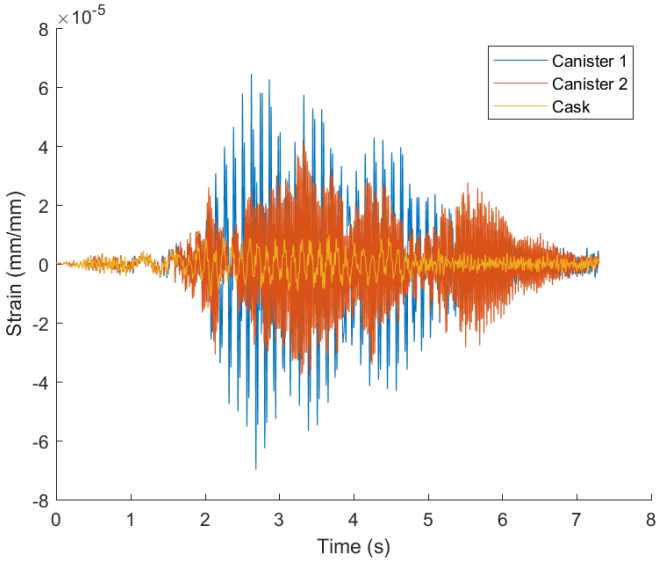

Figure 40. Strain time history for the canister fuel sensitivity study. Strains are adjusted for gravity.

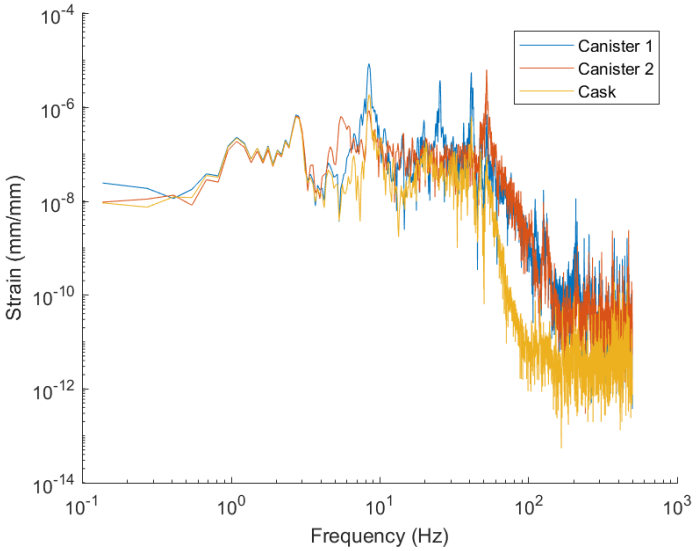

Figure 41. FFT of strain time histories in the canister fuel sensitivity study.

It is concluded from this study that canister motion within the cask can contribute to slightly higher fuel cladding strains, but the increase in strain is not enough to be of significant concern. It is not necessary to perform detailed analyses involving canister motion when the diametrical clearance is within the bounds

established in Section 4.3, 5 mm to 15 mm. If the diametrical gap between the canister OD and the cask ID is larger than 15 mm it would be reasonable to perform another sensitivity check, but unless the cladding strains could credibly reach or exceed 100 uE this phenomenon is not worth accounting for.

5.3.4 Fuel Rod Stiffness Sensitivity Study

The fuel rod sensitivity to changes in fuel rod stiffness is adequately covered by the two stiffness conditions that compose the library of fuel rod dynamic response results (1600+). The EIs in the two stiffness conditions were 14.3 N-m^2 and 50 N-m^2, representing bonded and unbonded fuel to cladding conditions, respectively. The results described in Section 5.2 show a strong trend that the higher stiffness fuel rod condition leads to relatively smaller strains, strain energy, and deflection in the fuel rod than the lower stiffness case. The highest fuel rod strains, strain energies, and deflections come from the lowest stiffness case, which is identical to the MMTT test configuration.

While it is possible to run the same analyses for any desired stiffness, it was concluded that the effort was not warranted by the results. The change in fuel response would have to be significant to be relevant, and there is no reason to suspect that fuel rod stiffness exists between the two extreme values that would lead to a significant change in response.

One of the general observations from this study is that the structural dynamic response of fuel rods is dominated by free vibration, rather than forced vibration. In a forced vibration scenario, the fuel rod stiffness could theoretically have a stronger influence on the response, particularly when the excitation frequency approaches the natural frequency of a fuel rod span. But what we have seen experimentally and through finite element modeling is that the fuel rod response is more closely related to a free vibration response.

It is concluded that the effect of varying stiffness is adequately covered in the two extreme fuel rod stiffness cases, and no additional consideration is necessary.

5.4 Strain Concentrations in Cladding from Fuel Pellets

This analysis treats the fuel rods as homogenized linear elastic beams. Some previous analyses suggests a stress concentration factor is appropriate to account for the influence of discrete fuel pellets within the cladding (Adkins et al. 2013). Fuel pellets are expected to be much stiffer than fuel rods, and they may form a mechanical or chemical bond with the surrounding cladding material that could influence the stress state of the fuel rod cladding. FEA is performed to explore the effects of the pellet to cladding interface, but the ultimate conclusion is that applying a stress concentration factor is not generally necessary.

The finite element model used in this sensitivity study is conceptually based on the ORNL CIRFT (Wang et al. 2016) test. The cladding and fuel pellet dimensions were chosen to represent the HB Robinson fuel rod for consistency with CIRFT test data. The model consists of a fuel rod sample that is approximately 6 inches long and sectioned into three approximately 2-inch-long segments. A bending moment is applied at the two end segments to put the middle 2-inch segment into a state of uniform bending. The model considers different configurations of fuel inside the cladding tube, including no fuel (empty cladding), cylindrical fuel pellets that are bonded to the cladding, and cylindrical fuel pellets that are free to slide relative to the cladding tube. The response of the 2-inch gage section is compared to the theoretical behavior of beams, in terms of deflection and stress.

The finite element model and the relevant cantilever beam closed form solution are shown in Figure 42. The red and green sections of the cladding tube are rigid bodies that are pinned at their center of mass, allowing rotation about the axis normal to the page. One of the pins is a slider that allows longitudinal motion. Moments are applied to the rigid bodies, causing the flexible body section of the fuel rod segment to bend. In a tube, this loading condition creates a nearly uniform state of bending that agrees with the closed form solution of a cantilever beam with a moment applied to the free end. The only modification to

the classic case is that the fuel rod segment ends are free to rotate, which allows the reference line to rotate. These boundary conditions put the point of maximum deflection at the center of the 2-inch gage section, where x = L/2.

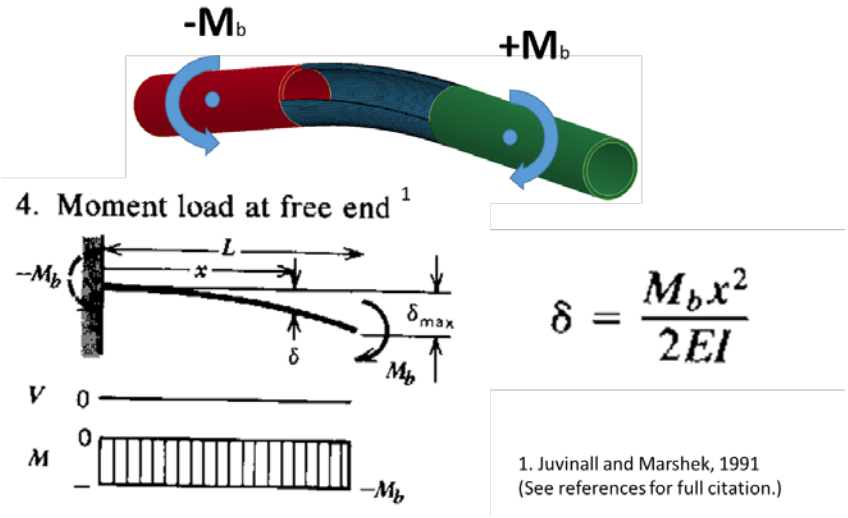

Figure 42. Fuel rod bending, equal and opposite applied moments.

Figure 43 shows the two main configurations of the finite element model in cutaway views. All the models used in this sensitivity study were fully three-dimensional. In this application, half-symmetry could have been used. Figure 43A shows the empty cladding tube version of the model. Figure 43B shows the cladding with the pellet cylinder configuration that is used in both the sliding contact case and the bonded interface case. The difference between the two pellet configurations is the contact definition. The sliding contact case uses LS-DYNA's automatic single surface contact option, which senses contact between all bodies and applies friction. The bonded contact case uses LS-DYNA's tied nodes to surface contact option to tie the nodes on the outer surface of the fuel pellets to the inside surface of the cladding tube. This connection type simulates a perfectly bonded interface by requiring the tied nodes to remain at the same location relative to the cladding tube surface. For example, extension of the cladding tube requires equal extension of the fuel pellets, leading to an effective increase in fuel rod stiffness.

The axial gaps between fuel pellets in Figure 43B are all 1 mm, which is a larger gap size than is typically observed in SNF. The relatively large gap size was selected for finite element modeling convenience. The purpose of this analysis is to illustrate the effect of fuel pellets on the fuel cladding stress state using a relatively coarse finite element mesh that solves quickly. A more precise calculation of stresses using a finer mesh can be done, but it would take more time and effort than is available for this report.

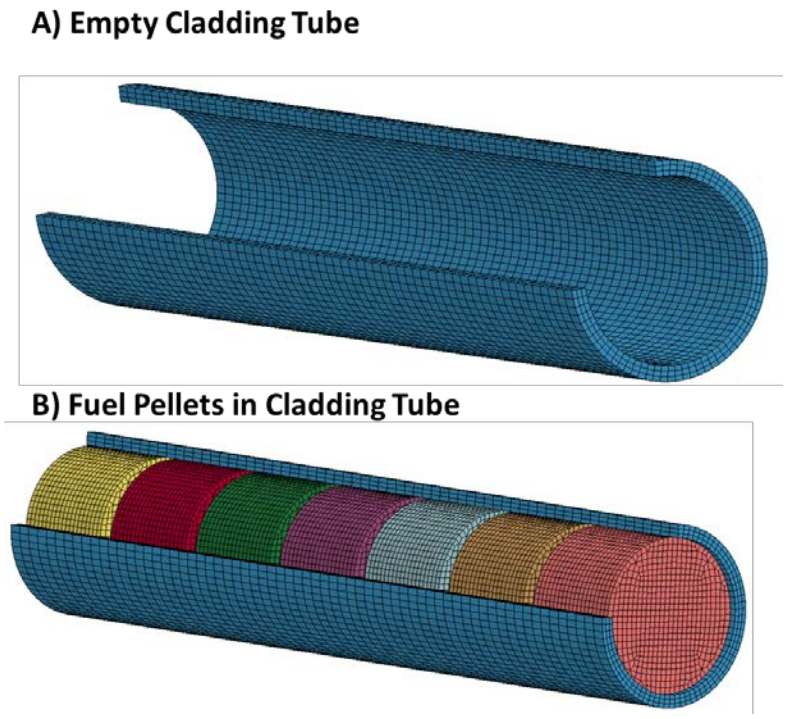

Figure 43. Flexible body fuel rod segment region.

The finite element model response of the empty cladding tube segment is plotted in Figure 44. The contours are axial strain and the deflection is scaled up by a factor of 100 to make the deflection shape visible. Note that the contours show an almost uniform strain distribution along the length of the cladding section. The strain distribution near the ends is non-uniform because of the rigid-to-flexible body interface. About 5 mm on each end are affected. Even with the end effects, Figure 44 shows that the model behaves very much like a classic beam. The FEA model results and beam theory are compared later in this section.

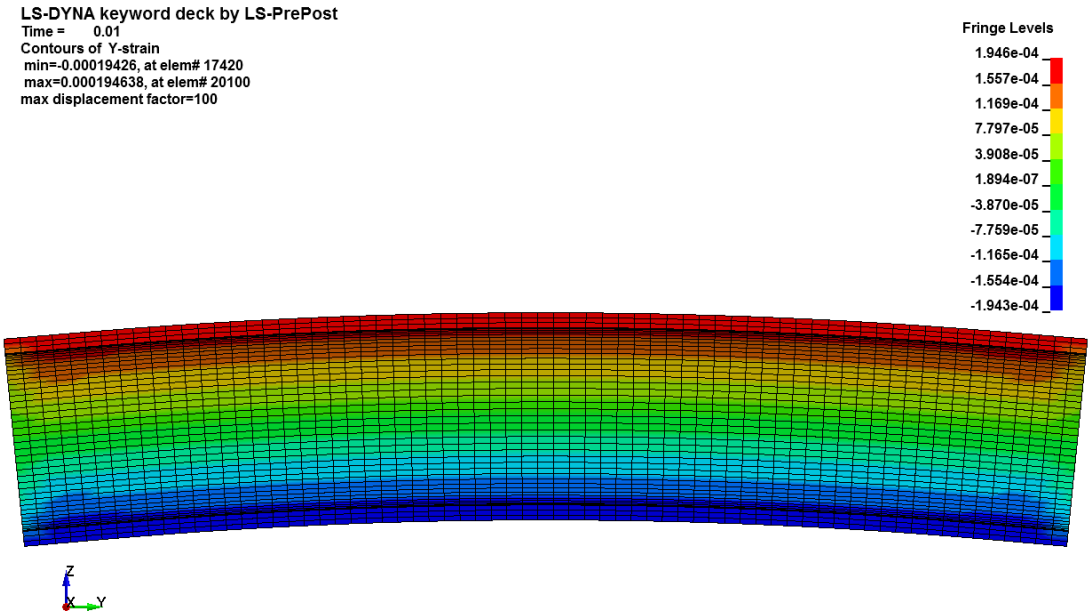

Figure 44. Empty cladding tube response, 100x amplified deflection, 1 N-m.

The finite element model response of the cladding tube segment with sliding pellet contact is plotted in Figure 45. The contours are axial strain and the deflection is scaled up by a factor of 100 to make the deflection shape visible. In this case, contact with the pellets is causing a sinusoidal pattern to occur in the stress contours. While the strain contour patterns in Figure 45 differ from the empty tube strains in Figure 44, the maximum strain values only differ in the third significant digit (199.3 uE compared to 194.6 uE). The pellets have very little practical effect on the strains at the common 1 N-m applied moment load.

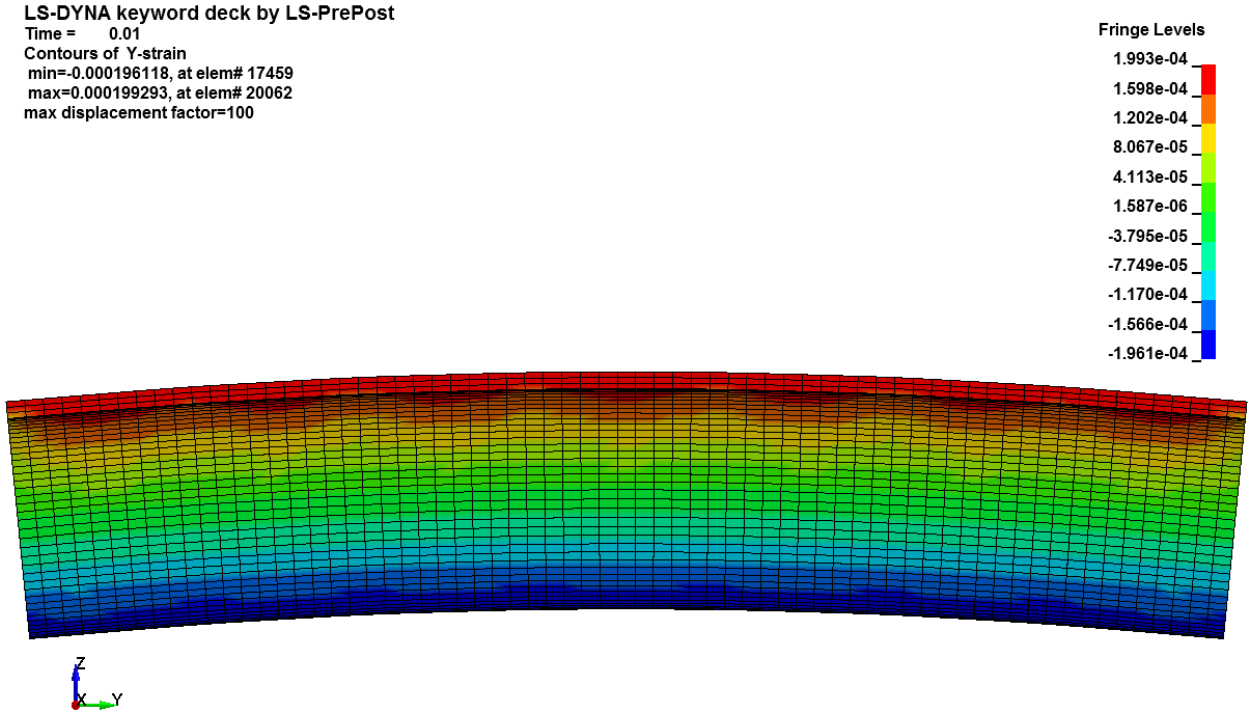

Figure 45. Sliding pellets case, 100x amplified deflections, 1 N-m.

The finite element model response of the cladding tube segment with bonded pellets to cladding is plotted in Figure 46. The contours are axial strain and the deflection is scaled up by a factor of 100 to make the deflection shape visible. Note that in this case, the strain contours are significantly altered from the previous cases, and the peak strain differs in the first significant digit. There is clear evidence of strain concentrations between the pellets. A closer look at the strain contours is provided in Figure 47. Note that the peak strains and the highest contour values are located on the inside surface of the cladding tube, while the location of maximum axial strain for a beam in bending is at the outer surface. Also note that the elevated strains associated with the strain concentrations extend through the cladding thickness to the outside surface. These two points are discussed in more detail in the next paragraphs as the FEA model behavior for the three cases is compared to beam theory.

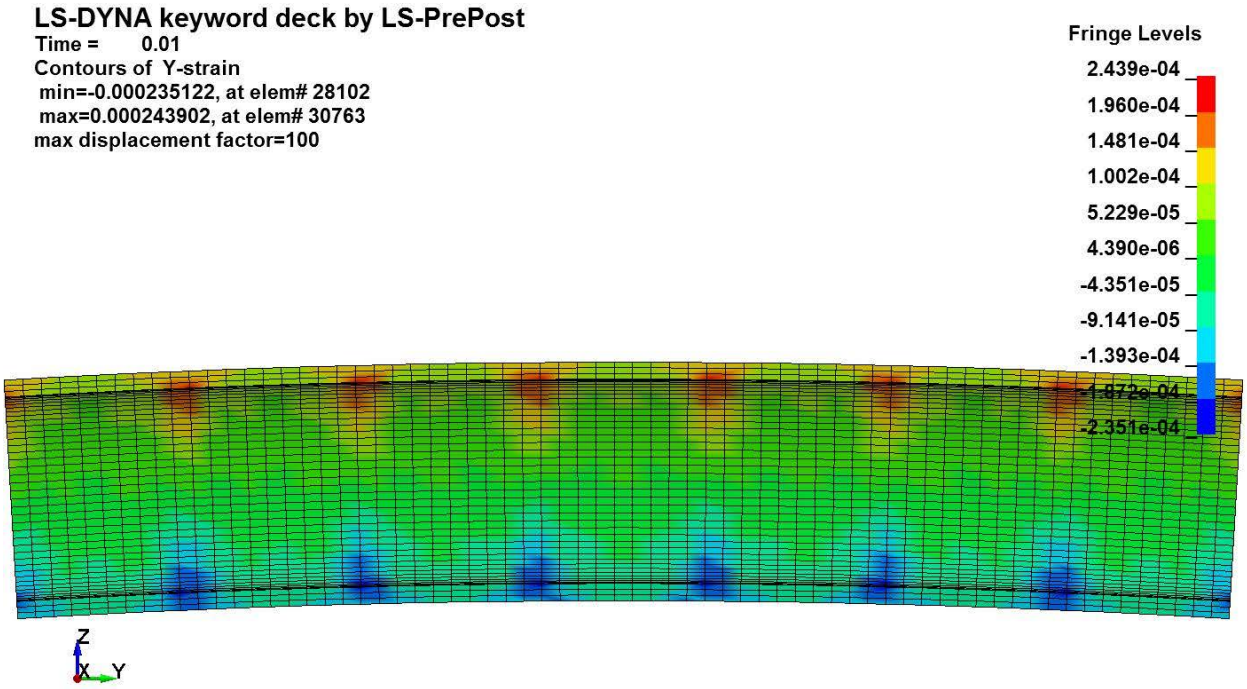

Figure 46. Bonded pellets case, 100x amplified deflections, 1 N-m.

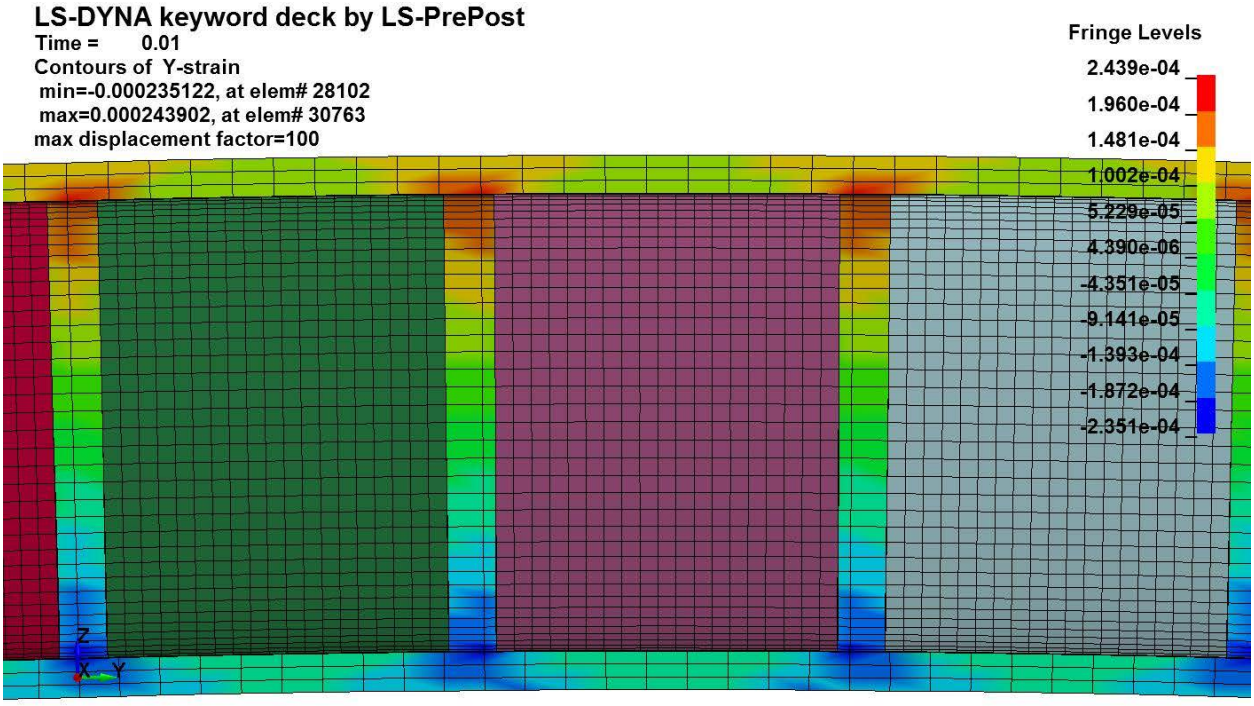

Figure 47. Bonded Pellets Case (Showing Pellets), 100x Amplified Deflection

The motivation for performing this separate modeling study of cladding and pellet interaction is the fact that whole fuel rods are represented as homogenized beams in the structural dynamic analyses following the analysis methodology described in Section 2. Strains calculated in the single-rod model are based on beam finite elements, which do not include the detail of pellets within the cladding. The intent of this

study is to determine whether the strains calculated in the single-rod model require an (upward) adjustment to account for stress concentrations caused by fuel pellet to cladding interaction. This is accomplished by comparing the FEA results to beam theory.

Table 9 starts the comparison of the fuel rod segment FEA to beam theory. The first row, Ideal Empty Tube, represents the closed form calculation of the empty tube response based on the geometry of the cladding tube segment. The next three rows are based on the FEA model responses. The applied bending moment is the same in all cases (1 N-m). The midspan deflection is the peak vertical (Z deflection), which occurs at the middle of the rod segment. The derived EI is calculated using the peak midspan deflection in Equation (2). The peak bending strain from a homogenized beam is calculated according to Equation (3), using the EI derived from Equation (2).

$$EI = \frac{M_b}{2\delta}\left(\frac{L}{2}\right)^2 \tag{2}$$

$$\varepsilon = \frac{M_b \cdot c}{EI} \tag{3}$$

The key takeaway from Table 9 is that the beam theory and FEA agree well for the empty tube and sliding pellet cases. The change in behavior happens when the pellets are bonded to the cladding. Bonding increases the fuel rod section stiffness and lowers the strain. The homogenized beam elements can be expected to calculate the strains according to Table 9 as long as the EI properties are defined to represent the bonded fuel pellet state.

Table 9. Comparison of FEA results and beam theory.

	Applied Bending Moment, Mb FEA Input (N-m)	Midspan Deflection, delta, FEA results (m)	Derived EI ($N\text{-}m^2$)	Peak Bending Strain from Homogenized Beam (uE)
Ideal Empty Tube (Theory)	1	1.4E-05	27.5	196
Empty Segment (FEA)	1	1.37E-05	28.0	193
Sliding Pellet (FEA)	1	1.35E-05	28.4	190
Bonded Pellet (FEA)	1	8.11E-06	47.4	114

Table 10 looks more closely at the strain results from the theoretical empty tube and the three FEA cases. The average cladding outer surface strain is extracted from the FEA models by averaging the element strains all along the length of the cladding tube (labeled Outer Surface Elements in Figure 48). The average cladding inner surface strain is calculated in a similar manner, using the element set labeled Inner Surface Elements in Figure 48. Averaging the element values in this way eliminates the end effects and estimates what a homogenized beam element would predict for similar uniform bending loading conditions. The maximum outer and inner surface strain values are reported from the same sets of elements. Comparing the maximum strain to the average strain provides a basis for proposing stress concentration factors. Ko is the ratio of the maximum outer surface strain to the average outer surface strain. Ki is the ratio of the maximum inner surface strain to the average inner surface strain.

Table 10. FEA Strain Results to Define Stress Concentration Factors

	Avg. Cladding Outer Surface Strain (uE)	Avg. Cladding Inner Surface Strain (uE)	Max. Cladding Outer Surface Strain (uE)	Max. Cladding Inner Surface Strain (uE)	Ko Outer Surface	Ki Inner Surface
Ideal Empty Tube (Theory)	196	168	196	168	1.00	1.00
Empty Segment (FEA)	191	172	195	182	1.02	1.06
Sliding Pellet (FEA)	188	170	199	183	1.06	1.08
Bonded Pellet (FEA)	110	99	146	244	**1.33**	**2.46**

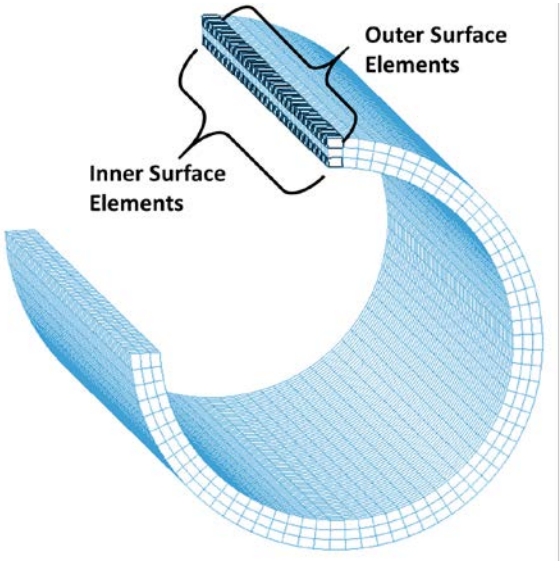

Figure 48. Stress Location Sketch

From Table 10, Ko and Ki for the theoretical empty tube are 1.00, because the stress state is uniformly distributed and there is no stress concentration. For the empty segment FEA, Ko and Ki are slightly above 1.00, but the difference is negligible and can be accounted for by the discretization of the finite element mesh and the location of the integration points at the center of each brick element. The sliding pellet FEA results are very close to the empty segment FEA results, which indicates that sliding pellets do not cause any significant stress concentrations. In the bonded pellet case, the local cladding stresses around the fuel pellets are significantly higher than the average stresses.

For the bonded fuel to cladding case, Ko and Ki are 1.33 and 2.46, respectively. These strain concentration factors come from a relatively coarse finite element mesh, with a pellet gap arrangement that was defined for modeling convenience. The Ko and Ki factors can be more precisely calculated if necessary for specific fuel pellet and cladding configurations. Precise fuel pellet geometric details, such as pellet chamfers and dish features, have the potential to affect the local cladding strain state. Additionally, the degree of bonding at the ends of the pellets and actual bond strength will affect the strain concentrations. For the purposes of this study, it is sufficient to note that Ko and Ki are significant for the fuel bonded to cladding case, and that Ki is greater than Ko.

The point of this analysis is to relate the strains calculated in a homogenized beam finite element to a realistic strain state that is affected by the presence of fuel pellets within the cladding. In the case of sliding fuel pellets, when the pellets are free to move relative to the cladding, the homogenized beam element model agrees with the more detailed model of a fuel rod section. But in the case of fuel pellets bonded to the cladding, the strain state of the fuel rod is expected to be more complicated than the homogenized beam element can calculate. In this example case, a fuel rod segment subjected to a 1 N-m bending moment, the homogenized beam element would calculate an outer surface strain of 114 uE (from Table 9), but a detailed FEA model would calculate 146 uE on the outer surface and 244 uE on the inner surface (Figure 11).

For the purposes of analyzing the NCT shock and vibration response of SNF transported in the Atlas railcar, with the peak cladding strains calculated to be below 100 uE, the local strain concentrations in the cladding in the bonded fuel case are not relevant. The strain concentrations would have to be orders of magnitude higher to raise the fuel cladding strains enough to challenge the strength of the material. Strain concentrations in the cladding are expected to exist, but they only become relevant in loading conditions that are much closer to a potential failure. For shock and vibration loading during NCT, the load magnitudes are too low to be concerned with defining precise failure conditions.

To illustrate this point, Figure 49 shows the bonded fuel pellet FEA model results for an applied load of 50 N-m. Because this is a linear FEA model with a linear contact option, the strain state scales by approximately a factor of 50. The peak local axial strain on the inside surface of the cladding is 11,907 uE, which is enough to cause plastic deformation. On the outer surface of the cladding, the peak axial strain is between 7,000 uE and 8,000 uE, which is below the anticipated yield strain of the irradiated material. Plastic strain on the inside surface suggests the strain state would redistribute under local plastic deformation. It is unknown whether the fuel to cladding bond is strong enough to survive the applied load; if not, the strains would redistribute and likely reduce to the sliding pellet case, which has no strain concentrations. The strain state in Figure 49 shows high local strains, but it is does not necessarily describe a strain state that would cause a through-wall failure in the fuel cladding. The high strains might be classifiable as the result of self-limiting secondary stresses that would be relieved when the fuel bond breaks or the inner surface experiences plastic deformation. While this issue is not relevant to the current study, it is recommended that fuel rod failure conditions be studied in detail to support 30 cm and 9 m package drop loading scenarios.

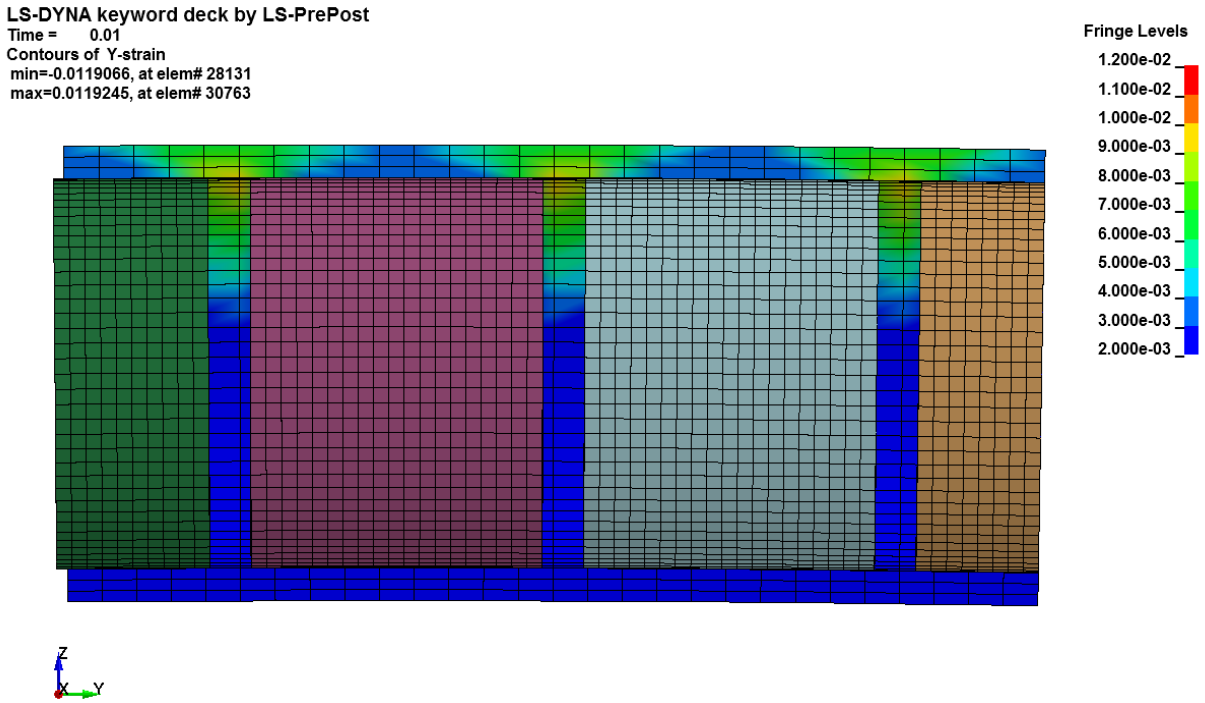

Figure 49. Bonded condition, 50 N-m applied bending moment, 1:1 deflection scaling.

Another area in which the strain concentrations might be relevant is in the fatigue evaluation, which is documented in Section 6. Fatigue analyses was performed for the low-stiffness cases (which assumes sliding between pellets and cladding) and the high-stiffness cases (which assumes the pellets and cladding are bonded). This study does not apply a stress concentration factor to either stiffness configuration because the homogenized beam finite element model strain results are directly comparable to the CIRFT test data. The CIRFT test fatigue data are based on nominal fuel rod section strains (not the peak strain concentrations). Local strain concentrations similar to the ones shown in Figure 47 are expected to have occurred in the CIRFT testing because fuel rod section failures regularly occurred at the pellet-to-pellet interfaces, right where the FEA model predicted significant strain concentrations. The effect of the strain concentrations caused by pellet to clad bonding is inherent to the CIRFT test data, so there is no need to additionally penalize the strains calculated in Section 5.2.

5.5 Cladding Strain Evaluation Conclusions and General Applicability

The results of the fuel rod structural dynamic analysis demonstrate that the fuel cladding strains remain low throughout a broad range of cases. The variation of railcar speed covers the anticipated range of railcar speeds in anticipated SNF transportation. The variation of cask designs covers the current fleet of licensed SNF packages in the United States, and potential future package designs are not expected to be significantly outside the current range. The fuel rod stiffness was varied between low (no bonding between fuel and cladding) and high (perfect bonding between fuel and cladding). The three track conditions assumed in this study are standard tests used in AAR S-2043 certification. The three track conditions were chosen because they cover the behavior observed during the MMTT on the open rail, and they generally cover vertical and lateral cask loading conditions. The 1600+ fuel rod analysis cases cover a very broad range of conditions, and they predict peak strains in the fuel cladding to be lower than the strains observed during the MMTT.

The single-rod finite element model was shown to match test data to within a reasonable tolerance. This demonstrates that the basic physics and engineering assumptions of the model are sufficient to predict the fuel rod behavior.

Sensitivity studies were conducted to demonstrate that changes in fuel rod geometry are not expected to cause significant changes in strains.

Fuel rod stiffness is not expected to be a significant factor because increasing stiffness generally lowers the strains. The dominant physical phenomenon is that stiffer fuel rods require more load and more energy to bend in order to cause higher strains. Changing stiffness also changes the fuel rod natural frequency, but the analytical results do not predict any significant resonance response from the shift in fuel rod natural frequency to NCT shock and vibration loads.

SNF in a welded canister is predicted to have slightly higher peak strains than SNF in a bare fuel cask, but the difference is not significant enough to cause any concerns. Diametrical clearances of 5 mm and 15 mm were considered, and the increase in peak strains was less than an order of magnitude in the most unfavorable configuration. For a structural analysis of fuel rod cladding during NCT, the loading increase would have to be much larger to have any practical effect.

The effect of fuel pellets on the strain distribution of a fuel rod was explored with a finite element model that resembles the ORNL CIRFT test. When fuel is present but not bonded to the cladding, the resulting stress concentration in bending is negligible. When fuel pellets are bonded, significant strain concentrations develop, but it is generally not necessary to account for the stress concentrations during NCT because the shock and vibration loads are too low for the potential stress concentrations to have any practical effect. The ORNL CIRFT fatigue data are based on the nominal stress and strain state, so it is consistent with the homogenized beam element of the single-rod model. The stress concentrations caused by bonded fuel are relevant for consideration when the loads are strong enough to cause structural failure of the fuel cladding, but that is outside the range of NCT shock and vibration loads. It would be appropriate to consider stress concentrations in the cladding for 30 cm or 9 m SNF package drop loading conditions, but the critical question is whether they would actually contribute to a structural failure or would instead be self-limited by the strength of the fuel cladding bond. The authors would like to explore this issue in the future, but it is outside the scope of this report.

Based on this analysis the authors conclude that the strains in fuel rod cladding during NCT shock and vibration events are very low, and there are no uncertainties that could increase the loads enough to cause a fuel rod failure. It would take a change in conditions that are far beyond the range of conditions considered in this report. If shock and vibration loads on the fuel rods were increased by an order of magnitude, it would likely be necessary to change from a single-rod model to a column of rods or a full fuel assembly model in order to account for rod-to-rod contact.

6. Fuel Rod Fatigue Analysis

A fuel rod fatigue analysis is needed to demonstrate that fuel cladding maintains its integrity during NCT shock and vibration loadings because fatigue is a typical engineering concern. Structural analysis typically calculates the maximum stress or strain in the most limiting configuration, which can occur at any arbitrary moment in time. This section performs a fatigue analysis for SNF transported by the Atlas railcar on a 2,000-mile trip over the US rail system, based on the library of 1600+ fuel rod structural dynamic analyses described in this report. Additionally, the elements of the fatigue analysis are evaluated to demonstrate that a fatigue analysis of intact fuel assemblies is generally not necessary for NCT transportation in the United States.

The MMTT provided valuable data related to long-term fuel rod vibration and fatigue. The MMTT recorded a complete set of data during the westbound rail transportation leg from Baltimore, Maryland, to Pueblo, Colorado. The entire journey was recorded with strain gages placed at a variety of fuel rod locations and accelerometers placed at various locations throughout the conveyance system. The body of data shows that the shock and vibration environment on SNF inside a transportation package is very mild. The mechanical loads transmitted to the fuel rods are best measured by strain gages, because they measure the deflection (local strain) of the fuel rod cladding. The accelerometer data are also useful, but are not directly applicable because accelerometers measure motion, which includes rigid body motion, and do not directly relate to strain. A summary of the data from the MMTT is provided in Section 6.1.

One of the key observations from the MMTT was that the captive track tests performed on the railcar conveyance system at the TTCI facility in Pueblo bounded the response of the system on the open rail. The library of fuel rod results generated in Section 5.2 was based on standard TTCI tests and is expected to bound the response of the SNF during transportation on the US rail system. The three track configuration cases (pitch and bounce, single bump, and twist and roll) were analyzed for speeds up to 80 mph, so they include and exceed all credible NCT train speeds. Section 6.2 summarizes the fatigue evaluation for each of the three TTCI tests analyzed with FEA. The analyses provide the information needed to assemble a fatigue analysis for a 2,000-mile trip.

Based on the available structural dynamic analysis results and the experimental test data from the MMTT, there are a number of different ways to approach a fatigue analysis. Section 6.3 describes a few different approaches that arrive at the same result: the cladding fatigue is negligible. The simplest approach is to take the highest strain value of 20 uE and note that it is below 100 uE. This means that there are zero significant cladding strain cycles expected on a 2,000-mile trip. The use of 100 uE as a strain amplitude threshold for negligible fatigue damage was discussed in Klymyshyn et al. 2018, and is discussed in more detail in Section 6.3.1.

A second way to approach fatigue analysis is to assume that a certain number of track events occur during the 2,000-mile trip. A value of 5,000 track events was chosen for this study, based on the track feature estimates presented in Klymyshyn et al. 2018. The library of single rod responses to track features was evaluated and the maximum values for strain cycle amplitudes, number of strain cycles over 10 uE, and the accumulated damage fraction were used to estimate fuel cladding fatigue fraction resulting from a 2,000-mile trip. The cumulative fatigue damage fraction was calculated to be 6.69E-12 or 1.70E-12, using two different methods of calculating cumulative fatigue damage from the fuel rod FEA results. Since a damage fraction of 1.0 indicates a fuel cladding failure, the accumulated damage is many orders of magnitude below failure. This analysis is detailed in Section 6.3.2.

A more detailed way to approach to the fatigue analysis is to use the MMTT strain gage data as a guide to estimate the fatigue response of SNF carried by the Atlas railcar. This approach attempts to take credit for the fact that most of the time during the westbound rail transportation leg the fuel rods were experiencing a random vibration state that was very low in vibration energy, and completely negligible from a fatigue standpoint. Of the 144 hours of transit time, the system was only in motion for 59 hours. During the 59 hours of motion, the strain gage signal strengths suggest that most of that time the fuel rods were

experiencing a negligible, low-energy vibration state. Section 6.3.3 describes an analysis based on the MMTT data and the library of single-rod model fatigue analyses described in Section 6.2. This analysis calculates a fatigue damage that is in the same order of magnitude as the track event methods (3.23E-12, which is between 1.70E-12 and 6.69E-12).

These fatigue analyses all agree that fatigue in fuel rod cladding is negligible. Section 6.4 lays out an argument that fatigue evaluation of intact fuel rod cladding is unnecessary for NCT. The margins on the fatigue analyses are so high, and there is very little that could change the analysis for fuel assemblies in the current fleet.

6.1 MMTT Data Summary for Rail, Ship, Heavy-Haul Forms of Transportation

The MMTT consisted of three forms of transportation: heavy-haul truck in Spain, dedicated rail in the United States, and large ship. The large ship transport actually consisted of coastal ship and transatlantic ship transport. There was also a component of non-dedicated rail when the cask was shipped back to ENSA, but this component was not analyzed for fatigue because it was not representative of normal conditions of transport. The handling tests at ENSA will also be mentioned, but they were not analyzed for fatigue. McConnell et al. (2018) provide detailed information about each transportation mode.

The primary method used to evaluate fatigue on the MMTT data was the calculation of cumulative fatigue damage, using Miner's Rule, ASTM International (ASTM) rainflow counting, and the irradiated zircaloy design strain cycle amplitude vs number of cycles to failure (S-N) curve by O'Donnell (1964). The fatigue analysis process is described in detail in Klymyshyn et al. 2018.

Miner's Rule is a method for calculating accumulated damage fraction from strain cycles of non-uniform amplitude. A fatigue damage fraction of 1.0 indicates that fatigue failure is expected, but note that NCT shock and vibration response of SNF cladding is calculating damage fractions many orders of magnitude below 1.0.

ASTM rainflow counting is a formal process for counting strain cycles from an arbitrary or random strain history. Some method for calculating strain cycles and amplitudes from the strain gage data was needed to evaluate the MMTT data, and rainflow counting was used by Adkins et al. 2013. ASTM lists other methods for counting fatigue cycles from random vibration data, but the choice of method is not critical when the strain amplitudes are as low as discussed in this report.

The cumulative fatigue damage calculation was applied to all transportation modes in the MMTT. The westbound rail transportation mode was described in detail in *Modeling and Analysis of the ENSA/DOE Multimodal Transportation Campaign* (Klymyshyn 2018) and is summarized in this report. The heavy-haul truck, coastal ship, and transatlantic ship transport are described in more detail in this report, and full fatigue calculations from the MMTT data are included for these modes of transportation.

Also, it is important to note that the peak strains and the strain cycle amplitudes are not necessarily the same values. The peak strain was just the largest magnitude strain after filtering, while the strain cycle amplitudes were calculated from the rainflow counting algorithm. This difference can result in the strain cycle amplitudes being determined to be larger than the reported peak strains, but if a differential does exist, it will only be on the order of a few microstrains. For the purposes of this report, both values will be mentioned, but all strains associated with cycle counts and fatigue calculations use the strain cycle amplitudes.

6.1.1 Westbound Rail

The westbound rail transportation mode involved dedicated rail from Baltimore to Pueblo on a Kasgro KRL 370355 railcar (shown in Figure 50). Figure 51 and Figure 52 show the hourly maximums for peak values and for RMS values, respectively; both accelerometers and strain gages are shown. Klymyshyn

(2018) provides more detail about these calculations, but these figures provide a summary of the shock and vibration environment experienced by the entire system. Overall, the assemblies experienced the highest peak accelerations of the various components measured, but the peak strains experienced by fuel cladding remained very low. These low strains lead to negligible cumulative fatigue.

Figure 50. Kasgro KRL 370355 railcar used for the westbound rail.

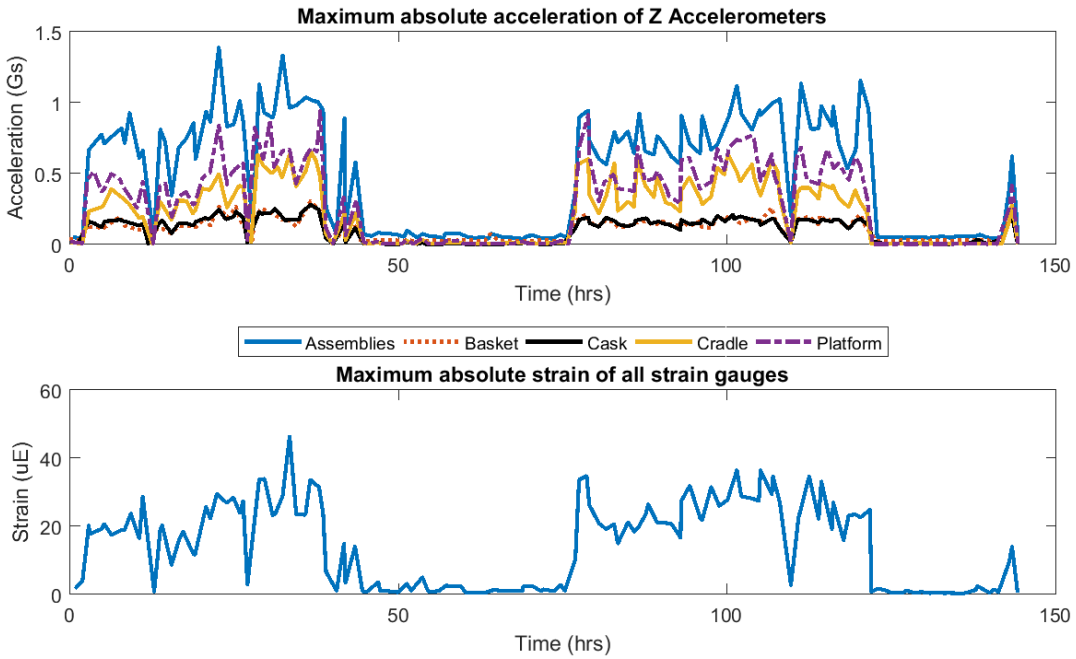

Figure 51. Westbound rail peak hourly maximums.

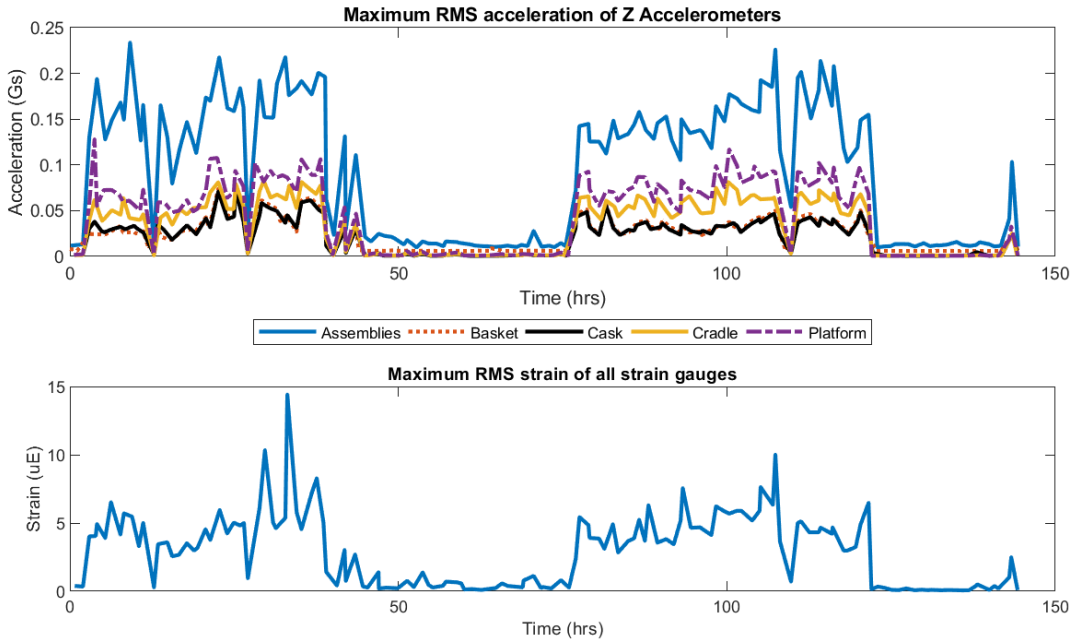

Figure 52. Westbound rail peak hourly 10-second sliding RMS.

Figure 53 shows the total damage experienced by each strain gage throughout the westbound rail test. The highest total fatigue is less than 10^{-10}, and a value of 1 means failure is expected. Therefore, none of the strain gages are measuring a fatigue close to failure. However, because the S-N curve needed to be extrapolated beyond the range of actual test data, the fatigue damage is best approximated as zero.

Since the fatigue damage numbers were negligible, counting the number of strain cycles provides another insight into the fatigue response. The total number of strain cycles, averaged over all the strain gages, was 5.97E+7. The anticipated strength at this number of cycles is 267 uE. However, most of these cycles are just noise. The number of cycles above 10 uE was 3,800, which has a limit of 1,366 uE for the strain amplitude. Both of these limits are much higher than the actual maximum strain of 46 uE. Therefore, for the westbound rail, the fatigue damage is negligible.

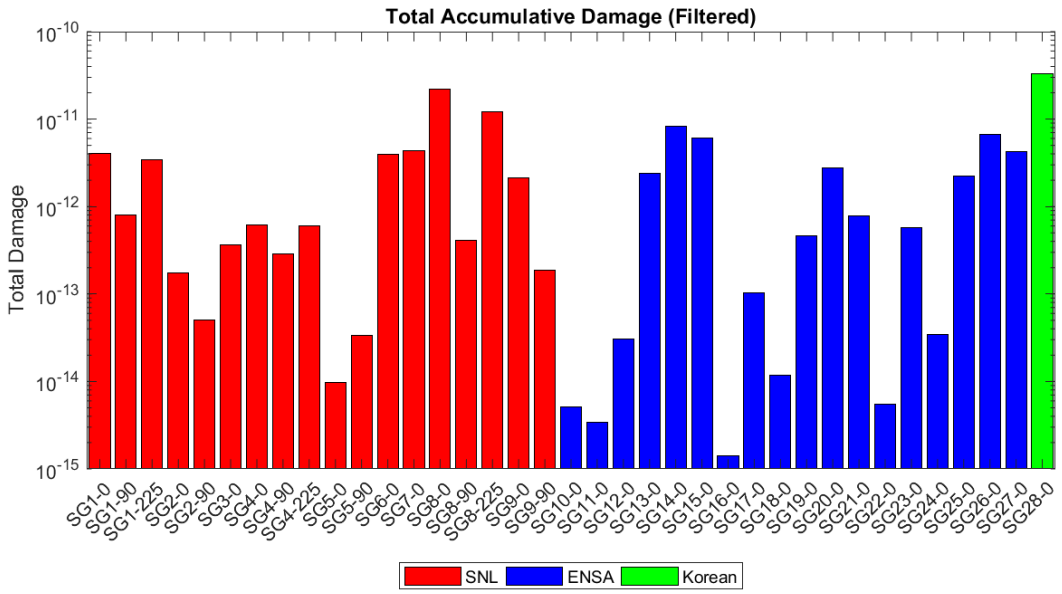

Figure 53. Westbound rail cladding fatigue damage.

6.1.2 Heavy-Haul Truck

The heavy-haul truck test, seen in Figure 54, was a two-day trip around northern Spain. The test began at the ENSA facility, traveled south with an overnight stop, and returned to the ENSA facility. Figure 55 and Figure 56 show the hourly maximums for peak values and for RMS values, respectively; both accelerometers and strain gages are shown. Overall, the shock and vibration environment was less severe for the heavy-haul truck than for westbound rail. Unlike the rail, the platform experienced the highest accelerations in the system, but those high accelerations did not translate to high strains. The peak strains were all low, and the RMS strains were all lower than 8 uE (RMS). The RMS strains arguably better represent the actual shock and vibration environment because they reduce the effect of short but large impacts, as well as include the settling of the system after a road impact.

Figure 54. Heavy-haul truck setup and convoy.

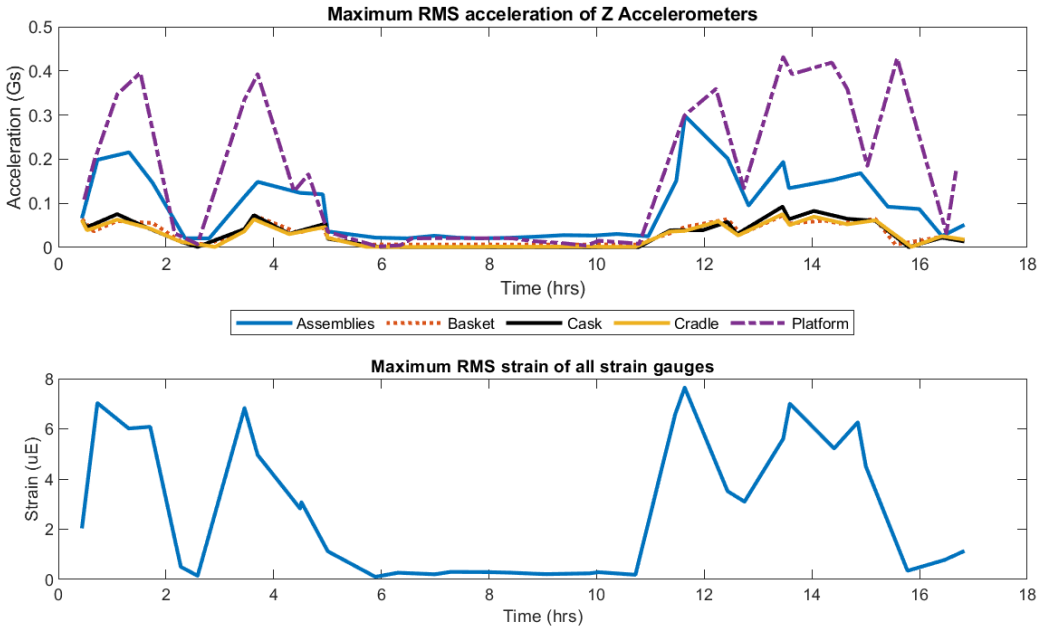

Figure 55. Heavy-haul peak hourly maximums.

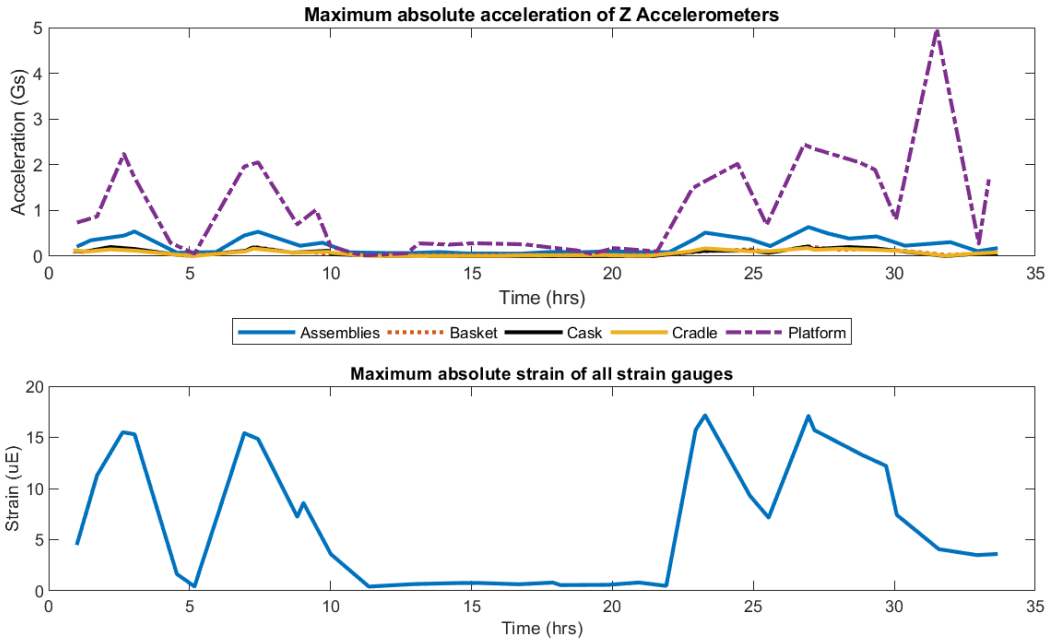

Figure 56. Heavy-haul peak hourly 10-second sliding RMS.

In the heavy-haul truck transport, the strains measured are much lower than those of westbound or eastbound rail in the United States. The maximum cycle amplitude from the rainflow counting was 17 uE compared to 46 uE for the westbound rail. Figure 57 shows the total fatigue for each strain gage over the course of the test. The total fatigue damage ranges from 2.49E-18 to 9.31E-14. For the westbound rail, the fatigue damage ranges from 2E-14 to 3E-10, much higher than the heavy-haul truck, even when the shorter distance traveled is considered.

The total number of strain cycles was 1.32E+7. On average, the number of cycles measuring at least 10 uE is 0.0006% of the total number of cycles. For comparison, the number of cycles measuring at least 10

uE in the westbound rail is 0.013% of the total number of cycles. However, there were many periods during both tests when the system was not moving, so another way to compare the heavy-haul truck and the westbound rail would be to find the time the system spent moving. In both transportation tests, the system was moving for about 40% of the total data collection time, 37% for the heavy-haul truck and 41% for the westbound rail. These values are close enough that no normalization is required.

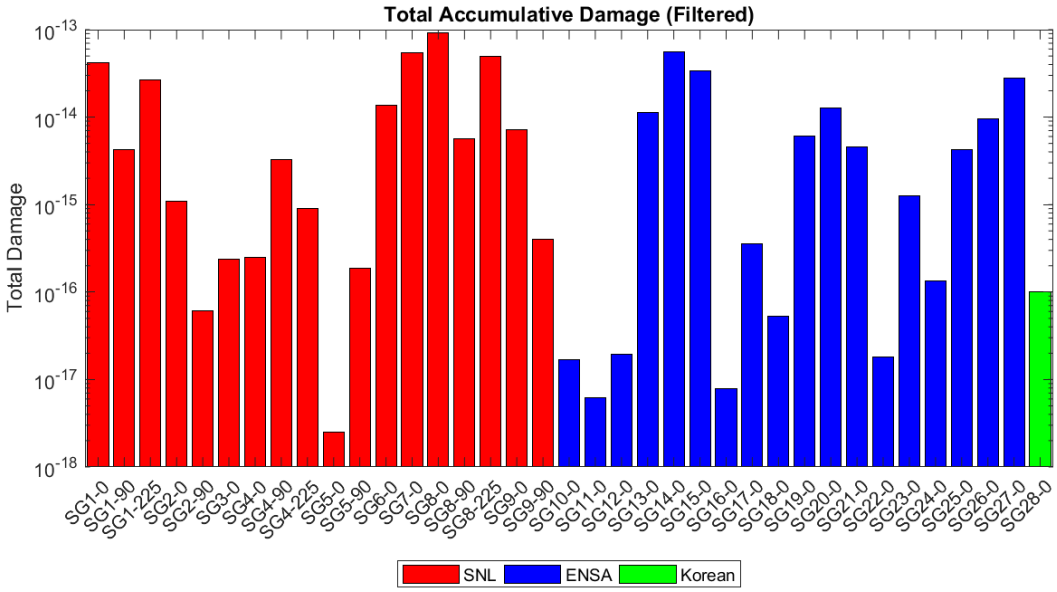

Figure 57. Heavy-haul truck cladding fatigue damage.

6.1.3 Coastal and Transatlantic Ship

The coastal ship transport was used to move the cask from Santander, Spain to Zeebrugge, Belgium, shown in Figure 58. A transatlantic ship (Figure 59) then transported the cask to Baltimore, Maryland. The shock and vibration environment on the ships was much lower than on the westbound rail or heavy-haul truck. The peak hourly strains were right around the level of noise, which led to even smaller cumulative fatigue levels. Figure 60 and Figure 61 show the hourly maximums for the coastal and transatlantic ships.

Figure 58. Coastal ship from Santander, Spain to Zeebrugge, Belgium.

Figure 59. Transatlantic ship from Zeebruges, Belgium to Baltimore, Maryland.

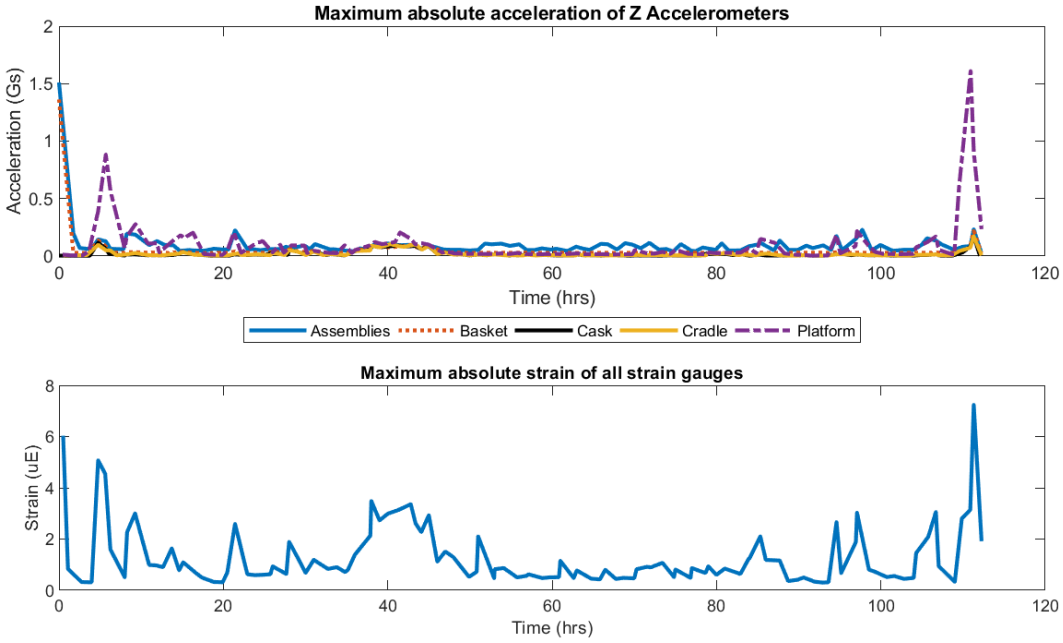

Figure 60. Coastal ship peak hourly maximums.

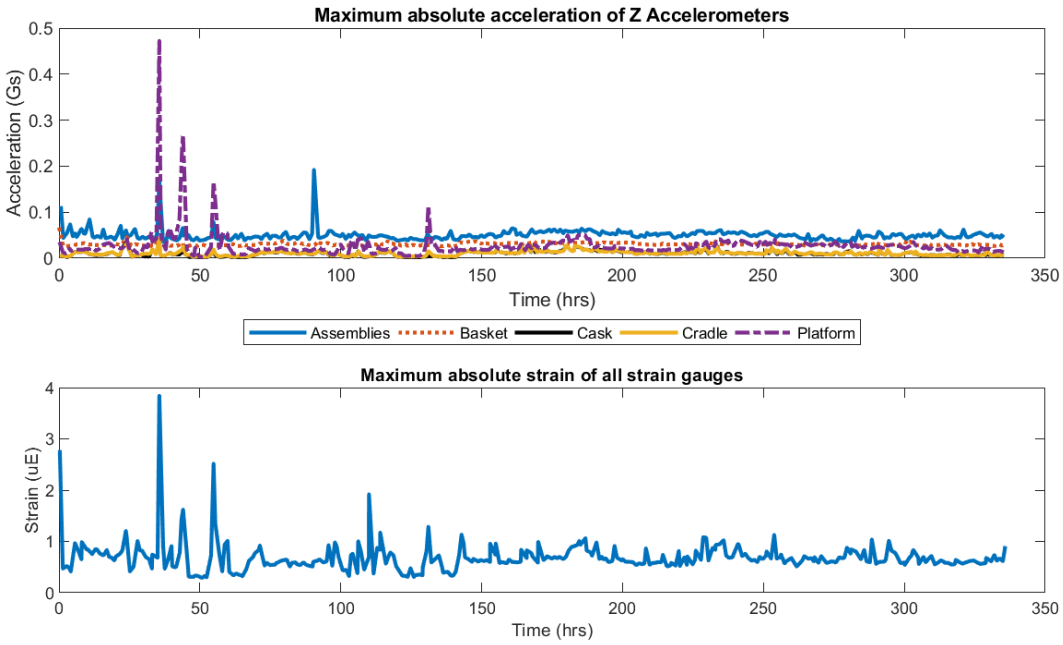

Figure 61. Transatlantic ship peak hourly maximums.

The maximum cycle amplitude from the rainflow counting was 11 uE for the coastal ship and 4 uE for the transatlantic ship. Figure 62 shows the total damage for the coastal ship, and Figure 63 shows the total damage for the transatlantic ship. The maximum damage for the coastal ship was 5.4E-88 and 7.6E-108 for the transatlantic ship. Both values are many orders of magnitude smaller than the maximum damage from the heavy-haul truck and westbound rail.

For both ships, cycles at 10 uE or greater were rare. Using the maximum values of the highest strain gage, only 2E-5% of cycles for the coastal ship were at least 10 uE. Combining results from both ships, that number drops to 4E-6%. The coastal ship's percentage is an order of magnitude lower than the heavy-haul truck percentage. However, both the heavy-haul truck and the westbound rail used the average values for all the strain gages. Using the same average would show 0 cycles over 10 uE for both ships.

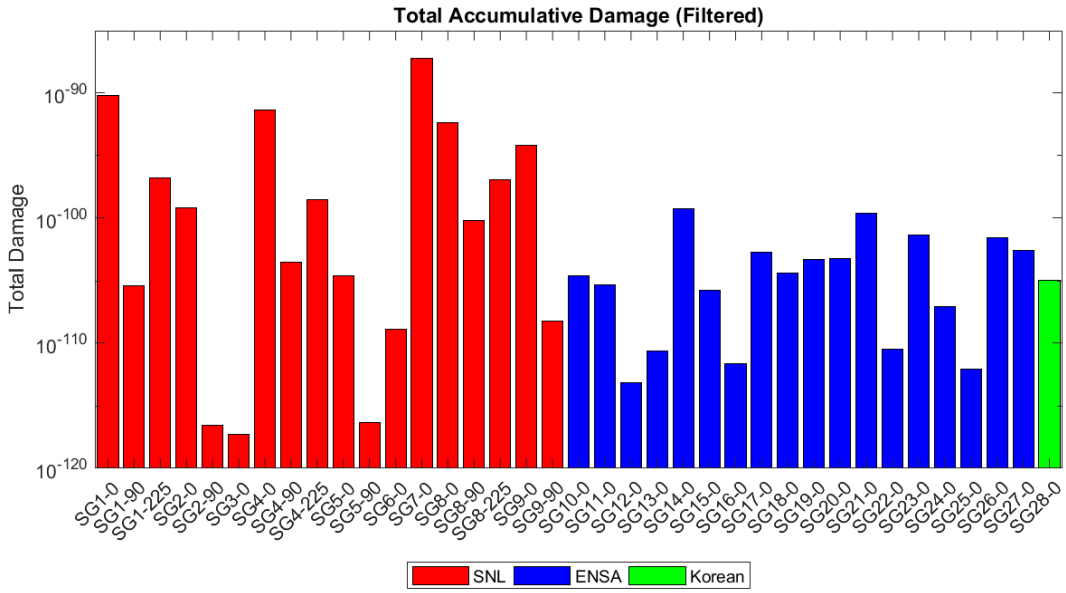

Figure 62. Coastal ship cladding fatigue damage.

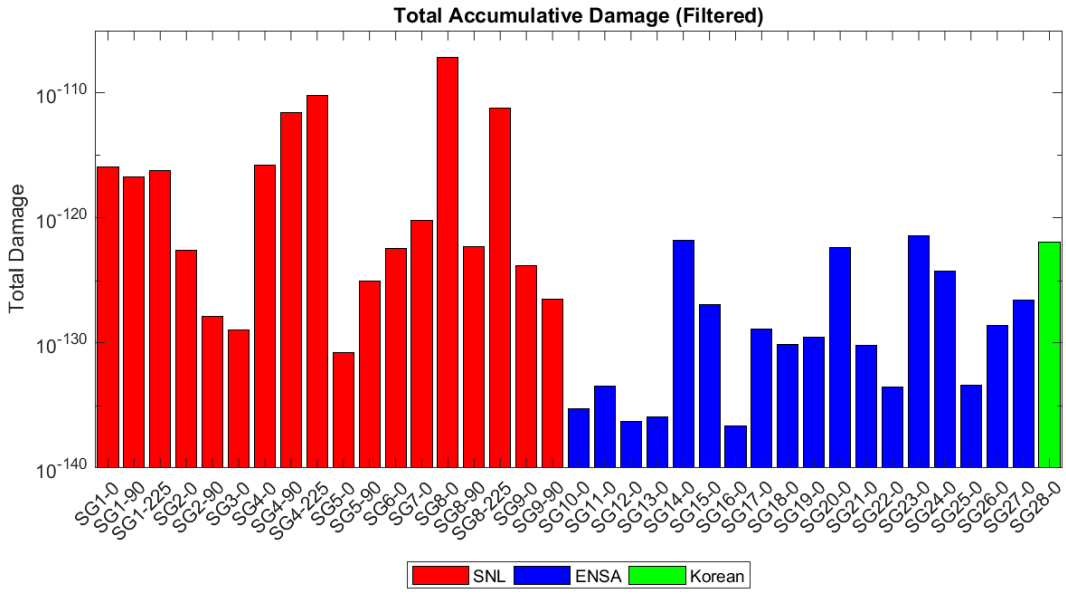

Figure 63. Transatlantic ship cladding fatigue damage.

In summary, the strain values recorded by the rainflow counting are smaller and much rarer than those for the heavy-haul truck and westbound rail. For this reason, the ship journeys should not be considered as limiting or even significant factors in the life-expectancy of the used fuel.

6.2 Fatigue Analysis of Single-Rod Model Results

Three sets of track conditions were run through the single-rod model: pitch and bounce, single bump, and twist and roll. These track conditions are also used by TTCI in their own modeling. Each track condition has two stiffness values of the single rod: a high stiffness and a low stiffness. The single-rod model had perturbation inputs from 17 different cask systems. Each cask system has its own acceleration response, which will cause unique strain and fatigue responses on the single-rod model for each cask. The analysis

looked at four different methods of determining the overall damage to the cladding: the single event fatigue damage fraction, peak cycle strain, count of cycles of 10 uE, and maximum one-second RMS.

The single event fatigue damage fraction is calculated from rainflow counting and Miner's Rule. The peak cycle strain and the number of cycles over 10 uE used the strain cycle amplitudes calculated from the rainflow counting. The maximum one-second RMS use the one-second window with a one-second slide calculation. In the sections below, all 17 casks systems are summarized in envelope plots. These plots show the range over which all the casks values fall; the lower bound is the cask with the lowest value at that speed and the upper bound is the cask with the highest value at the respective speed. The lower and upper bound casks can be different for each speed. Appendix B provides more detailed graphs.

6.2.1 Pitch and Bounce

The pitch and bounce test track consists of evenly spaced vertical track perturbations which excite vertical response modes of the railcar along 390 feet of track. Section 4.1 has more details about the test and the NUCARS model that analyzes the Atlas railcar response to the test conditions. The range of speeds for the pitch and bounce analysis was from 30 to 80 mph, with a resolution of 5 mph.

6.2.1.1 Low Stiffness

Figure 64 shows the envelope plot for the single event fatigue damage fraction, with a vertical log scale. Overall, the damage from the single event is small, with the largest value of 3.40e-16 occurring during the 60 mph run. The general shape of the fatigue envelope increases as the speed increases to 60 mph, and as the speed increases further, the fatigue envelope decreases and levels out.

Figure 65 shows the envelope plot for the peak cycle strain. Similar to fatigue, the peak strain increases as speed increases to 60 mph, where it hits its peak of 11 uE, and then it decreases slightly and levels out. With the low peak strain, the number of strain cycles over 10 uE is only three for the entire set of cask systems, with all three occurring during the 60 mph run.

Figure 66 shows the envelope plot for the one-second maximum RMS value. Again, the basic shape is similar to the other metrics. The values increase approaching 60 mph, the maximum of 6.9 uE (RMS) occurs at 60 mph, and the values decrease and settle out at higher speeds.

In summary, the pitch and bounce test conditions with low stiffness has a maximum for all values at 60 mph. However, these values are still small and, when applied to a full trip, do not add up to any significant damage.

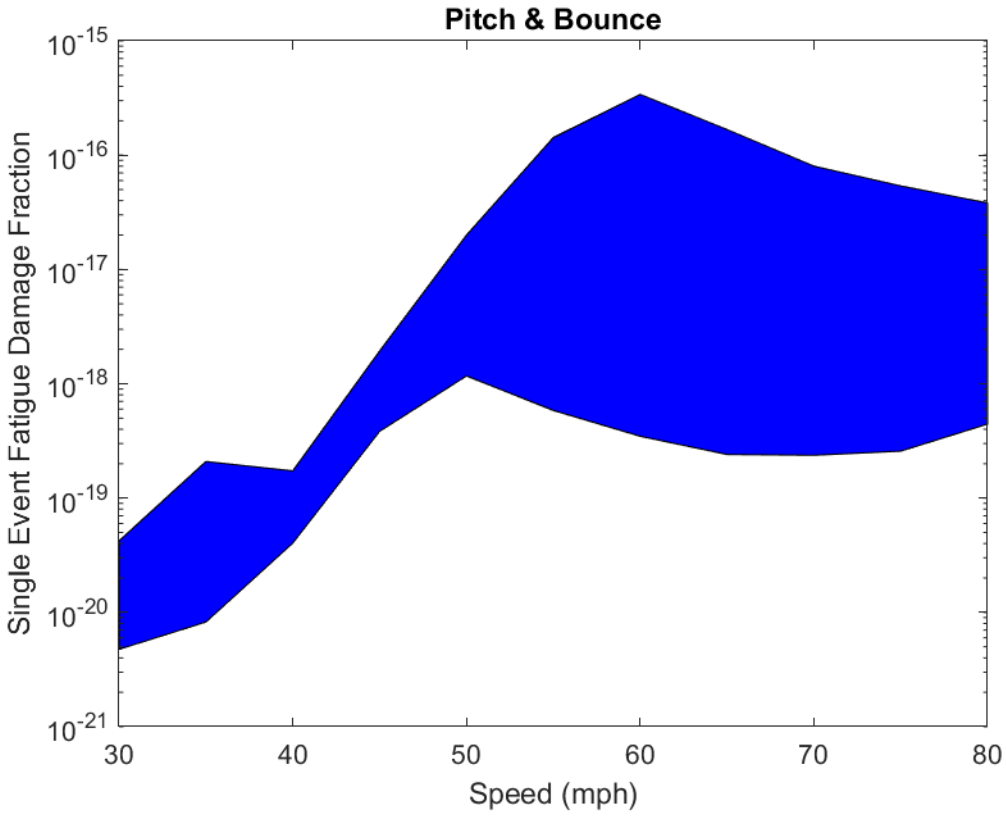

Figure 64. Log-scale single event fatigue damage fraction for low stiffness.

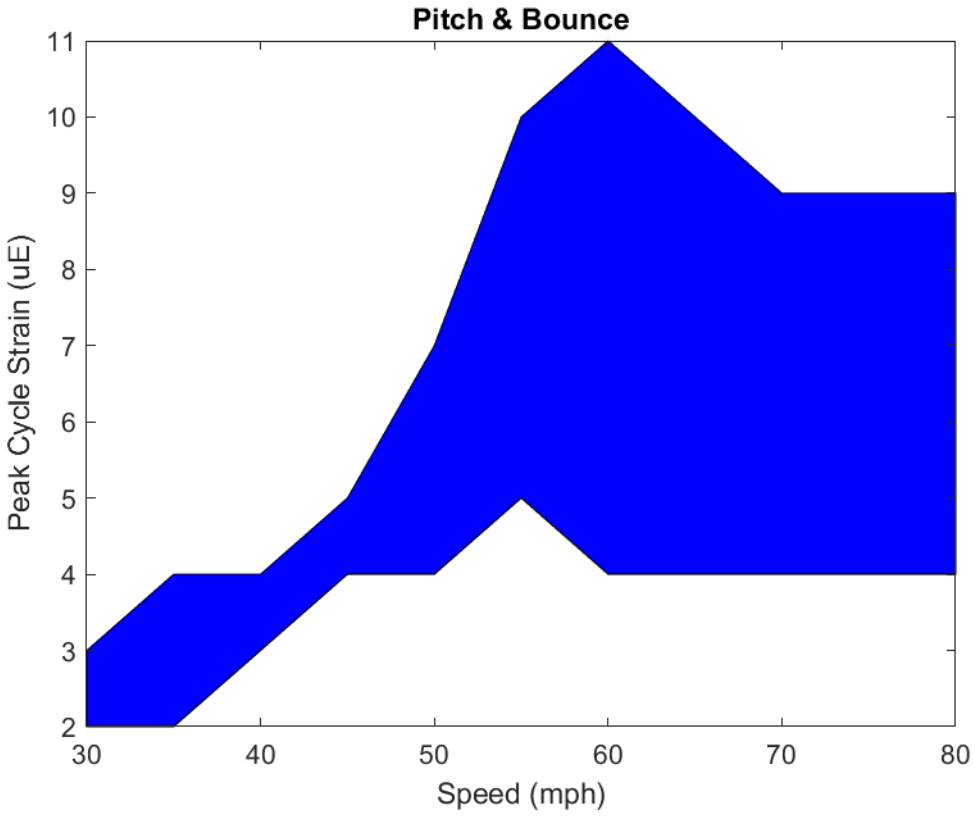

Figure 65. Peak cycle strain for low stiffness.

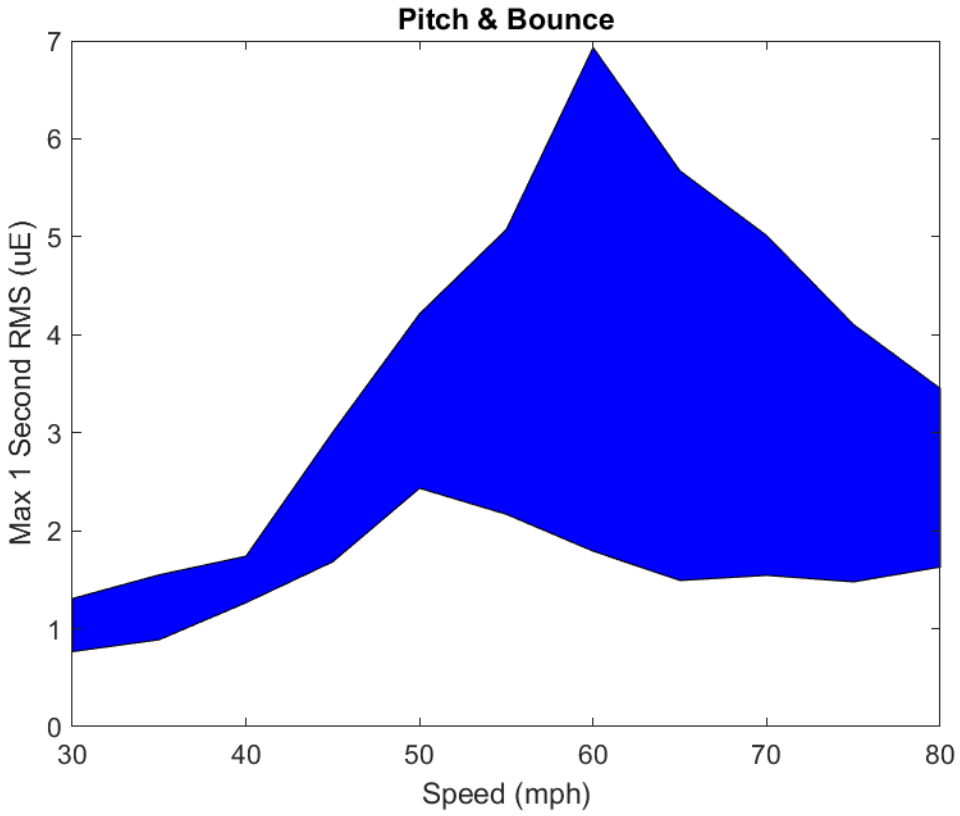

Figure 66. Maximum one-second RMS value for low stiffness.

6.2.1.2 High Stiffness

Figure 67 shows the single event fatigue damage fraction for the high-stiffness single-rod model. Overall, the damage fraction is lower for the higher stiffness model than the lower stiffness model. The peak value of 3.97e-19 occurs at 60 mph, but there is a secondary peak at 75 mph that was not present in the low-stiffness model.

Figure 68 shows the peak cycle strain. In this case, the maximum value of 4 uE occurs both at 60 mph and 75 mph, consistent with the fatigue having two peaks. Also, there is much less variation in the high-stiffness peak cycle strain compared to the low-stiffness peak cycle strain. Notice that at 50 mph, all casks predict the same peak cladding strain, and the high stiffness case has much lower strains in general than the low-stiffness case (compare to Figure 65).

Figure 69 shows the maximum one-second RMS values. Here, there is a clear peak at 60 mph, with the maximum value of 2.1 uE (RMS). Unlike the previous two graphs, there is no secondary peak at 75 mph, but there is an elbow at 75 mph that is not present in the low-stiffness RMS plot.

In general, all the values in the high-stiffness single-rod model are even smaller than in the low-stiffness model. Therefore, even less damage is expected in this case.

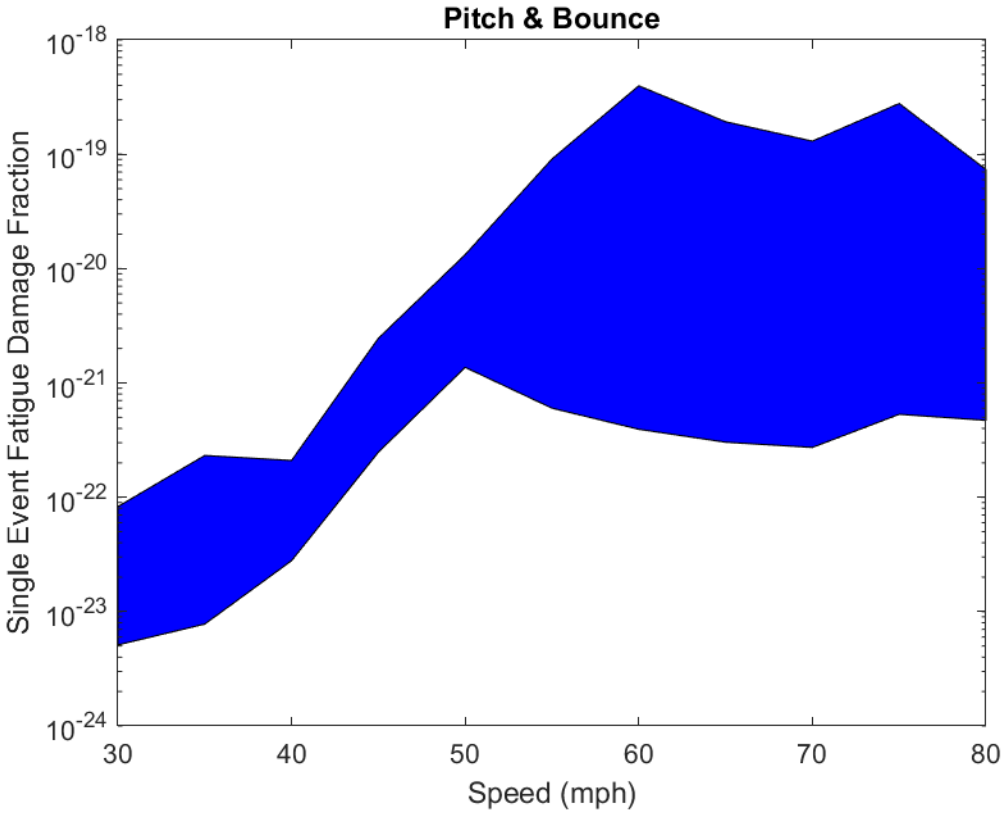

Figure 67. Log-scale single event fatigue damage fraction for high stiffness.

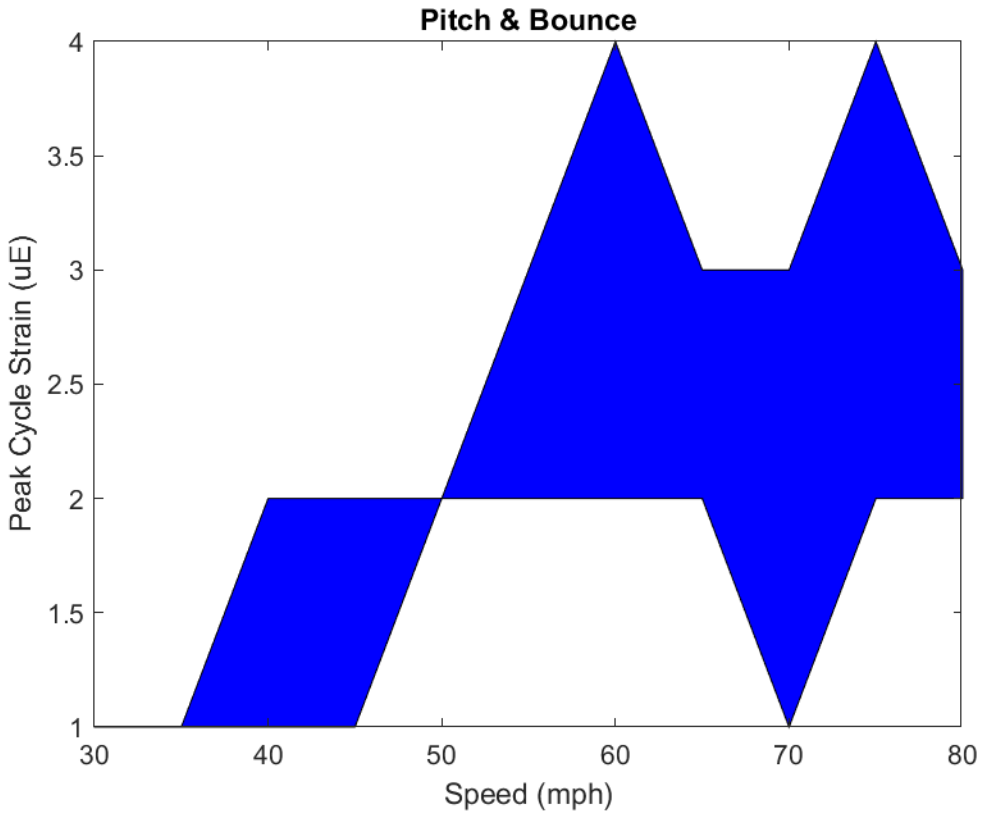

Figure 68. Peak cycle strain for high stiffness.

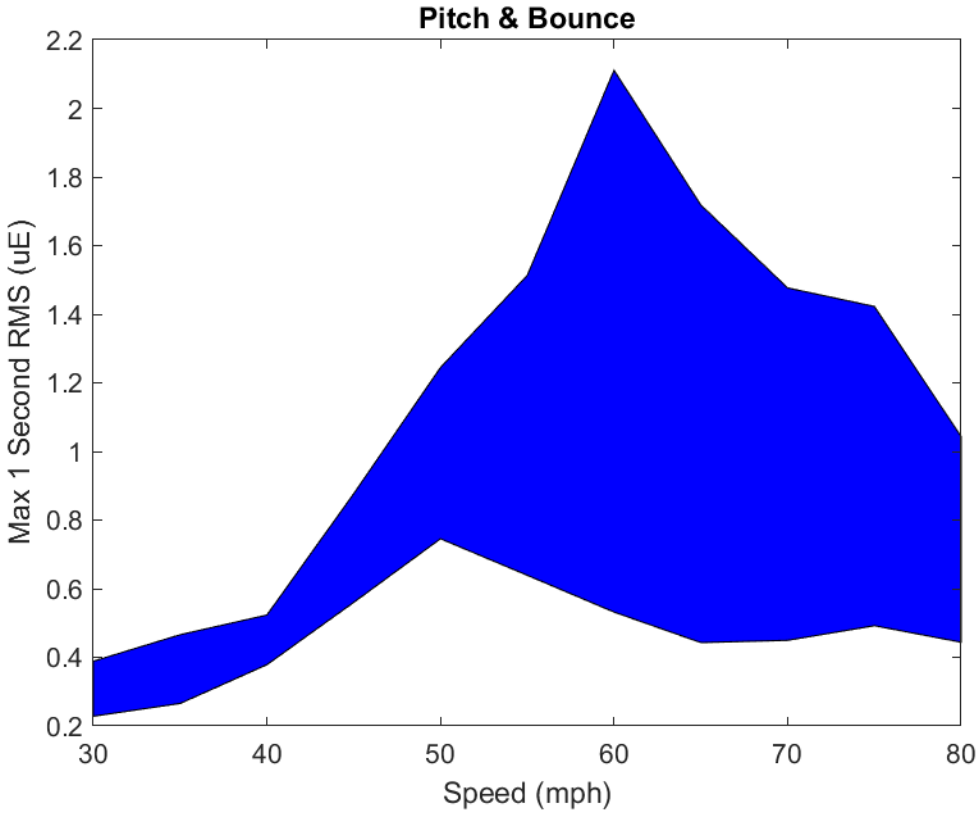

Figure 69. Maximum one-second RMS value for high stiffness.

6.2.2 Single Bump

The single bump test section consists of a vertical track perturbation measuring one inch in height by 20 feet in length, which imparts a vertical impulse to the railcar. This test section is similar to a level crossing, where a railroad crosses over a road. Similar events were encountered in the open-rail journey in the MMTT and were found to correspond to peaks in the strain gage data. Section 4.1 has more details about the test conditions and the NUCARS model used to analyze the Atlas railcar response to the test conditions. The range of speeds for this analysis was 30−80 mph, with a resolution of 5 mph.

6.2.2.1 Low Stiffness

Figure 70 shows the envelope plot for the single event fatigue damage fraction. Compared to the low-stiffness pitch and bounce analyses, the single bump has less fatigue damage variation for each speed. Also, the peak damage of 2.45e-16 occurs at 80 mph, so as the speed increases, the damage increases as well. The damage is similar to the pitch and bounce peak damage.

Figure 71 shows the plot for the peak cycle strains. Like the damage fraction, the peak cycle strain increases as speed increase, with the peak of 14 uE occurring at 80 mph. For the number of cycles greater than 10 uE, only speeds of 70 mph and faster had any counts. Appendix B has a more detailed graph breaking down the counts into the different casks systems.

Figure 72 shows the plot for the maximum one-second RMS. Just as in the other plots, the RMS generally increases as the speed increases, with the peak of 4.8 uE (RMS) happening at 80 mph. Interestingly, even though the peak damage fraction was greater in the single bump analyses than in the pitch and bounce analyses, the maximum one-second RMS value was smaller.

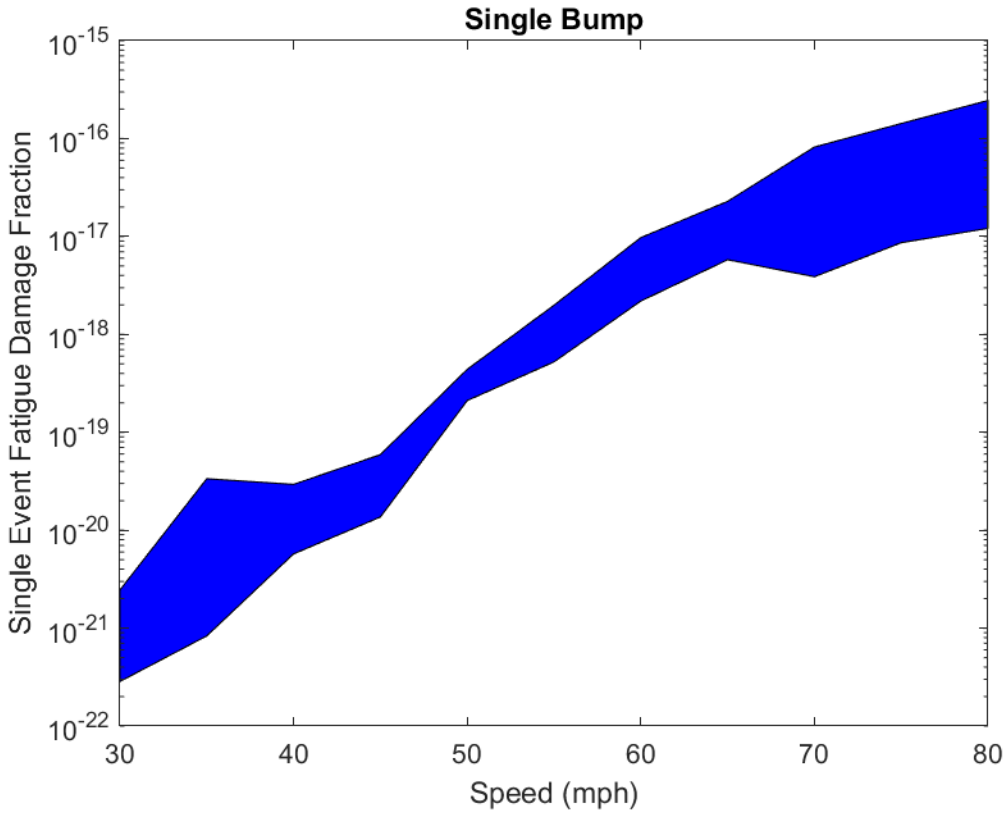

Figure 70. Log-scale single event fatigue damage fraction for low stiffness.

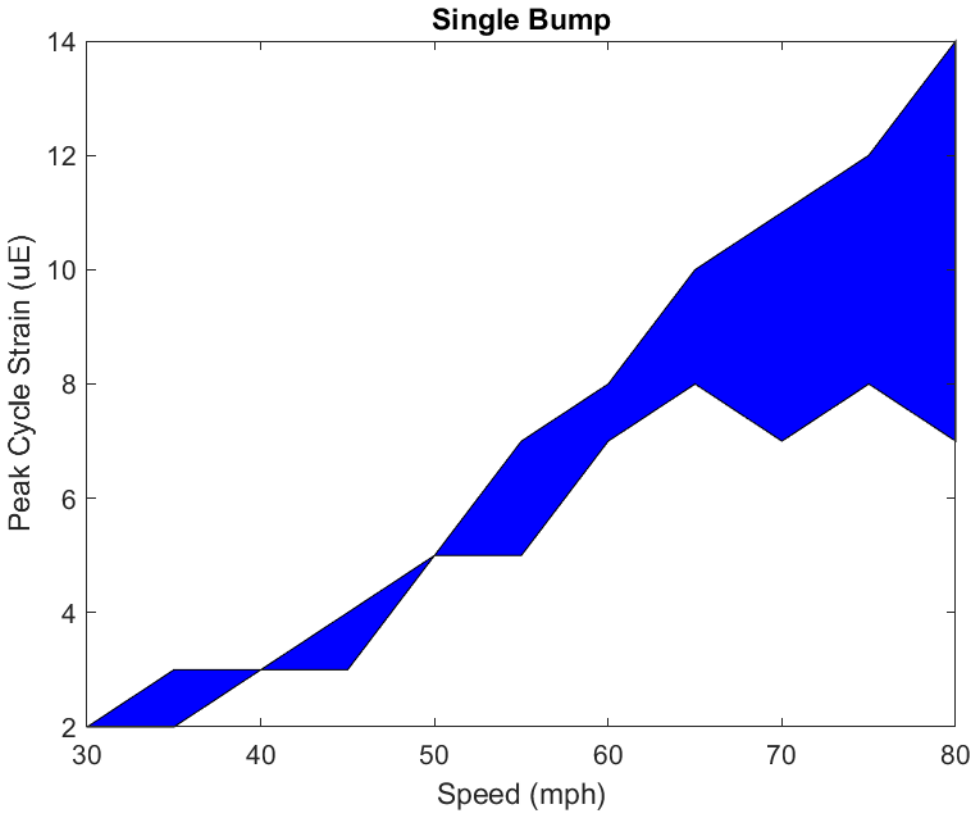

Figure 71. Peak cycle strain for low stiffness.

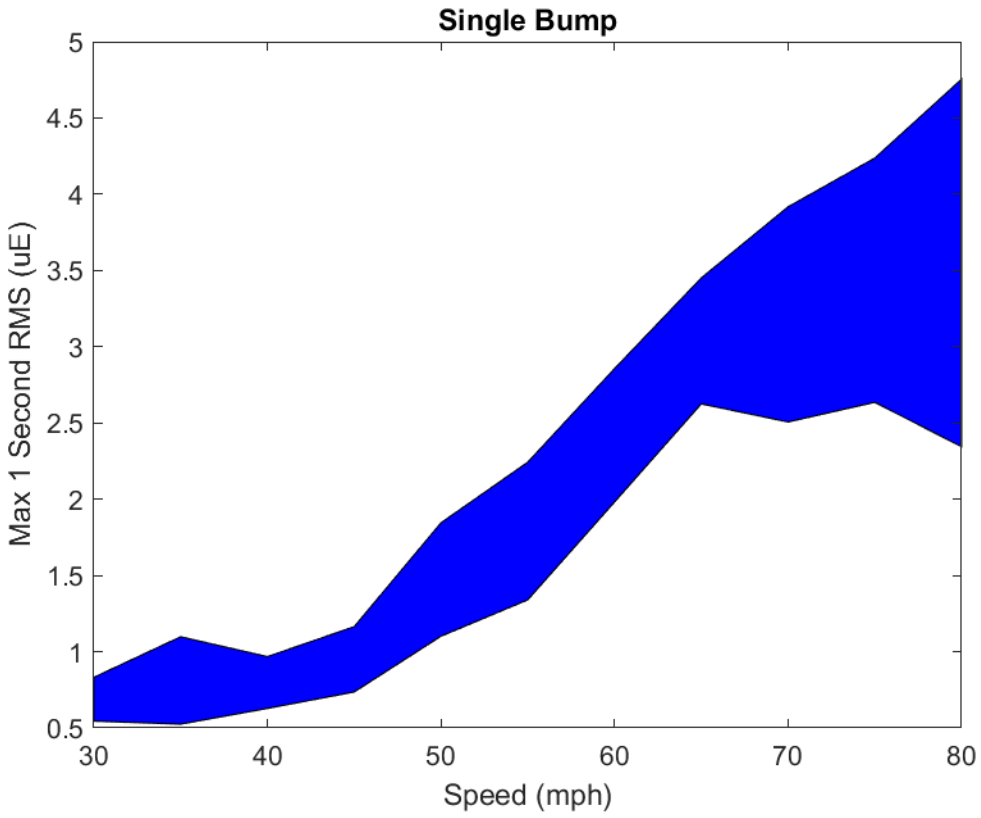

Figure 72. Maximum one-second RMS value for low stiffness.

6.2.2.2 High Stiffness

Figure 73 shows the single event fatigue damage fraction envelope plot. Unlike the low-stiffness model, the high-stiffness model shows much more variation in the upper bound. In fact, the maximum value of 5.23e-19 occurs at 50 mph, not 80 mph. There are also several other peaks and valleys in the data, such as the upper bound valley at 45 mph without a corresponding lower bound valley. However, even with this variation, the high stiffness shows less damage than the low stiffness, consistent with the trend in the pitch and bounce analyses. There is still a general increase in the damage as speed increases in the lower bound, but no such general trend in the upper bound.

Figure 74 shows the peak cycle strain. Similar to fatigue damage, peak cycle strain also has significant variation in the high-stiffness case as compared to the low-stiffness case, but a general increase as speed increases still exists. The maximum peak cycle strain of 4 uE occurs at 60, 75, and 80 mph, much lower than the maximum cycle strain of 14 uE in the low-stiffness case.

Figure 75 shows the maximum one-second RMS plot. In the high-stiffness analyses, the upper bound has significant variation, with seemingly periodic valleys. The maximum value of 1.4 uE (RMS) occurs at 80 mph, but 40, 50, and 60 mph all come close to that maximum value. Although the lower bound has a more apparent increase in RMS strain as speed increases, the upper bound provides less evidence of this trend. Just as in the pitch and bounce analyses, the high-stiffness values in the single bump run are all smaller than the low-stiffness values; however, these values still show nearly zero damage.

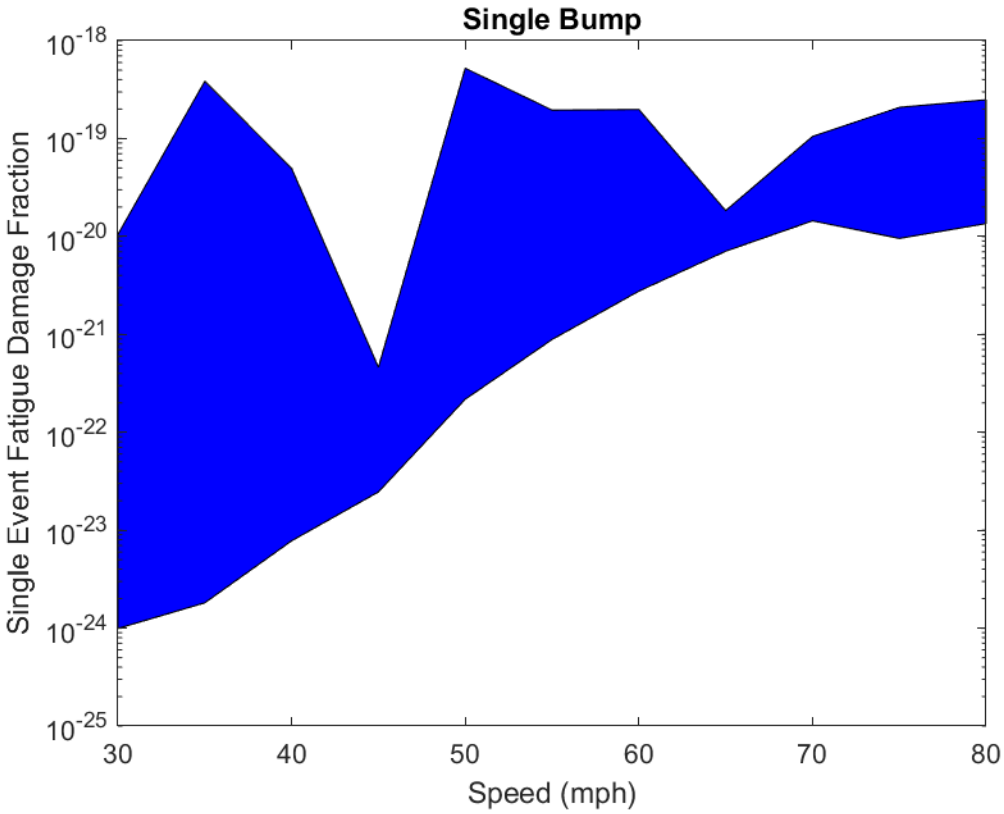

Figure 73. Log-scale single event fatigue damage fraction for high stiffness.

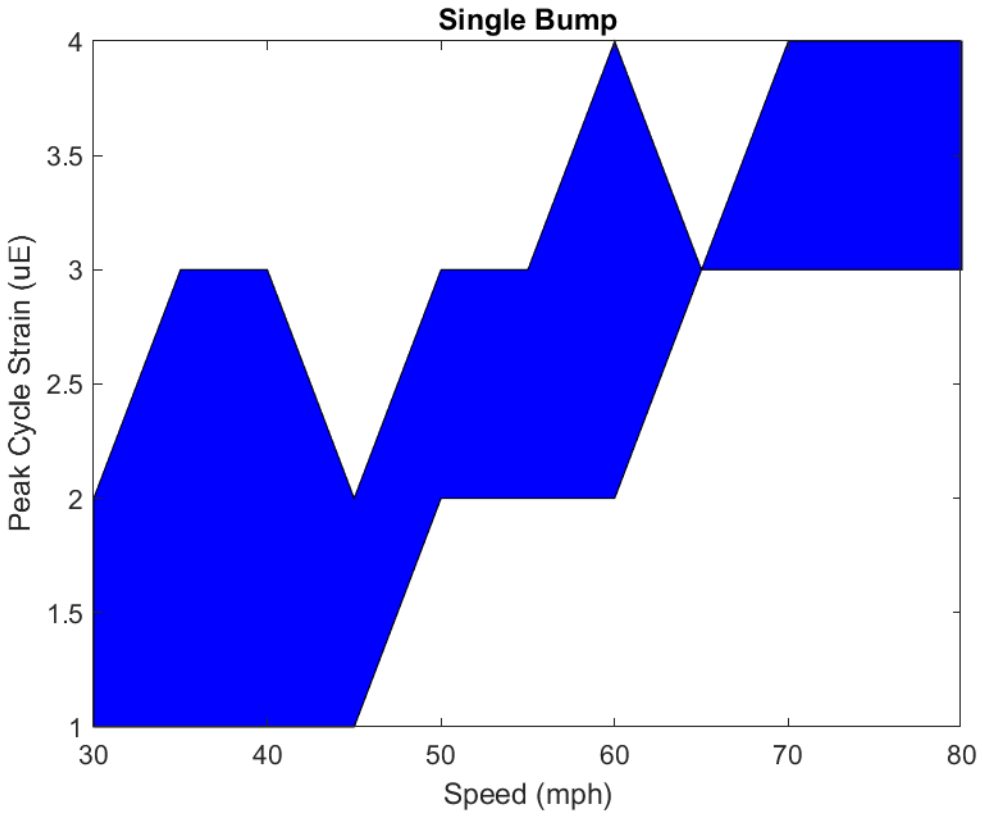

Figure 74. Peak cycle strain for high stiffness.

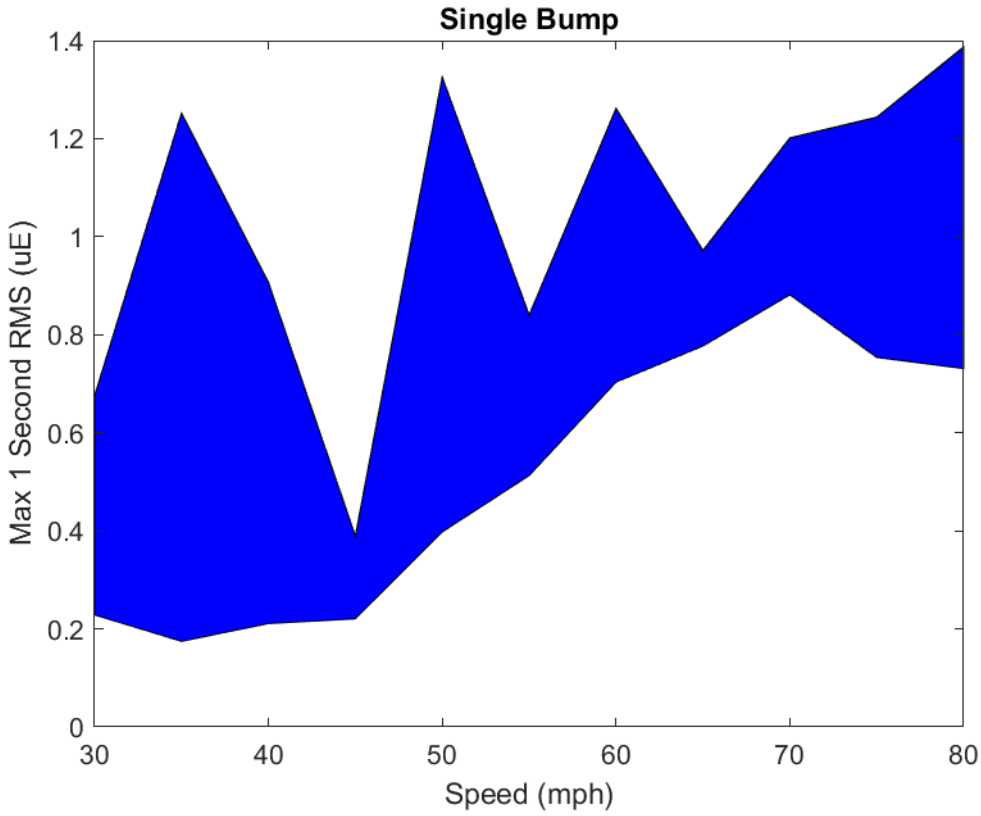

Figure 75. Maximum one-second RMS value for high stiffness.

6.2.3 Twist and Roll

The twist and roll test track is similar to the pitch and bounce test track, except that the vertical perturbations of the left and right rails are out of phase, exciting lateral and roll modes of the railcar. The length of the contoured track section is 410 feet, slightly longer than the pitch and bounce test track. Section 4.1 has more details about the test and the NUCARS model that calculates the response of the Atlas railcar to the test track conditions. The range of speeds for this analysis was 15-80 mph, with a resolution of 5 mph.

6.2.3.1 Low Stiffness

Figure 76 shows the single event fatigue damage envelope plot. In low-stiffness twist and roll analyses, the maximum fatigue damage of 1.49e-17 occurs at 75 mph, but the trends are somewhat different than the pitch and bounce and the single bump analyses. After about 30 mph, the upper bound stays relatively constant although 30, 75, and 80 mph have the largest values. The lower bound has a valley at 50 mph, with a steady increase to 80 mph. Although the peak damage is much lower than observed in the pitch and bounce and the single bump analyses, lower speeds in twist and roll can cause more damage than lower speeds in the other two track conditions. However, these damage fractions are still miniscule.

Figure 77 shows the peak cycle strain envelope plot. The maximum value of 6 uE occurs at 30, 75, and 80 mph, corresponding to the same peaks as in the damage fraction. After 30 mph, there does not seem to be the same general trend of increasing values with increasing speed as there was in the pitch and bounce and the single bump analyses.

Figure 78 shows the maximum one-second RMS strain envelope plot. The maximum value of 2.6 uE (RMS) occurs at 75 mph, and there is a subtle positive trend with speed and maximum one-second RMS.

Overall, twist and roll, when looking at the low-stiffness values, is a less damaging track condition than the pitch and bounce and the single bump conditions.

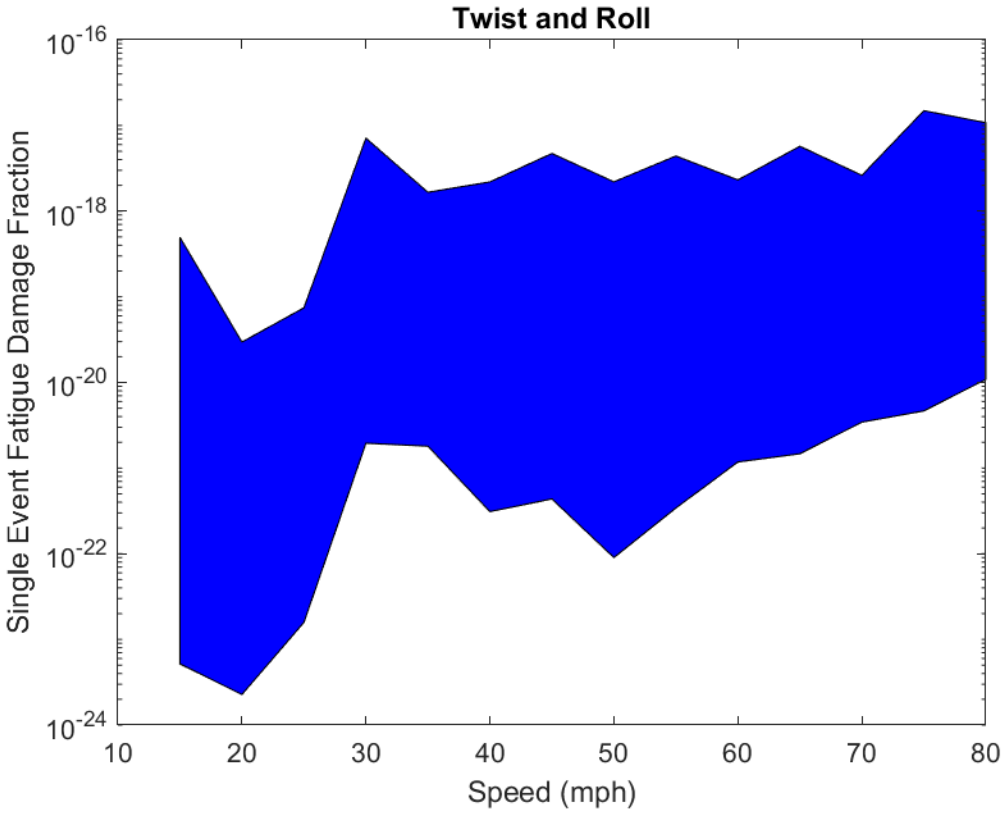

Figure 76. Log-scale single event fatigue damage fraction for low stiffness.

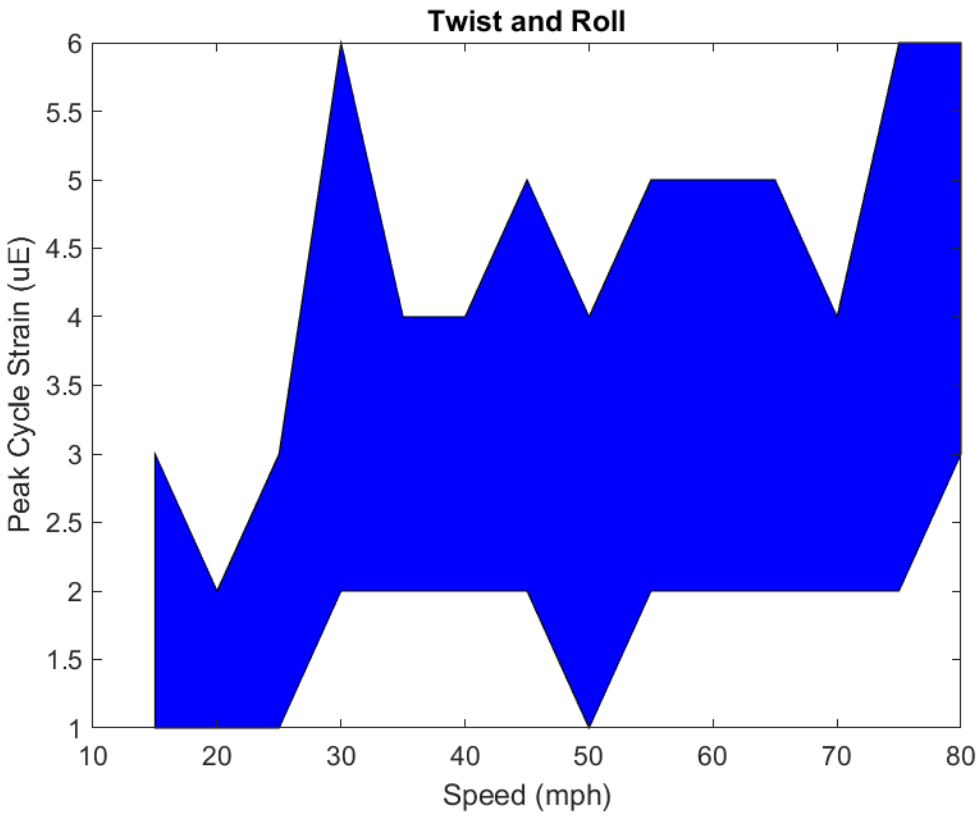

Figure 77. Peak cycle strain for low stiffness.

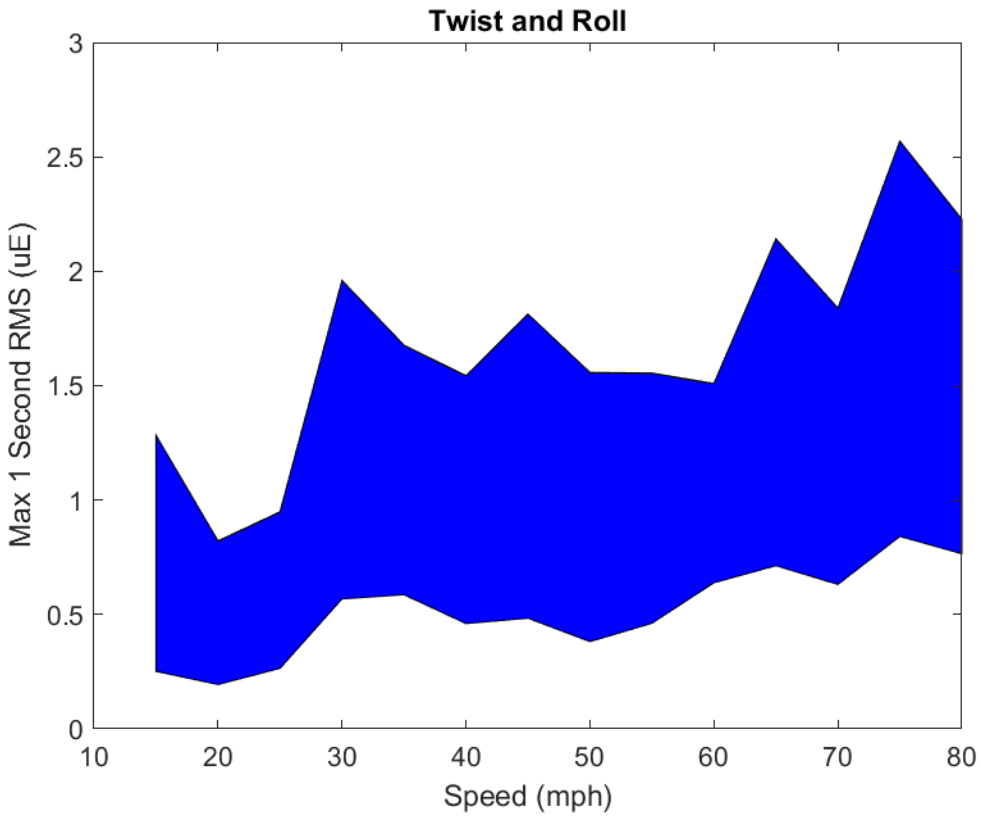

Figure 78. Maximum one-second RMS value for low stiffness.

6.2.3.2 High Stiffness

Figure 79 shows the single event fatigue damage fraction envelope plot. The high-stiffness twist and roll results had a maximum fatigue damage of 1.52e-19 at 60 mph. With the high stiffness, however, the trends are different from the low stiffness. First, there is a general increase in damage as speed increases. Second, the peak damage is much closer to the pitch and bounce and the single bump analyses, and low speed fatigue is also closer in magnitude to the other analyzed tests. One similarity is that a peak still remains at 50 mph. Overall though, the damage fractions are still small.

Figure 80 shows the peak cycle strain envelope plot. The maximum value of 3 uE occurs at 60 and 75 mph, which correspond to the speeds of the two highest peaks in the fatigue damage fraction. The peak cycle strain for the high-stiffness twist and roll analyses seems even more constant than that of the low-stiffness twist and roll for speeds above 30 mph.

Figure 81 shows the maximum one-second RMS strain envelope plot. The maximum value of 1.0 uE (RMS) occurs at 60 mph. The same slightly positive trend in the one-second RMS strain from the low-stiffness twist and roll is still apparent in the high-stiffness twist and roll and the same general conclusion that twist and roll is less damaging than single bump or pitch and bounce still seems to be true.

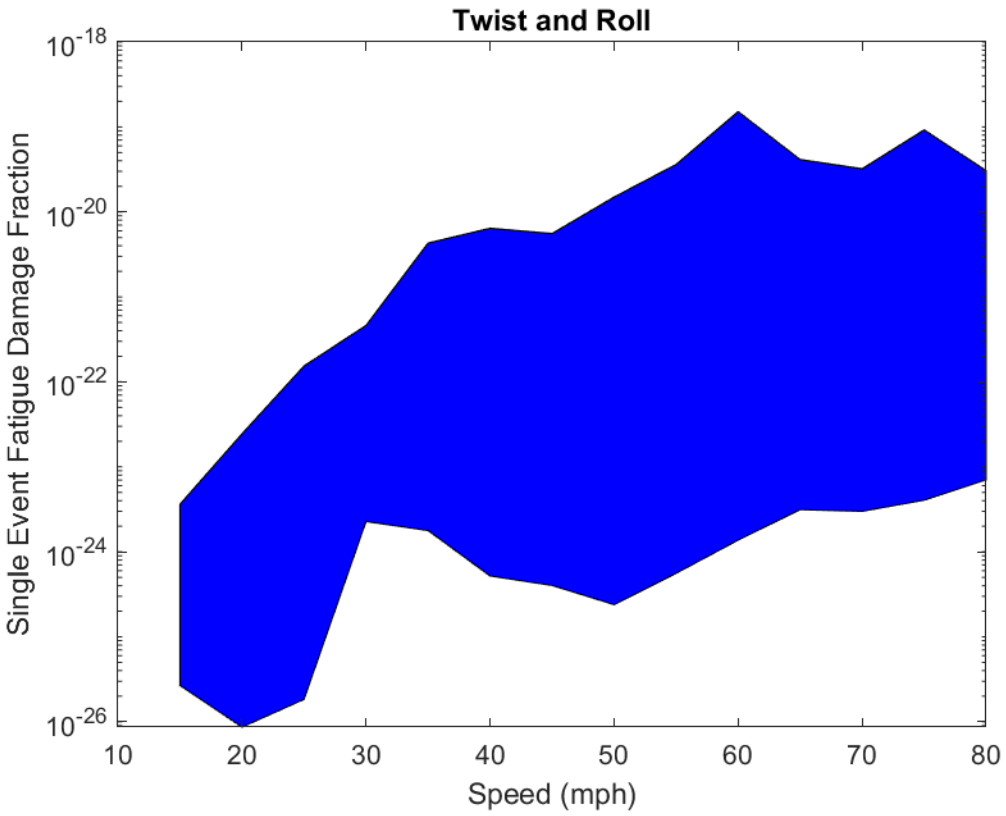

Figure 79. Log-scale single event fatigue damage fraction for high stiffness.

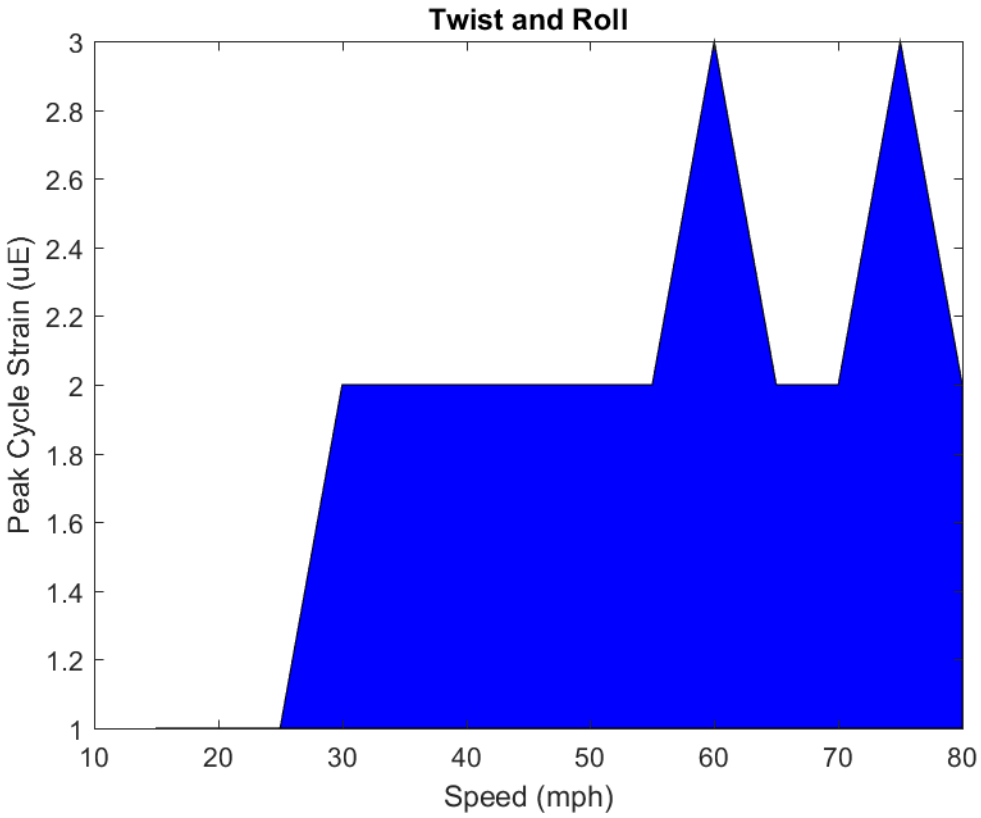

Figure 80. Peak cycle strain for high stiffness.

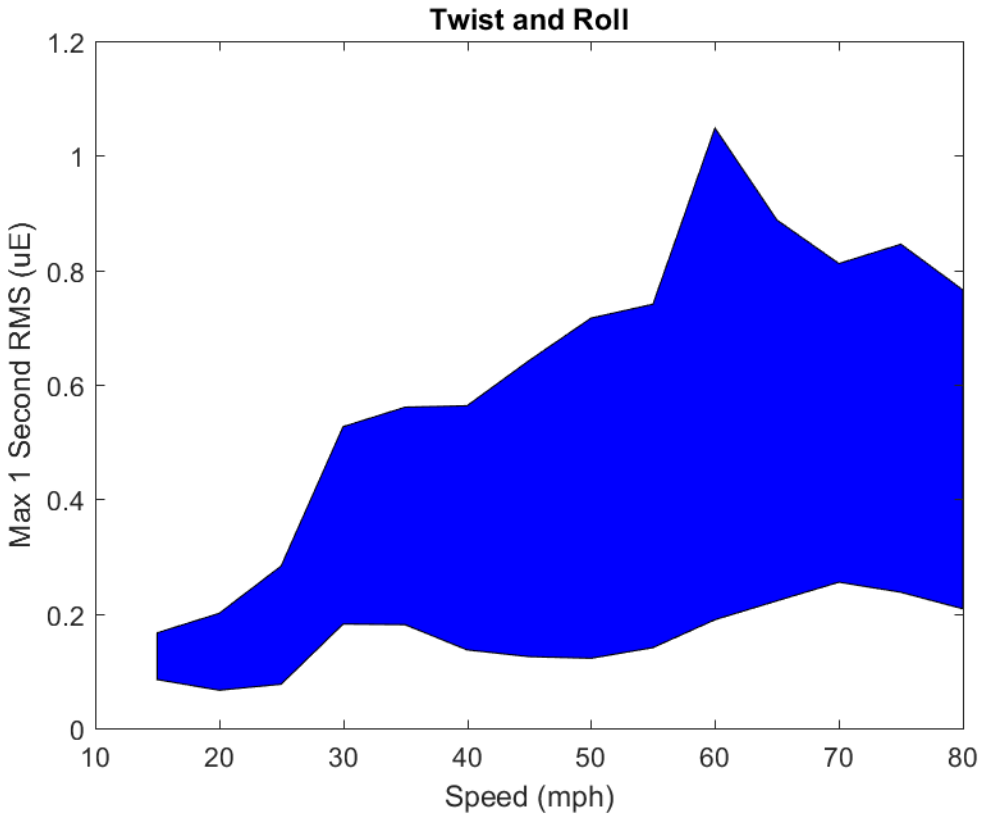

Figure 81. Maximum one-second RMS value for high stiffness.

6.2.3.3 Lateral Motion

In the twist and roll analyses, higher accelerations were observed in the lateral direction than in the vertical direction. Because of this observation, the SNF cladding fatigue was also calculated for lateral loading. The previous analyses were all based on the vertical motion of the system.

Figure 82 shows the single event fatigue damage fraction envelope plot. The low-stiffness twist and roll analyses had a maximum lateral fatigue damage fraction of 3.52e-21 at 75 mph and the high-stiffness twist and roll analyses had a lower maximum lateral fatigue damage fraction of 6.54e-25 at 80 mph. Both of these values are significantly lower than the vertical fatigue damage fractions.

Figure 83 shows the peak cycle strain envelope plot. The maximum of 2 uE occurs at 35, 40, 50, 55, 60, 65, 70, 75, and 80 mph for the low-stiffness test. The maximum peak cycle strain was 1 uE for all speeds for the high-stiffness test, but is not visible in the graphic. Strain values are rounded to the nearest microstrain, and all data points on the plot are either 1 uE or 2 uE.

Figure 84 shows the maximum one-second RMS strain envelope plot. For the low-stiffness test, the maximum value of 0.6 uE occurs at 80 mph. For the high-stiffness analyses, the maximum value of 0.2 uE also occurs at 80 mph.

Overall, the strain and fatigue values of the lateral component of the twist and roll analyses are much lower than any of the strain and fatigue values from the vertical component, even though higher accelerations were observed in the lateral direction compared to vertical direction. In the MMTT, the 0-degree (vertical) strain gages were more limiting than the 90-degree (lateral) strain gages, so this result is consistent with previous observations.

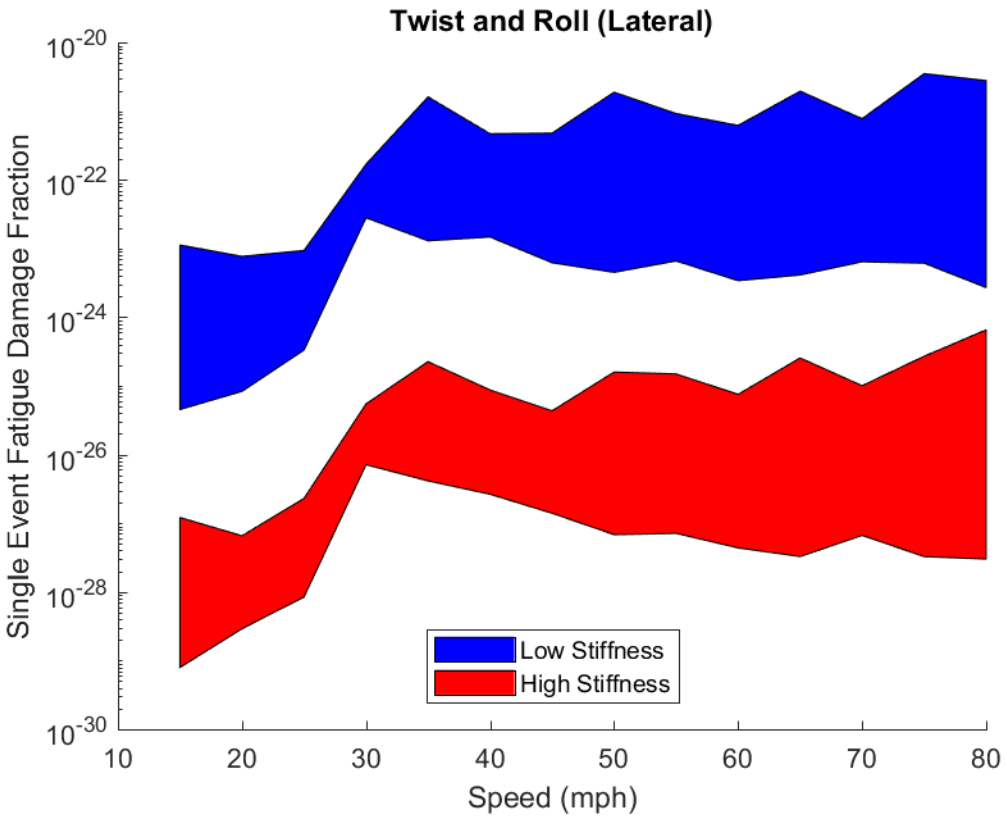

Figure 82. Log-scale single event fatigue damage fraction for twist and roll lateral motion.

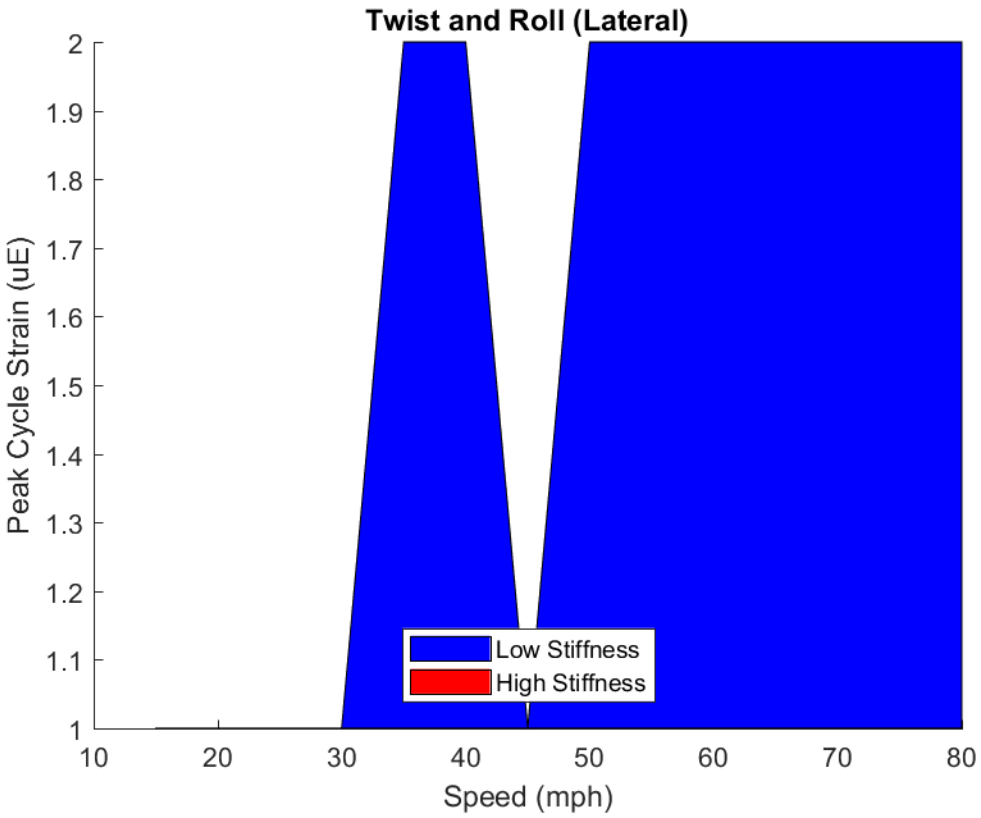

Figure 83. Peak cycle strain for twist and roll lateral motion. (High Stiffness = 1 uE in all cases)

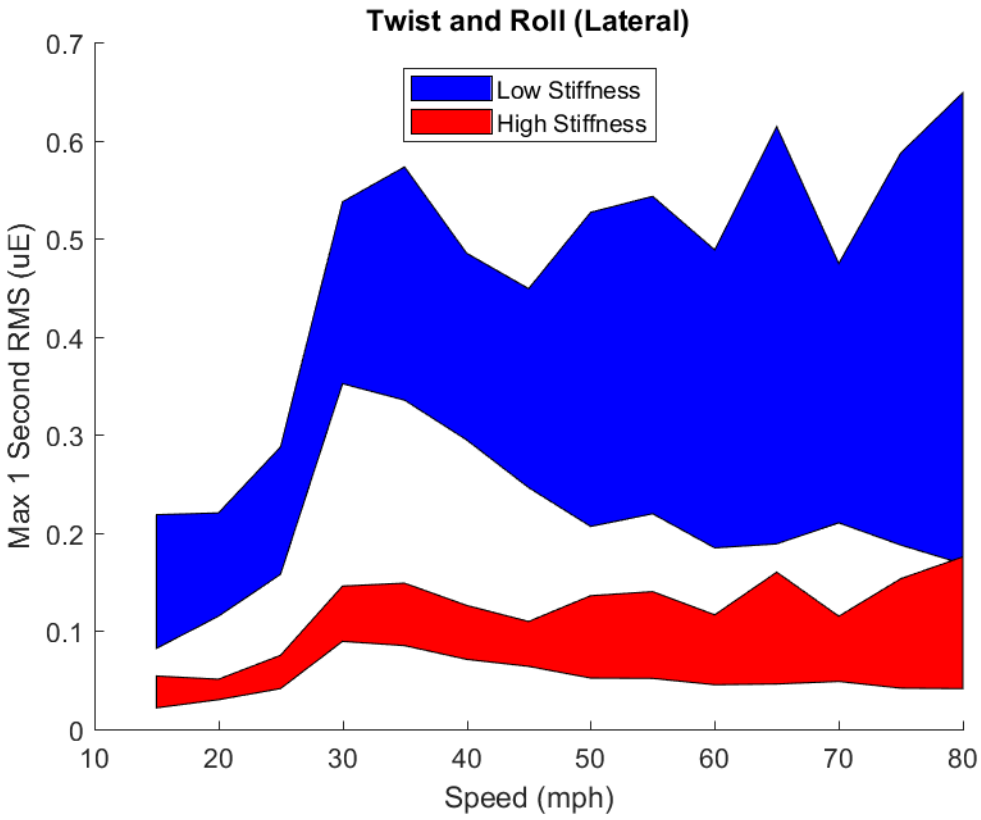

Figure 84. Maximum one-second RMS value for twist and roll lateral motion.

6.3 Fatigue Analysis for Generic 2,000-Mile Rail Trip

This study uses three methods for performing a fatigue analysis to represent a 2,000-mile cross-country rail trip in the United States. The peak strain value method is described in Section 6.3.1. The track feature method is described in 6.3.2. The RMS signal strength method is described in Section 6.3.3. All three methods derive the same conclusion that the fatigue damage to fuel rod cladding is approximately zero. The details of the three fatigue analyses are described in the following sections.

6.3.1 Peak Strain Value Method

The single-rod model calculated the structural dynamic response of a fuel rod to a library of test track conditions at speeds of up to 80 mph. More than 1,600 fuel rod responses were calculated. The maximum cladding strain calculated in any case was only 20 uE. This number comes directly from the single-rod model results reported in Section 5.2 and is slightly higher than the strain cycle amplitude of 14 uE that was calculated in Section 6.2 using the ASTM rainflow counting method. Using the peak strain value is a shortcut that avoids a step of calculation. Note that the strain values are so low (20 uE and 14 uE) that both values could be approximated as 0 uE. To put the small strain values into perspective, 20 uE is below the typical number of significant digits that would be reported in a structural analysis of cladding.

The strains are also very small in the context of an S-N curve. The O'Donnell S-N curve for irradiated zirconium alloy is used in this study to define accumulated fatigue damage (O'Donnell 1964). Table 11 lists the S-N relationship from the O'Donnell curve in the first two columns. The third column lists the number of cycles required to cause a damage fraction of 0.01, which is helpful in establishing a bound where the strain cycles are too small to be relevant to the accumulated damage fraction.

Table 11. O'Donnell Fatigue Curve Reference Table

# of Strain Cycles	Strain Amplitude (uE)	Cycles to Reach a Damage Fraction of 0.01
10,000	1,160	100
100,000	786	1,000
1.0E+06	533	10,000
1.0E+07	361	100,000
1.0E+08	245	1.0E+06
1.0E+09	166	1.0E+07
1.0E+10	112	1.0E+08
1.0E+11	76	1.0E+09
1.0E+12	52	1.0E+10
1.0E+13	35	1.0E+11
1.0E+14	24	1.0E+12
1.0E+15	16	1.0E+13
1.0E+16	11	1.0E+14
1.0E+17	7	1.0E+15
1.0E+18	5	1.0E+16
1.0E+19	3	1.0E+17
1.0E+20	2	1.0E+18
1.0E+21	1.6	1.0E+19
1.0E+22	1.1	1.0E+20
1.0E+23	0.7	1.0E+21

The shaded rows mark the 10 uE strain amplitude threshold that Klymyshyn et al. (2018) used to count strain cycles, and it was used again in this study. Strain amplitude cycles below 10 uE are not counted because it would take over 1E+14 cycles for a 10 uE strain circle to contribute a damage fraction of 0.01. If we assume the strain cycle is a 60 Hz vibration, it would take more than 52,000 years of continuous vibration loading to achieve 1E+14 cycles and consume 1% of the cladding fatigue life. The westbound rail leg of the MMTT only recorded 4,000 cycles above 10 uE in 59 hours of travel.

From Table 11, a 20 uE repeated strain cycle would require about 1E+14 strain cycles to reach failure, and 1E+12 cycles to use a noticeable amount of fatigue life. If the strain cycle is a 60 Hz vibration, it would take 53,000 years to fail the cladding and about 530 years to consume 1% of the total fatigue life. From this, it can be concluded that 20 uE is too small of a strain value to have any practical effect on the fatigue life of the cladding during NCT shock and vibration loads by rail.

100 uE is a reasonable threshold for deciding whether a strain value is worth evaluating in detail for fatigue. From Table 11, a 100 uE strain amplitude cycle would have to repeat 1E+8 times to consume 1% of the material's fatigue life. For a 60 Hz vibration, that would take about 19 days to accumulate a 1% damage fraction, and about 1,900 days to reach a fatigue failure.

6.3.2 Track Feature Method

In rail transportation, track features provide a basis for estimating the number of fatigue cycles that are expected from a 2,000-mile trip. Klymyshyn et al. (2018) provided an estimate of the number of track

features expected on a 2,000-mile trip on the US railway system in Table 4.1.2. A precise counting of track features along a proposed transit path can be made, but this analysis assumes that 5,000 track features can be expected.

The library of single-rod model results was evaluated in Section 6.2 for fatigue. The greatest number of cycles over 10 uE was 3. The largest strain cycle was 14 uE. If it is assumed that every track feature caused 3 cycles of 14 uE, then that is 15,000 cycles at a strain cycle amplitude of 14 uE. Using the O'Donnell S-N relationship, that amounts to an accumulated fatigue damage of 6.69E-12 for a 2,000-mile rail trip.

Alternatively, the maximum fatigue damage fraction from Section 6.2 was 3.40e-16 and repeating that damage 5,000 times would only accumulate a damage fraction of 1.70E-12 for a 2,000-mile rail trip.

Either way of calculating the fatigue based on track features arrives at a near-zero accumulated fatigue damage. Note that the accumulated fatigue damage is so small that the assumed number of track features (5,000) could be changed by many orders of magnitude and the calculation would still arrive at a near-zero accumulated fatigue damage. A precise count of track features would only be necessary if the strain cycles were significantly higher.

One clear trend in the fuel rod analysis for the Atlas conveyance is that the high-stiffness cases all have very low strain signal strength, and never experience strain cycle amplitudes above 10 uE. If the fuel is in a high-stiffness condition, from pellets bonded to the cladding, the strain cycle estimate would drop from 15,000 to zero. Because the strain cycle amplitudes are so low, there is no practical difference between 15,000 or zero cycles. In one case the fatigue damage is approximately zero; in the other case the fatigue damage is identically zero.

Similarly, the speed of the railcar is related to the number of strain cycles. The analyses go up to train speeds of 80 mph, but the events that cause strain cycles above the 10 uE threshold occur at 60 mph and higher. The 15,000 strain cycles estimated in this fatigue analysis essentially assumes that the train crosses 5,000 track features at speeds of 60 mph or greater. This is a very unrealistic, but conservative, assumption. The next fatigue calculation method uses the MMTT data to make a more realistic estimate of the number of strain cycles that can be expected.

6.3.3 RMS Signal Strength Method

The MMTT provides valuable data on the long-term shock and vibration environment SNF is expected to experience during NCT. It was only one test, but the continuous data collection system used in the test means that the response of the conveyance system for every second of the journey was recorded. These data provide insight into what an SNF system can be expected to experience. Typical fatigue analyses make conservative assumptions about the strain amplitudes and cycle counts to provide an assurance of safety. This fatigue analysis uses the MMTT fatigue data as a basis for making a reasonable estimate of the fatigue demands on SNF.

The first estimate of realistic fatigue is to note that all of the 1,600+ analysis cases described in Section 6.2 indicate lower strains and strain signal strength than were witnessed in the MMTT westbound rail leg. It can reasonably be concluded that all the analyzed Atlas railcar transportation configurations can be expected to experience lower accumulated fatigue damage than was recorded in the MMTT. The MMTT concluded that fatigue damage was approximately zero, or that it would take over 10 billion 2,000 mile trips to threaten a fatigue failure. The MMTT conditions can be characterized as approximately zero fatigue damage, or approximately infinite fatigue life, and the analysis of this report confirms that the Atlas railcar and all of its cask and cradle configurations can expect similar or better fatigue capacity.

A more detailed estimate of fatigue is based on the strain gage signal strength observed during the MMTT westbound rail leg. The signal strength is quantified by taking the RMS of a 1-second window of data,

then sliding the window 1-second and repeating the RMS operation. A histogram is created for each second of data to illustrate how much time is spent at each signal strength.

Figure 85 shows the strain RMS histogram for Strain Gage 8, which had the highest hour of strain signal strength over all fuel rod strain gages in the MMTT westbound rail leg. Other strain gages had higher one-second RMS signal strength values (the maximum was almost 15 uE (RMS), as seen in Figure 51), but Strain Gage 8 was chosen for this calculation because its signal strength was highest for longest. The histogram shows the signal strength distribution is heavily weighted to the low end, which represents the fact that the railcar remained stationary during the period of data recording. 0.3 uE (RMS) is used as the threshold to divide stationary time from motion time. The high end of the strain signal strength range is most important because only at the high ranges do any relevant strain cycles occur. As discussed above, 10 uE is used as the threshold for counting strain cycles. In the time between crossing track features that drive a significant transient response, the SNF experiences a steady-state random vibration that has an average signal strength of about 1.5 uE (RMS). The maximum signal strength recorded for Strain Gage 8 was 9.7 uE (RMS).

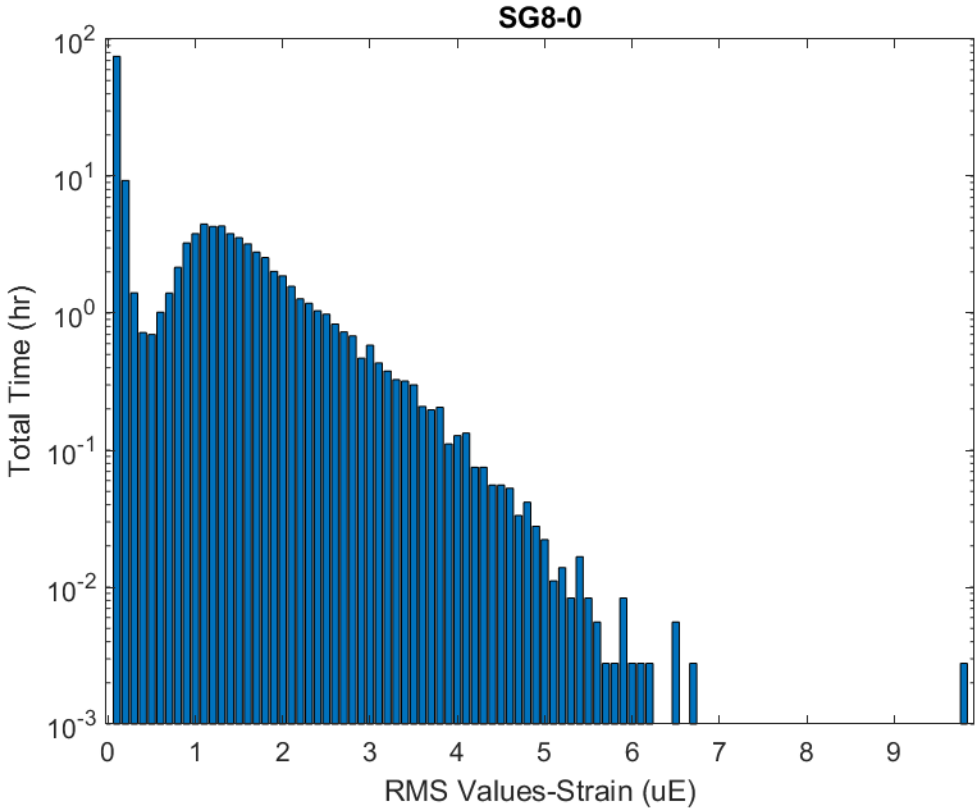

Figure 85. Log scale of total time spent at various RMS values for Strain Gage 8.

The Atlas railcar analysis calculated a similar range of strain signal strength, using the same calculation techniques applied to the MMTT data. The RMS values calculated in Section 6.2 for the 1,600+ cases are all below 6.9 uE (RMS). Strain cycles above the 10 uE threshold only occur when the signal strength is 3.4 uE (RMS) or higher. The minimum threshold for 1 strain cycle is 3.4 uE (RMS), the minimum threshold for 2 strain cycles is 4.7 uE (RMS), and the threshold for 3 strain cycles is 6.9 uE (RMS).

Table 12 combines information from the MMTT and the fatigue analysis of SNF in the Atlas railcar analyses. The strain signal strength ranges are divided into useful categories in the first column. The next column lists the total number of seconds from the MMTT that Strain Gage 8 signal strength was within each category. The next column lists the number of strain cycles that are anticipated to occur within each

signal strength category for the Atlas railcar analyses. The final column sums that anticipated total number of strain cycles (over 10 uE). This method estimates that 7,240 cycles would occur. Assuming that each strain cycle has an amplitude of 14 uE, the damage fraction is 3.23E-12, which is many orders of magnitude below the failure criterion of 1.0.

Table 12. Fatigue cycle estimate for Atlas based on MMTT data.

Strain RMS Ranges	Seconds during MMTT	Strain Cycle Counts for Atlas	Total # Strain Cycles
0.0 to 0.3 uE (rest)	308520	0	0
0.3 to 3.4 uE	204440	0	0
3.4 to 4.7 uE	5870	1	5870
4.7 to 6.9 uE	670	2	1340
6.9 uE +	10	3	30
TOTAL	519510	-	7240

Other reasonable analytical approaches could be used to evaluate the MMTT fatigue data and inform a realistic estimate of strain cycle counts for the Atlas railcar SNF fatigue evaluation. But any methodology is expected to arrive at the conclusion that SNF is not anticipated to experience any significant fatigue loading during NCT using the Atlas railcar.

6.4 Fatigue Evaluation Conclusions and General Applicability

The fatigue evaluation considers the full library of 1,600 single-rod model-calculated responses. Each individual fuel rod structural dynamic response represents the reaction of the fuel rod to a broad set of railcar conditions. The range of train speeds goes up to 80 mph, which bounds the anticipated railcar speed under NCT. The range of cask masses covers the range of currently licensed packages in the United States. The analysis results support the conclusion that the fatigue damage of the fuel rod cladding is negligible within the entire range of responses.

These results support the conclusion that the MMTT provided a bounding (more severe) shock and vibration environment for SNF than would be expected from any of the Atlas railcar configurations. The sensitivity studies of Section 5.3 indicate some variation in response from different fuel assembly designs, canister systems, or fuel cladding to pellet bonding can be expected, but none of the sensitivities are significant enough to challenge the fuel cladding fatigue strength for the number of anticipated strain cycles.

The engineering mechanics models of this analytical study are well validated against test data, as shown by Klymyshyn et al. (2018). The engineering mechanics models calculate results according to the fundamental laws of physics and well-established engineering mechanics theories. This analysis has considered the full range of anticipated rail transportation configurations. An extreme change in configuration that is outside the boundaries considered in this study would be necessary to threaten cladding fatigue failure. A few examples are noted in the following paragraphs.

This study only considered undamaged fuel rods. The results of this study suggest that any intact fuel rod that is transported under NCT in a rail cask will remain undamaged from beginning to end. One possible exception to the findings of this study is the case where pre-existing damage in a loaded SNF assembly is not recognized at the time of loading. This condition was not evaluated in this study, but it would take a significant increase in stress or strain to cause a fuel rod failure because the shock and vibration energy is so low.

Similarly, this study did not consider debris inside the fuel compartment. An example is broken standoff pins from certain fuel basket designs. If this type of loose debris is inside the cask, it could change the standard loading conditions on fuel rods from an intermittently supported beam to an intermittently supported beam that also has to support additional mass. This study did not consider the presence of debris, but because the vibration energy is so low, it is hard to imagine an increase in cladding stresses that would be high enough to cause fatigue failure.

A key feature of the Atlas railcar design is that its suspension system meets the requirements of AAR S-2043, which demands a relatively smooth ride. The MMTT used a railcar with a suspension system rated for general freight, and the MMTT test data demonstrated that the MMTT configuration would not pass AAR S-2043. The difference in suspension system is thought to be the key difference between the Atlas railcar response and the MMTT response. In practice, any railcar design used to transport SNF in the United States is expected to meet the requirements of AAR S-2043. However, it is possible to move SNF on US railways without an AAR S-2043 railcar if the railroads choose to allow it. In such a case, the suspension system could provide a worse ride quality than the Atlas railcar assumed in this analysis, but it is hard to imagine that it would be significantly worse than the MMTT test configuration. It is not credible to assume that a railroad would allow the operation on its system of a railcar that has an inappropriate suspension system that would cause an order of magnitude increase in loads. The Atlas railcar is a good representative of AAR S-2043-compliant railcar designs, and the Kasgro flatbed railcar used in the MMTT is a good representative of all other modern railcars that might be used to transport SNF on a limited basis.

This page is intentionally left blank

7. Conclusions

This study completes the analysis of the MMTT by applying the knowledge gained from the test to an evaluation of irradiated SNF transportation using the Atlas railcar. The analysis demonstrates that the MMTT provided a more conservative shock and vibration environment for the fuel rods and fuel assemblies than would be expected of a railcar system that is compliant with AAR S-2043.

This analysis used the same kinds of engineering mechanics numerical models and methods that were validated against MMTT test data by Klymyshyn et al. (2018). The Atlas railcar model used in this study was developed for the Atlas railcar AAR S-2043 certification process and represents a conventional industry model. PNNL modified the model to represent the 17 different licensed SNF packages with SDOF systems to produce credible cask motion in response to select track conditions and a bounding set of train speeds. This created a broad range of cask dynamic responses that covers the anticipated range of response of SNF transported by the US rail system.

The response of a single, representative SNF rod to the large set of cask motions was calculated and evaluated using explicit dynamic FEA. Both low fuel rod stiffness conditions and high fuel rod stiffness conditions were evaluated. Across all cask motion cases, the models predict the peak cladding strains will remain below the strains recorded during the MMTT.

The calculated results are not sensitive to variations in fuel assembly design. The results are slightly influenced by the presence of a fuel rod canister, but the effect is not strong enough to significantly change the calculated strains. The presence of fuel pellets inside the cladding was evaluated and found to be inconsequential for NCT shock and vibration, but worth studying for package drop scenarios.

Fuel rod cladding fatigue of the Atlas railcar configuration was evaluated using three different approaches that all led to the same conclusion: the MMTT test configuration provided a more limiting SNF fatigue environment than the Atlas railcar.

Based on all of these observations, it is concluded that no further structural dynamic analysis of SNF under NCT rail transportation is necessary. For AAR S-2043-compliant railcars operating on US rail systems, the analysis of this study demonstrates that the loads and strains on the cladding are so low as to be negligible. For railcar conveyance systems that are not AAR S-2043-compliant, the MMTT test configuration is expected to prove an adequate estimate of performance. It would take a significant change in cask motion or anticipated fuel rod loads, by at least an order of magnitude from the MMTT test data or Atlas railcar model-calculated response, to warrant a new structural dynamic analysis of fuel cladding.

It is recommended that SNF response to package drop conditions be evaluated to complete the NCT evaluation. It is possible that the fuel pellet interaction that is negligible for railcar transportation shock and vibration conditions could be relevant in 30 cm package drop scenarios.

This page is intentionally left blank

8. References

AAR (Association of American Railroad). 2017. "Performance Specification for Trains Used to Carry High-Level Radioactive Material." AAR S-2043, Wood Dale, Illinois.

Adkins H, K Geelhood, B Koeppel, J Coleman, J Bignell, G Flores, J-A Wang, S Sanborn, R Spears, and N Klymyshyn. 2013. Used Nuclear Fuel Loading and Structural Performance Under Normal Conditions of Transport – Demonstration of Approach and Results on Used Fuel Performance Characterization. FCRD-UFD-2013-000325, Pacific Northwest National Laboratory, Richland, Washington

ANSYS, Inc. 2017. *ANSYS Mechanical User's Guide*, Release 18.1. Canonsburg, Pennsylvania.

AREVA (AREVA Federal Services, Inc.). 2018. *Atlas Railcar Phase 2 Final Report, Rev 1*. Report No. DE-NE0008390, Washington, D.C.

Chopra, A. 2012. *Dynamics of Structures*, 4th ed., pp. 83-90. Prentice Hall, New Jersey.

Kalanina, E.A., Wright, C., Ammerman, D.J., Grey, C.A., Arviso, M.. 2019. *Shaker Table Test*. SAND2019-3120R, M3 Report, Sandia National Laboratories, Albuquerque, New Mexico.

Kalinina, E.A., Wright, C., Gordon, N., Saltzstein, S.J., Lujan, L., Norman, K.M. 2018. *Data Analysis of ENSA/DOE Rail Tests*. SFWD-SFWST-2018-000494, Sandia National Laboratories, Albuquerque, New Mexico.

Klymyshyn, N.A., Ivanusa, P., Kadooka, K., Spitz, C., Jensen, P.J., Ross, S.B., Hanson, B.D., Garcia, D., Smith, J., Lewis, S. 2018. *Modeling and Analysis of the ENSA/DOE Multimodal Transportation Campaign*. PNNL-28088, Pacific Northwest National Laboratory, Richland, Washington.

Klymyshyn, N.A., Sanborn, S.E., Adkins, H.E. Jr, Hanson, B.D. 2013. *Fuel Assembly Shaker Test Simulation*. PNNL-22507, Pacific Northwest National Laboratory, Richland, Washington.

LSTC (Livermore Software Technology Corporation). 2013. *LS-DYNA® Keyword User's Manual, Volume I, Version R7.0*. Livermore, California.

MathWorks, Inc. 2019. *MATLAB Primer*. Natick, Massachusetts.

McConnell, P.E., Ross, S.B., Grey, C.A., Uncapher, W.L., Arviso, M., Garmendia, R., Perez, I.F., Palacio, A., Calleja, G., Garrido, D., Casas, A.R., Garcia, L.G., Chilton, W., Ammerman, D.J., Walz, J., Gershon, S., Saltzstein, S.J., Sorenson, K., Klymyshyn, N.A., Hanson, B.D., Pena, R., Walker. R. 2018. *Rail-Cask Tests: Normal-Conditions-of- Transport Tests of Surrogate PWR Fuel Assemblies in an ENSA ENUN 32P Cask*. SFWD-SFWST-2017-000004, Sandia National Laboratories, Albuquerque, New Mexico.

O'Donnell, W.J., Langer, B.F. 1964. "Fatigue design basis for zircaloy components." *Nuclear Science and Engineering* (20):1–12.

TTCI (Transportation Technology Center, Inc.). 2018. *NUCARS User Manual*, Version 2018.1. Pueblo, Colorado.

Saltzstein, Sylvia J., Sorenson, Ken B., Hanson, B. D., Shimskey, R. W., Klymyshyn, N. A., Webster, R. A., Jensen, P. J., MacFarlan, P. J., Billone, Mike, Scaglione, John, Montgomery, Rose, and Bevard, Bruce. EPRI/DOE High-Burnup Fuel Sister Rod Test Plan Simplification and Visualization. United States: N. p., 2017. Web. doi:10.2172/1395752.

Wang, J.-A., Wang, H., Jiang, H,. Yan, Y., Bevard, B.B., Scaglione, J.M. 2016. *FY 2016 Status Report: Documentation of All CIRFT Data including Hydride Reorientation Tests*. ORNL/SR-2016/424, Oak Ridge National Laboratory, Oak Ridge, Tennessee.

This page is intentionally left blank

Appendix A

Single-Rod Model Structural Dynamic Results

This appendix presents the detailed results of the single fuel rod structural dynamic model introduced in Section 5.2. Fuel rod responses are shown for each of the 17 casks and cradles employed on the Atlas railcar. Sections A.1 and A.2 detail the study results using the low stiffness and high-stiffness fuel rods modeled in this work, respectively. In each section, the results from each of the three test sections ─ pitch and bounce, single bump, and twist and roll ─ are evaluated in respective sections.

A-1. Low-Stiffness Tests

A-1.1 Pitch and Bounce

Figure A-1, Figure A-2, and Figure A-3 show the detailed results for the low-stiffness fuel rod model on the pitch and bounce section, showing peak strain, strain energy, and deflection, respectively. Across all speeds, the highest and lowest peak strain, strain energy, and deflection were observed for the HI-STAR 60 and HI-STAR 190XL casks, respectively. These represent the lightest and heaviest casks used on the Atlas railcar. A similar trend follows for all tests and configurations evaluated in this work; that is, lighter casks tend to elicit a stronger strain response in the fuel rods, compared to heavier ones. However, the figures also show this trend is not consistent across all speeds. For example, Figure A-1 shows that a number of casks predict higher strain responses than the HI-STAR 60 at 55 mph. From the figures it is noted that lighter casks tend to peak at greater speeds compared to heavier ones.

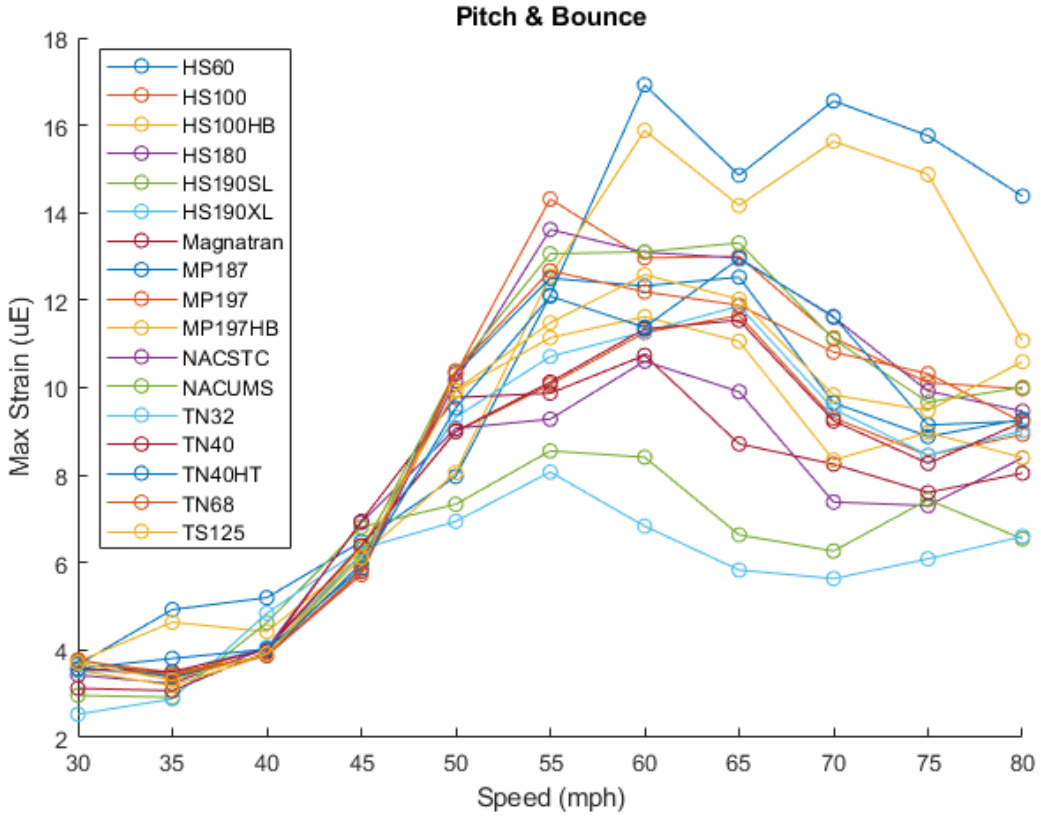

Figure A-1. Peak strain, low-stiffness model on the pitch and bounce test section.

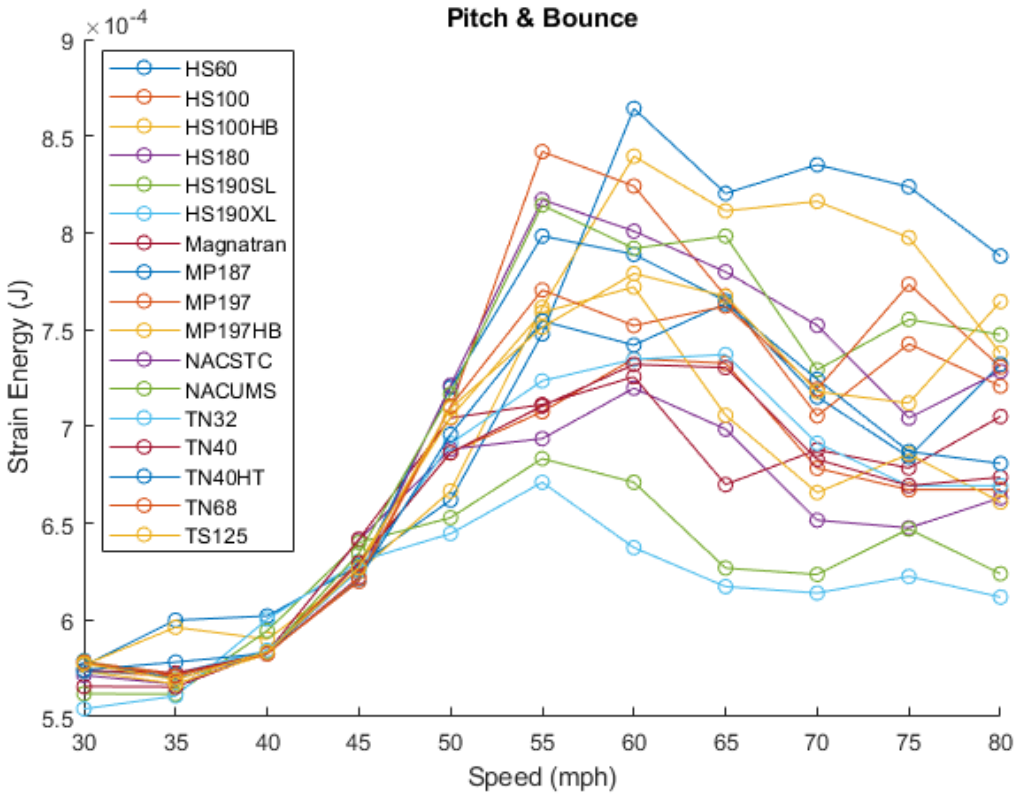

Figure A-2. Peak strain energy, low-stiffness model on the pitch and bounce section.

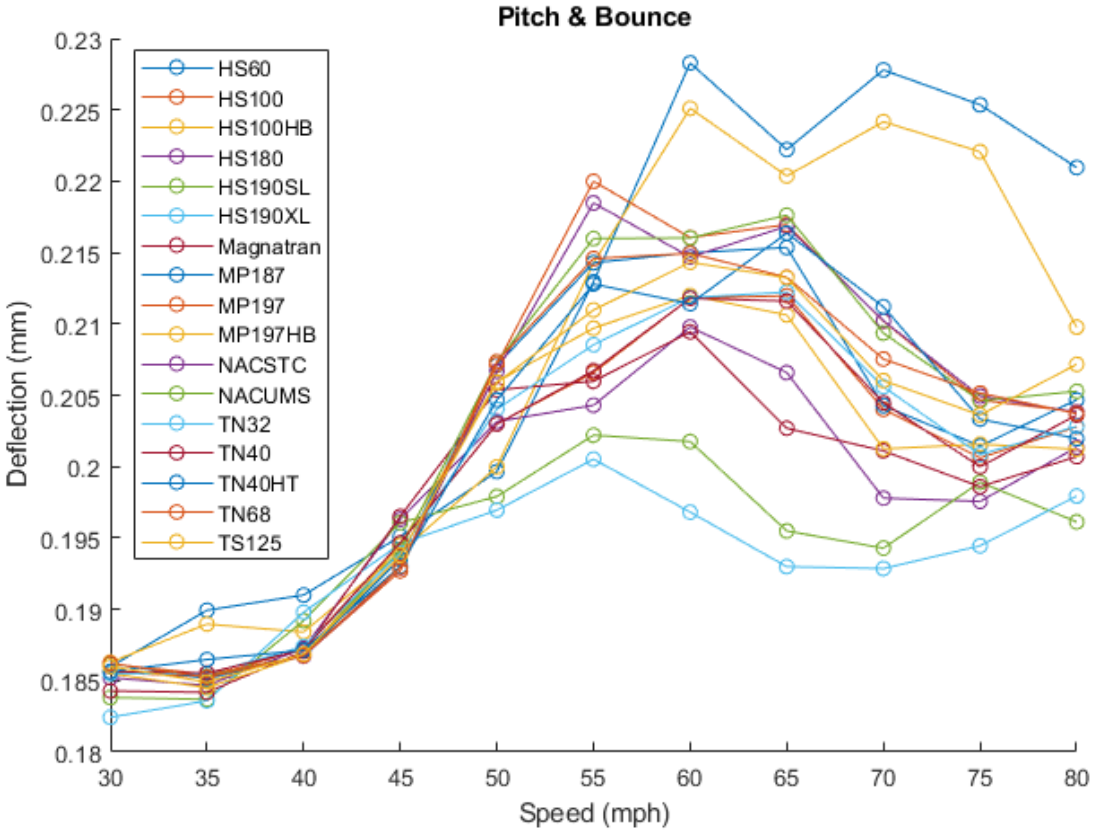

Figure A-3. Peak deflection, low-stiffness model on the pitch and bounce section.

A-1.2 Single Bump

Figure A-4, Figure A-5, and Figure A-6 show the detailed results for the low-stiffness fuel rod model on the single bump section, showing peak strain, strain energy, and deflection, respectively. The fuel rod response increases monotonically with respect to train speed; no clear resonance was observed. As with the pitch and bounce test section, lighter casks tended to produce a stronger response.

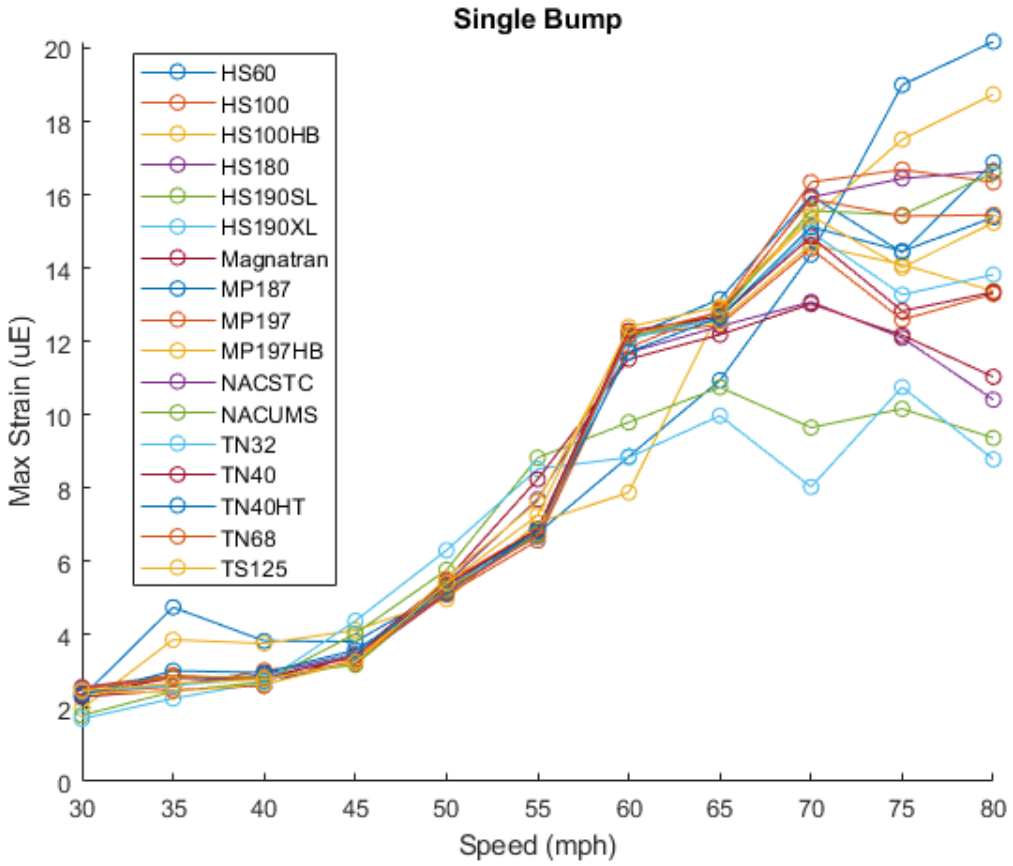

Figure A-4. Peak strain, low-stiffness model on the single bump section.

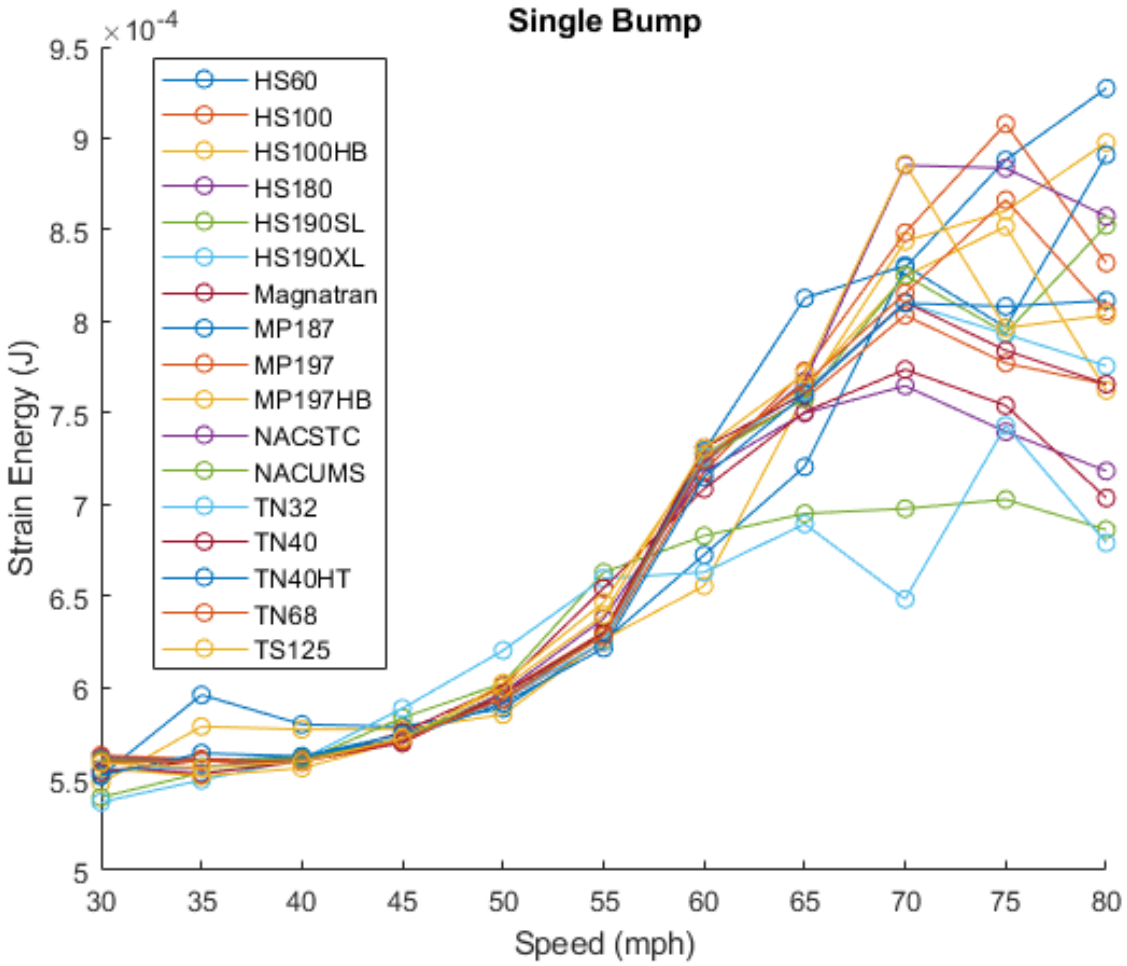

Figure A-5. Peak strain energy, low-stiffness model on the single bump section.

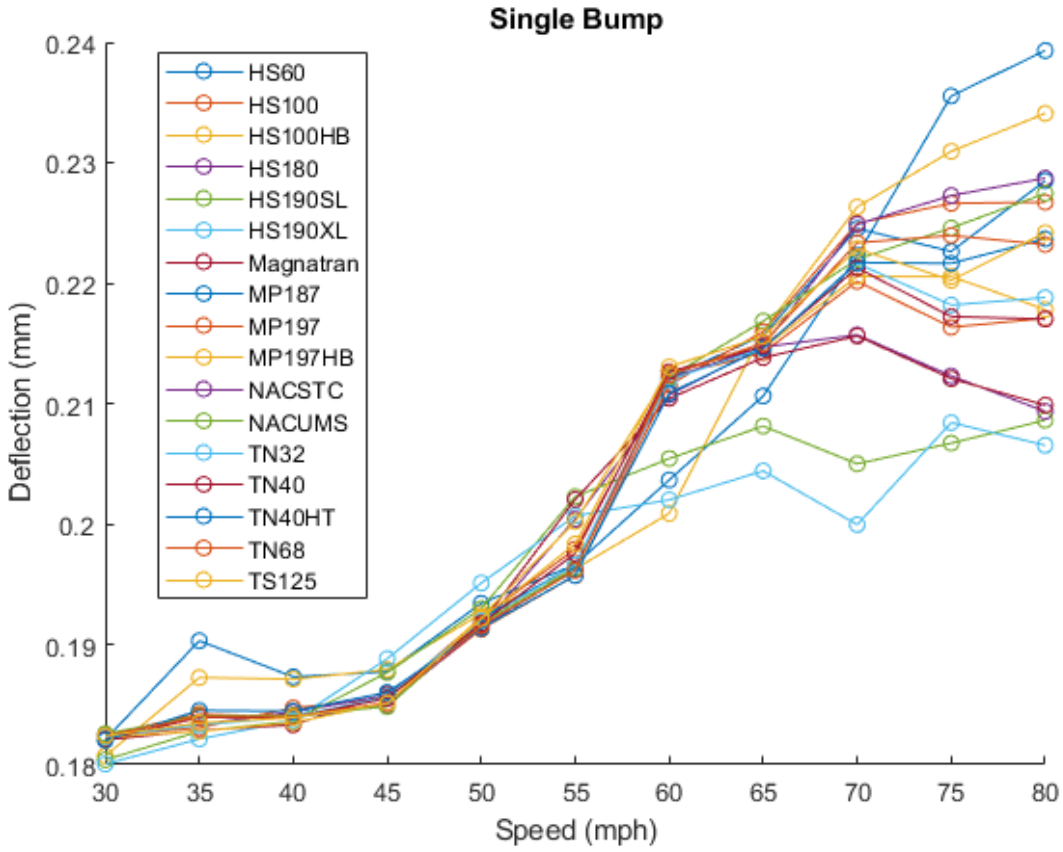

Figure A-6. Peak deflection, low-stiffness model on the single bump section.

A-1.3 Twist and Roll

Figure A-7, Figure A-8, and Figure A-9 show the detailed results for the low-stiffness fuel rod model on the twist and roll section, showing peak strain, strain energy, and deflection, respectively. The vertical cask motion was applied in these cases. Two apparent resonance speeds are present, between around 30−35 mph and 65−75 mph. Again, the effect of cask mass on fuel rod response is evident in that the lighter casks tend to have a stronger response, with peaks forming at higher train speeds.

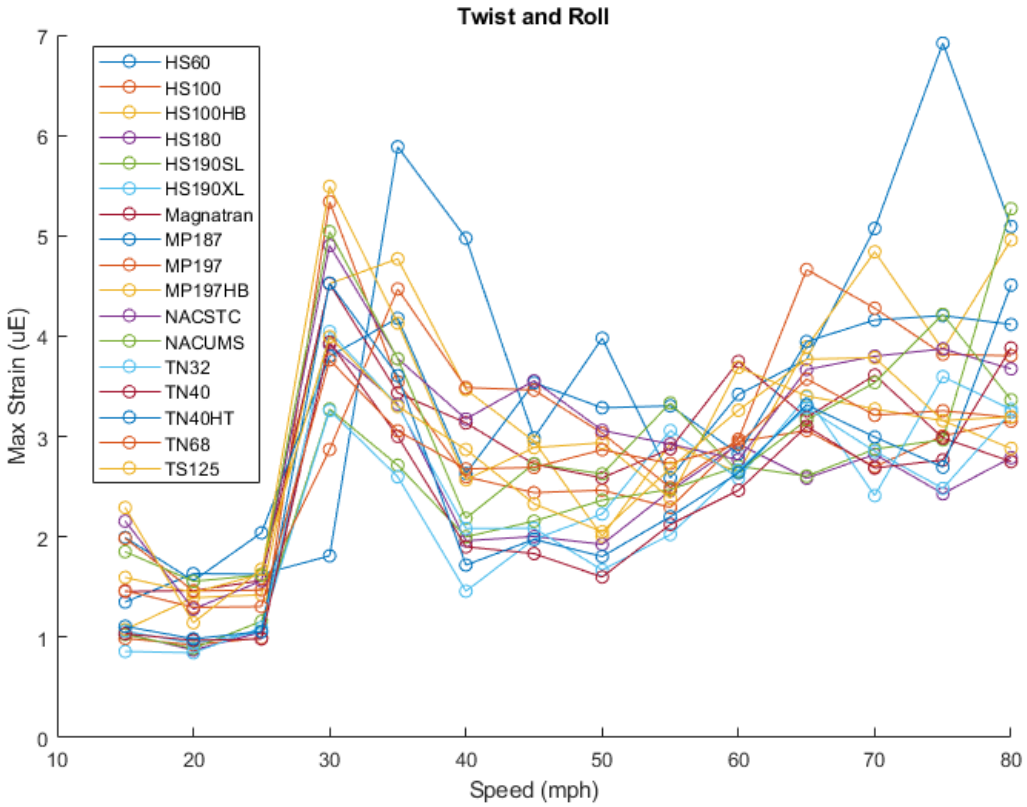

Figure A-7. Peak strain, low-stiffness model on the twist and roll section, vertical loading.

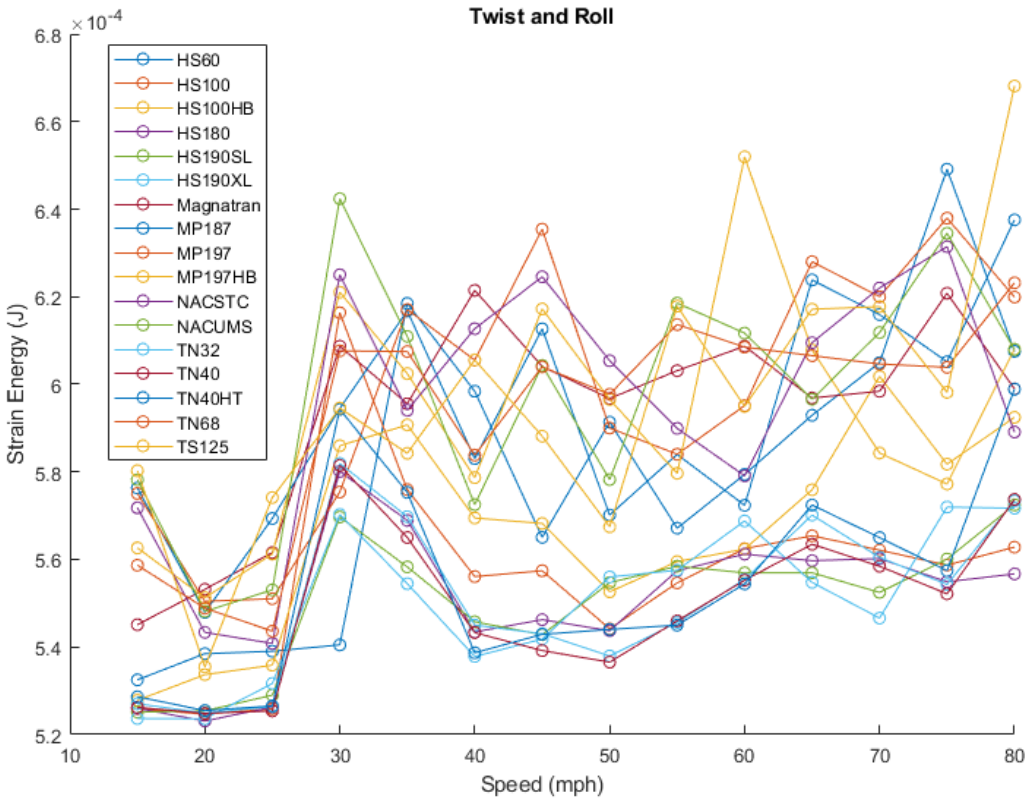

Figure A-8. Peak strain energy, low-stiffness model on the twist and roll section, vertical loading.

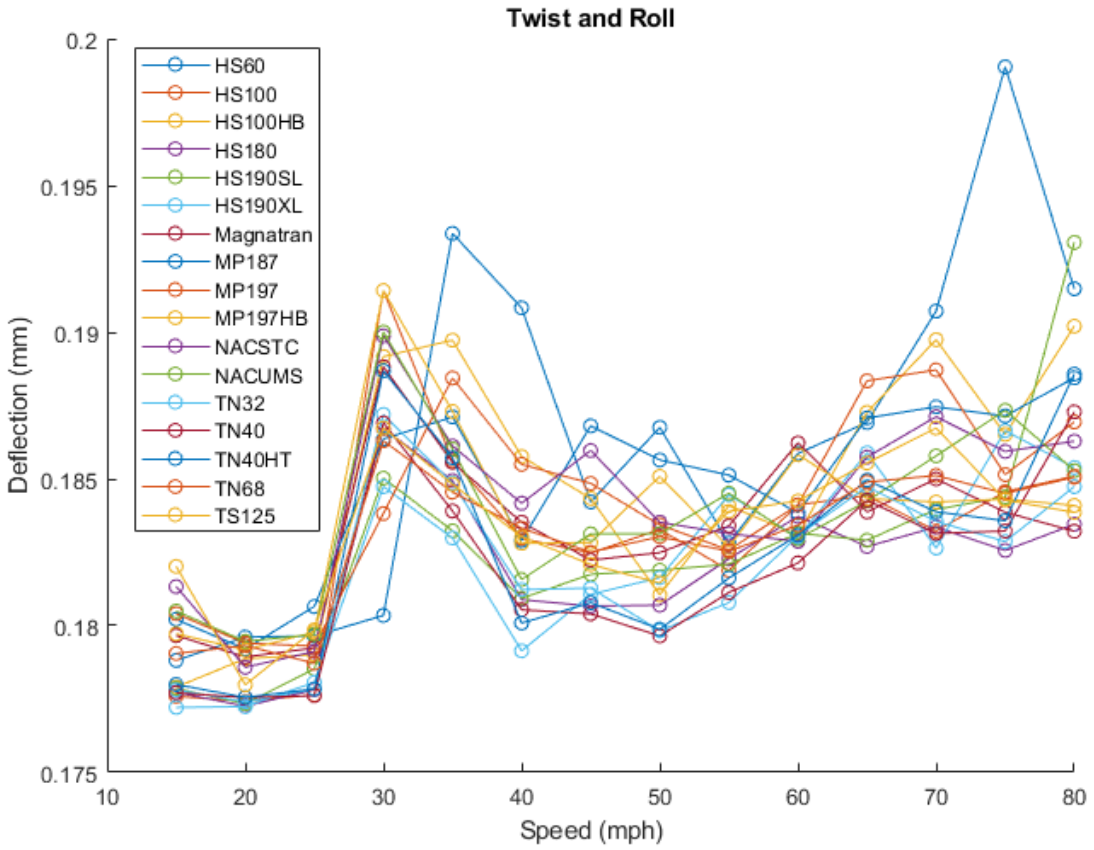

Figure A-9. Peak deflection, low-stiffness model on the twist and roll section, vertical loading.

Figure A-10, Figure A-11, and Figure A-12 show the detailed results for the low-stiffness fuel rod model on the twist and roll section, showing peak strain, strain energy, and deflection, respectively. The lateral cask motion was applied in these cases. The lateral response is smaller than the vertical response, but on the same order of magnitude. Unlike the vertical case, resonance speeds are not clearly visible, aside from an obvious increase in response at around 25−30 mph.

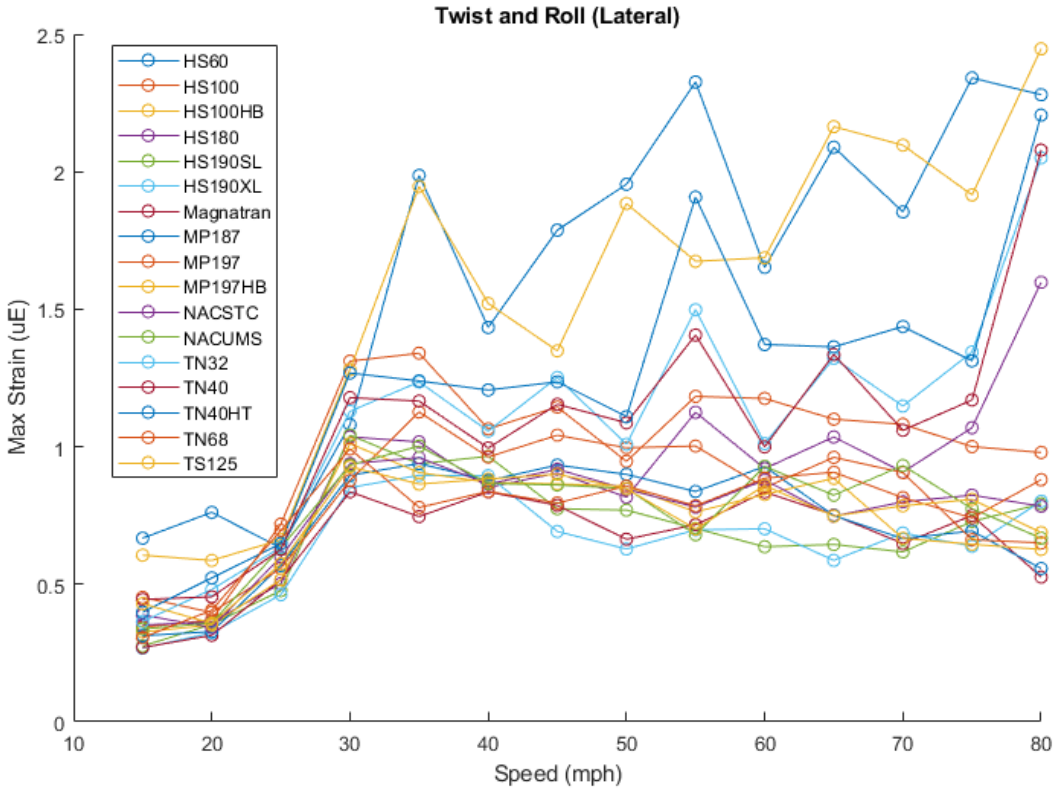

Figure A-10. Peak strain, low-stiffness model on the twist and roll section, lateral loading.

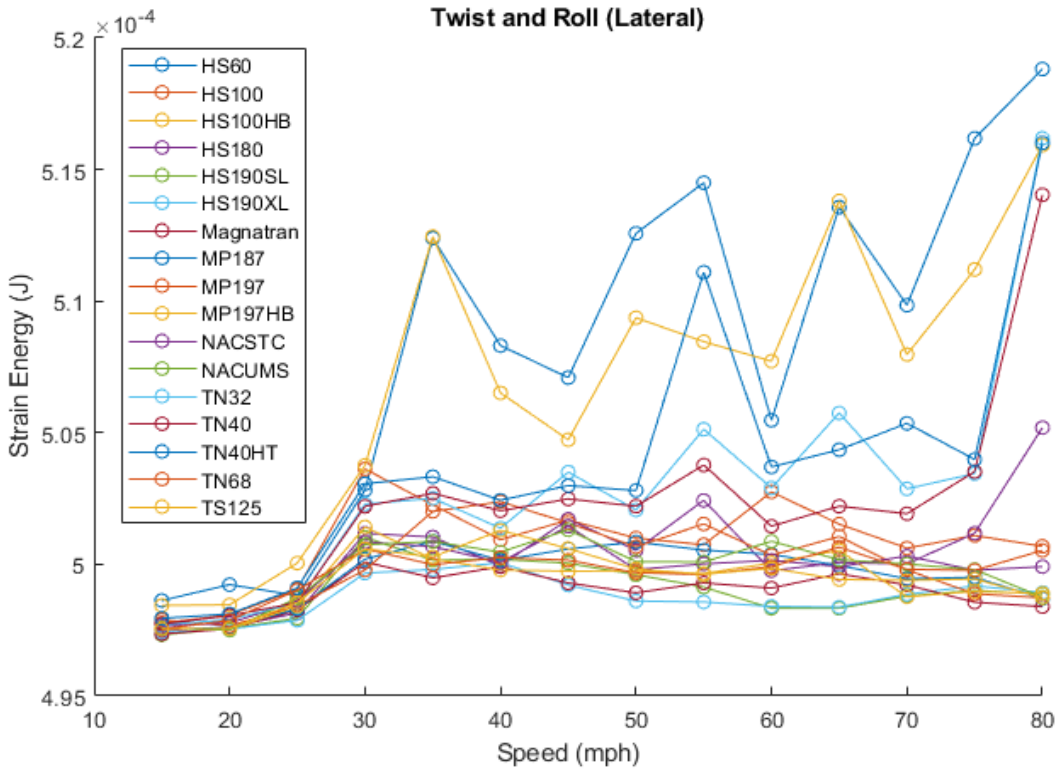

Figure A-11. Peak strain energy, low-stiffness model on the twist and roll section, lateral loading.

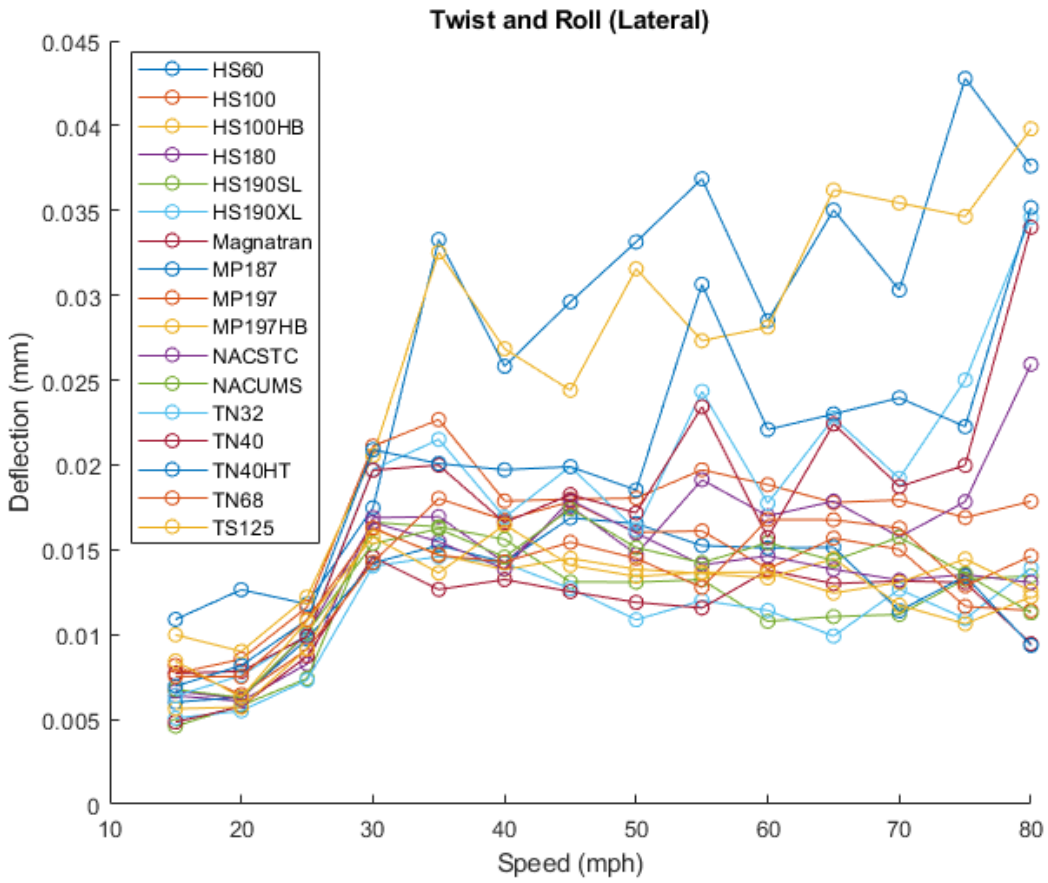

Figure A-12. Peak deflection, low-stiffness model on the twist and roll section, lateral loading.

A-2. High-Stiffness Tests

A-2.1 Pitch and Bounce

Figure A-13, Figure A-14, and Figure A-15 show the detailed results for the high-stiffness fuel rod model on the pitch and bounce section, showing peak strain, strain energy, and deflection, respectively. The results show a trend similar to that of the low-stiffness model, with an obvious resonance speed occurring at intermediate train speeds and apparent dependence on cask mass. The response was smaller than the low-stiffness model, which is a trend observed in all three test sections.

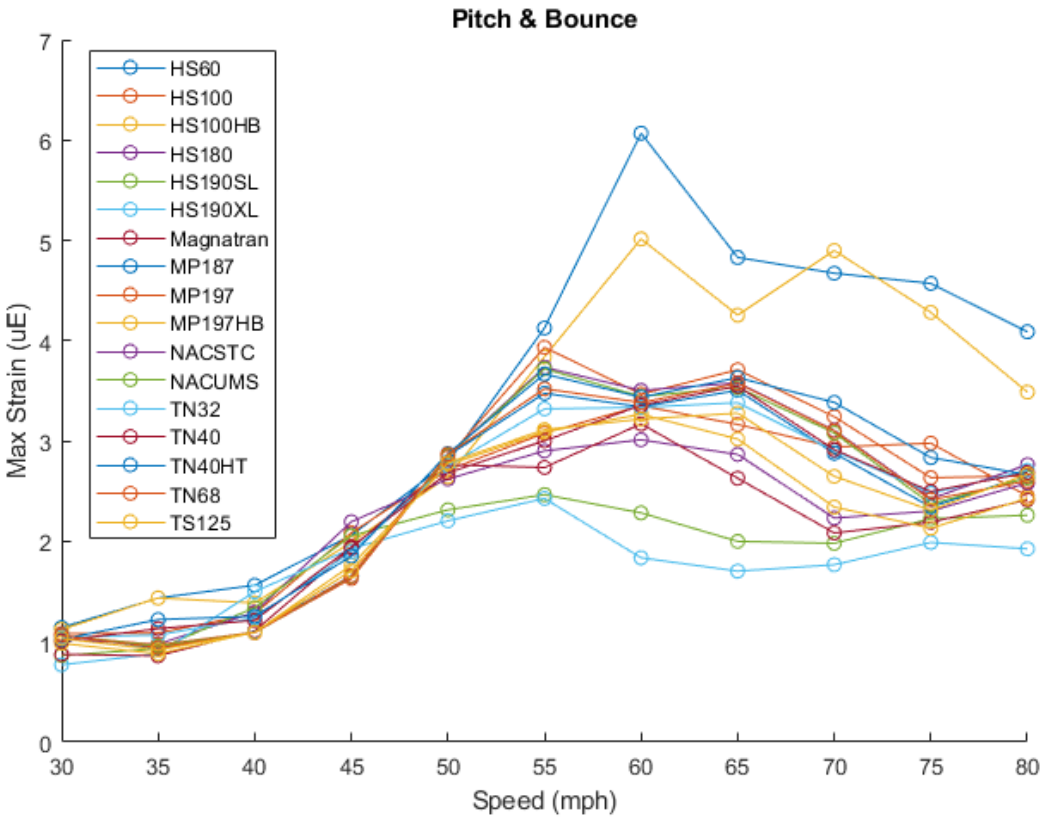

Figure A-13. Peak strain, high-stiffness model on the pitch and bounce section.

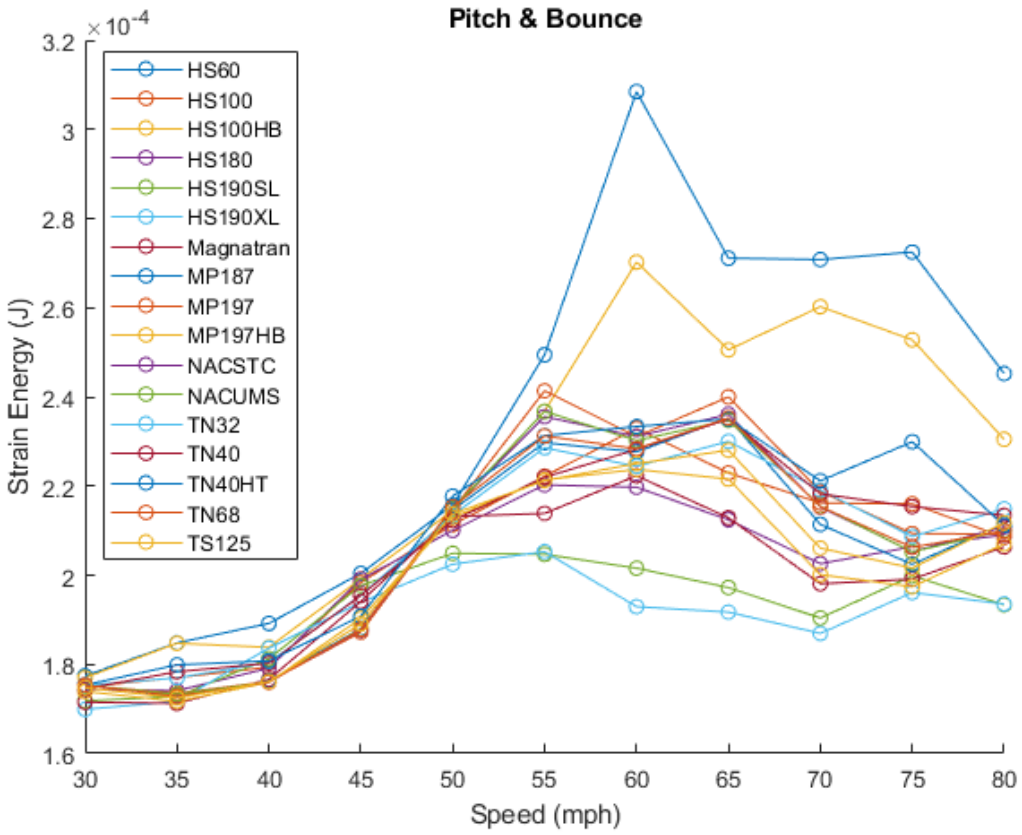

Figure A-14. Peak strain energy, high-stiffness model on the pitch and bounce section.

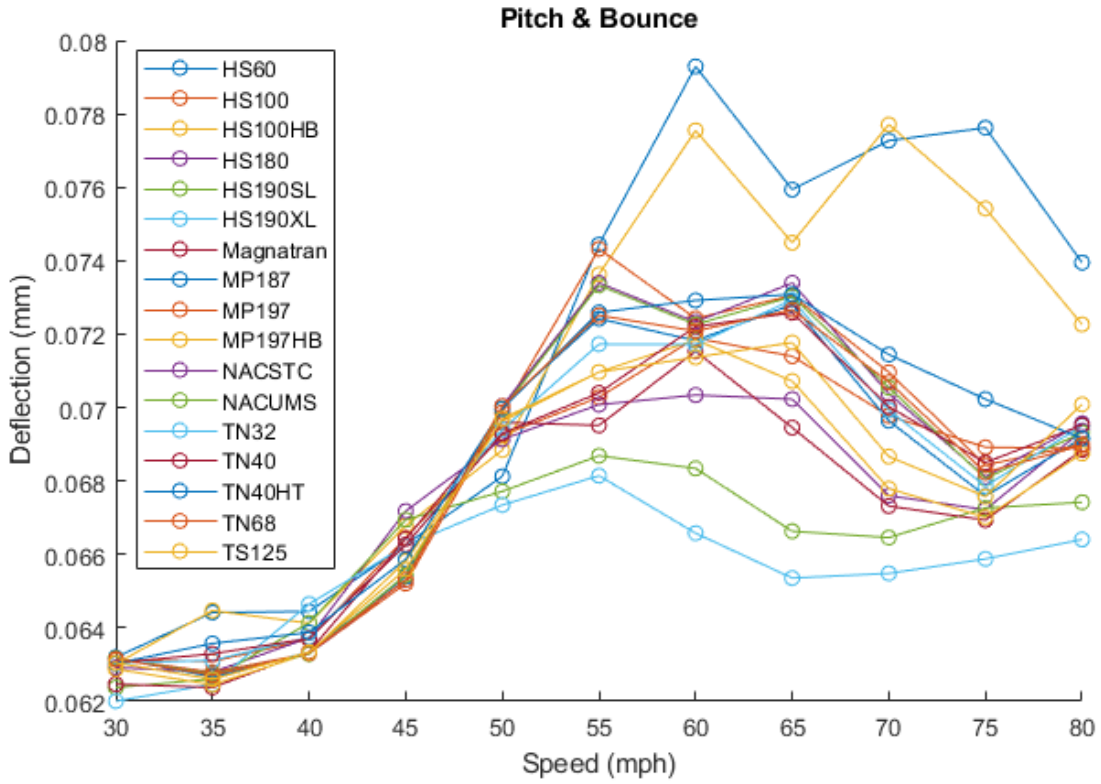

Figure A-15. Peak deflection, high-stiffness model on the pitch and bounce section.

A-2.2 Single Bump

Figure A-16, Figure A-17, and Figure A-18 show the detailed results for the high-stiffness fuel rod model on the single bump section, showing peak strain, strain energy, and deflection, respectively. The results show a trend similar to the low-stiffness model, with more or less monotonically increasing response with speed. Some small peaks occur at lower train speeds, unlike the low-stiffness model, but the strains are small enough to be negligible.

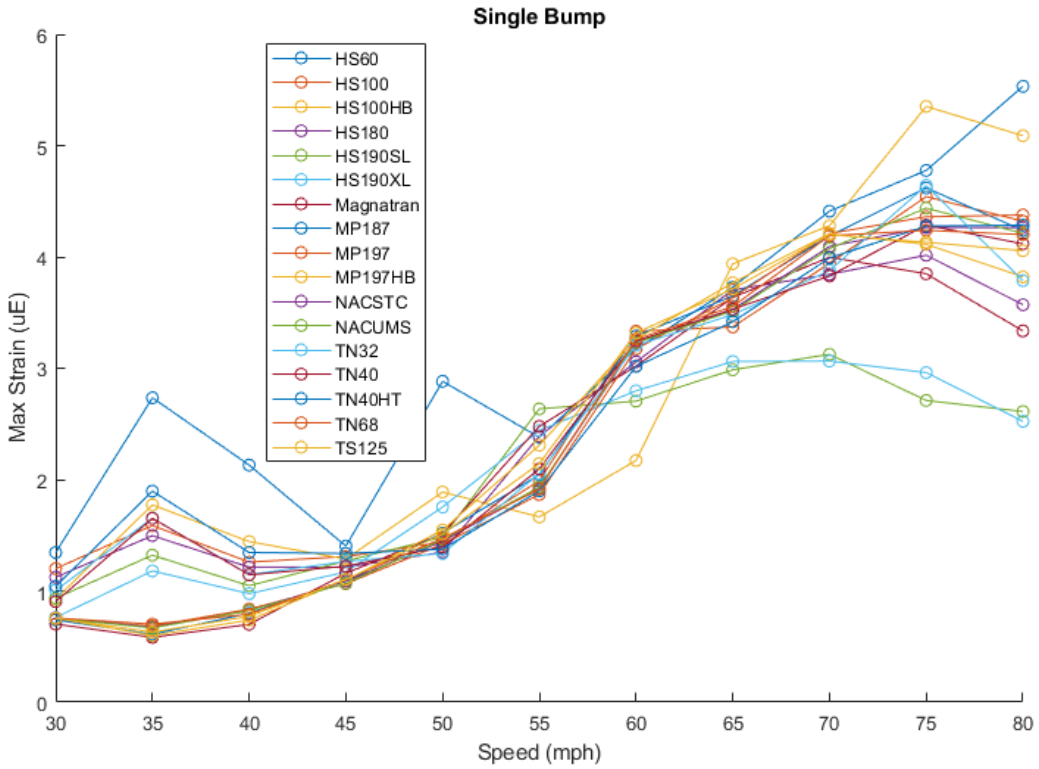

Figure A-16. Peak strain, high-stiffness model, single bump section.

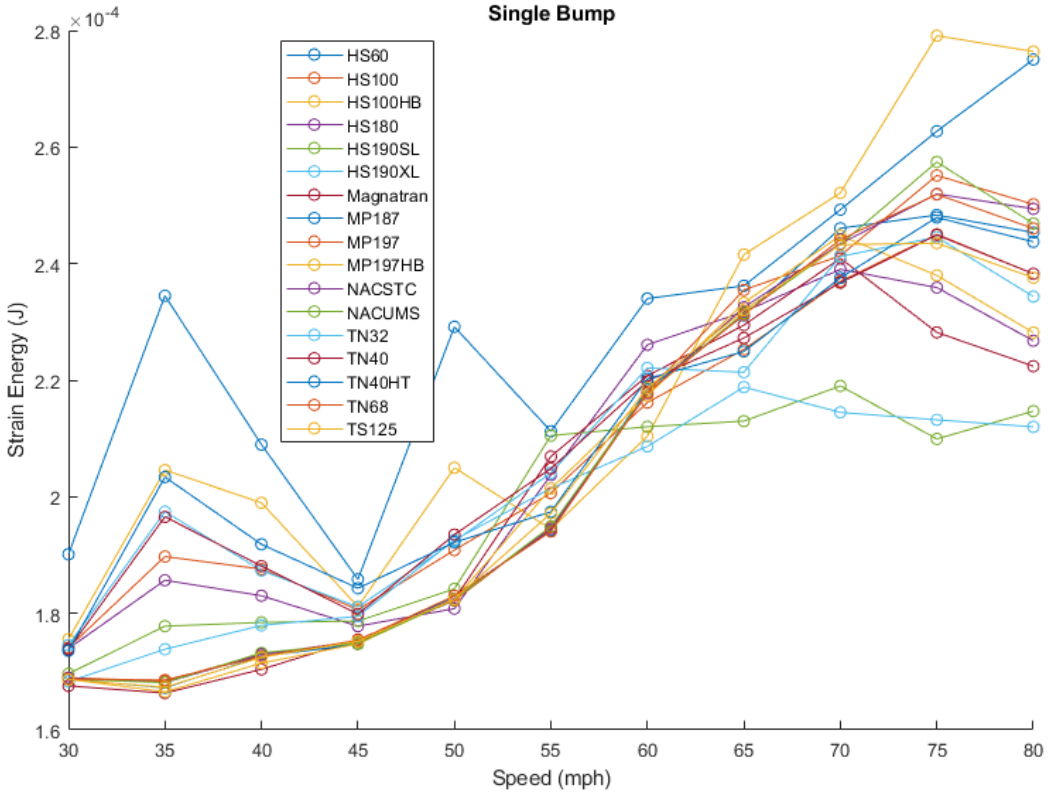

Figure A-17. Peak strain energy, high-stiffness model, single bump section.

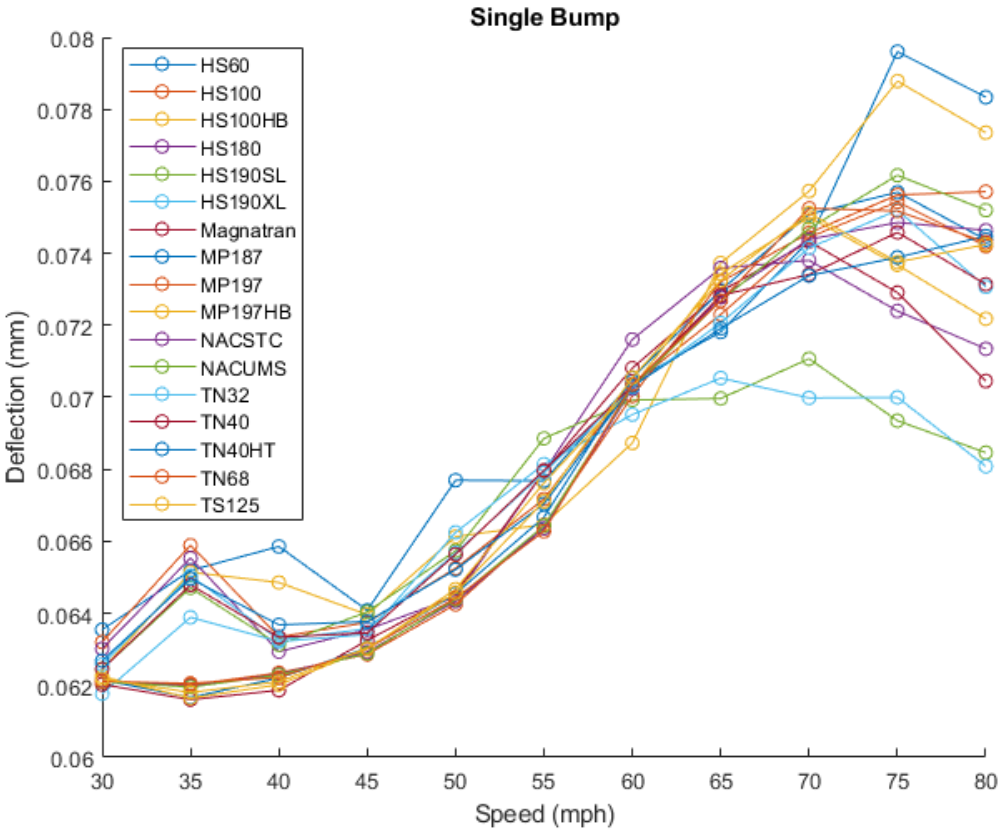

Figure A-18. Peak deflection, high-stiffness model, single bump section.

A-2.3 Twist and Roll

Figure A-19, Figure A-20, and Figure A-21 show the detailed results for the high-stiffness fuel rod model on the twist and roll section, showing peak strain, strain energy, and deflection, respectively. The vertical cask motion was applied in these cases. Similar to the low-stiffness model, two resonance speeds are observed in the response.

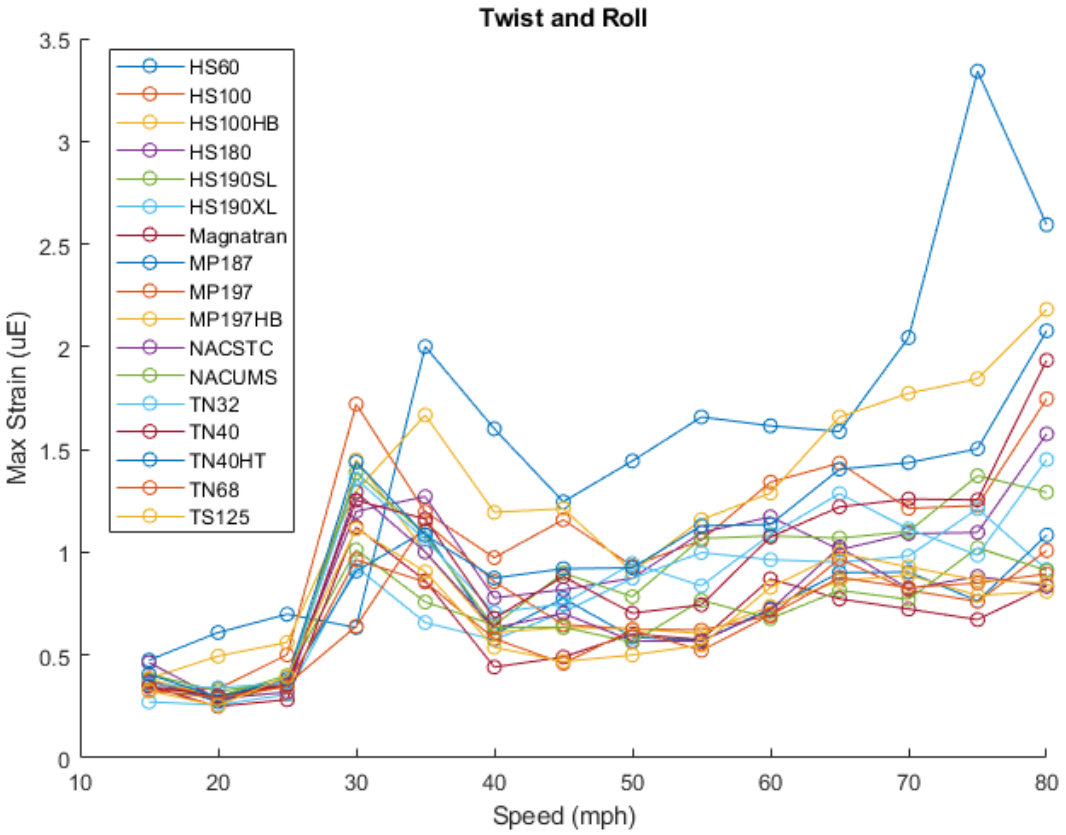

Figure A-19. Peak strain, high-stiffness model, twist and roll section, vertical loading.

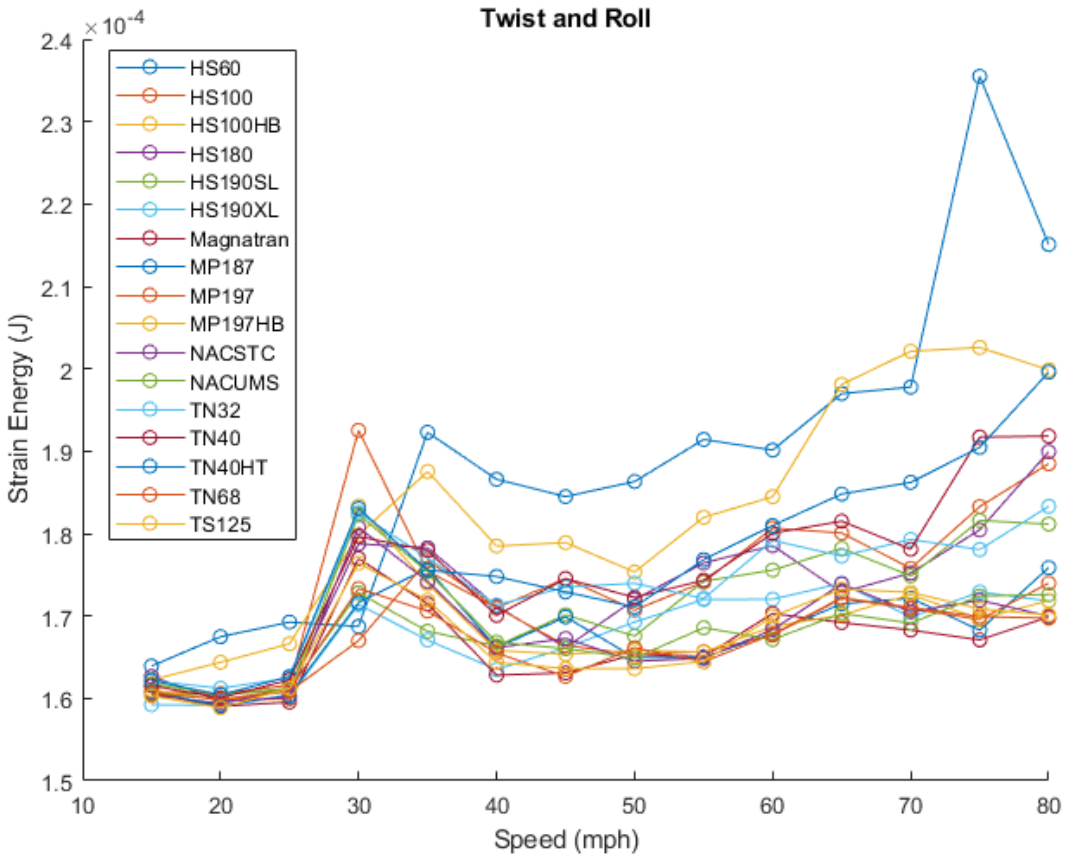

Figure A-20. Peak strain energy, high-stiffness model, twist and roll section, vertical loading.

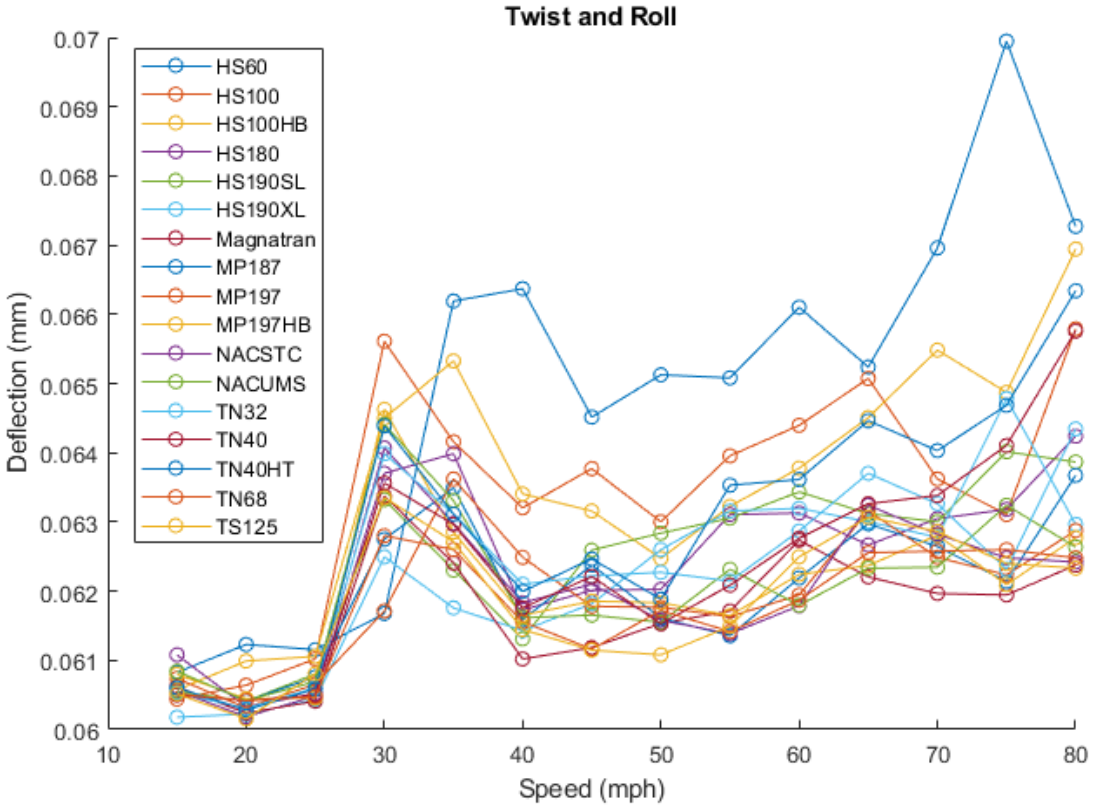

Figure A-21. Peak deflection, high-stiffness model, twist and roll section, vertical loading.

Figure A-22, Figure A-23, and Figure A-24Figure A-23 show the detailed results for the high-stiffness fuel rod model on the twist and roll section, showing peak strain, strain energy, and deflection, respectively. The lateral cask motion was applied in these cases. Again, the trend in fuel rod response with speed is similar to that of the low-stiffness model. The strains observed are even smaller; the largest does not even exceed 1 uE.

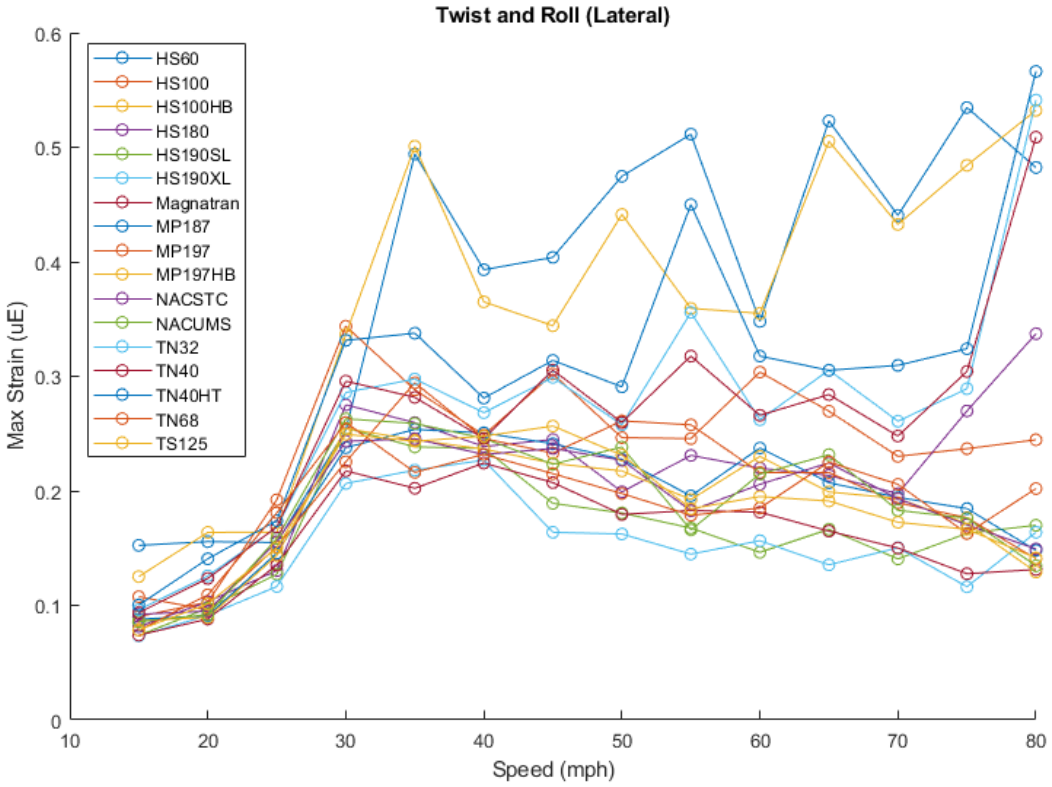

Figure A-22. Peak strain, high-stiffness model, twist and roll section, lateral loading.

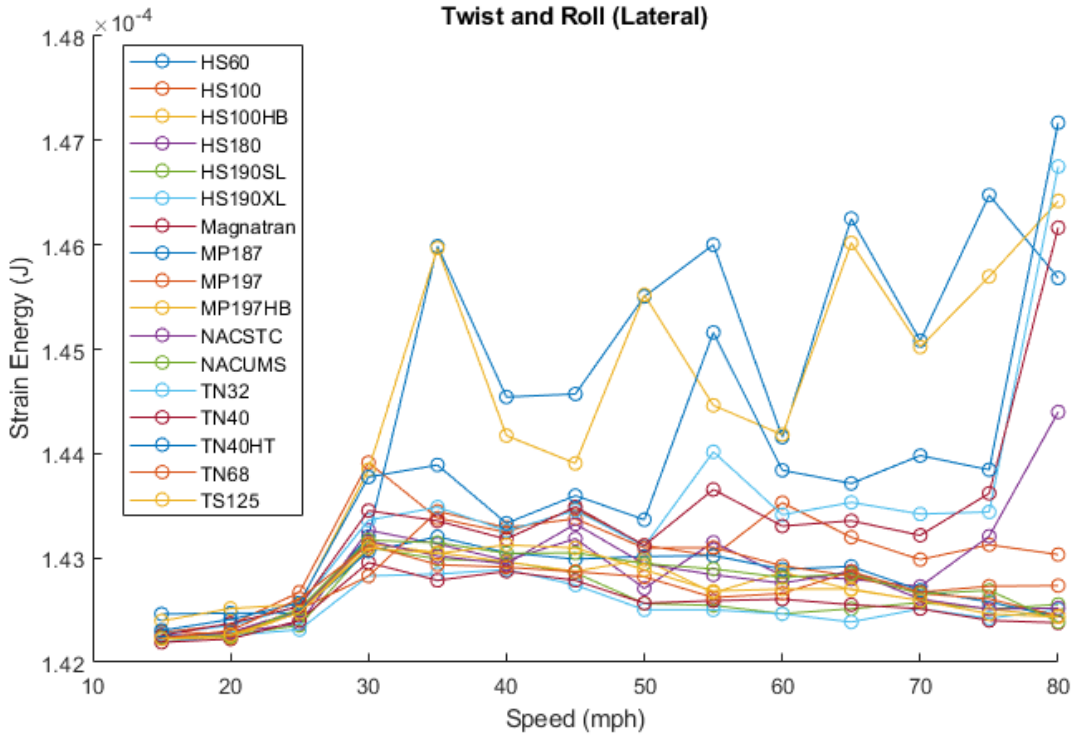

Figure A-23. Peak strain energy, high-stiffness model, twist and roll section, lateral loading.

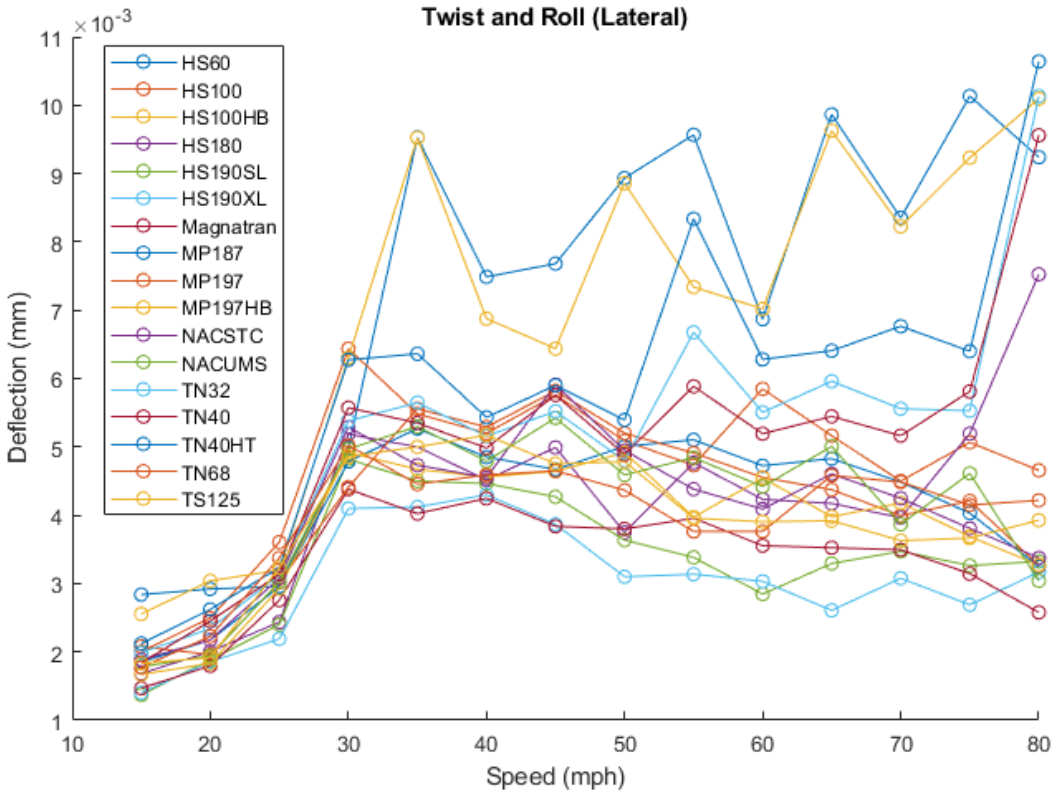

Figure A-24. Peak deflection, high-stiffness model, twist and roll section, lateral loading.

This page is intentionally left blank.

Appendix B

Single-Rod Model Fatigue Analysis Results

This appendix contains the detailed graphs related to fatigue analysis in Section 6.2.

B-1. Pitch and Bounce

B-1.1 Low Stiffness

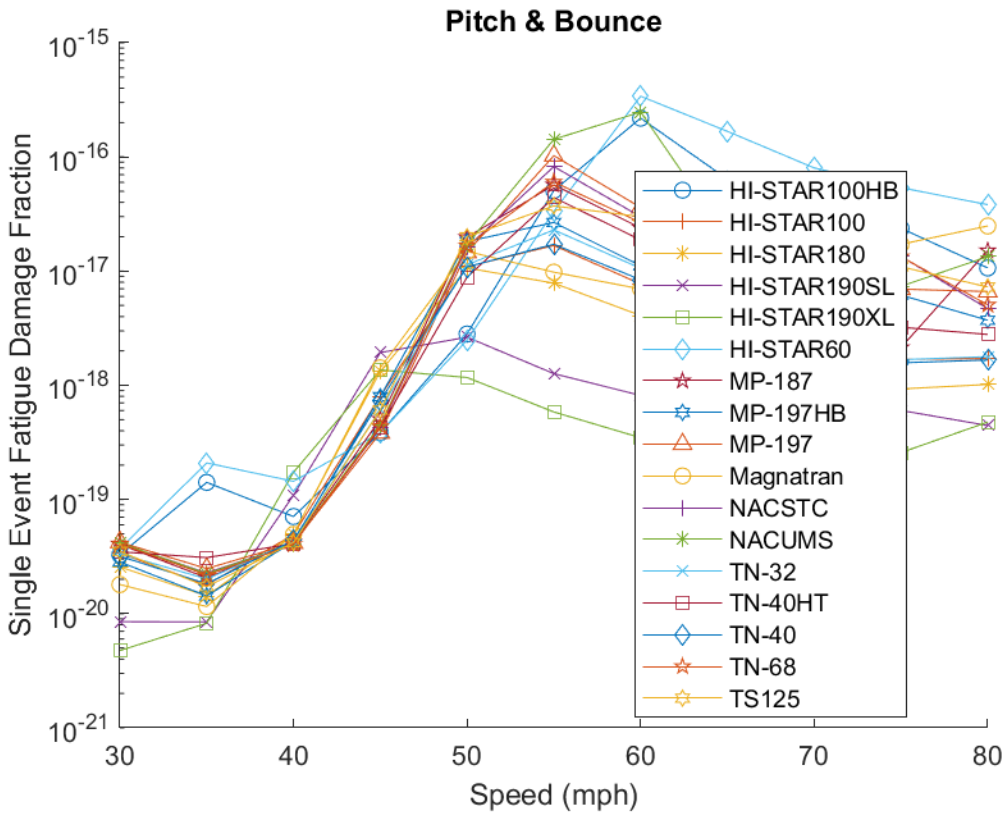

Figure B-1. Log-scale single event fatigue damage fraction for low stiffness.

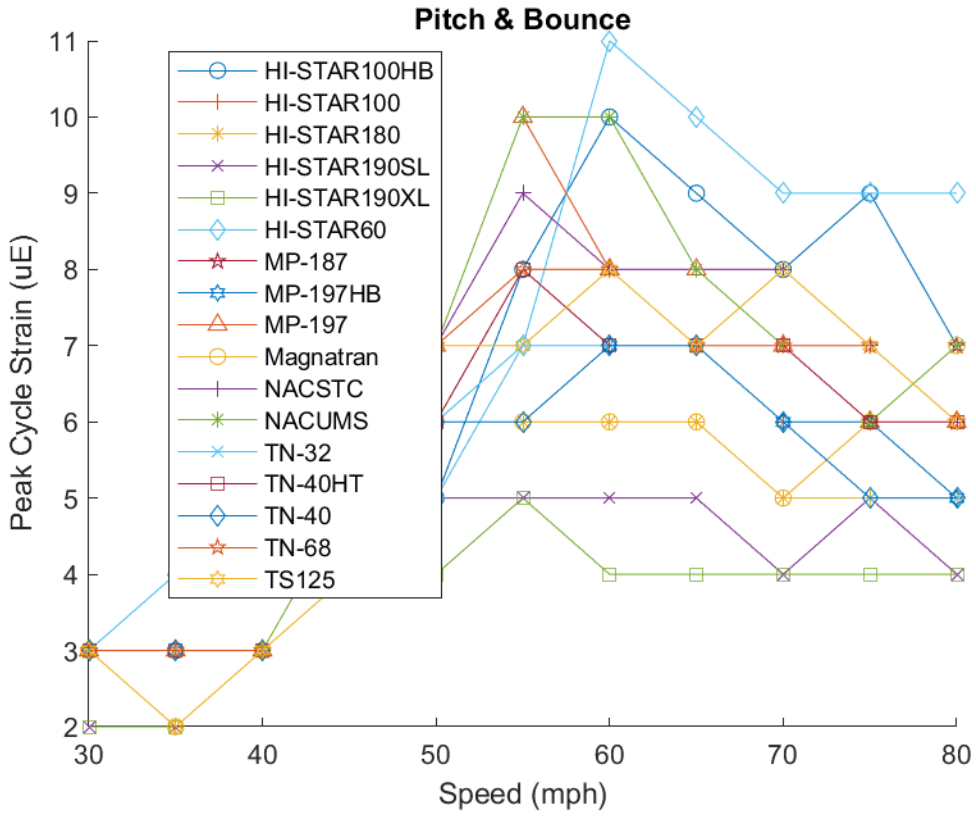

Figure B-2. Peak cycle strain for low stiffness.

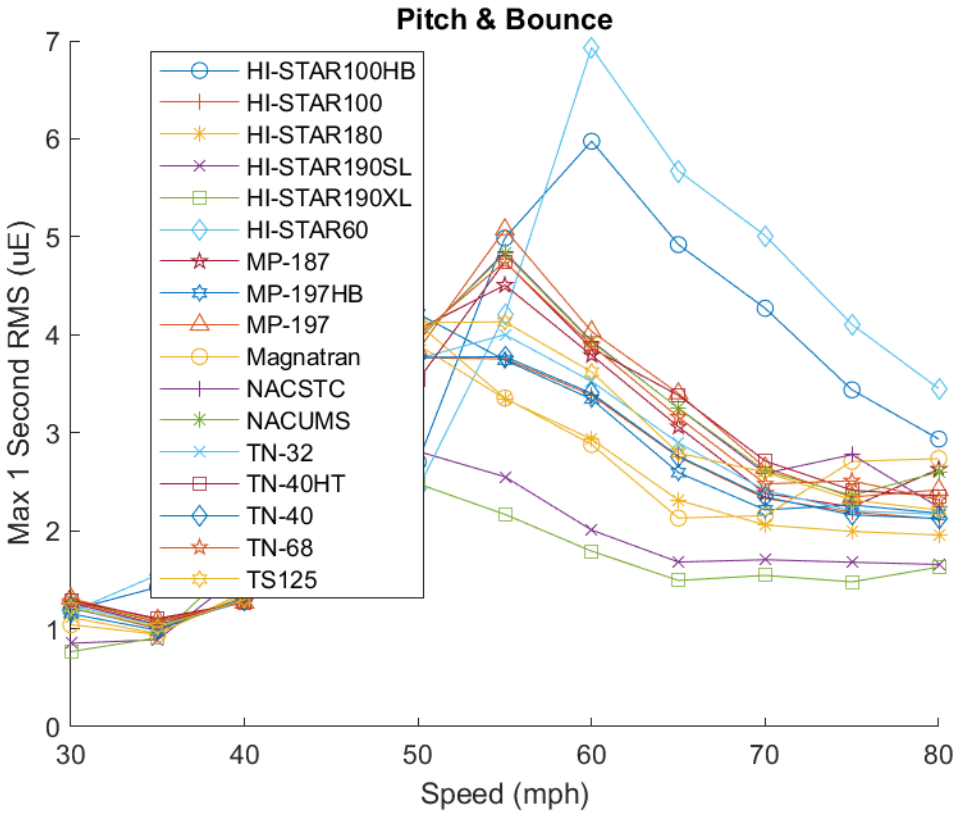

Figure B-3. Maximum one-second RMS value for low stiffness.

B-1.2 High Stiffness

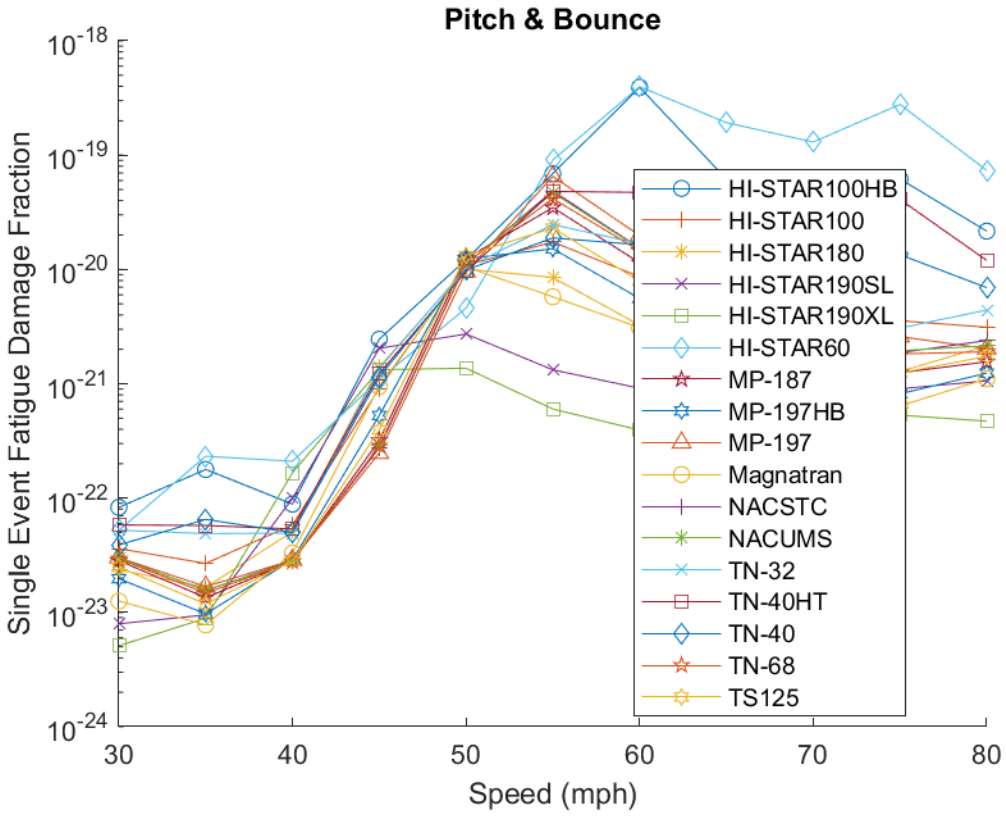

Figure B-4. Log-scale single event fatigue damage fraction for high stiffness.

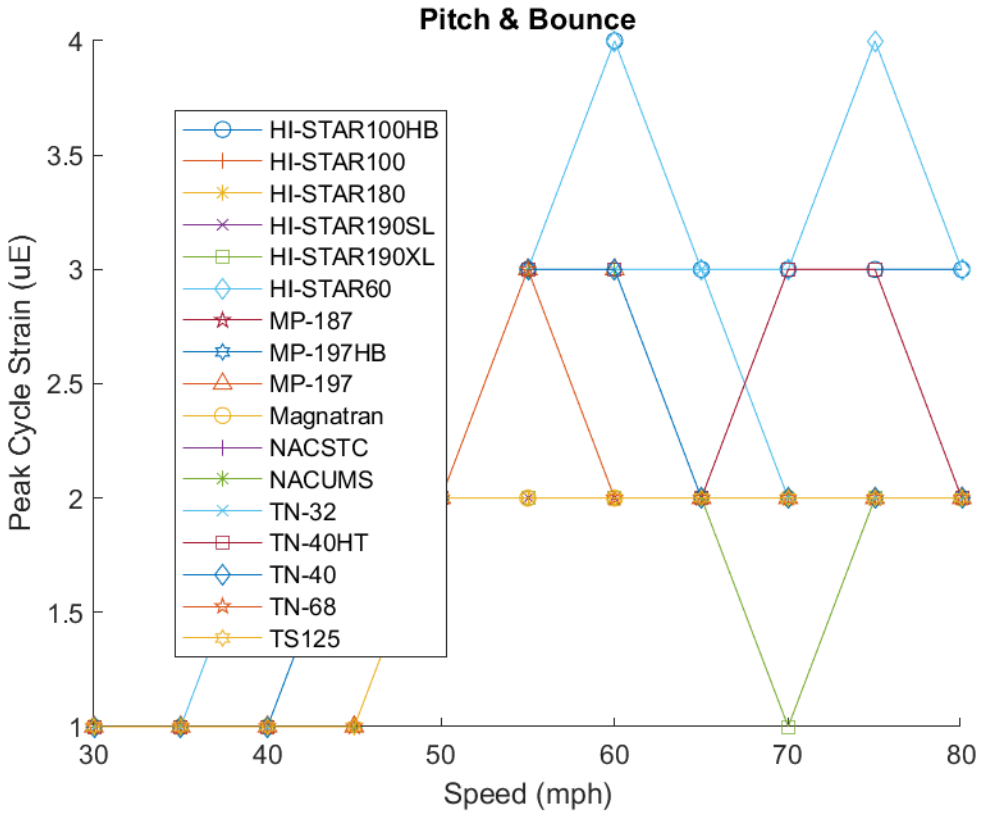

Figure B-5. Peak cycle strain for high stiffness.

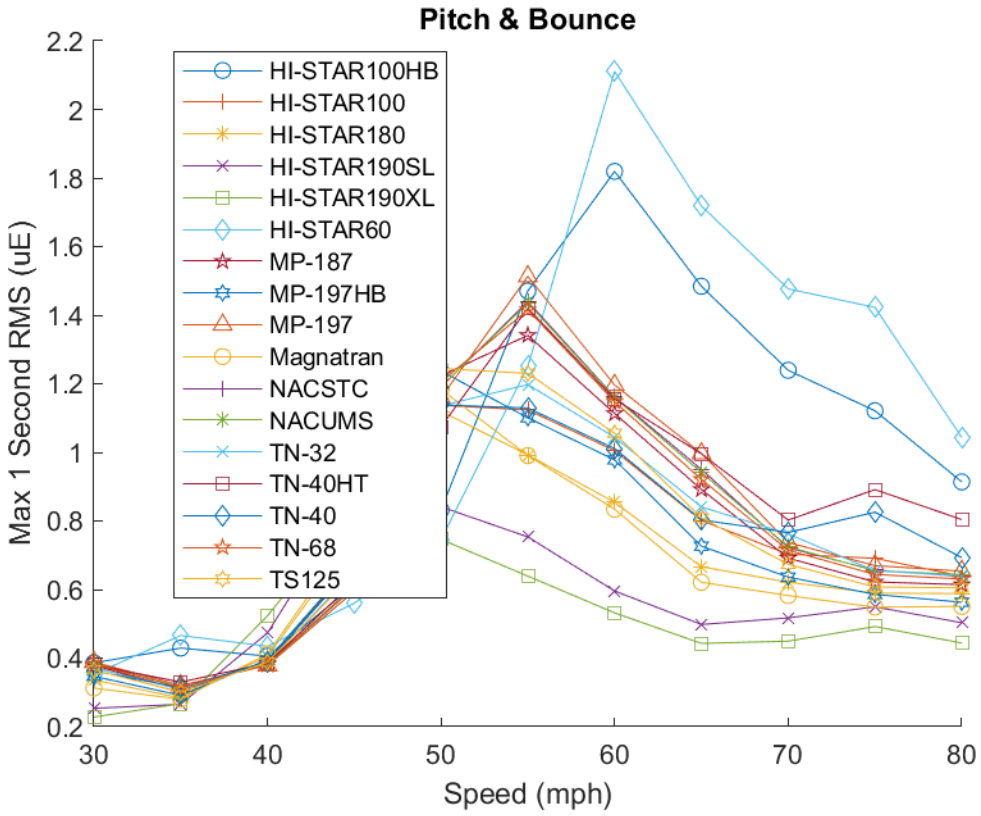

Figure B-6. Maximum one-second RMS value for high stiffness.

B-2. Single Bump

B-2.1 Low Stiffness

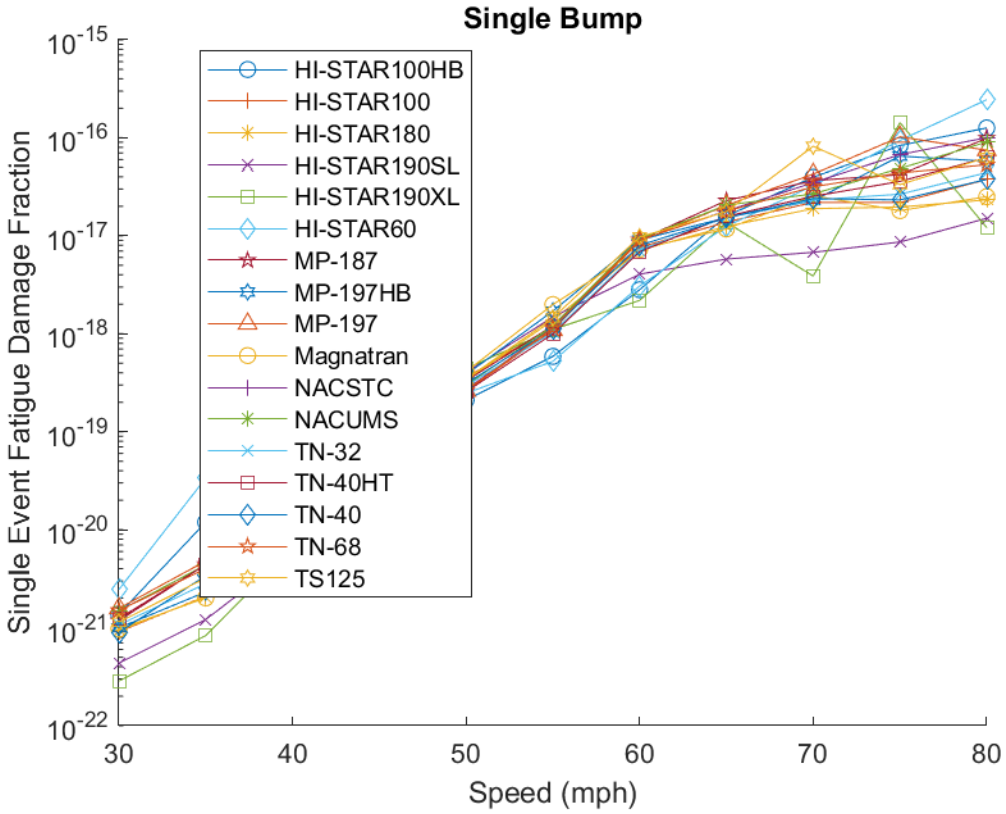

Figure B-7. Log-scale single event fatigue damage fraction for low stiffness.

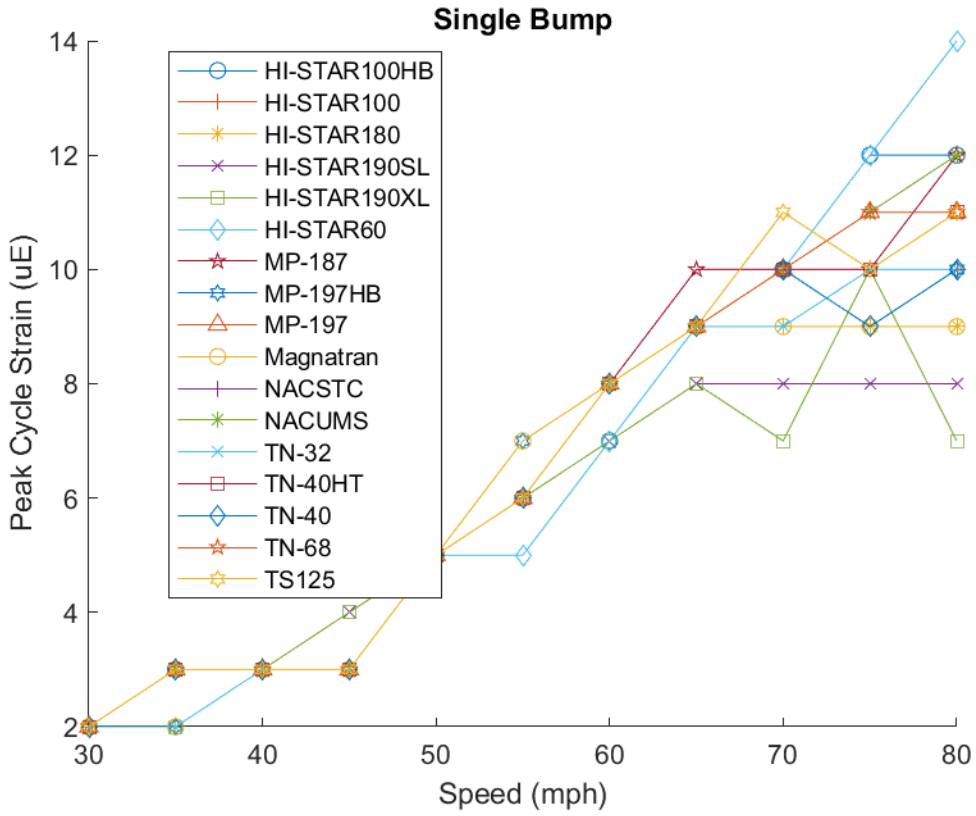

Figure B-8. Peak cycle strain for low stiffness.

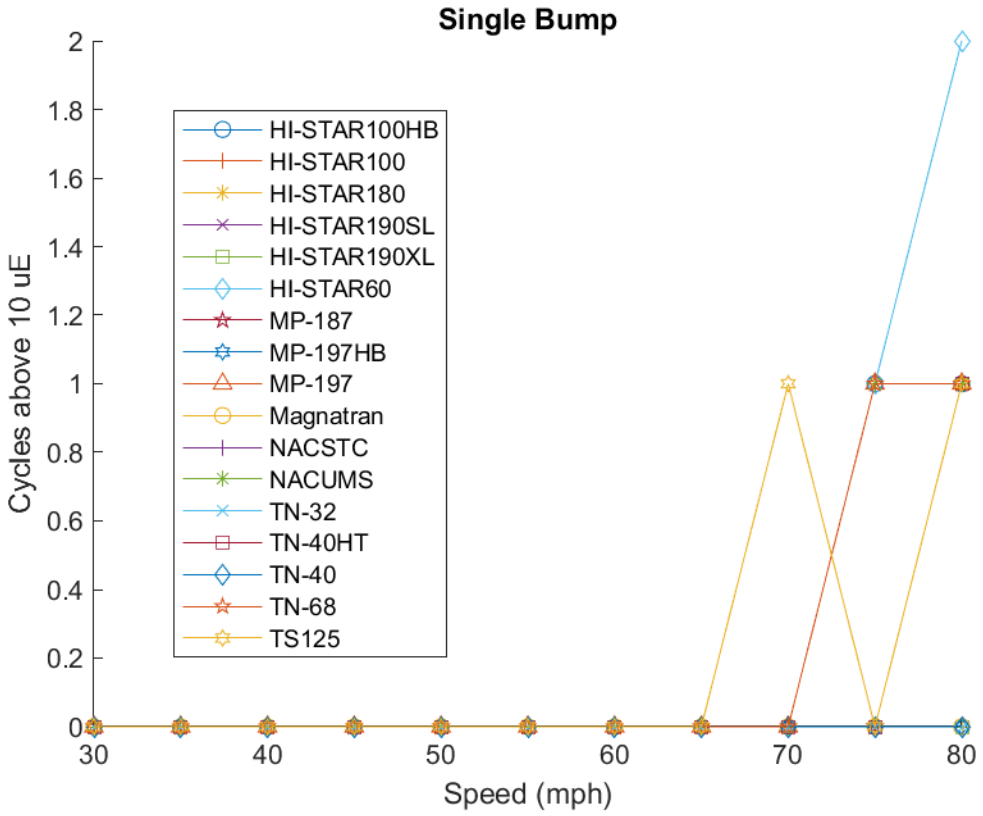

Figure B-9. Number of cycles over 10 uE for low stiffness.

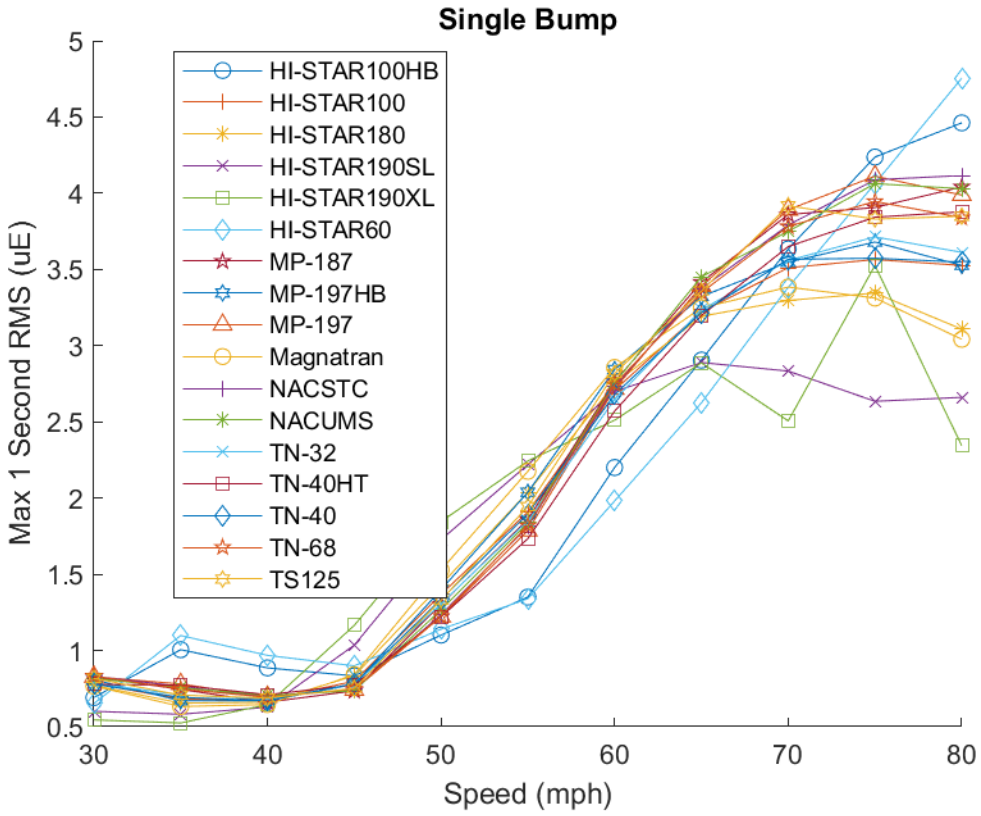

Figure B-10. Maximum one-second RMS value for low stiffness.

B-2.2 High Stiffness

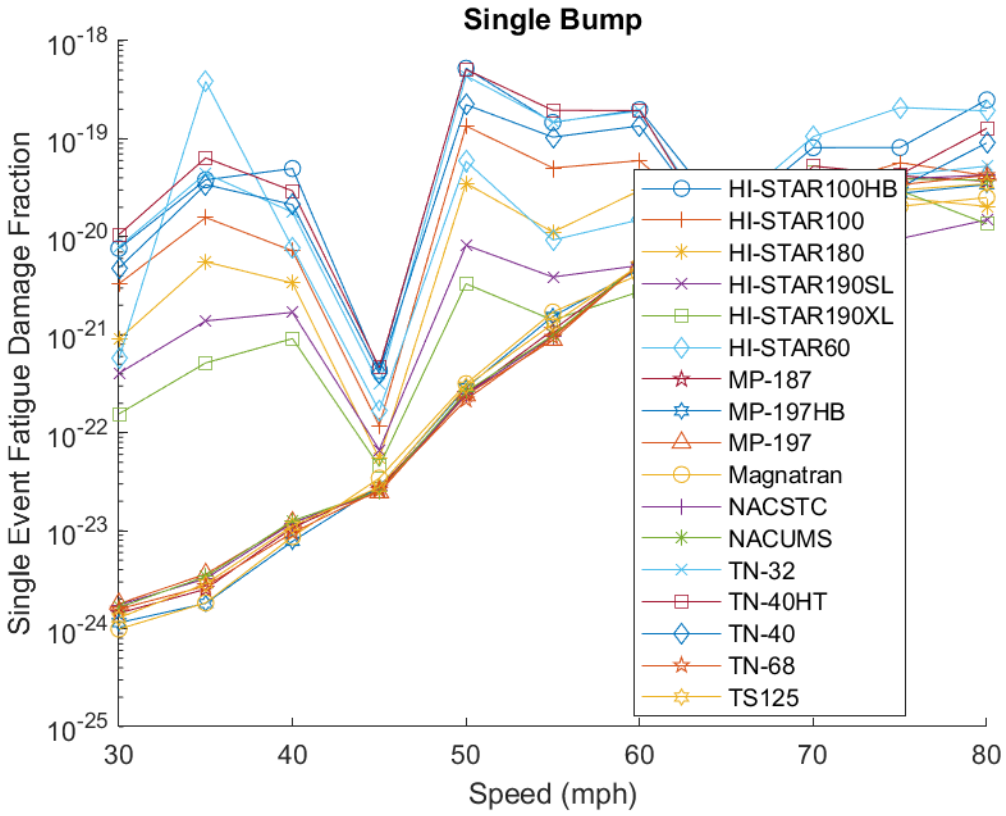

Figure B-11. Log-scale single event fatigue damage fraction for high stiffness.

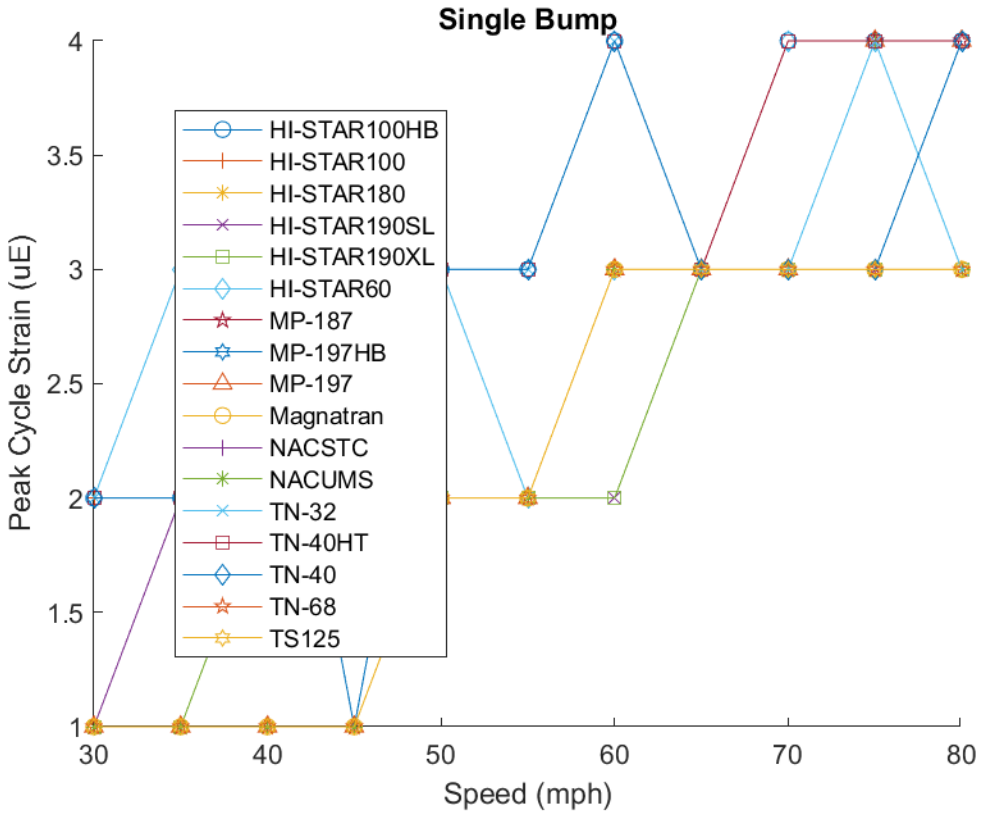

Figure B-12. Peak cycle strain for high stiffness.

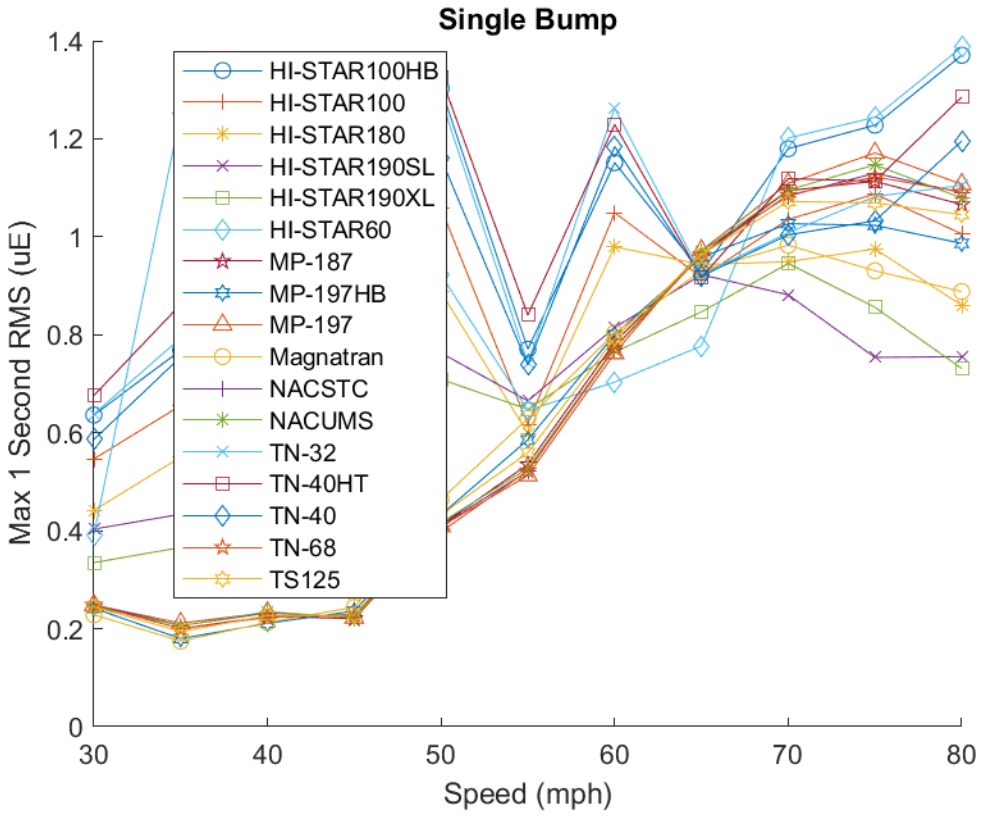

Figure B-13. Maximum one-second RMS value for high stiffness.

B-3. Twist and Roll

B-3.1 Low Stiffness

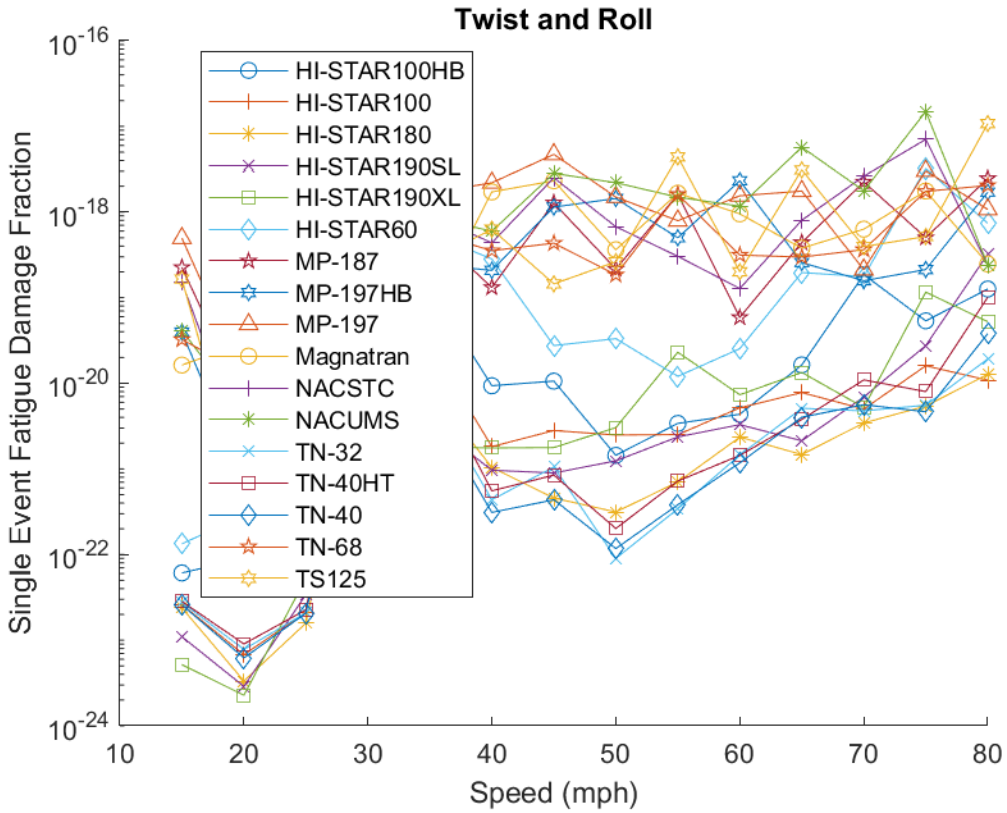

Figure B-14. Log-scale single event fatigue damage fraction for low stiffness.

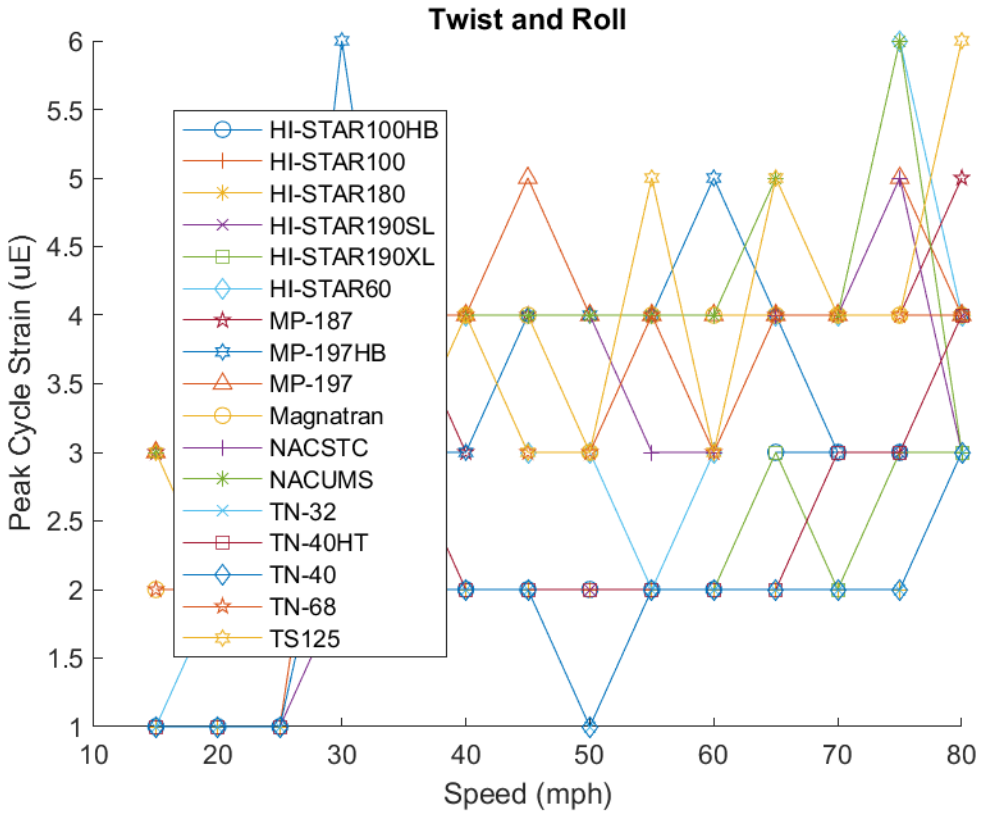

Figure B-15. Peak cycle strain for low stiffness.

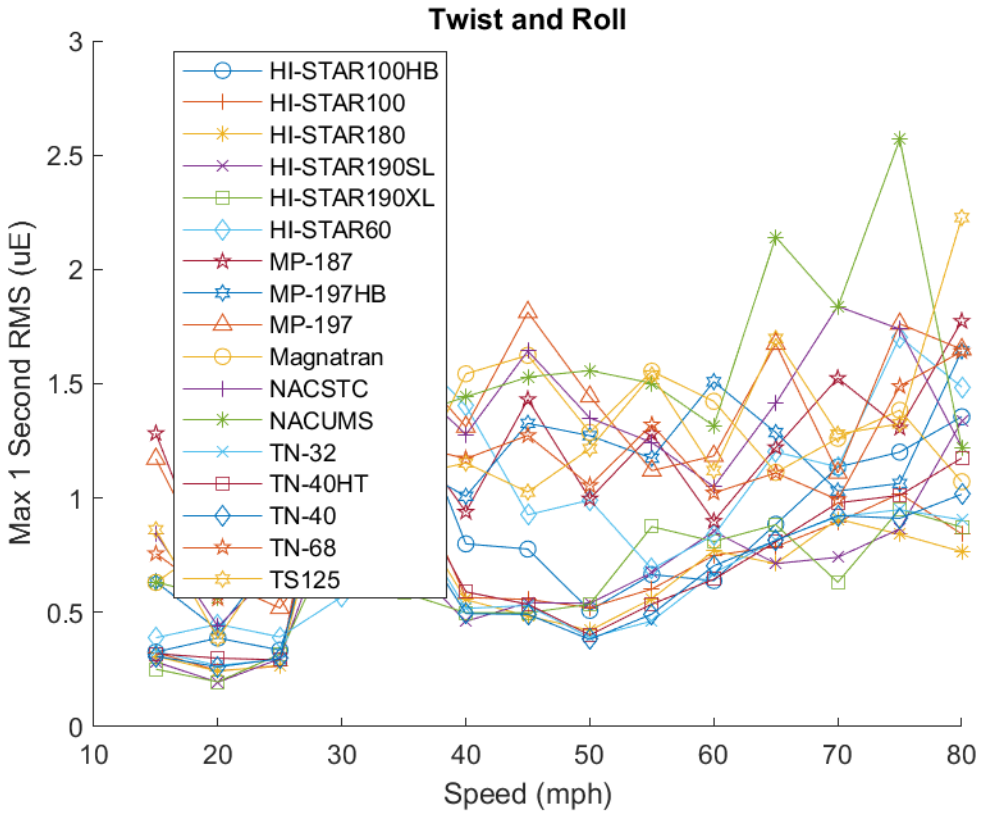

Figure B-16. Maximum one-second RMS value for low stiffness.

B-3.2 High Stiffness

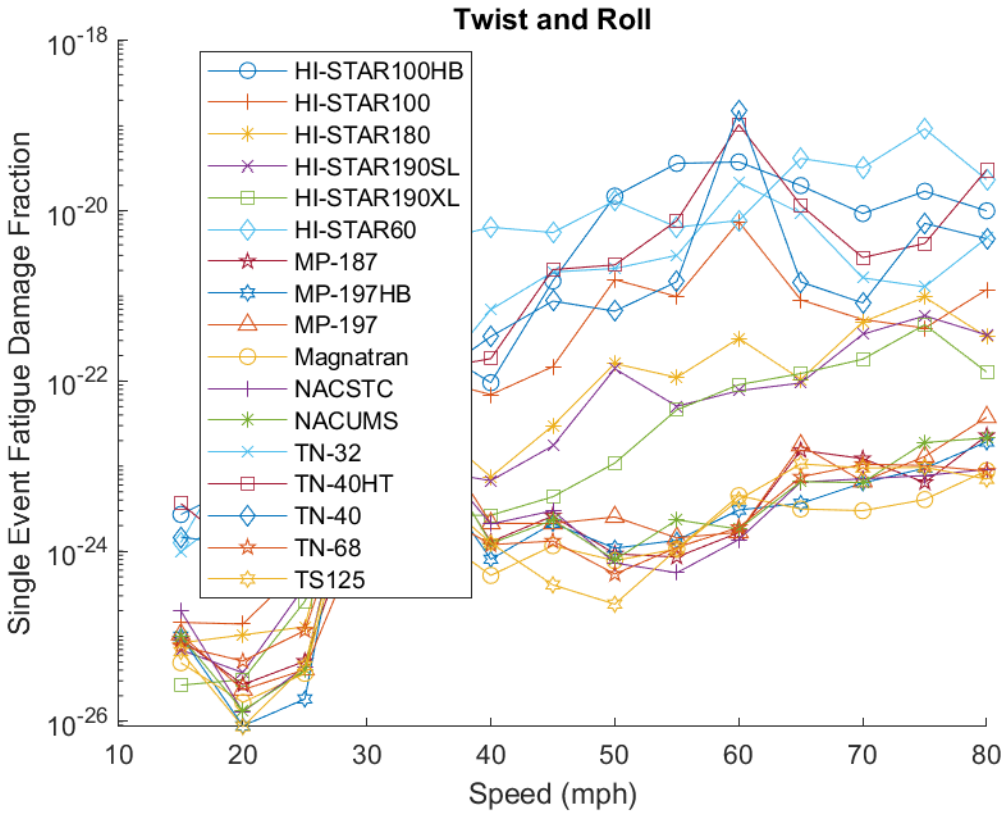

Figure B-17. Log-scale single event fatigue damage fraction for high stiffness.

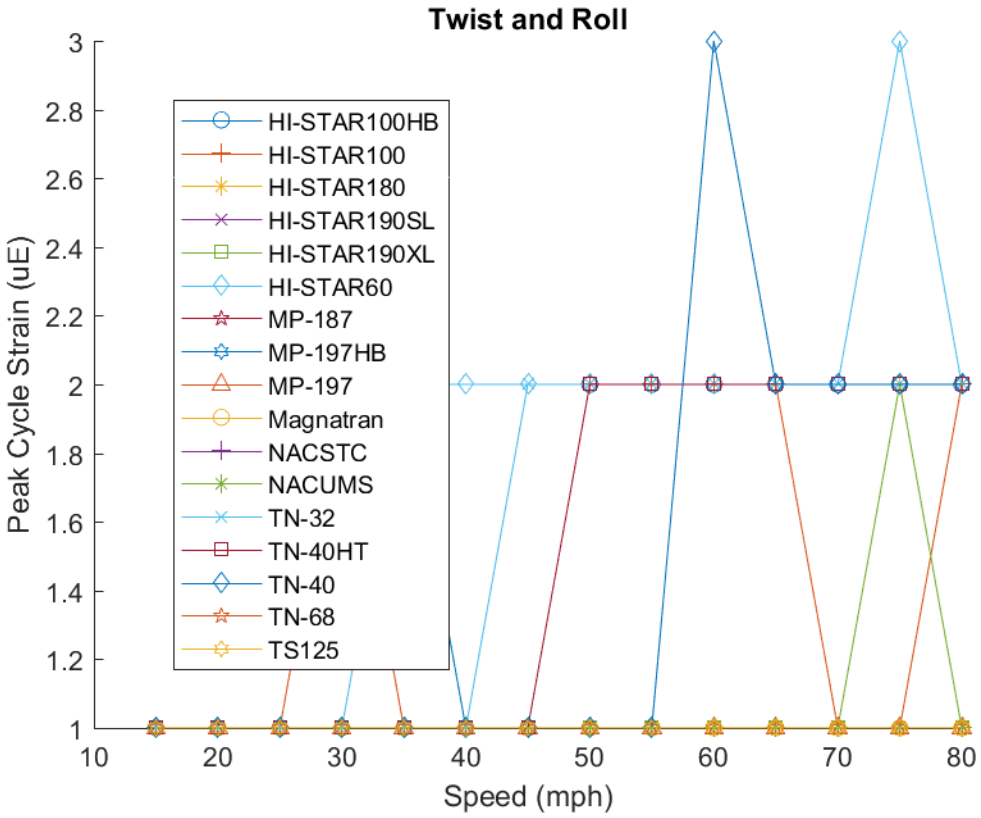

Figure B-18. Peak cycle strain for high stiffness.

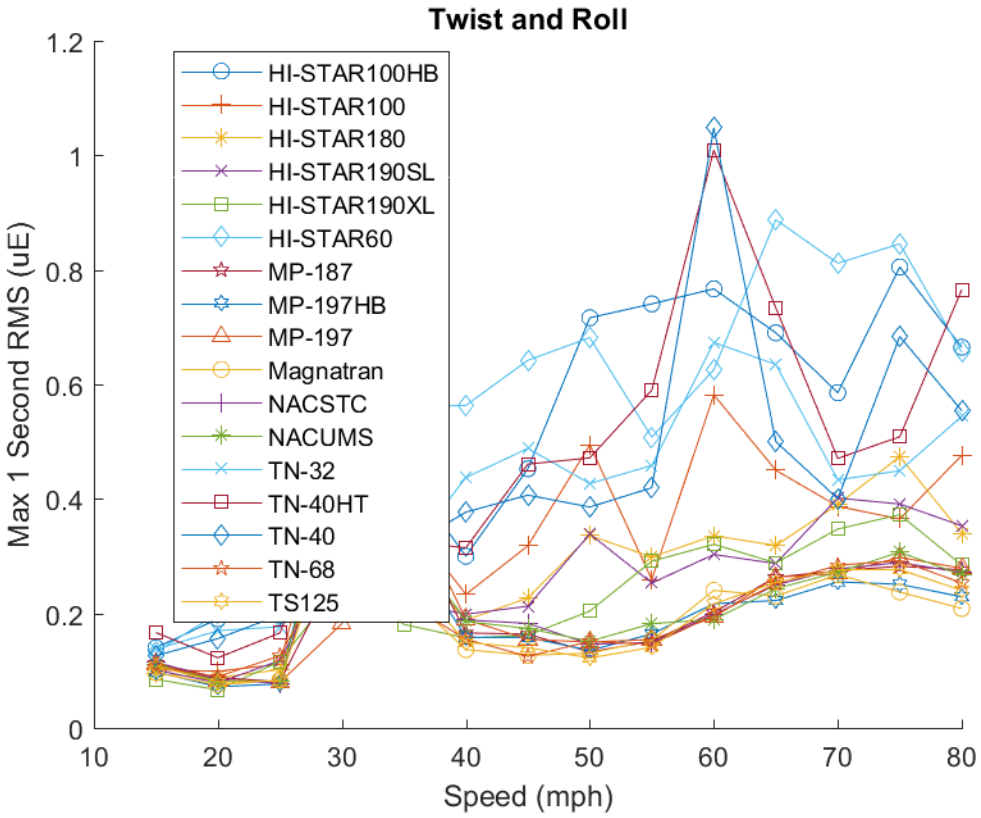

Figure B-19. Maximum one-second RMS value for high stiffness.

B-4. Twist and Roll – Lateral

B-4.1 Low Stiffness

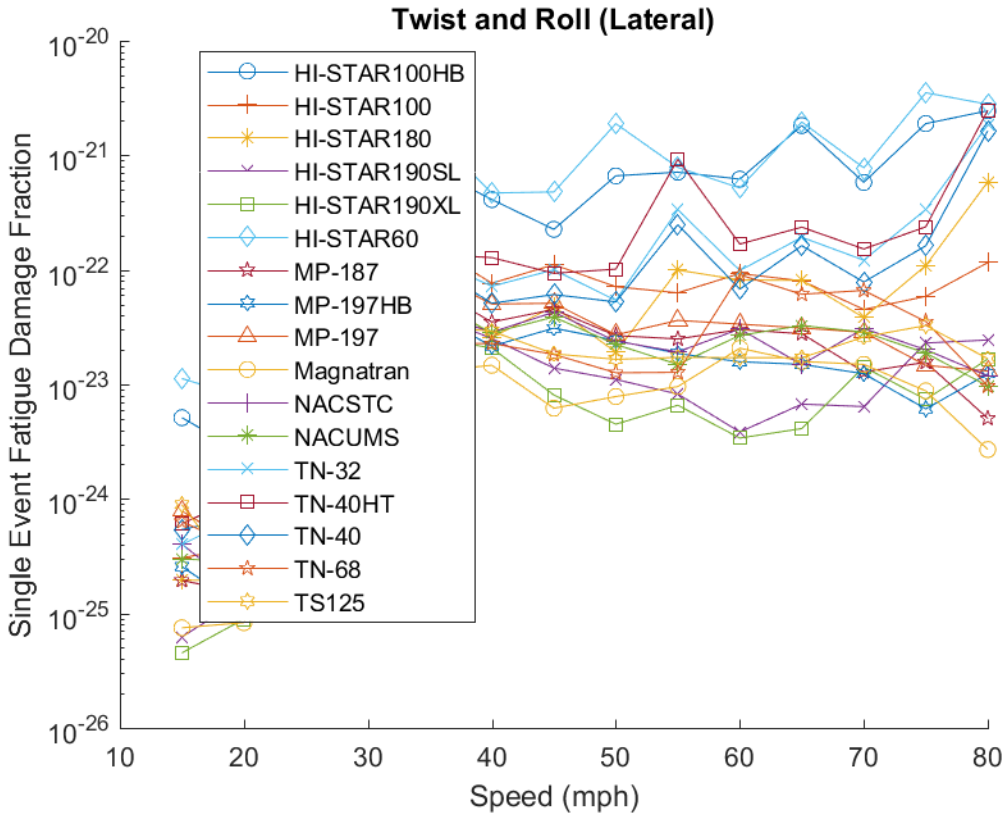

Figure B-20. Log-scale single event fatigue damage fraction for low stiffness.

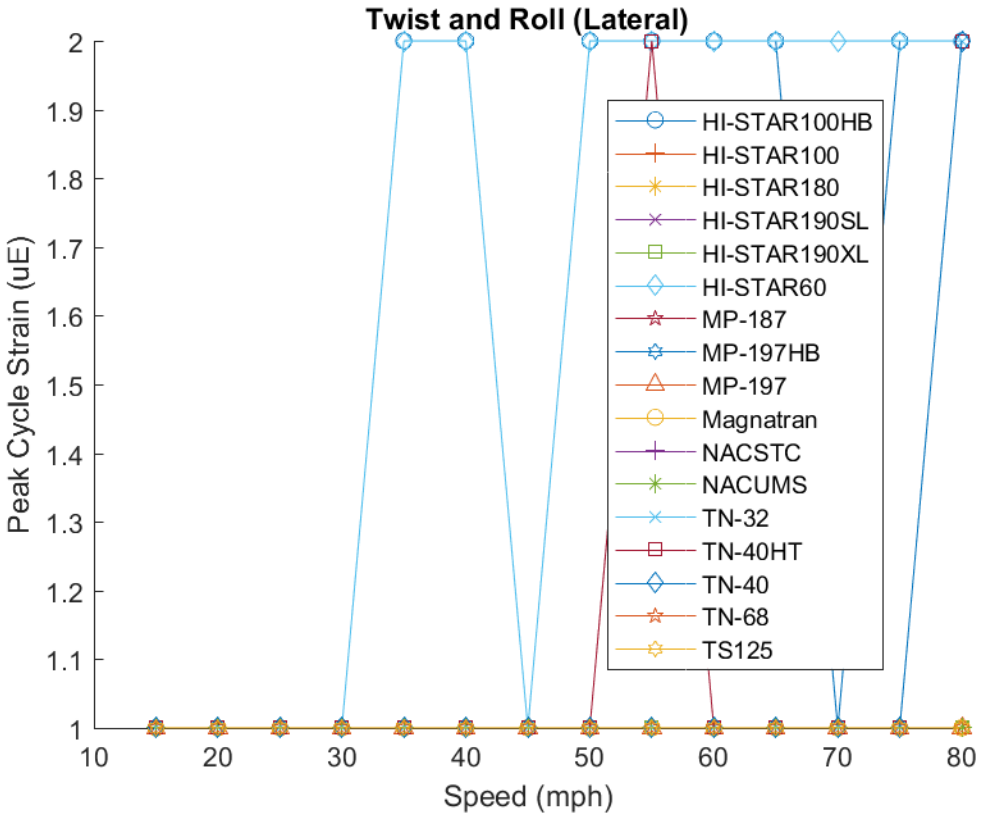

Figure B-21. Peak cycle strain for low stiffness.

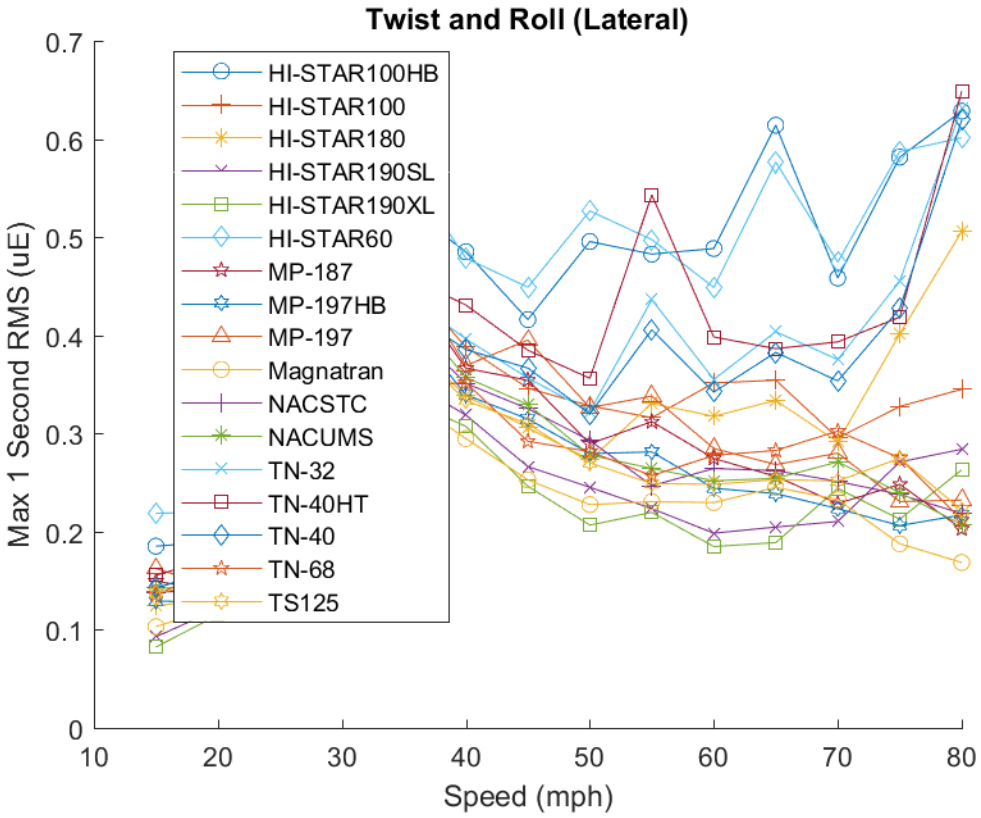

Figure B-22. Maximum one-second RMS value for low stiffness.

B-4.2 High Stiffness

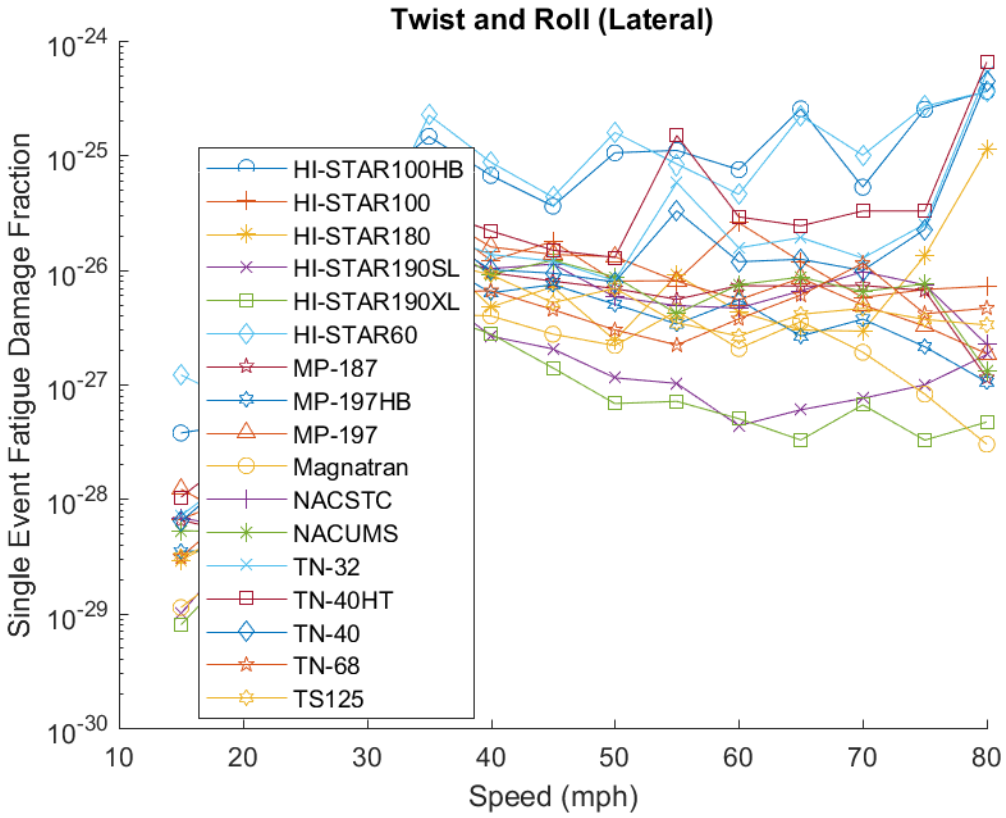

Figure B-23. Log-scale single event fatigue damage fraction for high stiffness.

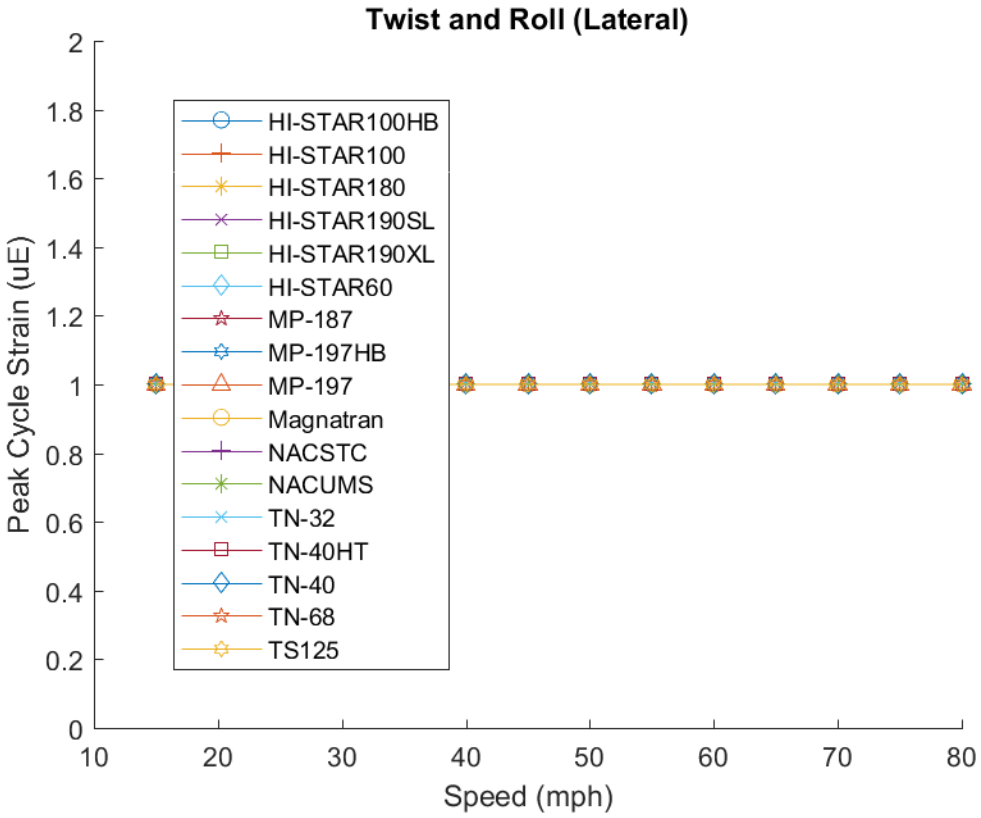

Figure B-24. Peak cycle strain for high stiffness.

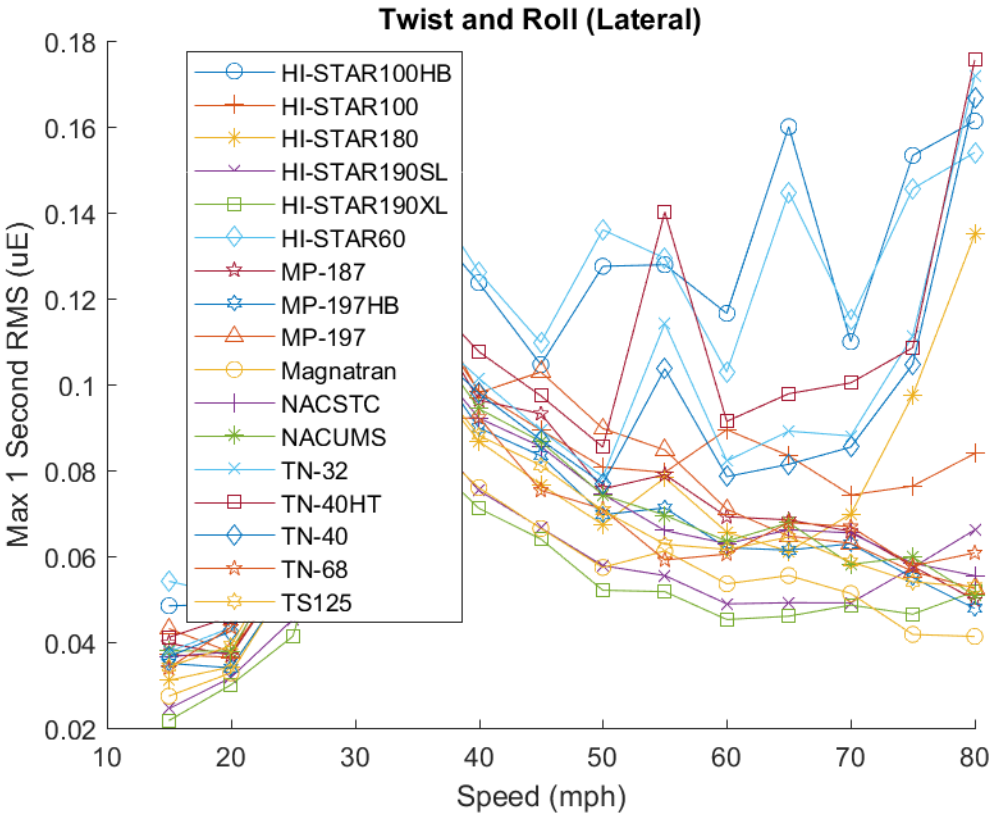

Figure B-25. Maximum one-second RMS value for high stiffness.